

Solar Transients

From The Sun to Earth

Coronal Bright Fronts, Radio Bursts, and

Energetic Protons

Mohamed ElSayed Nedal AbulAinain Mohamed



A thesis submitted for the degree of
Doctor of Philosophy

Institute of Astronomy and National Astronomical Observatory,
Bulgarian Academy of Sciences
Solar and Space Weather Research
March 6, 2024

Supervisor: Assoc. Prof. Kamen Asenov Kozarev

Acknowledgments

To my family, professors, and friends ...

Abstract

This interdisciplinary thesis advances our understanding of solar transients by investigating the early dynamics of Coronal Bright Fronts (CBFs), diagnosing solar Type III radio bursts, and forecasting Solar Energetic Proton (SEP) integral fluxes. Integrating these studies, we reveal the relationships among these phenomena and their implications for space weather forecasting and hazard mitigation. Our analysis of 26 CBFs, using the SPREADFAST framework and data from AIA and LASCO instruments, unveils temporal evolution, plasma properties, and compressional characteristics. The second study, employing LOFAR and PSP, characterizes 9 Type III radio bursts in the combined dynamic spectrum and 16 in the LOFAR spectrum alone. PFSS and MHD models offer insights into plasma conditions and magnetic fields, advancing our understanding of Type III radio bursts triggered by accelerated electrons associated with CBFs and solar flares. Addressing forecasting, a BiLSTM neural network using OMNIWeb data from 1976 to 2019 predicts SEP fluxes, emphasizing the hazardous influence of energetic particles on Earth and technology. This work provides a unified framework, highlighting the interconnected nature of solar transients and their collective impact on space weather.

Contents

1	Introduction	2
1.1	Background and Motivation	2
1.1.1	Coronal Waves	3
1.1.2	Solar Radio Bursts	4
1.1.3	Solar Energetic Protons (SEP) Forecasting	5
1.2	Objectives and Scope	6
1.3	Outlines	7
2	Remote Observations – Early-stages and Later-stages of Eruption	8
2.1	Introduction	8
2.2	EUV Observations	9
2.3	Data Analysis and Methods	12
2.4	CBF Kinematics and Geometric Modeling - Case Study May 11, 2011	13
2.4.1	Event Context	13
2.4.2	Low Corona Part	14
2.4.3	Middle/Outer Corona Part	17
2.5	Statistical Study	17
2.6	Wavetrack: A Flexible Framework for Automated Recognition and Tracking of Wave-Like Events in Solar Imagery	24
2.6.1	Overview	24
2.6.2	Image Filtering Techniques	26
2.6.3	Wavetrack for Coronal Wave Tracking	27
2.6.4	Wavetrack for Filament Tracking	27
2.6.5	Fourier Local Correlation Tracking (FLCT) Model	27
2.6.6	Results	27
2.7	Geomagnetic Storms: CME Speed De-Projection vs. In Situ Analysis	32
2.7.1	Overview	32
2.7.2	GSs and IP Phenomena	34
2.7.3	GSs and Solar Phenomena	34
2.7.4	PyThea 3D De-Projection Tool	35
2.7.5	Results	35
2.8	Discussion	42
2.8.1	CME Kinematics and Coronal Shockwave Characteristics	42
2.8.2	Statistical Study and Correlations	42
2.8.3	Unveiling Dynamic Coronal Features with Wavetrack	42
2.8.4	Coronal Bright Front (CBF) Kinematics	43
2.8.5	Geometric Centers (GC) and Centers of Mass (CM)	43
2.8.6	Projection Effects: The Challenge of Subjectivity in CME Speed Determination	43
2.8.7	Correlation between GSs, Coronal, and Near-Sun Parameters	44
2.8.8	Correlation between GSs and IP Parameters	44
2.8.9	GS Strength Forecasting: Unraveling Magnetic Structures	44
2.9	Conclusions	44

3 Solar Radio Observations: Integrating Space-based and Ground-based Data for Coronal Diagnostics	47
3.1 Introduction	47
3.2 Observations	49
3.2.1 PSP Observations	49
3.2.2 LOFAR Observations	52
3.3 Methods	52
3.3.1 Imaging of radio sources	52
3.3.2 Modeling	54
3.4 Results and discussion	54
3.4.1 Detection and characterization of type III radio bursts	54
3.4.2 Imaging of radio emission sources	54
3.4.3 Plasma diagnostics and magnetic field analysis	55
3.5 Summary and conclusions	56
4 Modeling and Forecasting of Solar Energetic Protons (SEP)	64
4.1 Introduction	64
4.2 Early-Stage SEP Acceleration by CME-Driven Shocks	66
4.2.1 Overview	66
4.2.2 Event Selection	68
4.2.3 Coronal SEP Acceleration	68
4.2.4 Input Data and Spectral Fitting	68
4.2.5 Transport of Accelerated SEPs and Comparison with ERNE Observations	69
4.2.6 Results and Discussions	70
4.2.7 Conclusions	71
4.3 Solar Proton Flux Forecasting with Deep Learning Models	71
4.3.1 Data preparation	71
4.3.2 Method	74
4.3.3 Results and discussion	76
4.3.4 Conclusions	86
5 Summary	90
5.1 Future Work	91
5.2 Definitions and Acronyms	91
A	92
A.1 Kinematics of the CBFs in the Middle/Outer Corona	92
A.2 Persistent Imaging Technique	92
A.3 Resolving the radio emission location ambiguity	92
A.4 Machine Learning Terminologies	119
A.4.1 Mathematical Representation of the LSTM NN Model	121
A.4.2 Evaluation Metrics	122
A.5 Deep Learning Model Configuration	122
A.6 Description of Skill Scores	123

List of Tables

2.1	List of the CBF events with their associated flares and CMEs.	9
2.2	Mean values and their standard deviation of the wave parameters in the radial direction and the lateral direction for the left and right flanks, at the front, peak, and back sides of the wave for the event occurred on May 11, 2011, in the SDO/AIA FOV.	16
2.3	Mean, median, and standard deviation of the shock parameters output, from the interaction of the S2M spheroid with the MAS MHD model results, for the shock's cap and flanks and for the whole shock surface, for the event on May 11, 2011.	17
2.4	Statistics of the EUV wave kinematics in the SDO/AIA FOV for the 26 events. LL and LR refer to the lateral left and right flanks, respectively. Rad refer to the radial front direction.	19
2.5	Characteristics of GSs, ICMEs, and IP Shock Waves. Magnetic Obstacle (MO) categorized as Flux-rope (Fr), Small rotation flux-rope (F-), Large rotation flux-rope (F+), Complex (Cx), or Ejecta (E). The timestamp includes month (mm), day (dd), and time (UT). Dst is measured in nT, speed in $km\ s^{-1}$, Δ (duration from ICME start to MO start) in hours, B_z in nT, hit locations denoted as n (nose), f (flank), */** (fast/slow speed), u (streamer/no clear ICME). Additional abbreviations: X: magnetic field/plasma density/temperature; d/u: downstream/upstream side of the shock interface; M_{ms} : Mach number. Credit goes to Miteva et al. (2023).	37
2.6	Parameters of the solar origin, SFs, and CMEs for GSs from Table 2.5. All times are in UT, speeds in $km\ s^{-1}$, AW and MPA in degrees. Credit goes to Miteva et al. (2023). . .	38
2.7	CME Speeds ($km\ s^{-1}$) for Observers 1 and 2. Credit goes to Miteva et al. (2023). . . .	38
2.8	Table displaying Pearson correlation coefficients among the GS Dst index, CME speed, and various solar parameters, with the respective sample sizes indicated in parentheses. Credit goes to Miteva et al. (2023).	39
2.9	Tabular representation of Pearson correlation coefficients between the GS Dst index and various parameters of IP phenomena. The data is derived from Wind satellite measurements, unless otherwise stated, with the corresponding sample sizes indicated in parentheses. Credit goes to Miteva et al. (2023).	41
3.1	Characteristics of the type III bursts detected via the automatic algorithm from the combined spectrum.	53
4.1	Summary of the performance results of the models for the validation and test sets.	84
4.2	Confusion matrix for the energy channel ≥ 10 MeV predictions in the test set.	84
4.3	Comparing the skill scores with previous models. The dashed entries mean the data is unavailable (Whitman et al. (2023) for more details).	85
4.4	The MSE/MAE for the validation and test sets over six forecasting windows.	85
A.1	Radial distances and densities at the first (R_1) and last (R_2) radio sources were obtained from the $2.5 \times$ Newkirk model, as well as their impact parameters r_1 and r_2 , respectively. .	118
A.2	Configuration of the ML model. (1) refers to the error value for 1-day forecasting. Same for (2) refers to 2-day forecasting, and (3) for 3-day forecasting. *In the 1D-CNN layer, 32 filters, a kernel size of 5, and strides of 1 were used.	123

List of Figures

2.1	Distribution of the source location of the CBFs on the solar disk. The blue dots are the events that we included in Table 2.1, while the orange dots are the events that we did not include in the table.	10
2.2	Illustration for the annulus method used to extract kinematic data from AIA images. (A) shows the full Sun disk with the relevant region highlighted for analysis (green sector). The white box outlines the AIA FOV. (B) displays the extracted annular region mapped onto polar coordinates, with the actual data extent marked by the white curve. Black lines indicate the directions used for measuring radial and lateral motions. (C) shows a stacked plot of intensity along the radial direction, with green markers highlighting intensity peaks and their corresponding distances from the CBF wavefront. The white lines represent the time interval during which the CBF is tracked within the AIA FOV. This figure is curated from (Kozarev et al. 2017).	11
2.3	J-map plots for the event of May 11, 2011, for the radial direction (middle plot) and the left and right flanks of the wave in the lateral heliocentric direction (the left and right plots, respectively). Blue, green, and orange filled symbols are the positions of the CBF front, peak, and back, respectively. The uncertainty of the average measurements is shown as red bars.	12
2.4	Synthetic shock model divided into three segments; the cap zone in blue and the flank zones are in red and green.	13
2.5	AIA running-difference images capture a coronal wave evolving over 9 minutes near the Sun’s western limb, exhibiting markedly changing intensity and structure as observed in 171, 193, and 211 Å.	14
2.6	Time-series kinematics of the CBF parameters for the front, peak, and back positions in the AIA FOV, with measurement uncertainties shown as small bars over the data points. The horizontal lines in the speed and acceleration panels denote the mean speeds and accelerations for the wave front, peak, and back with respective colors. The left and right columns represent the lateral kinematic measurements in the left and right flanks of the wave, respectively. The middle column represent the kinematic measurements in the radial direction.	15
2.7	Top panel – Height-time profile compiled from AIA and LASCO measurements for the event occurred on May 11, 2011, fitted with two CME kinematics models from the photosphere up to $17 R_{\odot}$. Middle panel – Difference between the fitting and the real observations. Bottom panel – Relative residuals in %.	18
2.8	Extrapolated radial kinematics for the event occurred on May 11, 2011, based on the ballistic model of Gallagher et al. (2003) up to $17 R_{\odot}$.	19
2.9	Dynamic spectra of the EUV waves kinematics in the AIA FOV. The panels from the top to the bottom are the wave speeds, acceleration, mean intensity, and thickness. The left column is for the lateral left flank, the central column is for the radial direction, and the right column is for the lateral right flank.	20
2.10	Histograms of along-field-lines model plasma parameters in the solar corona for all the 26 events. The vertical dashed red lines are the mean values.	22
2.11	Scatter plots of 8 coronal plasma-parameter pairs that exhibit parameterizable relationships. The <i>VSHOCKMEAN</i> is filtered to take only events with speeds $<4000 \text{ km s}^{-1}$	23
2.12	Time profile of the mean shock density jump for the 26 in-sample historical events studied with SPREAdFAST.	24
2.13	Time profile of the mean aspect ratio of the 26 historical events studied with SPREAdFAST.	25

2.14 Wavetrack images showing progression of a CBF and filament on May 11, 2011. Three snapshots captured ~2 minutes apart track the CBF and filament over time. Credit goes to Stepanyuk et al. (2022)	28
2.15 Wavetrack images of a May 11, 2011 eruption, with CBF mask applied. Four image pairs shown, separated by 2 minutes, to track CBF over time. Credit goes to Stepanyuk et al. (2022)	29
2.16 FLCT model output for four image pairs from Fig. 3. Left: the plane-of-sky velocity vectors. Right: plane-of-sky speed. Credit goes to Stepanyuk et al. (2022)	30
2.17 Analysis of the center of mass and geometric centers' motion during the May 11, 2011 event. The different rows present the X-, Y-, and R- positions for both GC and CM, the distance between GC and CM in kilometers, and the angle between these two points over time. Credit goes to Stepanyuk et al. (2022)	31
2.18 3D reconstructions of a CME (E03) using the spheroid, ellipsoid, and GCS model from the PyThea tool performed by observers 1 and 2 (top and bottom row, respectively). Credit goes to Miteva et al. (2023)	35
2.19 Scatter plot illustrating the relationship between the Dst index and CME speed, incorporating data from the SOHO/LASCO instrument (represented by filled circles) and 3D de-projections (depicted by empty circles). Credit goes to Miteva et al. (2023)	39
2.20 Comprehensive scatter plots illustrating the relationships between Dst index and various solar wind parameters, including Wind/ACE ICME speed, IP shock speed, Mach number, duration of sheath region, Bz, magnetic field jump, temperature jump, and density jump. Credit goes to Miteva et al. (2023)	40
 3.1 Radio dynamic spectra for a single burst obtained from multiple instruments. The top-left panel is from the LOFAR/LBA instrument, the top-right is from the PSP/FIELDS instrument, the bottom-left is from the STEREO/SWAVES instrument, and the bottom-right is from the Wind/WAVES. The vertical red dashed line denotes the start time of the burst.	50
3.2 Top view of the spacecraft positions in the ecliptic plane at 12:15 UT on April 3, 2019, with the Sun-Earth line as the reference point for longitude. The Earth's location is representative of the positions of LOFAR, Wind/WAVES, and GOES-15/XRS instruments. The spacecraft were connected back to the Sun by a 400 km/s reference Parker Spiral. The black arrow represents the longitude of AR12737 and the blue arrow represents the longitude of the AR12738. The gray dotted lines are the background Parker spiral field lines. The black dashed spiral shows the field line connected to the AR12737, and the blue dashed spiral is connected to the AR12738. The figure is generated using the Solar MAgnetic Connection Haus (Solar-MACH) tool (Gieseler et al. 2023)	51
3.3 Exploring the X-ray and extreme ultraviolet (EUV) emissions from the Sun. The top panel showcases a cutout region of the SDO/AIA 193 Å image of the solar disk along with the STEREO-A EUVI 195 Å point of view. The white curve is the limb of the solar disk as seen by AIA from the right side. The red and blue colors are the contours of the line-of-sight magnetogram from the SDO/HMI instrument. The levels are (50, 100, 150, 300, 500, 1000) Gauss. The middle panel shows the X-ray flux from the GOES-14 spacecraft shows minimum activity. The bottom panel shows the time series of the ESP Quad band from the SDO/EVE instrument, which shows the solar irradiance in the extreme ultraviolet (EUV) band.	58
3.4 Automatic detection of type III radio bursts from the combined radio dynamic spectrum of LOFAR and PSP instruments. The dashed horizontal lines separates the LOFAR frequency range (top) and the PSP frequency range (bottom)	59
3.5 Automatic detection of type III bursts observed by LOFAR. The red symbols along the fit lines are the (f, t) coordinates of the image snapshots shown in Figure 3.6.	59
3.6 Persistence imaging for the 16 type III bursts detected in the LOFAR dynamic spectrum. The label shows the observation frequencies in MHz and times in (minutes:seconds from 12:00:00 UT). Here, the color coding is not absolute, but rather each panel has its own color code.	60

3.7	Different viewing angles for the deprojection of the radio sources of the sixth burst using the $2.5 \times$ Newkirk electron-density model on the PFSS solution. The black arrow points toward the Earth's LOS. The yz plane is the POS as seen from the Earth. The red dashed line is a spline curve fit for the sources' centroids. The red, black, and blue curves are the open northern, closed, and open southern field lines, respectively. The opacity of the closed field lines is decreased for better visualization.	61
3.8	Synthesized maps of plasma parameters obtained using the FORWARD toolset, with the 70%-contour of radio emission of the sixth burst at the first timestamp (12:34:06.8 UT) at the frequency of 72.26 MHz depicted on top of the 2D POS cuts. The left column represents, from top to bottom, plasma density, magnetic field, and the total plasma dynamic pressure. The right column represents, from top to bottom, the temperature, plasma beta, and the Alfvén speed.	62
3.9	Coronal plasma parameters sampled from the 2D maps by the source centroids. The top panel shows (from left to right) the plasma density profiles from the MAS model, $2.5 \times$ Newkirk model, and the theoretical densities under the fundamental and harmonic assumptions, plasma temperature, and magnetic field. The bottom panel shows, from left to right, the total plasma dynamic pressure, Alfvén speed, and plasma beta. The x-axis is inverted to demonstrate a progression of increasing radial distance from the Sun as the observer moves towards the right.	63
4.1	Data splitting for all input features, showing the training, validation, and testing sets. Daily data from 1976-12-25 00:00 to 2019-07-30 00:00. The gray shading labels the solar cycles from SC21 to SC24.	73
4.2	Correlation matrices show the correlation between the features in the training, validation, and test sets.	74
4.3	Architecture of a single BiLSTM layer. The blue circles at the bottom labeled by $(x_0, x_1, x_2, \dots, x_i)$ are the input data values at multiple time steps. The purple circles, on the other hand, are the output data values at multiple time steps labeled by $(y_0, y_1, y_2, \dots, y_i)$. The dark green and light green boxes are the activation units of the forward layer and the backward layer, respectively. The orange and yellow circles are the hidden states at the forward layer and the backward layer, respectively. Both the forward and backward layers compose a single hidden BiLSTM layer. The figure is adopted from Olah (2015) .	75
4.4	Illustration of the sliding window technique for a sample of 10 timesteps, where each number denotes a distinct time step. As an example here, the input horizon (blue color) length is 4 timesteps and the output horizon length is 3 timesteps. The input window slides 1 time step at a time across the entire data sequence to generate 4 distinct input and forecast horizon pairs. The purple, orange, and green colors of the output horizon represent 1-day, 2-day, and 3-day ahead forecasting, respectively. The timesteps of 1-day ahead forecasting across the data sequences are then concatenated into a single timeseries list that is called 1-day ahead prediction. The same for 2-day and 3-day ahead.	75
4.5	Benchmarking of 10 models, shows the Huber loss for the validation and test sets.	76
4.6	<i>Left Panel</i> - The Huber loss vs. the number of training epochs for the BiLSTM model for the validation and test sets, for the 3 energy channels. <i>Middle Panel</i> - The mean absolute error (MAE); the model's metric vs. the number of training epochs. <i>Right Panel</i> - Shows how the learning rate of the Adam optimizer changes over the number of epochs.	77
4.7	Correlation between the model predictions and observations for 1-day, 2-day, and 3-day ahead for >10 MeV (top panel), >30 MeV (middle panel), and >60 MeV (bottom panel). The panels in the left column represent all the points of the validation set, those in the right column represent all the observations points with daily mean flux ≥ 10 pfu.	78
4.8	Same as Figure 4.7 but for the test set.	79
4.9	Comparison between the model outputs and observations of the test set for the 3 energy channels. In addition to the rolling-mean window correlation for 1-day ahead predictions.	80
4.10	The model's forecasts for the out-of-sample testing set for the >10 MeV channel are shown at forecast horizons of 1 day, 2 days, and 3 days ahead, using samples of data from December in selected years mentioned in the top-left side of the plots.	81
4.11	The model's forecasts for the out-of-sample testing set for the >30 MeV channel are shown at forecast horizons of 1 day, 2 days, and 3 days ahead, using samples of data from December in selected years mentioned in the top-left side of the plots.	82

4.12	The model's forecasts for the out-of-sample testing set for the >60 MeV channel are shown at forecast horizons of 1 day, 2 days, and 3 days ahead, using samples of data from December in selected years mentioned in the top-left side of the plots.	83
4.13	Temporal heatmap shows a comparison between the model outputs and observations for the rolling-mean window correlation of the integral >10 MeV proton flux at six predicting windows. The top panel represents the validation set and the bottom panel represents the testing set. The numbers on the y-axis are the mean R values.	86
4.14	Correlation between model predictions and observations for the integral >10 MeV proton flux of the validation (top two rows) and testing (bottom two rows) sets.	87
4.15	Correlation between model predictions and observations for the integral >10 MeV proton flux of the testing set.	88
4.16	Comparison between the model's forecast and the observations for the integral >10 MeV proton flux at forecast horizon of 1 hour ahead. The top panel represents a sample of the validation set and the bottom panel represents a sample of the testing set.	88
A.1	Top panel: Height-time profile on June 12, 2010, using AIA and LASCO data, fitted with two CME kinematics models. Middle panel: Fitting vs. real observation difference. Bottom panel: Relative residuals in %.	93
A.2	Same for the event on August 14, 2010.	94
A.3	Same for the event on December 31, 2010.	95
A.4	Same for the event on January 28, 2011.	96
A.5	Same for the event on March 7, 2011.	97
A.6	Same for the event on August 4, 2011.	98
A.7	Same for the event on August 8, 2011.	99
A.8	Same for the event on March 7, 2012.	100
A.9	Same for the event on March 13, 2012.	101
A.10	Same for the event on July 23, 2012.	102
A.11	Same for the event on April 21, 2013.	103
A.12	Same for the event on May 13, 2013.	104
A.13	Same for the event on May 15, 2013.	105
A.14	Same for the event on May 22, 2013.	106
A.15	Same for the event on June 21, 2013.	107
A.16	Same for the event on October 25, 2013.	108
A.17	Same for the event on December 12, 2013.	109
A.18	Same for the event on December 28, 2013.	110
A.19	Same for the event on July 8, 2014.	111
A.20	Same for the event on December 5, 2014.	112
A.21	Same for the event on May 12, 2015.	113
A.22	Same for the event on September 20, 2015.	114
A.23	Same for the event on October 29, 2015.	115
A.24	Same for the event on November 9, 2015.	116
A.25	Same for the event on April 1, 2017.	117
A.26	Schematic shows the locations of the radio sources for the +Z and -Z solutions of Equation 3.4. The Sun is located in the middle as an orange circle, with a horizontal dashed black line representing the POS. The vertical dashed green line represents the Sun-Earth LOS. The dashed blue and red circles represent the plasma spheres of density equivalent to the observation frequencies of the innermost and outermost radio sources at R_1 and R_2 , respectively, under the Newkirk model assumption of spherically-symmetric density distribution. The impact parameters r_1 and r_2 are the projection of R_1 and R_2 on the POS. The dot-dashed blue and red circles are the circles passing through the impact parameters r_1 and r_2 , respectively.	119
A.27	Cut of the flux density at 700 kHz observed by Wind (left panel) and STEREO-A (right panel). Note: for STEREO-A, there is no exact frequency channel at 700 kHz; therefore we selected the nearest one (675 kHz).	120

Chapter 1

Introduction

1.1 Background and Motivation

The Sun, an ordinary main-sequence star situated at the center of our solar system, exhibits various forms of activity and variability on multiple spatial and temporal scales. Some of the main manifestations of solar activity relevant to space weather research are transient energetic eruptive phenomena such as solar flares, Coronal Mass Ejections (CME), and wide-ranging emissions of electromagnetic radiation and energetic particles (Schwenn 2006; Pulkkinen 2007). These eruptive events originate due to the sudden release of free magnetic energy stored in complex, twisted or sheared magnetic field structures in the solar atmosphere (Moore et al. 2001; Priest & Forbes 2007; Zhang et al. 2012; Amari et al. 2014). The energetic phenomena are driven by the rapid dissipation of magnetic energy via magnetic reconnection which can accelerate large numbers of electrons to relativistic energies and heat plasma to tens of million Kelvin (Shibata & Magara 2011; Benz 2017).

The eruptive solar events drive major disturbances in the near-Earth space environment and planetary environments across the heliosphere, collectively termed *space weather* (Schrijver & Siscoe 2010a; Eastwood et al. 2017). Enhanced fluxes of Solar Energetic Particles (SEPs), plasma ejecta, and electromagnetic radiation emitted during solar eruptions can impact the geomagnetic field, radiation belts, ionosphere, thermosphere, and upper atmosphere surrounding the Earth (Schwenn 2006; Pulkkinen 2007). Adverse effects range from disruption of radio communications to damage of satellites, power grid failures, aviation hazards due to radiation risks for airline crew and passengers, and increased radiation exposure for astronauts (Lanzerotti 2001). The societal dependence on space-based infrastructure has increased exponentially, escalating the vulnerability to space weather disturbances. Recent studies estimate a severe space weather event could lead to trillion-dollar economic damages in the US alone (Oughton et al. 2017). Besides the near-Earth space environment, solar eruptive transients also drive adverse space weather effects across the solar system impacting activities such as deep space exploration and astronomy (Lilensten et al. 2014).

Therefore, advancing our understanding of the origins and propagation characteristics of solar eruptive phenomena, as well as quantifying their impacts on geospace and planetary environments, has become an extremely important pursuit for nations worldwide. Fundamental research seeks to uncover the physical processes involved using observations coupled with theory and modeling. Concurrently, significant efforts are underway to develop next-generation space environment modeling and forecasting capabilities for predicting the impacts of solar variability. The field combining these research and predictive aspects related to Sun-Earth connections is broadly termed *heliophysics* (Schrijver & Siscoe 2010b). It encompasses understanding the fundamental solar, heliospheric and geospace plasma processes; coupling across multiple spatial and temporal scales; quantifying the impacts on humanity's technological systems and space-borne assets; and utilizing this knowledge to prevent or mitigate adverse effects (Schrijver et al. 2015; Schrijver 2015). NASA's Living With a Star program and the National Science Foundation's Space Weather activities exemplify strategic efforts to advance scientific understanding and predictive capabilities across the interconnected domains of heliophysics (Brewer et al. 2002).

The present thesis focuses on studying several important phenomena related to solar eruptive activity and its impacts from the perspective of heliophysics research and space weather. The specific topics investigated include: (1) the propagation and evolution characteristics of large-scale coronal disturbances termed Extreme Ultra-Violet (EUV) waves that are triggered by CMEs and solar flares; (2) the generation, propagation and plasma characteristics of solar radio bursts emitted by accelerated electron beams

traveling along open magnetic field lines in the corona; (3) the forecasting of SEP events which constitute one of the major components of space radiation hazards at Earth.

These diverse topics are united by the common theme of seeking to uncover the origins and propagation mechanisms of key transient phenomena resulting from solar eruptions, utilizing observational data, analytical theory and modeling, and data science techniques. The phenomena have been studied for several decades using observations from multiple space missions, but gaps persist in our understanding of their underlying physics and space weather impacts. The thesis aims to provide new insights that help address some of the outstanding questions, guided by the overarching goals and framework of heliophysics research. Each research topic investigated in this thesis is explored in detail within its dedicated chapter. These chapters delve into the relevant background, significance, observational challenges, and knowledge gaps associated with each topic. Additionally, a concise overview of key literature related to each topic is provided here, followed by a more in-depth review within each specific chapter.

1.1.1 Coronal Waves

Coronal waves, or Coronal Bright Fronts (CBFs), also known as EUV waves, are large-scale arc-shaped bright fronts or disturbances observed propagating across significant portions of the solar corona following the eruption of CMEs and solar flares (Thompson et al. 1998; Nindos et al. 2008; Vršnak & Cliver 2008; Magdalenić et al. 2010a; Veronig et al. 2010; Warmuth 2015). They are best observed in EUV and white-light coronal emission, as well as in radio wavelengths, spanning distances of up to several 100 Mm with speeds ranging between $100\text{-}1000 \text{ km s}^{-1}$, faster than the local characteristic speed in the solar corona, transforming into shock waves (Pick et al. 2006; Thompson & Myers 2009; Nitta et al. 2013; Liu & Ofman 2014). These structures consist of piled-up plasma with higher density, making them appear brighter in white-light images.

The discovery of coronal waves dates back to observations obtained with the Extreme ultraviolet Imaging Telescope (EIT) instrument on the Solar and Heliospheric Observatory (SOHO) launched in 1995, appearing as bright propagating fronts in 19.5 nm wavelength imaging of Fe XII emission lines formed at $\sim 1.5 \text{ MK}$ plasma (Thompson et al. 1998). Subsequent studies based on SOHO/EIT and the Transition Region and Coronal Explorer (TRACE) imaging found correlations between coronal waves and CMEs, favoring an interpretation as fast-mode magneto-hydrodynamic (MHD) waves driven by CME lateral expansions (Biesecker et al. 2002).

Since 2010, the initiation and evolution of coronal waves are being exquisitely observed with unprecedented resolution by the Atmospheric Imaging Assembly (AIA) on the Solar Dynamics Observatory (SDO) spacecraft (Lemen et al. 2012) across multiple EUV passbands sensitive to a wide temperature range (Nitta et al. 2013). Alternatively, shock waves can be indirectly observed through the detection of type II radio bursts, which are commonly associated with shock waves in the solar corona Vršnak & Cliver (2008). The AIA instrument has provided valuable insights into the dynamics of the low solar corona over the past decade, thanks to its exceptional spatial and temporal resolution. Equipped with telescopes observing the solar disk in bands 193 and 211 Å, the AIA instrument has demonstrated its ability to distinguish compressive waves in the lower corona Patsourakos et al. (2010); Ma et al. (2011); Kozarev et al. (2011). These observations offer valuable information about the kinematics and geometric structure of CBFs. To accurately study the evolution of the wave's leading front, observations off the solar limb are preferred to mitigate projection effects, which may introduce ambiguities in estimating time-dependent positions and the global structure of the wave Kozarev et al. (2015).

In situ observations of shock waves have revealed their classification into quasi-parallel, quasi-perpendicular, sub-critical, and super-critical shocks based on the angle between the wavefront normal vector and the upstream magnetic field lines Tsurutani (1985). Quasi-parallel shocks have a shock-field angle (θ_{BN}) smaller than 45° , while quasi-perpendicular shocks have θ_{BN} greater than 45° . Supercritical shocks, often associated with accelerated particles, are promising candidates for generating type II radio bursts Benz & Thejappa (1988). However, obtaining accurate estimates of shock strength and obliquity solely from remote observations is challenging.

Coronal waves exhibit diverse morphology and kinematics ranging from circular fronts to narrow jets or expanding dome-like structures (Veronig et al. 2010). A taxonomy of wave properties based on extensive observational surveys can be found in papers by Muhr et al. (2014) and Nitta et al. (2013). However, despite being observed for over two decades since their serendipitous discovery, fundamental questions remain regarding the physical nature and drivers of coronal waves (Chen 2016; Vršnak & Cliver 2008; Warmuth 2015). The debate centers around two competing interpretations – the wave versus pseudo-wave (or non-wave) models. The wave models envisage coronal waves as fast-mode MHD

waves or shocks that propagate freely after being launched by a CME lateral over-expansion or an initial flare pressure pulse (Wills-Davey et al. 2007; Vršnak & Cliver 2008). The pseudo-wave models interpret them as bright fronts produced by magnetic field restructuring related to the CME lift-off process rather than a true wave disturbance (Delannée & Aulanier 1999; Chen et al. 2002). Extensive observational and modeling studies have been undertaken to evaluate the two paradigms (Patsourakos & Vourlidas 2012; Long et al. 2017), but a consensus remains elusive. Addressing these outstanding questions related to the nature and origin of coronal waves is imperative, since they are being incorporated into models as a primary agent producing SEP events and geomagnetic storms following CMEs (Rouillard et al. 2012; Park et al. 2013). Their use as a diagnostic tool for CME and shock kinematics predictions in these models requires discriminating between the different physical mechanisms proposed for their origin.

The present thesis undertakes an extensive statistical analysis of coronal EUV wave events observed by SDO to provide new insights into their kinematical properties and relationship to CMEs. We focus on analyzing their large-scale evolution as a function of distance and direction from the source region, leveraging the extensive EUV full-disk imaging capabilities of SDO spanning nearly a decade. Statistical surveys to date have mostly focused on initial speeds and morphological classifications rather than large-scale propagation characteristics. Our study aims to uncover systematic trends in their propagation kinematics using a combination of techniques and data products, as well as exploring relationships between different pairs of kinematical parameters compared to previous works. We also comprehensively evaluate associations with CME and solar flare parameters in order to discriminate between wave and pseudo-wave origins. The results have important implications for incorporating coronal waves into predictive models of CMEs and SEP events for future space weather forecasting.

1.1.2 Solar Radio Bursts

Solar radio emissions have been the subject of extensive study and research due to their connection with solar activity and their potential impact on Earth's atmosphere and technology. One area of particular interest is solar radio bursts, which are intense bursts of electromagnetic radiation originating from the Sun. These bursts can be classified into different types based on their characteristics and associated phenomena. Solar radio bursts, including type III bursts, serve as remote diagnostics for the study of energetic electrons within the solar corona. These bursts result from transient energetic electron beams injected into the corona, which then propagate along interplanetary magnetic field (IMF) lines (Ergun et al. 1998; Pick et al. 2006; Reid 2020). As these electron beams traverse the corona, they induce plasma waves, also known as *Langmuir waves*, which subsequently transform into radio emission at the local plasma frequency or its harmonic components (Melrose 2017). The frequency of the radio emission is directly linked to the plasma density, making type III bursts a valuable tool for investigating the inner heliosphere and understanding the underlying processes that drive solar active phenomena, such as CMEs and solar flares (Reid & Ratcliffe 2014; Kontar et al. 2017). These bursts offer insights into the acceleration of energetic electrons in the corona and their transport along magnetic field lines (Reid & Ratcliffe 2014). The generation of electromagnetic emission at radio frequencies through plasma emission mechanisms is a key aspect of solar radio bursts, shedding light on the dynamic interplay between non-thermal electron distributions and the ambient plasma (Melrose 1980).

Pioneering observations of solar radio bursts were made in the 1940s leading to their classifications (Wild et al. 1963). Subsequent spectrographic studies uncovered emission mechanisms, source regions and particle diagnostics (Suzuki & Dulk 1985). Magnetic reconnection models of flares provided theoretical explanations for particle acceleration generating radio bursts (Holman et al. 2011). Radio imaging spectroscopy using interferometric imaging arrays coupled with high time-frequency resolution spectrometers enables tracking radio sources as a function of frequency and position on the Sun, yielding particle acceleration locations and trajectories through the corona into interplanetary space (Krucker et al. 2011; Klassen et al. 2003a,b). This provides a unique diagnostic of energetic particle transport from the Sun to the Earth which is crucial for improving SEP forecasting models.

Different types of bursts are observed, classified based on their spectral characteristics as documented in radio burst catalogs (Wild et al. 1963). The present thesis focuses on detailed analysis of solar type III radio bursts and their associated phenomena. In radio spectrograms, type III radio bursts manifest as intense enhancements of radio flux exceeding background levels. These bursts exhibit rapid frequency drifts over timescales ranging from seconds to minutes, reflecting the underlying plasma dynamics (Reid & Vilmer 2017). Notably, they are observable across a broad spectrum of frequencies, spanning from GHz to kHz, and corresponding wavelengths extending from metric to decametric (Wild & McCready 1950; Lecacheux et al. 1989; Bonnin et al. 2008). This phenomenon is detectable by ground-based instruments

on Earth as well as various spacecraft within the heliosphere, underscoring the significance of plasma dynamics in their manifestation.

Furthermore, these bursts arise from the propagation of energetic electron beams ejected during magnetic reconnection. The observed rapid drift from high to low frequencies over seconds directly corresponds to the propagation of these electron beams from the Sun's lower corona, outward along open magnetic field lines, potentially extending beyond 1 astronomical unit (AU). This characteristic signature signifies the initial escape of flare-accelerated electrons into interplanetary space, making type III bursts a crucial precursor for subsequent SEP activity (Cane et al. 2002; MacDowall et al. 2003). Investigating their source locations, plasma environments, and beam kinematics based on multi-wavelength observations coupled with plasma emission theory is therefore vital for improved understanding of coronal particle acceleration and transport processes relevant for SEP forecasting models.

While type III bursts have been studied for over 50 years since their initial discovery by Wild & McCready (1950); Wild (1950a,b), gaps persist in our understanding of their exciter beams and emission mechanisms. Key outstanding questions pertain to the detailed electron acceleration and injection sites, beam configurations and energy spectra, drivers of burst onset and duration, and the role of density fluctuations in propagating beams (Reid & Kontar 2018b,a; Li & Cairns 2012). Recent work combines imaging and spectral data with modeling to constrain radio burst excitors in unprecedented detail (Chen et al. 2013; Kontar et al. 2017). Key challenges remain in reconciling emission models with observations and predicting radio diagnostics. Advancing our knowledge of these aspects through coordinated observations and modeling can help constrain the predictions of energetic electron properties based on radio diagnostics. The present work undertakes detailed investigation of a solar type III burst combining imaging and radio spectral data to derive electron beam trajectories and coronal densities, and models the emission sources. The results provide insights into the corona plasma environment and energetic electron transport relevant for SEP forecasting applications.

1.1.3 Solar Energetic Protons (SEP) Forecasting

Solar energetic protons are high-energy particles that are believed to originate from the acceleration of particles in the solar corona during solar flares and CMEs (Aschwanden 2002; Lin 2005, 2011; Klein & Dalla 2017; Kahler et al. 2017). They are typically characterized by their high energy levels – with some particles having energies in the relativistic GeV/nucleon range – and their ability to penetrate through spacecraft shielding, causing radiation damage (Reames 2013; Desai & Giacalone 2016). The fluence and energy spectrum of SEP are influenced by several factors, including the strength of the solar flare or CME that produced them, and the conditions of the interplanetary environment (Kahler et al. 1984, 1987; Debrunner et al. 1988; Miteva et al. 2013; Trottet et al. 2015; Dierckxsens et al. 2015; Le & Zhang 2017; Gopalswamy et al. 2017). In this thesis, I will refer to solar energetic protons as SEPs since they are the major constituents of solar energetic particle events.

SEP exhibit a strong association with the solar cycle, with the frequency and flux of SEP events peaking during the maximum phase of the solar cycle (Reames 2013). This is thought to be due to the increased activity of the Sun during this phase, which leads to more frequent and powerful flares and CMEs. Previous studies have shown a relationship between the occurrence frequency of SEP and the sunspot number (SN; Nymmik, 2007; Richardson et al., 2016). However, the exact relationship between the solar cycle and SEP is complex and not fully understood. Hence, more work is needed to better understand this connection, as previous studies have reported intense SEP events during relatively weak solar activity (Cohen & Mewaldt 2018; Ramstad et al. 2018).

SEP have been a subject of interest and research in heliophysics for decades. It is hypothesized that shock waves generated in the corona can lead to an early acceleration of particles. However, SEP have sufficient energy to propagate themselves by *surfing* the IMF, and therefore, the expanding CME is not necessary for their transport (Reames 2000; Kóta et al. 2005; Kozarev et al. 2019, 2022). While this theory has gained acceptance, there is an ongoing debate among scientists over the specific mechanisms and conditions responsible for SEP production and acceleration.

The creation, acceleration, and transport mechanisms of SEP are complex and involve a combination of magnetic reconnection, shock acceleration, and wave-particle interactions (Li et al. 2003, 2012; Ng et al. 2012). The specific mechanisms responsible for SEP production and acceleration can vary depending on the type and strength of the solar event that triggered them. Further research is imperative to better understand the processes involved in the production and transport of SEP in the heliosphere. This will facilitate the development of more precise models that assist in minimizing the impact of SEP on astronauts and space-based assets.

The arrival of SEPs in the near-Earth space environment constitutes one of the major components of adverse space weather (Reames 1999; Vainio et al. 2009). Solar energetic particle events consist primarily of protons (and some heavy ions), accelerated to very high energies by CME-driven shock waves during large solar eruptive events. The gradual SEP events, so called due to their long durations from several hours to a few days, involve protons accelerated to energies above ~ 10 MeV which can penetrate Earth's magnetic field and atmosphere, posing radiation hazards to humans and equipment in space and at polar regions (Reames 2013). Impulsive SEP events, on the other hand, are rapid releases of energetic particles, dominated by electrons and ions like Helium-3 (${}^3\text{He}$), associated with impulsive flares and magnetic reconnection events on open field lines in the Sun's corona (Nitta et al. 2015). These events are characterized by enrichments of ${}^3\text{He}$ compared to the normal Helium-4 (${}^4\text{He}$) ratio, along with enhancements of heavy elements like Iron (Fe) and highly charged particles, indicating temperatures around 5–10 million Kelvin (Reames 2021).

Initial SEP forecasting models were based on empirical correlations between proton intensity profiles and CME or solar flare properties (Kahler et al. 2007). The complex physics of CME shock acceleration combined with modeling the transport of SEPs through turbulent interplanetary magnetic fields presents major challenges for first-principles based SEP forecasting models (Aran et al. 2006; Laitinen & Dalla 2017). As an alternative approach, empirical and data-driven models based on statistical/machine learning techniques applied to historical SEP event data have shown considerable promise for operational forecasting over the past decade (Laurenza et al. 2009; Camporeale 2019; Kozarev et al. 2022). This motivates detailed investigation of data-driven SEP forecasting models using state-of-the-art machine learning algorithms which can outperform conventional empirical methods.

The emergence of deep learning techniques has enabled application of sophisticated machine learning models to SEP forecasting, yielding improved predictions since they can capture complex nonlinear relationships between parameters which has been leveraged for diverse space weather applications recently (Florios et al. 2018; Camporeale 2019). Opportunities exist for novel forecasting approaches utilizing deep learning algorithms and expanded input parameters. However, applications to SEP forecasting problems are still limited, presenting an important research gap which I aim to address in this thesis. I developed deep Neural Network (NN) models for predicting the intensity profile of energetic protons in three integral energy channels; >10 , >30 , and >60 MeV, utilizing various sets of inputs parameters. This will be explained in more detail in the respective chapter. The developed model is trained and tested on a database of historical SEP events spanning the previous four solar cycles, with the goal of producing SEP flux forecasts over three output windows; one-day, two-day, and three-day in advance of particle arrivals near Earth. Such capability can provide actionable information for mitigating radiation effects from extreme SEP events. The study demonstrates the potential of state-of-the-art machine learning algorithms to achieve significant enhancement of SEP forecasting capabilities building upon conventional empirical methods.

1.2 Objectives and Scope

This PhD thesis delves into various aspects of solar phenomena, including Coronal Bright Fronts (CBFs), solar type III radio bursts, and Solar Energetic Particle (SEP) events. The overarching goal is to gain a deeper understanding of the physical processes occurring in the Sun's corona and how they relate to solar eruptions and energetic particle radiation.

Coronal Bright Fronts (CBFs)

One area of research focuses on CBFs, the leading edges of CMEs observed in the lower solar corona. The specific objectives here are to:

- Analyze and characterize the properties of historical 26 CBF events observed by the AIA instrument onboard the SDO spacecraft between 2010 and 2017.
- Investigate the relationship between the kinematics of these CBFs and the surrounding coronal plasma environment.

This research utilizes data from the AIA instrument in the EUV 193 Å band. Techniques like base-difference images, J-maps, and the SPREAdFAST framework are employed to derive kinematic measurements. 3D geometric models of the CBF wavefronts are generated based on these measurements.

Additionally, potential shock properties within the CBFs are explored by fitting a geometric spheroid surface model to the kinematic data.

To extend the analysis of EUV wave kinematics into the middle corona, existing models developed by Byrne et al. (2013) and Gallagher et al. (2003) are incorporated. Finally, the research explores relationships between modeled plasma parameters within the corona to understand the underlying physical mechanisms driving the CBF dynamics.

Solar Radio Bursts

A separate area of research focuses on the generation and propagation of type III radio bursts. Here, the objectives are to:

- Unravel the physical mechanisms responsible for the production of type III radio bursts.
- Identify the location of the sources of these bursts within the solar corona.
- Investigate the relationships between the observed radio bursts, coronal magnetic field structures, and the surrounding coronal plasma environment.

The scope of this research is limited to analyzing a specific set of type III bursts observed on April 3, 2019, utilizing data from the LOFAR and PSP instruments. This analysis involves:

- Comparing the observations with existing models of the solar corona to identify discrepancies and limitations of these models.
- Exploring potential sources for the observed radio bursts, focusing on small-scale reconnection events and active regions on the solar surface.

Solar Energetic Particle (SEP) Forecasting

The final strand of this research tackles the challenge of forecasting SEP integral flux. Here, I aim to:

- Develop a cutting-edge BiLSTM neural network model capable of predicting the daily SEP integral flux over a 3-day window.
- Specifically, the model will predict SEP intensity for three energy ranges: >10 MeV, >30 MeV, and >60 MeV.
- I then evaluate the BiLSTM model's performance by comparing it to established forecasting models.

The development and evaluation process leverages historical SEP data encompassing the past four solar cycles. Here is a breakdown of the specific scope:

- Solar and interplanetary magnetic field data serve as the input for the BiLSTM model.
- The model's accuracy is assessed for 1-day, 2-day, and 3-day SEP flux forecasts.
- A combination of metrics and correlation analysis between predicted and observed SEP flux is used to gauge the model's effectiveness.

By investigating these diverse aspects of solar activity, this research contributes to a deeper understanding of the Sun's dynamics and ultimately improves our ability to predict potentially hazardous space weather events impacting Earth.

1.3 Outlines

This dissertation investigates several aspects of CMEs, solar radio bursts, and SEP events. It explores the kinematics of CBFs in the low and middle solar corona, analyzing 26 CBFs associated with SEP events near Earth, observed between 2010 and 2017, to understand their kinematics evolution. The analysis utilizes the SPREAdFAST framework to gain statistical insights into the shocks and plasma parameters of CBFs, contributing to space weather forecasting and SEP event studies (Chapter 2). Additionally, a separate study within this chapter presents a method for recognizing and tracking solar

phenomena like CME-driven shock waves using wavelet transform and image filtering. This versatile method, demonstrated on SDO/AIA telescope observations, holds promise for developing deep-learning solar datasets. Another collaborative study in Chapter 2 investigates the correlation between geomagnetic storm intensity and solar and IP phenomena. This research, which utilizes 3D reconstructions of CMEs via the PyThea framework, highlights the importance of considering CME speed and magnetic structure orientation for accurate geomagnetic storm strength prediction.

Chapter 3 focuses on solar type III radio bursts by analyzing an event observed on April 3, 2019. This research, which utilizes multi-wavelength data from LOFAR and PSP alongside PFSS and MHD models, successfully identifies and characterizes 16 type III radio bursts. It determines their frequency drift, electron beam speeds, and a common origin within a short timeframe. The study also provides valuable insights about plasma conditions along the bursts' trajectories, revealing discrepancies compared to theoretical expectations.

Chapter 4 delves into SEP events. One collaborative study models the acceleration and transport of SEPs during coronal shock events using telescopic observations and dynamic models. This research, conducted through the SPREAdFAST framework, simulates SEP acceleration and heliospheric connectivity, validating results with observations at 1 AU. Another study in this chapter addresses the crucial need for forecasting the integral flux of SEPs which is critical for safety in communication, navigation, space exploration, and aviation. This research develops SEP forecasting models using a BiLSTM neural network model based on various input parameters. The model's effectiveness is validated through out-of-sample testing and benchmarking against other existing models.

Finally, Chapter 5 summarizes the key findings presented throughout the dissertation.

Chapter 2

Remote Observations – Early-stages and Later-stages of Eruption

2.1 Introduction

Coronal Mass Ejections (CMEs) stand out as one of the prevalent expressions of solar activity. Typically discerned through white light observations (Vourlidas et al. 2003; Zhang & Dere 2006; Bein et al. 2011). CMEs exhibit various facets in ultraviolet and radio wavelengths (Bastian et al. 2001; Veronig et al. 2010). Notably, the early phases of CMEs are effectively observed in EUV light, facilitated by instruments like the Atmospheric Imaging Assembly (AIA) aboard the Solar Dynamics Observatory (SDO) (Lemen et al. 2011; Pesnell et al. 2012). These eruptions may induce shock waves in the solar corona when their propagation velocities surpass the local speed of information, typically represented by the fast magnetosonic speed. Such shock waves are visibly identified in EUV as EUV waves (Thompson et al. 1998), also acknowledged as Coronal Bright Fronts (Long et al. 2011, CBFs).

CBFs are disturbances that propagate over significant portions of the solar disk and off the solar limb. These waves can reach speeds faster than the local characteristic speed in the solar corona, transforming into shock waves. They are primarily driven by CMEs or solar flares (Thompson et al. 1998; Veronig et al. 2010; Vršnak & Cliver 2008; Magdalenić et al. 2010b; Nindos et al. 2011). In both radio and white-light observations, CBFs often appear as dome-shaped structures moving at speeds on the order of several hundred $km\ s^{-1}$ (Pick et al. 2006; Nindos et al. 2008; Thompson & Myers 2009). These structures consist of piled-up plasma with higher density, making them appear brighter in white-light images. Observing and studying coronal shock waves remotely is typically done through EUV observations using space-based instruments such as the AIA on the SDO spacecraft. Alternatively, shock waves can be indirectly observed through the detection of type II radio bursts, which are commonly associated with shock waves in the solar corona (Vršnak & Cliver 2008).

The AIA instrument has provided valuable insights into the dynamics of the low solar corona over the past decade, thanks to its exceptional spatial and temporal resolution. Equipped with telescopes observing the solar disk in bands 193 and 211 Å, the AIA instrument has demonstrated its ability to distinguish compressive waves in the lower corona (Patsourakos et al. 2010; Ma et al. 2011; Kozarev et al. 2011). These observations offer valuable information about the kinematics and geometric structure of CBFs. To accurately study the evolution of the wave’s leading front, observations off the solar limb are preferred to mitigate projection effects, which may introduce ambiguities in estimating time-dependent positions and the global structure of the wave (Kozarev et al. 2015). In situ observations of shock waves have revealed their classification into quasi-parallel, quasi-perpendicular, sub-critical, and super-critical shocks based on the angle between the wavefront normal vector and the upstream magnetic field lines (Tsurutani 1985). Quasi-parallel shocks have an angle (θ_{BN}) smaller than 45° , while quasi-perpendicular shocks have θ_{BN} greater than 45° . Supercritical shocks, often associated with accelerated particles, are promising candidates for generating type II radio bursts (Benz & Thejappa 1988). However, obtaining accurate estimates of shock strength and obliquity solely from remote observations is challenging.

Recent studies have further elucidated the characteristics of CBFs both on the solar disk and off the limb, confirming their wave-like nature (Nitta et al. 2013; Long et al. 2011; Olmedo et al. 2012). Coronagraph observations, such as those obtained from the Large Angle and Spectrometric COronagraph (LASCO) instrument on board the Solar and Heliospheric Observatory (SOHO) spacecraft (Domingo

et al. 1995), have extended the investigation of shock waves beyond $2.5 R_{\odot}$ (Vourlidas et al. 2003), while EUV observations have provided evidence linking CMEs and EUV waves (Patsourakos & Vourlidas 2009). Nevertheless, the appearance of shock waves in EUV observations is not yet fully understood (Kozarev et al. 2011). Emission measure modeling using the EUV channels of the AIA instrument allows for the estimation of temperature and density changes in the wavefront's sheath (Kozarev et al. 2011). By employing multi-wavelength studies from the SOHO/LASCO and SDO/AIA instruments, valuable information about the relationship between white-light coronagraph observations and EUV observations of CMEs has been uncovered, shedding light on the properties of CBFs closer to the Sun (Warmuth 2015). Factors such as the presence of nearby active regions or coronal holes can distort the initial morphological shape of CBFs (Ofman & Thompson 2002; Mann et al. 2003; Piantschitsch et al. 2018), and a connection between CBFs and chromospheric disturbances known as Moreton waves has been established (Thompson et al. 1999).

In this study, I focused on 26 CBF events up to $\sim 17 R_{\odot}$ by combining observations and modeling tools from the Solar Particle Radiation Environment Analysis and Forecasting–Acceleration and Scattering Transport (SPREAdFAST) framework (Kozarev et al. 2022). My aim is to estimate the ambient plasma interactions with CBFs and gain insights into the acceleration and transport of SEPs along the wavefronts of coronal shocks and compressive waves. In this chapter, I focus on the kinematics of CBFs, and the SEP aspect will be introduced in Chapter 4.

2.2 EUV Observations

We collected data from the SOHO/ERNE instrument, focusing on proton events within the energy range of 17–22 MeV, from 2010 to 2017. Initially, we obtained a total of 216 events. However, we applied several criteria to filter the data and arrive at the final list of events for this study. Firstly, we excluded 39 proton events that were not associated with EUV waves and had no identified CMEs or flares. Additionally, 72 proton events were excluded because they lacked EUV wave associations, despite having identified CMEs/flares. We also removed 6 events with uncertain EUV waves from our analysis. Furthermore, 37 events were discarded due to immeasurable EUV waves. Moreover, 36 events did not show measurable shock waves using our method of kinematics measurements. As a result, we proceeded with 26 events that exhibited measurable CBFs, allowing us to analyze them using our framework. To initiate the analysis, we utilized image sequences obtained from the EUV channel 193 Å of the AIA instrument. These images had a 24-second cadence and served as the primary input for the SPREAdFAST framework.

The 26 selected events (Table 2.1) were previously presented in our previous work (Kozarev et al. 2022). Table 2.1 provides details about the date of the CBF events, the start and end times of associated flares along with their class, and the source locations on the solar disk in helioprojective Cartesian coordinates. These coordinates were obtained from the Heliophysics Events Knowledge (HEK) database¹.

Figure 2.1 depicts the distribution of the CBFs on the Sun using the helioprojective coordinate system. The mean latitude and mean longitude of the CBFs were calculated as 56.35 and 378.04 arcsec, respectively. Additionally, the mean latitudes of CBFs in the northern and southern solar hemispheres were found to be 283.00 and -252.73 arcsec, respectively. As for the mean longitudes, they were -775.71 and 803.11 arcsec on the eastern and western sides, respectively.

CBFs appear relatively dim compared to the background solar disk. We found that channel 193 Å was most effective in clearly showing the wavefronts, although channel 211 Å proved better in some cases. Therefore, for each CBF event, we generated a sequence of base-difference images to study the evolution of CBFs. This involved subtracting the average of 10 images from all consecutive frames, with each frame separated by 24 seconds.

CBFs appear in AIA channels as quasi-spherical sheaths with brighter wavefronts, often interpreted as shock fronts (Vourlidas et al. 2003; Ontiveros & Vourlidas 2009; Kozarev et al. 2011; Ma et al. 2011). To analyze their radial and lateral evolution, we applied the Coronal Analysis of SHocks and Waves framework (Kozarev et al. 2017, CASHeW). This semi-automated technique involves extracting an annular region from AIA images and mapping it onto a polar projection (Fig. 2.2A). Intensity changes along radial and lateral directions are tracked to measure CBF kinematics. Users can interactively specify extraction lines and measure CBF positions (Fig. 2.2B,C). Extracted intensity pixels along the radial direction (CBF nose) throughout the event's duration within the AIA FOV are used to create a height-time plot (J-map).

¹HEK Database: www.lmsal.com/isolsearch

Table 2.1: List of the CBF events with their associated flares and CMEs.

ID	Event Date	Flare Start (UT)	Flare Max (UT)	Flare Class	EUV Wave Start (UT)	EUV Wave End (UT)	Source X (")	Source Y (")	CME on	V_{CME}	AW
0	2010/06/12	0:30	0:57	20	0:55	1:19	633	390	1:32	486	119
1	2010/08/14	9:38	10:05	4.4	9:30	10:08	697	-26	10:12	1205	360
2	2010/12/31	4:18	4:25	1.3	4:15	5:01	799	246	5:00	363	45
3	2011/01/28	0:44	1:03	13	0:45	1:59	949	218	1:26	606	119
4	2011/03/07	19:43	20:12	37	19:31	22:59	614	553	20:00	2125	360
5	2011/05/11	2:23	2:43	0.81	2:20	2:35	785	399	2:48	745	225
6	2011/08/04	3:41	3:57	93	3:43	4:20	546	200	4:12	1315	360
7	2011/08/08	18:00	18:10	35	17:45	18:43	812	215	18:12	1343	237
8	2012/03/07	1:05	1:14	130	0:00	0:40	-475	397	1:30	1825	360
9	2012/03/13	17:12	17:41	79	17:03	17:44	804	352	17:36	1884	360
10	2012/07/23	u	u	u	2:09	2:48	912	-243	2:36	2003	360
11	2013/04/21	u	u	u	6:35	7:35	937	181	7:24	919	360
12	2013/05/13	15:48	16:05	280	15:44	16:20	-927	186	16:08	1850	360
13	2013/05/15	1:25	1:48	120	1:06	1:50	-852	199	1:48	1366	360
14	2013/05/22	13:08	13:32	50	12:33	13:20	875	238	13:26	1466	360
15	2013/06/21	2:30	3:14	29	2:31	3:21	-869	-268	3:12	1900	207
16	2013/10/25	7:53	8:01	170	7:53	8:29	-914	-158	8:12	587	360
17	2013/12/12	3:11	3:36	0.22	3:03	3:33	750	-450	3:36	1002	276
18	2013/12/28	17:53	18:02	9.3	17:10	18:00	942	-252	17:36	1118	360
19	2014/07/08	16:06	16:20	65	16:06	16:51	-767	163	16:36	773	360
20	2014/12/05	5:28	5:37	2.1	5:42	6:21	872	-366	6:24	534	172
21	2015/05/12	2:15	3:02	2.6	2:18	2:49	960	-192	2:48	772	250
22	2015/09/20	17:32	18:03	21	17:28	18:11	660	-429	18:12	1239	360
23	2015/10/29	u	u	u	2:13	2:52	951	-167	2:36	530	202
24	2015/11/09	12:49	13:12	39	12:51	13:27	-626	-229	13:25	1041	273
25	2017/04/01	21:35	21:48	44	21:31	22:19	761	308	22:12	516	115

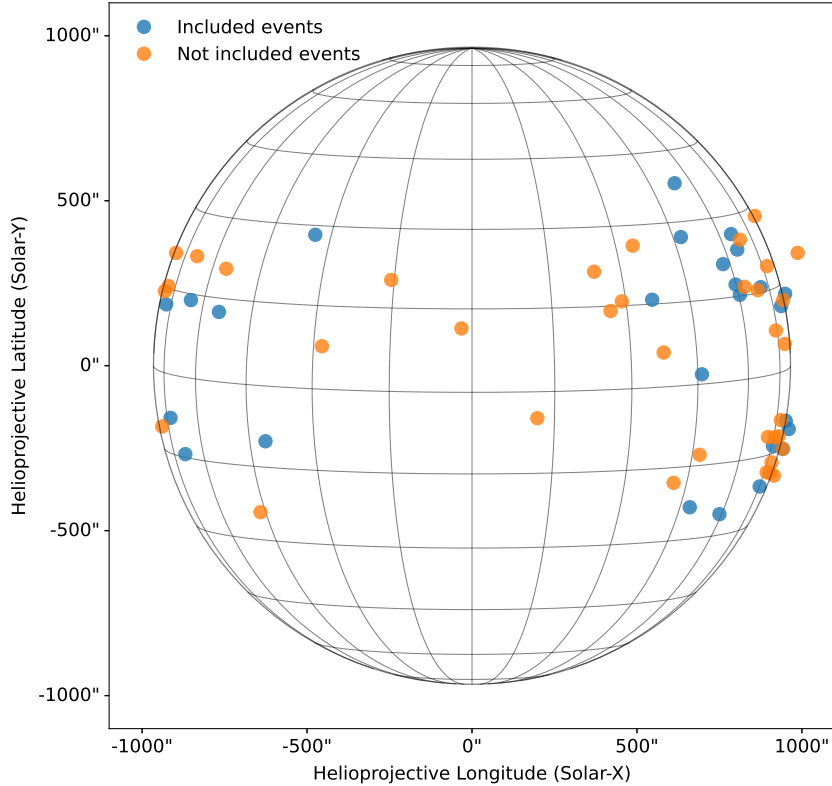


Figure 2.1: Distribution of the source location of the CBFs on the solar disk. The blue dots are the events that we included in Table 2.1, while the orange dots are the events that we did not include in the table.

The kinematics are determined through time-height maps, commonly known as J-maps (Sheeley Jr et al. 1999). These maps are generated by stacking columns of pixels in a desired direction from a solar image. The track's shape on J-maps depends on the feature's direction and speed, allowing identification of radial and lateral wave front positions over time.

Our analysis approximates radial and lateral wavefront positions using J-maps generated for each event. Assuming symmetrical expansion on both flanks, we treat the waves as spheroids defined by major and minor axes. Consequently, the radial direction is represented by a single value, while the lateral direction (parallel to the solar limb) uses two values for measurements in both left and right directions. However, lateral wave signatures may sometimes be visible in only one direction or be absent entirely. Due to data limitations, our final sample size is 26 events, prioritizing complete datasets that exclude events with missing radial, lateral, or combined measurements.

To extract relevant plasma parameters and perform modeling, we retrieve information on CBFs from the HEK database and consult Nariaki Nitta's catalog of coronal waves (Nitta et al. 2013)² to obtain necessary data. With the event list, we employ the SPREAdFAST framework to calculate kinematics, infer shock parameters, and determine plasma properties. Detailed summary plots of the modeled events can be found on the online SPREAdFAST catalog³.

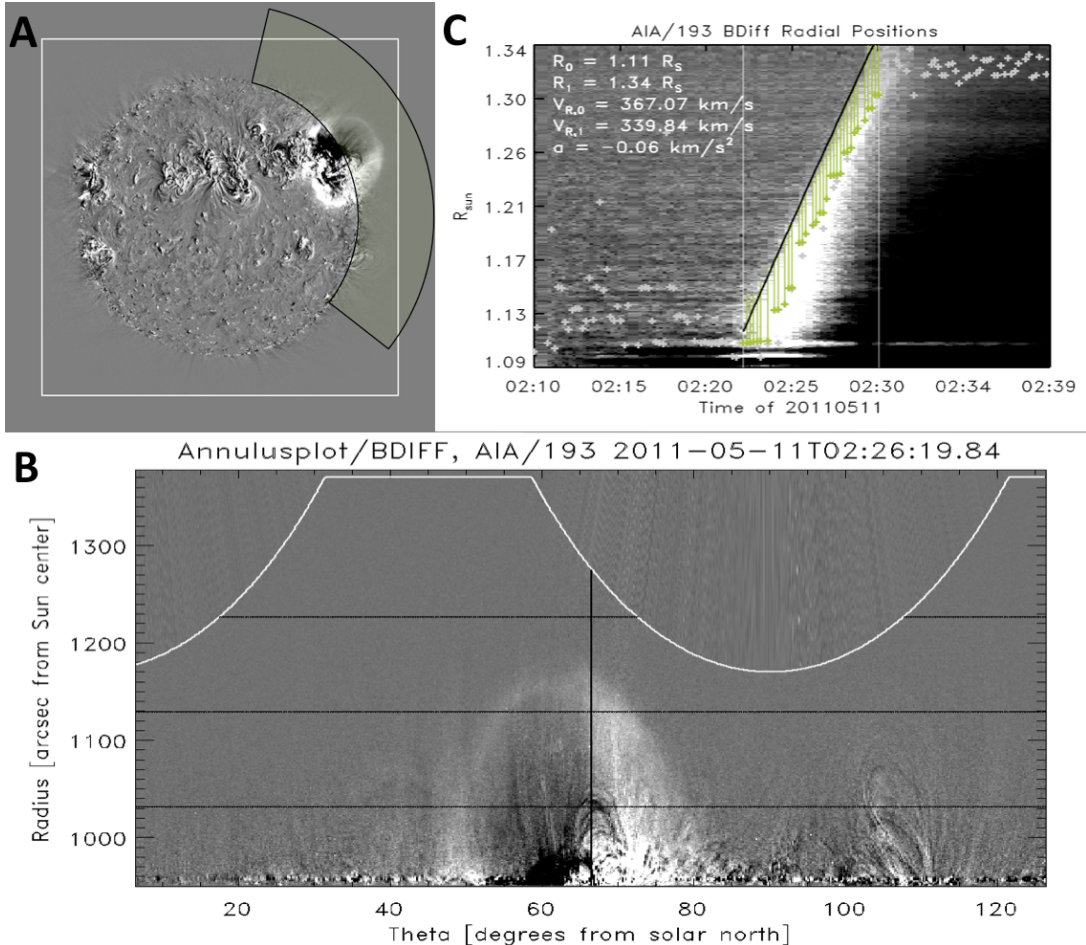


Figure 2.2: Illustration for the annulus method used to extract kinematic data from AIA images. (A) shows the full Sun disk with the relevant region highlighted (green sector). The white box outlines the AIA FOV. (B) displays the extracted annular region mapped onto polar coordinates, with the actual data extent marked by the white curve. Black lines indicate the directions used for measuring radial and lateral motions. (C) shows a stacked plot of intensity along the radial direction, with green markers highlighting intensity peaks and their corresponding distances from the CBF wavefront. The white lines represent the time interval during which the CBF is tracked within the AIA FOV. This figure is curated from (Kozarev et al. 2017).

²Nariaki Nitta's Catalog: https://lmsal.com/nitta/movies/AIA_Waves/index.html

³SPREAdFAST Catalog: <https://spreadfast.astro.bas.bg/catalog/>

To accurately determine the front, back, and peak of the EUV wave at each time step (Fig. 2.3), we applied several algorithms. Firstly, we utilized Savitzky-Golay filtering (Savitzky & Golay 1964) to smoothen the data. Next, we employed local minima/maxima ordering and proximity/intensity metrics algorithms. These algorithms enabled us to identify the wave positions and extract relevant parameters. For each CBF event, we manually specified the starting and ending times, indicated by vertical white lines in Figure 2.3. We also determined the starting and ending height, corresponding to the off-limb portion of the CBF within the AIA FOV.

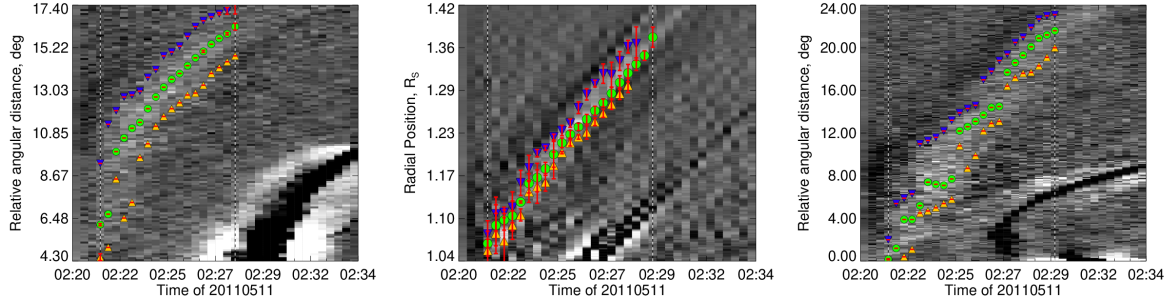


Figure 2.3: J-map plots for the event of May 11, 2011, for the radial direction (middle plot) and the left and right flanks of the wave in the lateral heliocentric direction (the left and right plots, respectively). Blue, green, and orange filled symbols are the positions of the CBF front, peak, and back, respectively. The uncertainty of the average measurements is shown as red bars.

By analyzing the intensity values, we defined the CBF positions as the locations with peak intensity at each time step. The front and back of the wave were set at 20% of the peak intensity. To obtain more comprehensive information about the CBFs, we applied the Levenberg-Marquardt least squares minimization (Markwardt 2009) along with a second-degree bootstrapping optimization technique (Efron 1979). This approach allowed us to fit fourth-order polynomials to the wave positions using Savitzky-Golay fitting. As a result, we obtained measurements for speeds, accelerations, intensities, and thicknesses of the waves in both the radial and lateral directions. The thicknesses and intensities are averages of the values between the peak and back for each time step. Measurements of the heights of CBFs with respect to the solar disk center were obtained⁴ for all the events analyzed in this study. These measurements were taken at the fastest segment of the leading edge of each CBFs over time. We also have measurements of the lateral positions of the CBF front relative to the nose direction. These were obtained in degrees and converted to km depending on the height of the lateral measurement above the solar surface.

2.3 Data Analysis and Methods

The Solar Particle Radiation Environment Analysis and Forecasting—Acceleration and Scattering Transport (Kozarev et al. 2022, SPREAdFAST) is a physics-based prototype heliospheric SEP forecasting system. It incorporates data-driven models to estimate the coronal magnetic field, dynamics of coronal shock waves, energetic particle acceleration, and scatter-based SEP propagation in the heliosphere. The system is based on the Coronal Analysis of SHocks and Waves framework (Kozarev et al. 2017, CASHeW) and provides timely predictions of SEP arrival times, maximum intensities, and SEP fluxes at various locations in the inner heliosphere. It contributes to space weather requirements, protecting ESA assets, aiding satellite operators, and providing lead times for mitigating impacts on electronics and humans in space activities.

Summary plots of the J-maps, including estimated positions and errors, can be found in the online SPREAdFAST catalog for each event. To create a unified lateral kinematics time series for each event, we average measurements from both lateral flanks. Additionally, we record the CBF mean intensity and thickness in both directions. To analyze the kinematic measurements deduced from the AIA FOV, we apply a Savitzky-Golay fit (Savitzky & Golay 1964), as described in Kozarev et al. (2019). Subsequently, we extrapolate the smoothed radial positions up to $\sim 17 R_\odot$ using the analytical CME kinematics models presented by Gallagher et al. (2003) and Byrne et al. (2013).

⁴LASCO CME Catalog: https://cdaw.gsfc.nasa.gov/CME_list/

Our next step involves developing multiple synthetic geometric shock models, known as the synthetic shock model (S2M) module, to describe the shock surface at a 24-second cadence. These models rely on extrapolated radial and lateral kinematic results, as well as the inferred major and minor axes of the spheroids representing compressive waves. The shock surface is created from the onset of the CBF until its nose reaches $10 R_{\odot}$ and is then propagated up to $\sim 17 R_{\odot}$. The propagation is based on the Magnetohydrodynamic Algorithm outside a Sphere (MAS) synoptic coronal MHD model's results. Consequently, the shock surface samples plasma parameters from the data cube of the MAS model at discrete points, determined by consecutively crossing magnetic field lines. The MHD data utilized in this study is represented as a 3D data cube consisting of plasma parameters. To analyze this data, a spheroid model was propagated through the data cube by scanning it without any direct interaction. At each point within the data cube, a search was conducted to identify the nearest four neighbors. By employing trilinear interpolation, the values at these points were estimated.

By sampling the shock surface, we obtain data for approximately 1000 field-crossing lines, potentially more depending on the desired resolution. For each event, the output consists of a set of data structures that describe each shock-crossing field line. These structures include the shock speed V_{shock} , plasma density n , density jump r , shock upstream magnetic field magnitude B_{mag} , shock-field angle θ_{BN} , Alfvén speed V_A , and Alfvén Mach number M_A .

To estimate the shock density jump, we follow the method of Kozarev et al. (2017) - we calculate the differential emission measure (DEM) before and during the event at each shock crossing and each timestep. The DEM is obtained using the model by Cheung et al. (2015). We integrate the DEM to obtain the average density, and take the ratio of densities during and before the event. Typically, the density jump within the AIA FOV is relatively small, usually below 1.2. However, beyond this region where observational information is lacking, we assign a value of 1.2, assuming a weak shock. For ease of analysis, we divide the synthetic shock model into three segments: the cap (representing the shock nose), Zone 1, and Zone 2 (referring to the shock flanks). This division allows us to examine the distribution of plasma parameters across different sectors of the shock surface. Figure 2.4 illustrates the evolution of the synthetic shock model in nine timesteps, with the cap zone colored blue and the shock flanks colored green and red.

2.4 CBF Kinematics and Geometric Modeling - Case Study May 11, 2011

In this section, I provide a detailed analysis of the event at the low corona region, demonstrating our method. Additionally, I investigate the plasma parameters along individual shock-crossing magnetic field lines in the AIA FOV.

2.4.1 Event Context

The eruption took place on May 11, 2011, at approximately 02:20 UT (Fig. 2.5). It originated from an active region situated in the northwestern sector (N18W52). The event involved a massive shock wave propelled by a fast partial-halo CME that occurred at 02:48 UT. The CME exhibited a linear speed of 745 km s^{-1} , a 2^{nd} -order speed at $20 R_{\odot}$ of 776 km s^{-1} , an acceleration of 3.3 m s^{-2} , an angular width (AW) of 225° , a central position angle (PA) of 320° , a measurement position angle (MPA) of 283° , a mass of 3.5×10^{15} gram, and a kinetic energy of 9.6×10^{30} erg. The mass and kinetic energy were uncertain due to projection effects, as reported by the SOHO-LASCO CME catalog. This was accompanied by a weak solar flare classified as B8.1 and an eruptive filament, as observed by the 193 Å EUV channel of the SDO/AIA instrument.

Furthermore, the eruption was associated with a type II radio burst, which commenced around 02:20 UT. This was observed by the Learmonth spectrogram (25–180 MHz) maintained by the Australian Space Weather Services and part of the CALLISTO global network. By examining the OMNI database⁵, we found no evidence of a geomagnetic storm occurring within three days from the onset of the eruption. Nevertheless, an increase in proton fluxes across all energy channels near 1 AU was observed using the SOHO/ERNE instrument. According to the Wind/EPACT catalog⁶ (Miteva et al. 2016, 2017), we found an SEP event detected by the SOHO/ERNE instrument at the Earth with onset time of 03:39 UT and

⁵OMNIWeb Database: <https://omniweb.gsfc.nasa.gov/>

⁶Wind/EPACT Catalog: <http://newserver.stil.bas.bg/SEPCatalog/>

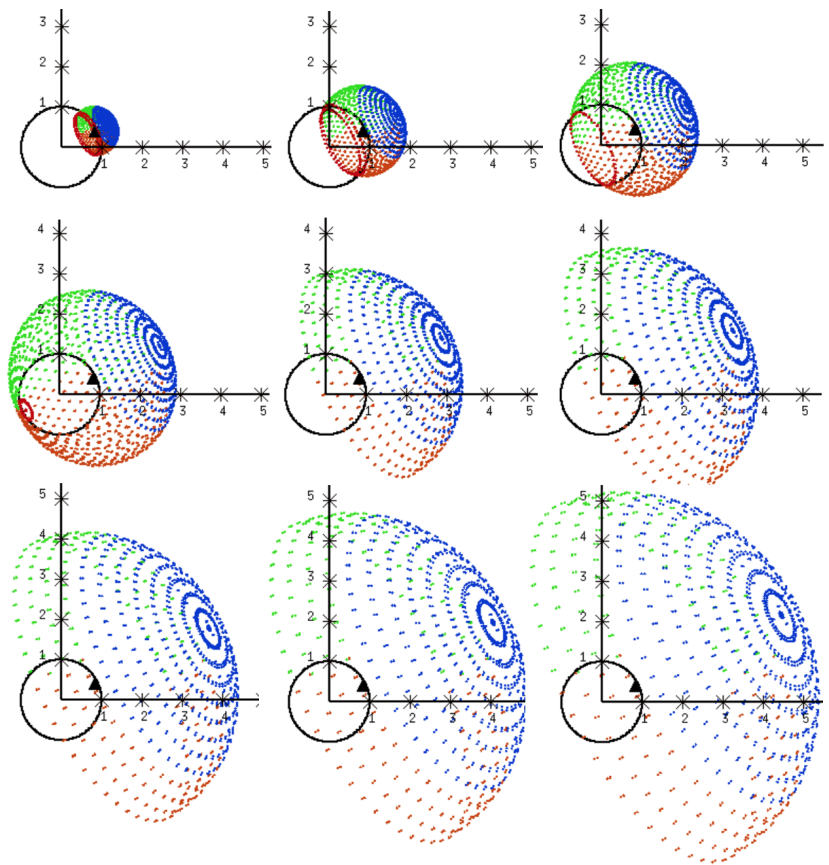


Figure 2.4: Synthetic shock model divided into three segments; the cap zone in blue and the flank zones are in red and green.

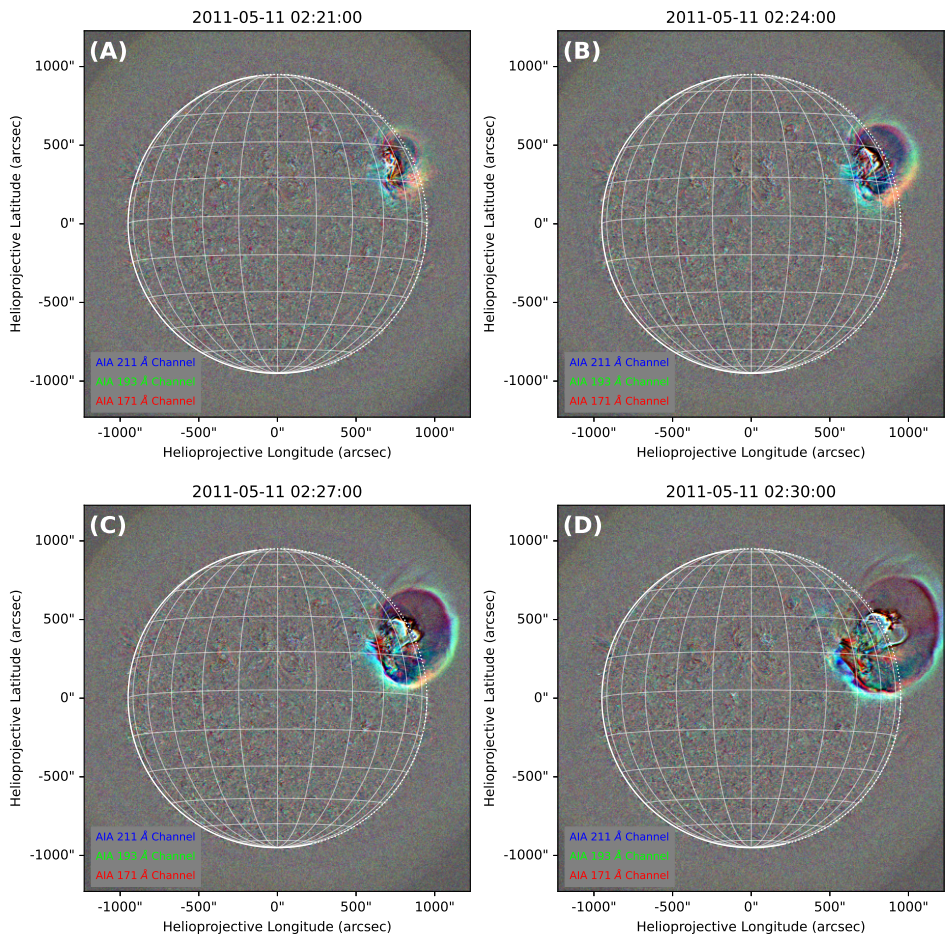


Figure 2.5: AIA running-difference images capture a coronal wave evolving over 9 minutes near the Sun's western limb, exhibiting markedly changing intensity and structure as observed in 171, 193, and 211 Å.

a J_p of 0.0133 protons/(cm² s sr MeV) in the energy channel 17-22 MeV. J_p is the peak proton intensity after subtracting the pre-event level.

2.4.2 Low Corona Part

To investigate the kinematics of the CBF event, we employed the CASHeW module within the SPREAd-FAST framework. As we see in Figure 2.3, the J-maps are displayed, illustrating the radial and lateral time-dependent evolution of the CBF in gray-scale. Since the wave is assumed to have a dome-like shape, the lateral direction is divided into left and right flanks. Bright features below the CBF in the J-maps are likely expanding loops. To estimate the uncertainty in the measurements, we varied slightly the radial (nose) direction three times. The corresponding positions are depicted in red, while the start and end times of the CBF are indicated by vertical dashed lines. Additionally, the front, back, and peak of the CBF are represented by blue down-pointing triangles, yellow up-pointing triangles, and green-filled circles, respectively.

Figure 2.6 presents the time series kinematic results of the shock wave parameters within the SDO/AIA field of view (up to $1.3 R_\odot$). The kinetics of the wavefront, peak, and back are color-coded as red, green, and blue, respectively. The subpanels from top to bottom display the estimated heliocentric distance, speed, acceleration, intensity, and thickness of the wave. These parameters are presented for both the radial (middle panel) and lateral directions (left and right panels).

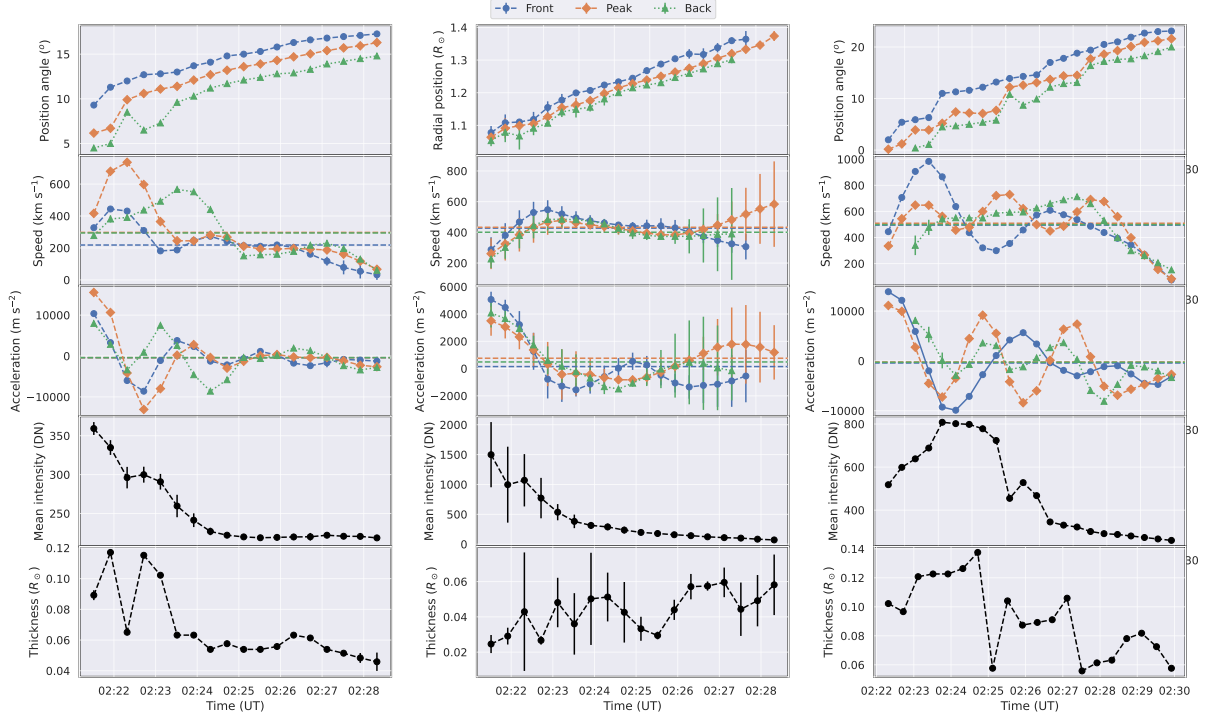


Figure 2.6: Time-series kinematics of the CBF parameters for the front, peak, and back positions in the AIA FOV, with measurement uncertainties shown as small bars over the data points. The horizontal lines in the speed and acceleration panels denote the mean speeds and accelerations for the wave front, peak, and back with respective colors. The left and right columns represent the lateral kinematic measurements in the left and right flanks of the wave, respectively. The middle column represent the kinematic measurements in the radial direction.

Analysis of Figures 2.3 and 2.6 reveals that the coronal wave was asymmetric in shape. The time-dependent evolution of the angular distance differed slightly between the left and right flanks. In Figure 2.3, the right flank (towards the solar equator) of the wave appeared for a little bit longer time, allowing the algorithm to capture it with a higher number of measurements until approximately 02:29 UT, same as for the radial direction. In contrast, the left flank (towards the solar pole) had fewer measurements available.

The coronal wave's initial appearance was slightly elongated, with an aspect ratio of 0.5. This indicates a longer major axis, creating a degree of asymmetry. At 02:25:31 UT, a striking change

occurred: the wave became perfectly circular, achieving an aspect ratio of 1. This signifies equal lengths for both axes, resulting in a symmetrical shape. However, this transformation was short-lived. The wave's morphology shifted again, becoming increasingly flattened. This signifies a growing minor axis compared to the major one, leading to an *over-expansion* of the wave along its minor axis. In this study, the aspect ratio is defined as the minor axis divided by the major axis of the wave's geometric surface. A value of 1 represents a perfectly symmetrical wave, while values greater than 1 indicate over-expansion along the minor axis. Conversely, values less than 1 point towards elongation along the major axis, reflecting a more radial expansion.

Regarding the radial direction, the event duration spanned from approximately 02:21 to 02:28 UT. The shock wave exhibited an average speed of approximately 420.46 km s^{-1} , while the average acceleration was around 463.92 m s^{-2} , calculated as the mean of the front, peak, and back sides of the wave. For the left flank in the lateral direction, the event duration spanned from around 02:21 to 02:28 UT. The average speed and acceleration were approximately 270 km s^{-1} and -400.62 m s^{-2} , respectively. For the right flank in the lateral direction, the event duration spanned from around 02:21 to 02:30 UT, lasting for one minute longer than the left flank. The average speed and acceleration were approximately 500.97 km s^{-1} and -297.18 m s^{-2} , respectively.

Comparing the lateral directions, the wave's sheath on the right flank was approximately six times the thickness observed on the left flank, while the radial direction exhibited a thickness roughly half that of the left flank. Notably, the peak speed in the radial direction was lower than that in the lateral direction; right flank, suggesting that the shock wave experienced compression in the direction of propagation, while expanding laterally to a greater extent than radially. Table 2.2 provides a summary of the statistical results.

To further explore the shock and plasma parameters at different sections of the coronal wave, we divided the shock surface into three segments: the Cap zone (shock nose), Zone 1, and Zone 2 (the shock flanks). This division is illustrated in Figure 2.4.

Table 2.2: Mean values and their standard deviation of the wave parameters in the radial direction and the lateral direction for the left and right flanks, at the front, peak, and back sides of the wave for the event occurred on May 11, 2011, in the SDO/AIA FOV.

Parameter	Direction	Front	Peak	Back
$\langle \text{speed} \rangle \text{ km s}^{-1}$	Lat. Left	218.46 ± 9.04	297.46 ± 5.45	293.94 ± 9.04
	Radial	427.46 ± 51.85	433.11 ± 82.86	400.81 ± 83.78
	Lat. Right	494.69 ± 0.00	509.25 ± 1.02	498.97 ± 9.21
$\langle \text{accel.} \rangle \text{ m s}^{-2}$	Lat. Left	-414.62 ± 227.23	-401.46 ± 164.62	-385.77 ± 227.23
	Radial	147.41 ± 1009.19	758.97 ± 1287.65	485.38 ± 1365.80
	Lat. Right	-415.04 ± 0.00	-209.81 ± 22.32	-266.68 ± 250.80
$\langle \text{intensity} \rangle \text{ DN}$	Lat. Left		250.60 ± 5.90	
	Radial		403.34 ± 143.30	
	Lat. Right		489.04 ± 2.86	
$\langle \text{thickness} \rangle R_{\odot}$	Lat. Left		0.07 ± 0.00	
	Radial		0.04 ± 0.01	
	Lat. Right		0.09 ± 0.00	

We summarize the results for the three segments in Table 2.3 to further investigate the shock and plasma parameters in different sections of the coronal wave. Notably, the mean shock speed at the flanks was higher than that at the Cap zone. We did not observe significant variations in the magnetic field across the different segments, indicating a relatively homogeneous magnetic structure. The shock density jump exhibited consistent values across all three segments.

In Kozarev et al. (2022) we investigated shock-crossing magnetic field lines during this event, and key plasma parameters were analyzed up to $10 R_{\odot}$. The study, utilizing DEM analysis, revealed consistent results with weak coronal shocks. Notably, the density jump within the AIA FOV was generally small, below 1.2, aligning with previous research. Beyond this view, lacking observational data, the density jump was set to 1.2. By inspecting the parameter evolution over all shock-crossing field lines, we found that the shock-field angle (θ_{BN}) and magnetic field amplitude ($|B|$) consistently decreased over time and radial distance.

The crucial parameter for diffusive shock acceleration (DSA), θ_{BN} , was further detailed, highlighting

Table 2.3: Mean, median, and standard deviation of the shock parameters output, from the interaction of the S2M spheroid with the MAS MHD model results, for the shock’s cap and flanks and for the whole shock surface, for the event on May 11, 2011.

Segment	Parameter	Statistics		
		Mean	Median	Stdv
All	V_{SHOCK} $km\ s^{-1}$	577.77	578.39	72.79
	θ_{BN} $^{\circ}$	70.06	0.63	44.83
	B_{MAG} G	0.046	0.038	0.070
	Density Jump	1.193	1.188	0.185
Cap	V_{SHOCK} $km\ s^{-1}$	555.18	550.86	42.46
	θ_{BN} $^{\circ}$	19.37	3.61	25.51
	B_{MAG} G	0.046	0.036	0.070
	Density Jump	1.193	1.188	0.015
Zone 1	V_{SHOCK} $km\ s^{-1}$	613.69	609.32	59.42
	θ_{BN} $^{\circ}$	6.46	0.21	50.92
	B_{MAG} G	0.045	0.045	0.066
	Density Jump	1.190	1.187	0.008
Zone 2	V_{SHOCK} $km\ s^{-1}$	631.37	614.23	73.07
	θ_{BN} $^{\circ}$	0.10	0.51	10.61
	B_{MAG} G	0.046	0.029	0.071
	Density Jump	1.194	1.188	0.016

its time-dependent distribution across the entire spheroid surface. Notably, there was a significant decrease in θ_{BN} angle within the first 50 minutes of the event. Additionally, dividing the spheroid into distinct regions revealed nuanced variations, with the cap/nose region exhibiting the lowest θ_{BN} values, while zone 2 consistently displayed higher values above 60° . All dynamic spectra for individual events are accessible on the SPREAdFAST catalog webpage⁷.

2.4.3 Middle/Outer Corona Part

We collected complementary measurements from the SOHO/LASCO instrument⁸ in order to expand the analysis of EUV waves’ kinematics in the middle/outer corona. These measurements specifically provide the radial distance of the CME leading edge associated with the coronal wave over time, which is referred to as the height-time profile of the CME.

Figure 2.7 displays the extended measurements of the EUV in the SOHO/LASCO FOV, reaching approximately $17 R_{\odot}$. To analyze the height measurements, we applied the models of CME kinematics proposed by Gallagher et al. (2003) and Byrne et al. (2013). Through a comparison, we determined that the model by Gallagher et al. (2003) provided a better fit with a χ^2 value of 0.13. Examining the bottom panel of the figure, we observe the residuals (i.e. the differences between the actual measurements and the fits) for both models. It becomes apparent that the residuals are generally lower for the Gallagher model when compared to the Byrne model. The efficacy of the Gallagher fitting model in accommodating both AIA and LASCO measurements is underscored by Figure 2.7. This alignment underscores the model’s proficiency in capturing the early stages of the solar event, particularly near the Sun.

Further insights can be gained by examining Figure 2.8, which demonstrates that the wave experienced a period of rapid acceleration between approximately 02:25 and 03:15 UT within a distance of approximately $5 R_{\odot}$ from the Sun. This behavior aligns with the fluctuations in wave acceleration depicted in Figure 2.6. At the same time, the wave speed had a sharp decrease from around $727\ km\ s^{-1}$ to $570\ km\ s^{-1}$ within an hour. Subsequently, the wave speed gradually increased over the following 3 hours, covering a distance of around $15 R_{\odot}$ and they it plateaued at approximately $723\ km\ s^{-1}$.

2.5 Statistical Study

We present a comprehensive statistical analysis of the kinematic characteristics and plasma parameters of coronal wave events observed in the AIA and LASCO FOVs.

⁷SPREAdFAST Catalog: <https://spreadfast.astro.bas.bg/catalog/>

⁸LASCO CME Catalog: https://cdaw.gsfc.nasa.gov/CME_list/

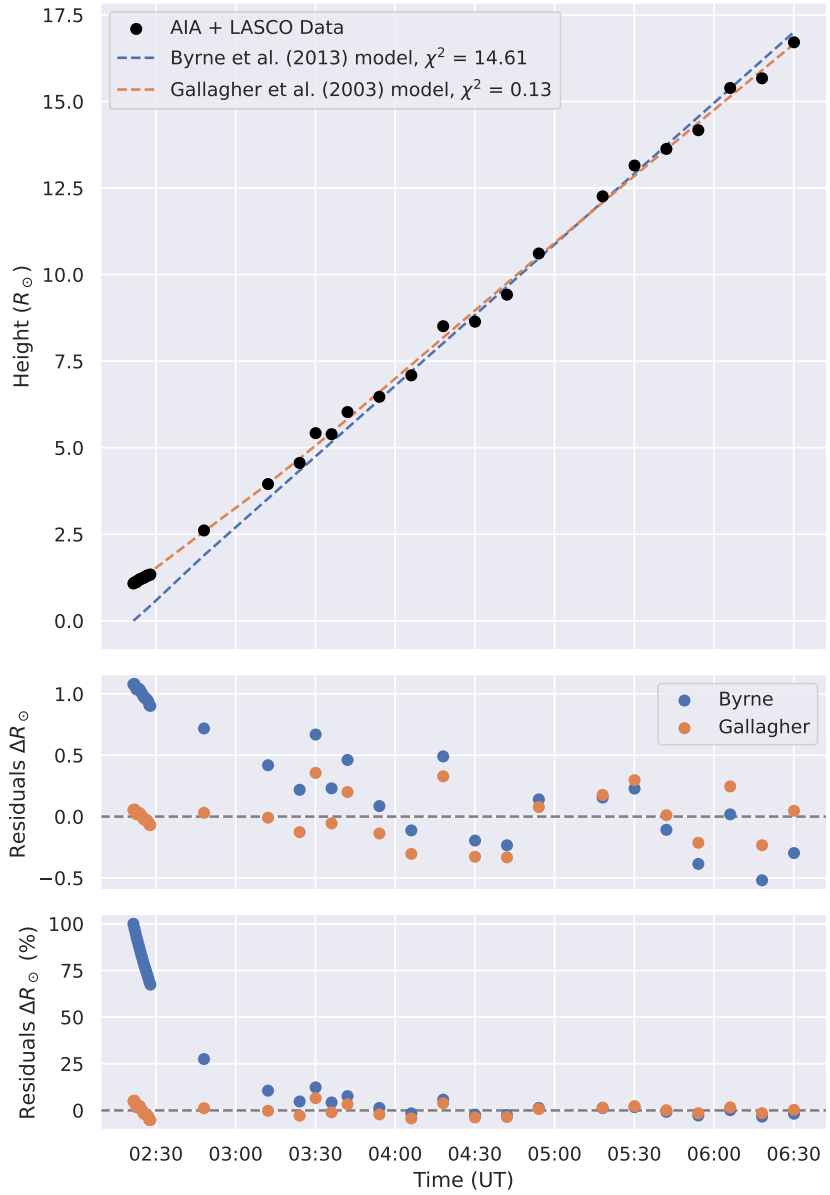


Figure 2.7: Top panel – Height-time profile compiled from AIA and LASCO measurements for the event occurred on May 11, 2011, fitted with two CME kinematics models from the photosphere up to $17 R_{\odot}$. Middle panel – Difference between the fitting and the real observations. Bottom panel – Relative residuals in %.

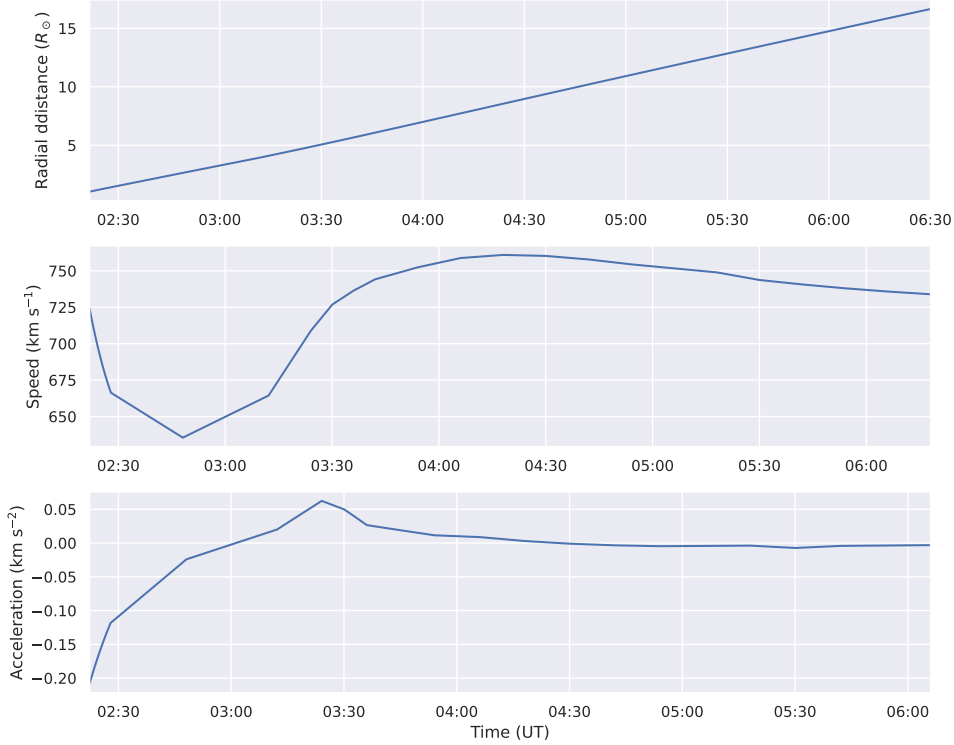


Figure 2.8: Extrapolated radial kinematics for the event occurred on May 11, 2011, based on the ballistic model of Gallagher et al. (2003) up to $17 R_{\odot}$.

An overview of the statistical parameters related to shock characteristics, including wave speed, intensity, and thickness in the AIA FOV, is presented in Table 2.4. The wave speeds are expressed in km s^{-1} , wave accelerations are in km s^{-2} , wave intensity in arbitrary units, and wave thickness in R_{\odot} , as the data have undergone multiple stages of processing.

Upon analyzing the data, we observed that the waves generally exhibited higher speeds, higher acceleration, lower mean intensities, and lower thickness in the radial direction compared to the lateral direction. This suggests that the waves were somewhat elongated in their early stages near the Sun, potentially due to the coronal conditions, including plasma densities and magnetic field strength and structure.

To illustrate the evolution of EUV waves' kinematics in the AIA FOV, we present Figure 2.9, which provides a cumulative view of dynamic spectra for all events. The figure showcases the parameter distribution as a function of distance for shock speed, acceleration, wave intensity, and wave thickness for the radial direction (the middle column) and the lateral directions; the left and right flanks in left and right columns, respectively. The colors in the figure represent the total count in each bin at each radial position step, or each position angle step.

Consistent with our expectations, the speed and intensity panels exhibit a decline in values as a function of distance. As the waves propagate away from the Sun, the wave drivers lose momentum through interactions with the medium, leading to a decrease in speed. Additionally, plasma densities decrease with distance, resulting in a corresponding decrease in wave intensity.

Table 2.4: Statistics of the EUV wave kinematics in the SDO/AIA FOV for the 26 events. LL and LR refer to the lateral left and right flanks, respectively. Rad refer to the radial front direction.

Aspect ratio	Speed (km s^{-1})			Accel. (km s^{-2})			Intensity (DN)			Thickness (R_{\odot})			
	LL	Rad	LR	LL	Rad	LR	LL	Rad	LR	LL	Rad	LR	
Max	2.00	1574.81	2053.73	983.58	28.19	81.01	13.89	1348.87	2431.95	1498.45	9.600	0.185	6.100
Min	0.84	2.11	40.30	2.30	-35.24	-81.01	-9.89	0.53	0.17	150.30	0.027	0.018	0.022
Mean	1.87	316.17	413.60	264.50	-0.15	0.98	0.13	438.99	681.46	442.46	0.715	0.059	0.231
Median	2.00	284.77	349.32	216.32	0.03	0.37	0.11	337.96	425.23	389.06	0.102	0.055	0.076
Stdv.	0.33	261.01	336.11	191.13	5.53	11.08	2.05	292.26	592.78	227.10	1.721	0.030	0.776

To investigate the bulk behavior of the modeled plasma above and at the shock surface, we sampled

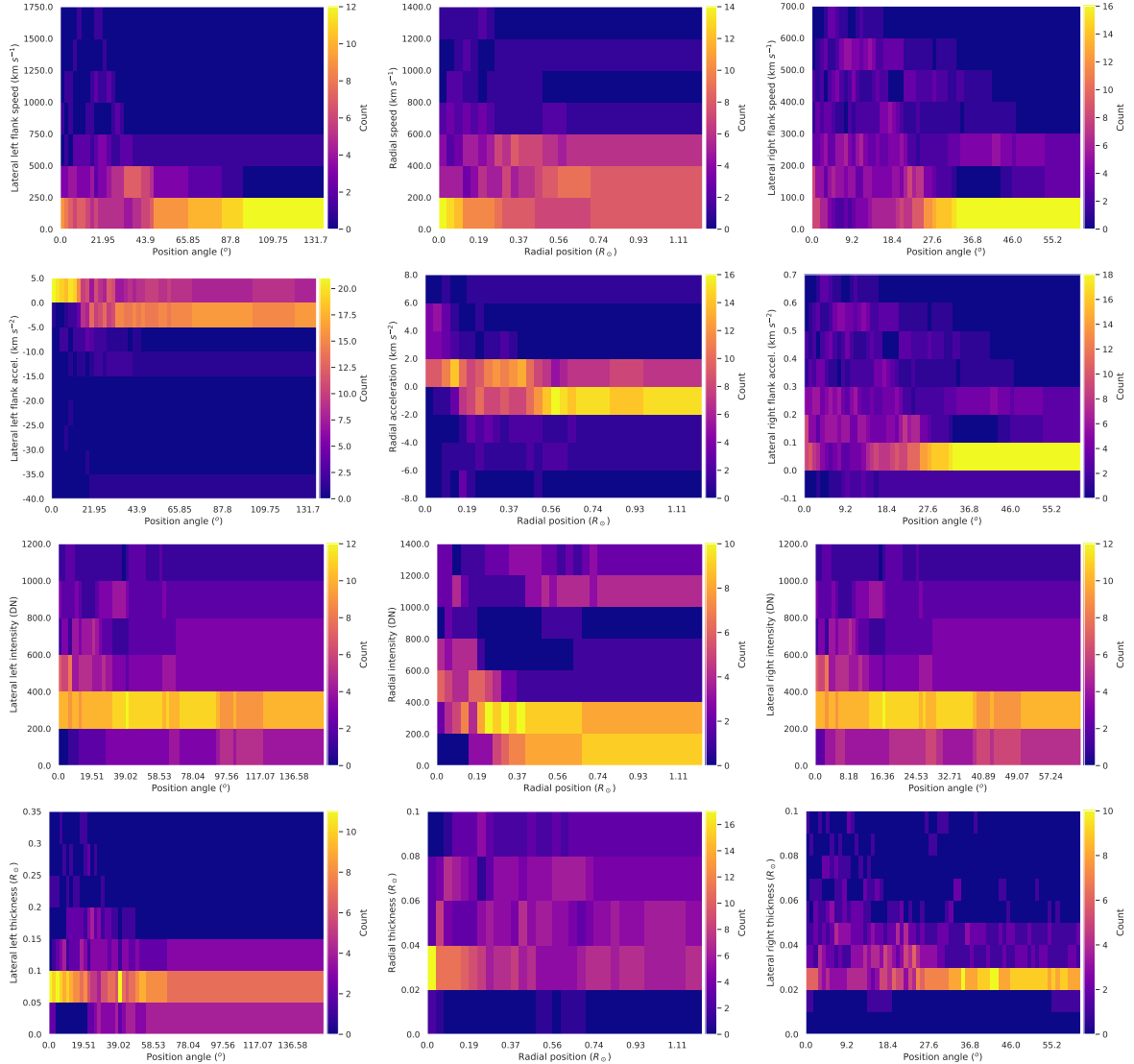


Figure 2.9: Dynamic spectra of the EUV waves kinematics in the AIA FOV. The panels from the top to the bottom are the wave speeds, acceleration, mean intensity, and thickness. The left column is for the lateral left flank, the central column is for the radial direction, and the right column is for the lateral right flank.

over 1000 field lines from the 26 events. The resulting histograms, shown in Figures 2.10, reveal correlations between various pairs of parameters. We investigated the correlations between five parameters – the shock-field angle (**THBN**), the coronal magnetic field (**BMAG**), the plasma density (**DENSITY**), the Alfvén speed (**VA**), the shock speed (**VSHOCK**), and the shock density jump (**SHOCKJUMP**).

The histograms show that there are weak to moderate correlations between some of the parameters. For example, there is a moderate positive correlation between *B MAG* and *DENSITY*, and a moderate positive correlation between *B MAG* and *VA*. These correlations suggest that there may be some underlying physical processes that connect these two parameters. The positive correlation between *B MAG* and *DENSITY* could be due to the fact that stronger magnetic fields can compress the plasma, leading to higher densities. The negative correlation between *B MAG* and *VA* could be due to the fact that stronger magnetic fields tend to speed up the Alfvén waves.

In addition to the anticipated correlations between the Alfvén speed with magnetic field and density, we discovered a highly skewed correlation between magnetic field values and the modeled shock density jump, as well as between magnetic field magnitude and density. The negative correlation between *B MAG* and *SHOCKJUMP* indicates that stronger coronal magnetic fields are associated with smaller density jumps across the shock surface. In other words, weak magnetic field correlates well with stronger shocks. This could be due to several possible mechanisms. For instance, stronger magnetic fields exert higher pressure, potentially resisting the compression of plasma by the shock wave, leading to a smaller density increase across the shock front. In addition, as mentioned earlier, stronger magnetic fields might lead to faster Alfvén waves, allowing the plasma ahead of the shock to react and reduce the density jump. These correlations will be further explored to establish a more definitive connection and to parameterize the shock density jump.

We also aim to investigate the event-averaged modeled plasma parameters and establish the observed connections between these parameters throughout entire events. To achieve this, we computed the mean, maximum, and summed values of the parameters for each event. The analysis revealed a set of parameter pairs that exhibit promising relationships suitable for parameterization. Among these pairs, we selected six representative cases for further examination.

The scatter plots presented in Figure 2.11 depict the chosen modeled parameter pairs. From left to right, top to the bottom, we plotted the logarithm of the summed values of the shock-field angle θ_{BN} versus the logarithm of the summed values of the absolute coronal magnetic field (A), the logarithm of the summed values of θ_{BN} versus the mean values of the shock speed (B), the logarithm of the summed values of θ_{BN} versus the logarithm of the summed values of the shock speed (C), the logarithm of the summed values of θ_{BN} versus the logarithm of the summed values of the shock density jump (D), the mean values of the absolute magnetic field versus the mean values of the shock speed (E), the logarithm of the summed values of the Alfvén speed versus the mean values of the shock speed (F), the mean values of the shock speed versus the mean values of the density jump (G), and finally the logarithm of the summed values of the Alfvén speed versus the mean values of the density jump (H).

To determine the best-fitting equations, we tested several models and found that power fits yield the most accurate results in this particular case. The graphs illustrating the fit parameters and the χ^2 are provided for reference.

The analysis of eight figures examining shock dynamics in EUV wave events revealed significant findings. In Figure (A), a weak positive correlation between coronal magnetic field strength and shock-field angle was observed, suggesting a nuanced relationship influenced by factors beyond magnetic fields. Figure (B) showcased a weak negative correlation between shock-field angles and mean shock speeds, hinting at a connection between complex shock geometries and slower wave speeds. In Figure (C), there appears to be a weak negative correlation between the logarithm of the shock-field angle and the logarithm of the sum of shock speeds, which is indicated by the faintly downward-sloping trendline. This hints at a slight tendency for larger shock-field angles to be associated with slower shock speeds. Figure (D) displayed a moderate positive correlation between shock density jump and shock-field angles, suggesting potential interactions between shock wave geometry and density variations.

Meanwhile, Figures (E), (F), (G), and (H) delved into relationships between solar coronal magnetic field strength, shock speeds, Alfvén speeds, and shock density jumps, revealing negative, lack of clear, and lack of consistent correlations, respectively. These findings emphasize the intricate nature of solar coronal shock dynamics, with multiple influencing factors contributing to observed correlations and scattering in the data. The comprehensive analyses underscore the need for more events and a nuanced understanding of various factors when interpreting the complexities of shock phenomena in the solar corona.

It is important to note that some outliers exist, but they do not undermine the overall correlation patterns. In future work, we will focus on developing and testing parameterizations for these identified

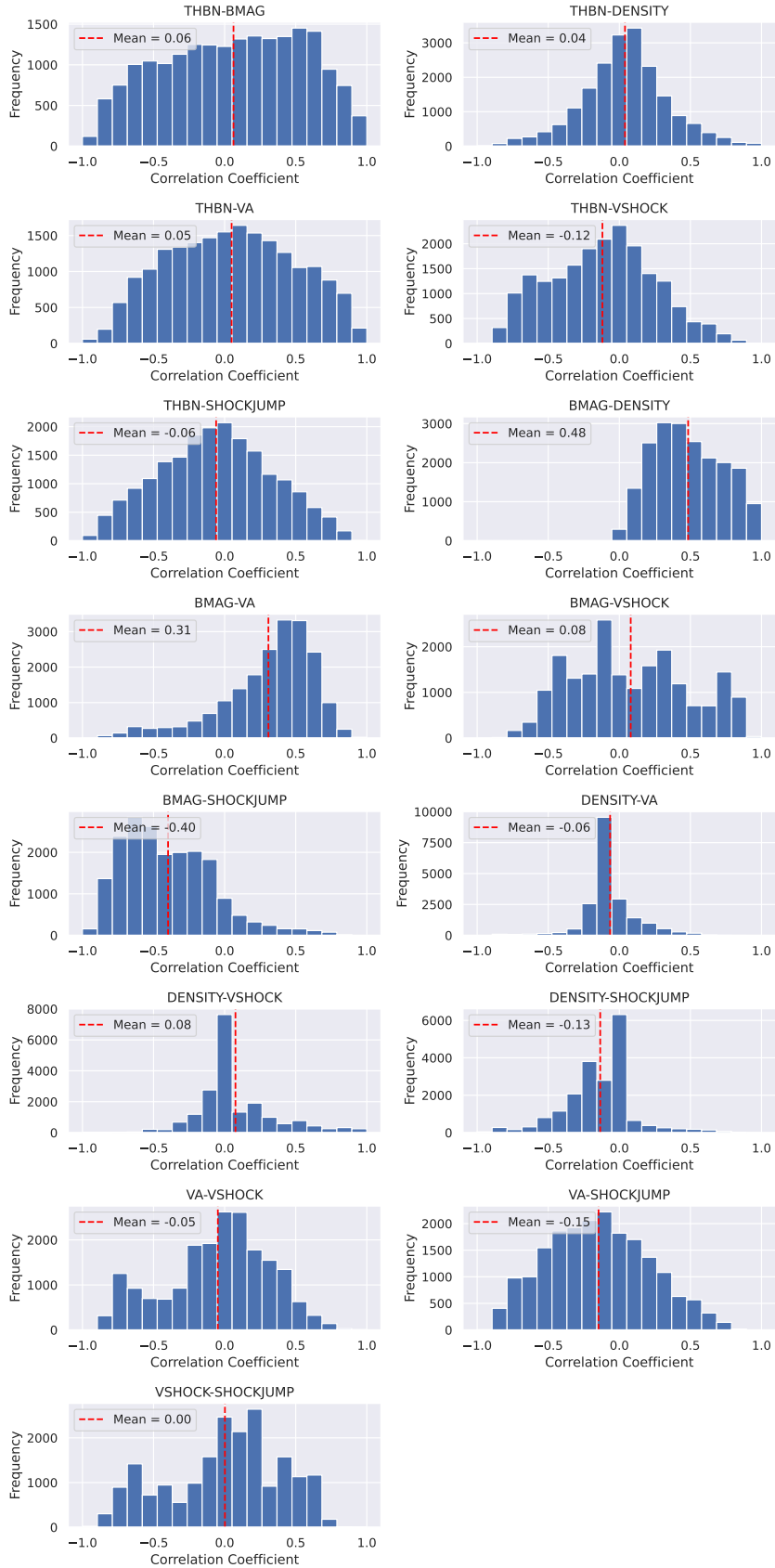


Figure 2.10: Histograms of along-field-lines model plasma parameters in the solar corona for all the 26 events. The vertical dashed red lines are the mean values.

connections in order to establish a set of synoptic MHD parameters that correspond one-to-one with the parameters we measure, such as shock density jump and shock speed. By accomplishing this, we will enhance the representation of shock parameters even in the absence of actual compressive waves.

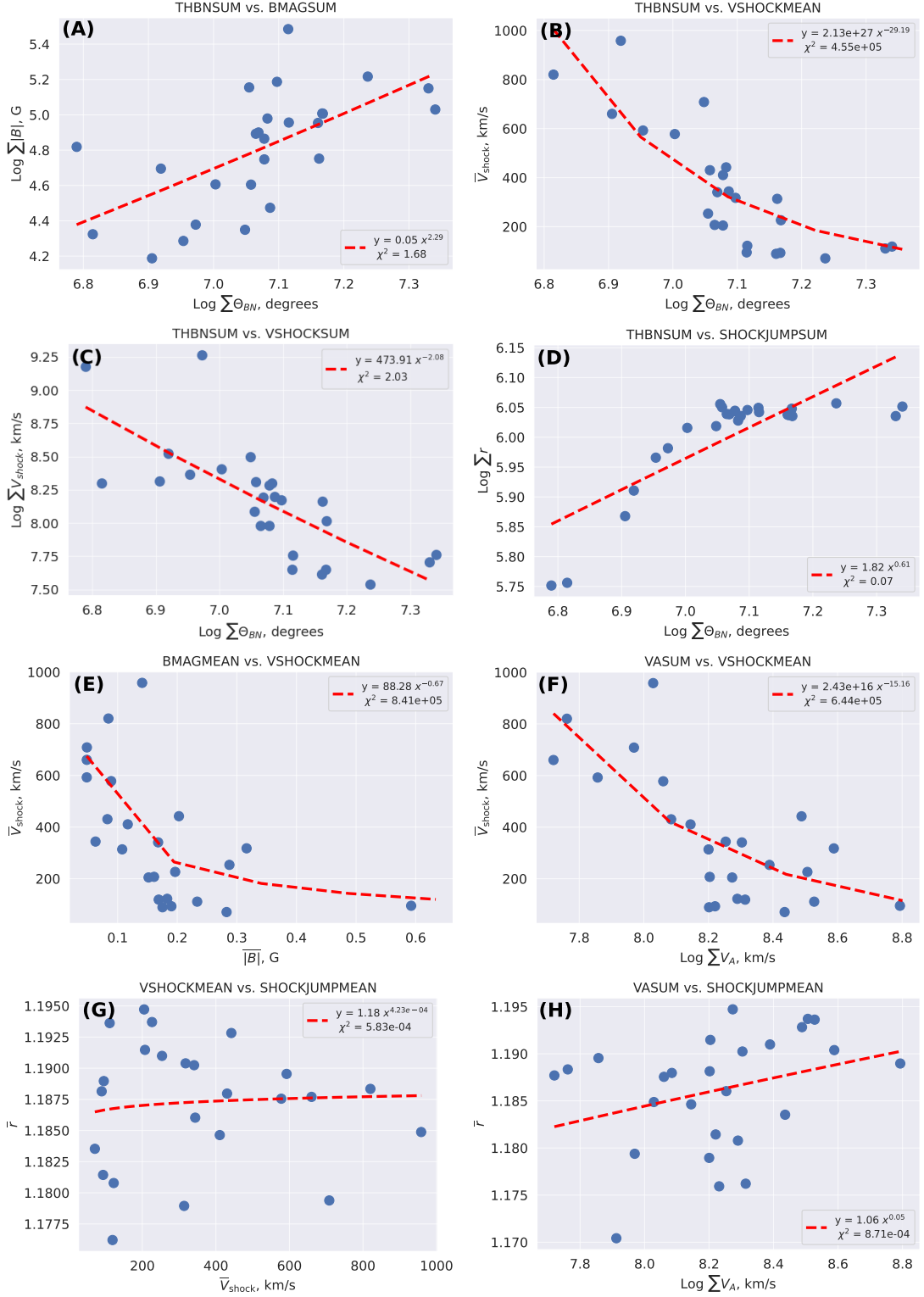


Figure 2.11: Scatter plots of 8 coronal plasma-parameter pairs that exhibit parameterizable relationships. The *VSHOCKMEAN* is filtered to take only events with speeds $< 4000 \text{ km s}^{-1}$.

Figure 2.12 depicts the temporal evolution of the mean shock density jump (r) for the 26 events within the studied sample. Each data point represents the average value across all shock-crossing points

for the respective timestep and event. All modeled events were constrained to 50 timesteps, each lasting 24 seconds. Consequently, the graph illustrates the mean aspect ratio for all events at each timestep. The profile exhibits an initial relatively low value of 1.2, gradually rising to nearly 1.4 before gradually returning to 1.2. The semi-transparent blue shading denotes the standard deviation error at each timestep.

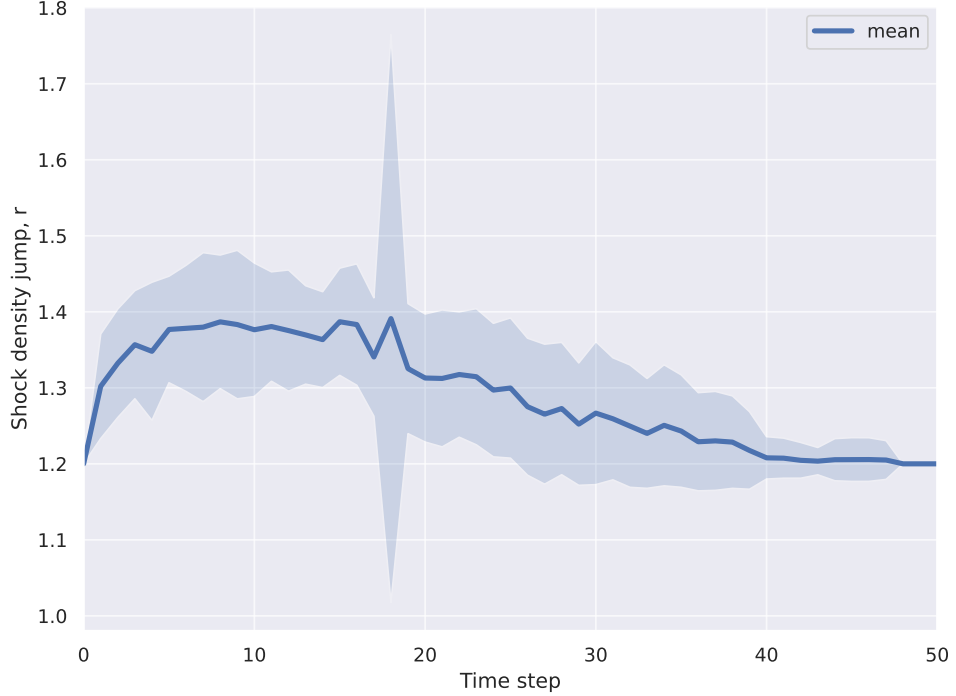


Figure 2.12: Time profile of the mean shock density jump for the 26 in-sample historical events studied with SPREAdFAST.

Finally, in Figure 2.13, I present the computed mean value of time-dependent aspect ratios for all events within our study. The analysis encompasses events confined to 50 timesteps, each lasting 24 seconds. Consequently, the graph illustrates the average aspect ratio across all events at each timestep, revealing a noticeable decrease in aspect ratio. This profile serves as a foundational reference for subsequent modeling phases in SPREAdFAST.

2.6 Wavetrack: A Flexible Framework for Automated Recognition and Tracking of Wave-Like Events in Solar Imagery

2.6.1 Overview

Solar eruptive events encompass a myriad of intricate phenomena, including flares, filament eruptions, coronal mass ejections (CMEs), and CME-driven shock waves. The principal drivers of solar energetic particles (SEPs) are acknowledged to be CME-driven shocks within the corona and interplanetary space. This acceleration primarily occurs through the diffusive shock acceleration (DSA) and shock drift acceleration (SDA) processes (Reames 2021). Efforts have been devoted to characterizing and modeling SEP acceleration under ideal conditions (Vainio & Laitinen 2008; Sokolov et al. 2009; Kozarev et al. 2013). Recent endeavors have shifted towards the development of more realistic CME-shock and SEP acceleration models, incorporating observational data (Vourlidas et al. 2012; Kwon et al. 2014; Kozarev et al. 2015, 2019).

Understanding the efficiency and spatial distribution of SEP acceleration necessitates a comprehensive grasp of CME-shock interactions with three-dimensional coronal fields Rouillard et al. (2016). The modeling of DSA requires the deduction of shock front shapes from observations, given the profound impact of the local magnetic field-shock angle on acceleration Guo & Giacalone (2013). Moreover, the lateral over-expansion of CMEs early in their evolution modifies the compressive front Bein et al. (2011);

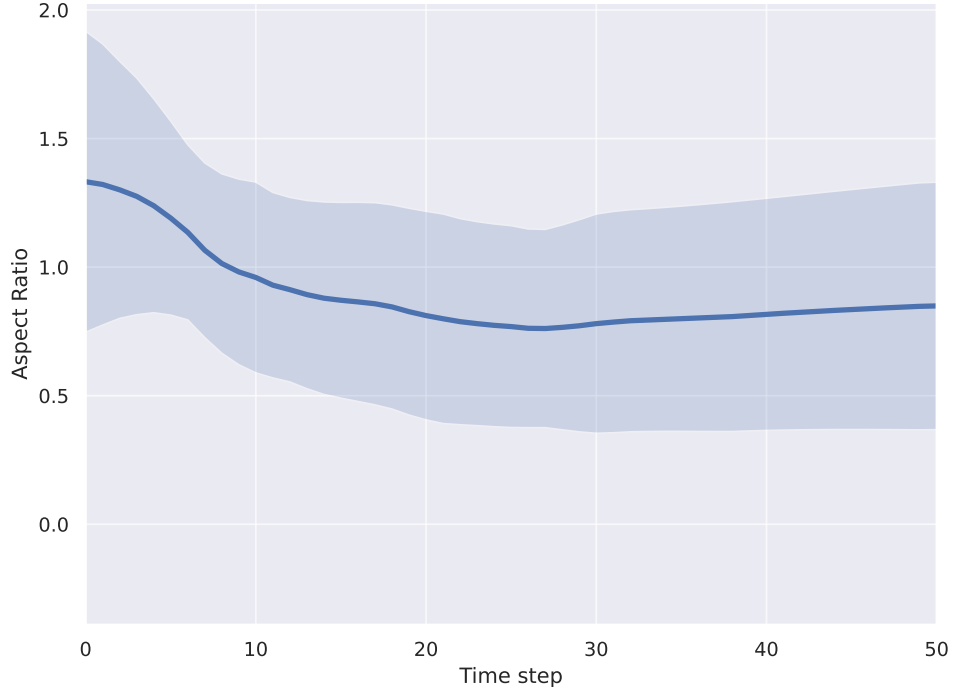


Figure 2.13: Time profile of the mean aspect ratio of the 26 historical events studied with SPREAdFAST.

Temmer (2016), necessitating improvements to the idealized shock surface descriptions used in modeling (Vourlidas et al. 2012; Kwon et al. 2014; Rouillard et al. 2016).

The utilization of extreme ultraviolet (EUV) imaging, facilitated by instruments such as STEREO/EUVI (Wuelser et al. 2004) and SDO/AIA (Lemen et al. 2012), enables the characterization of shocks. The high resolution and multi-wavelength coverage of these instruments permit the time-dependent modeling of SEP acceleration (Kozarev & Schwadron 2016; Kozarev et al. 2017, 2019). With the burgeoning demand for Big Data, solar feature detection has become more automated, employing fundamental techniques reviewed by Aschwanden (2010) and applied to features at various heights (Pérez-Suárez et al. 2011). Some of these techniques are tailored to detect specific solar features, such as sunspots and active regions (Curto et al. 2008).

EUV wave recognition and tracking pose challenges due to their weak intensity in proximity to other features. While algorithms for this purpose exist, their complexity is notable (Podladchikova & Berghmans 2005; Verbeeck et al. 2014; Long et al. 2014; Ireland et al. 2019). Specifically, CorPITA (Long et al. 2014) and AWARE (Ireland et al. 2019) fit shapes to flare-centered wave sectors but are constrained to the solar disk.

This study, led by Stepanyuk et al. (2022), introduces Wavetrack, a flexible, object-oriented Python library designed for general solar feature detection and tracking. Wavetrack integrates multiscale representation (Starck & Murtagh 2002), $\tilde{\Lambda}$ trous wavelets (Akansu 1991; Holschneider et al. 1989), and filtering at its core. Notably, Wavetrack has the capability to generate training sets for machine learning-based recognition.

Machine learning applications are gaining prominence in solar physics, spanning areas such as EUV irradiance mapping (Szenicer et al. 2019), solar flare prediction (Li & Zhu 2013), and magnetic flux generation (Kim et al. 2019). However, the potential of data-driven CME tracking is hindered by limited training sets. Wavetrack addresses this limitation by facilitating the conversion of results into annotated sets.

Central to Wavetrack is a method for general feature recognition and tracking, implemented as an accessible, open-source Python library. Its modular structure allows the configuration of applications by adjusting a few threshold parameters. The calculation scheme integrates multiscale data representation (Starck & Murtagh 2002) and the $\tilde{\Lambda}$ trous wavelet transform (Akansu 1991; Holschneider et al. 1989), supplemented by image filtering techniques for noise removal and edge enhancement.

Wavetrack distinguishes itself from existing algorithms by offering a flexible framework for detecting various solar features in EUV, white light, and other observations. Its modular design facilitates the gen-

eration of training sets for machine learning approaches, supporting automated analysis for deriving new insights from the extensive solar data. The Δ trous wavelet transform' employed by Wavetrack enables the isolation of features at different scales, effectively separating noise from the signal and enhancing edges. Wavelet coefficients encode the multiscale structure efficiently, with thresholding suppressing noise by zeroing insignificant values. Further refinement of the signal is achieved through filtering techniques. Morphological operations, such as opening, eliminate artifacts and smooth edges, while contrast enhancement sharpens edges and boundaries. The resulting output highlights features while suppressing noise.

Wavetrack strategically applies these techniques to recognize faint features like EUV waves and tracks them by identifying significant coefficients across wavelet scales. This approach avoids pre-processing steps, such as difference images, that may introduce false signals. The adaptability of Wavetrack is a key feature, allowing users to build specific applications by adjusting parameters such as thresholds and filters. Importantly, the original data remains unaltered, with only processed copies utilized for feature detection to prevent information loss.

Wavetrack, offered as an open-source tool, invites community involvement, enabling users to contribute modules, optimizations, and new techniques. This collaborative effort is poised to enhance solar data analysis capabilities in the era of Big Data, facilitating the discovery of new knowledge to deepen our understanding of the dynamic Sun.

In the realm of solar image processing and analysis, diverse techniques contribute significantly to understanding solar phenomena. This section delineates the methods employed, encompassing wavelet transform, image filtering, feature detection algorithms, machine learning, and solar feature tracking.

- **Wavelet Transform:** The application of the Δ trous wavelet transform' constitutes a fundamental multi-scale data representation concept widely employed in solar image analysis. This method facilitates the extraction of features at various decomposition and intensity levels, contributing to the comprehensive understanding of solar events.
- **Image Filtering:** Various image filtering techniques play a crucial role in enhancing and extracting specific features within solar images. These techniques, adept at detecting and tracking phenomena like CME shock waves and filaments, contribute significantly to the analysis of solar dynamics.
- **Feature Detection Algorithms:** Automated algorithms, leveraging image processing techniques, are instrumental in detecting and identifying diverse solar features, including sunspot groups, active regions, and eruptive fronts. These algorithms enhance the efficiency of solar feature identification across different types of observations.
- **Machine Learning:** The integration of machine learning methods, such as Convolutional Neural Networks (CNNs) and Generative Adversarial Networks (GANs), signifies a contemporary approach in solar image analysis. These methods find application in tasks ranging from predicting solar flares to generating magnetic flux distributions, enriching the analytical capabilities of solar researchers.
- **Solar Feature Tracking:** An essential facet of image analysis involves tracking the evolution of solar features over time. Tracking algorithms, instrumental in monitoring the movement and changes in features like CMEs, filaments, and EUV waves, contribute significantly to understanding dynamic solar processes.

The present study leveraged observations from the Atmospheric Imaging Assembly (AIA) instrument on the Solar Dynamics Observatory (SDO). The AIA instrument, functioning as an extreme ultraviolet (EUV) imager, offers high-resolution and high-temporal observations, particularly useful for detecting and characterizing large-scale shocks known as EUV waves or Coronal Bright Fronts (CBFs). Focusing specifically on the AIA channels centered on 193 \AA and 211 \AA wavelengths, the study utilized a standard AIA pipeline with the SunPy package to process the 193 \AA data.

The processing involved the creation of base images through the averaging of a series of images preceding the eruption. Subsequent construction of base difference images, achieved by subtracting the base images from the current raw image sequence, facilitated the enhancement of intensity changes caused by CBFs while mitigating static details and reducing noise. Given the typically dim nature of CBFs in EUV images, the study pre-selected a segment of the dynamic range where the shock wave is revealed from the base difference image of the sequence. The observations obtained from the SDO/AIA telescope were instrumental in studying and tracking the CBFs and their temporal evolution, providing essential data for analyzing the spatial and temporal relationships of CBFs and other solar dynamic features.

2.6.2 Image Filtering Techniques

Specific image filtering techniques, including thresholding, wavelet decomposition, and segmentation, formed the cornerstone of the method. Initial thresholding applied to the absolute values of pixels in the base difference images narrowed the dynamic range, concentrating on the segment containing the object of interest.

Subsequent to thresholding, the base difference images underwent Δ trous wavelet decomposition into multiple scales. Each wavelet coefficient underwent relative thresholding based on the statistical distribution of pixel intensities at each decomposition level. The segmentation process yielded object masks for each time step, subsequently multiplied by the original data to reveal the intensity of different parts of the object.

Given the variations in statistical distributions of pixel intensities in base and running difference images, tailored approaches were applied. In base difference images, pixel intensities were constrained to a specific segment, focusing on the object of interest, such as a CBF. Running difference images, employed to identify eruption initiation, depended on the specific features and objects under observation.

The Δ trous wavelet transform, constituting a multi-scale data representation, significantly contributed to the recognition and tracking of solar images. This hierarchical decomposition enabled the extraction of specific objects and their masks from imaging observations, facilitating their tracking and temporal evolution. The Δ trous wavelet decomposition enhanced the clarity and intensity of faint features like EUV waves, offering a flexible framework applicable to various solar phenomena across different wavelengths. This method emerges as a valuable tool for comprehensively analyzing and understanding the dynamics of solar features, including CME shock waves and filaments.

The study introduced the Wavetrack package, designed for automated detection and tracking of dynamic coronal features in solar observations. Utilizing wavelet decomposition, feature enhancement and filtering, and object recombination, Wavetrack identified and tracked features such as CBFs and eruptive filaments. This object-oriented Python framework, adaptable to both on-disk and off-limb features, enables tracking of features that bifurcate over time.

2.6.3 Wavetrack for Coronal Wave Tracking

In tracking coronal waves, Wavetrack utilized wavelet decomposition, feature enhancement, and filtering techniques. The Δ trous wavelet decomposition method enhanced faint features like EUV waves, capturing different scales of features through convolutions. Automated feature recognition, incorporating intensity thresholding, image posterization, median filtering, segmentation, and intensity level splitting, identified and isolated coronal wave features. The output comprised time-dependent pixel masks, representing the tracked coronal wave, applicable to generating final feature maps for both on-disk and off-limb features.

2.6.4 Wavetrack for Filament Tracking

For filament tracking, Wavetrack followed a process involving wavelet decomposition, feature recognition, object mask generation, and image recombination. The Δ trous wavelet decomposition identified different scales of features, and subsequent processing enhanced the features for ease of tracking. Object masks generated for each time step isolated filament features, and image recombination from weighted wavelet scales produced final feature maps. The choice of images, such as inverted AIA 193 \AA images, depended on source data and filament velocity.

2.6.5 Fourier Local Correlation Tracking (FLCT) Model

To determine the plane-of-sky velocity and speed of solar features, the study employed the FLCT model, utilizing the Fourier Local Correlation Tracking (FLCT) method. Through the analysis of consecutive solar images and the tracking of feature motion over time, the FLCT algorithm was applied to object masks derived from the Wavetrack methodology. The resultant output furnished detailed maps of instantaneous velocity, contributing to a deeper understanding of the expansion and evolution of solar features such as Coronal Bright Fronts (CBFs) and erupting filaments.

The overall methodology of the study integrated advanced image processing techniques, incorporating wavelet transform, image filtering, feature detection algorithms, and machine learning. This comprehensive approach facilitated an in-depth analysis of solar observations. Notably, the Wavetrack

package emerged as a versatile tool, specifically valuable in the tracking of dynamic coronal features. Its application provided significant insights into the intricate dynamics governing the solar environment.

2.6.6 Results

The study presents several examples and case studies that demonstrate the application of the Wavetrack package. Here are some of the examples mentioned:

1. **May 11, 2011 event:** The Wavetrack algorithm was used to track both an erupting filament and the coronal bright front it drives. The relationship between the driver and wave was studied using the segmented features from AIA 193 Å observations.
2. **September 29, 2013 event:** Wavetrack was applied to a large-scale filament in a slow eruption. The segmented filament feature was overlaid on the solar corona, and the on-disk feature was consistently tracked during the eruption.
3. **December 12, 2013 event:** Wavetrack was used to track the evolution of driven and non-driven regions of the CBF. The method revealed the relation between the CBF and eruptive features. These examples demonstrate the versatility of Wavetrack in recognizing and tracking various solar features, both on the solar disk and off the solar limb.
4. **June 07, 2011 event:** For this event, the variation in speed between the geometric center and center of mass is up to 300 km s^{-1} in the radial direction. The angle between the geometric center and center of mass changes quite a lot as different parts of the compressive front brighten and dim. However, the angle remains relatively stable, changing only slightly during this event.

Here, I will just focus on the first event since it was accompanied with a coronal bright front.

The Wavetrack methodology was applied to analyze three previously investigated eruptive events observed by the AIA telescope (Kozarev et al. 2015, 2017). In the first event on May 11, 2011, an erupting filament induced a relatively bright CBF on the northwest region of the solar disk near the limb. The second event, occurring on June 07, 2011, originated close to the southwest limb and featured a large and luminous CBF. On December 12, 2013, the third event, also originating near the southwest limb, was examined.

Figure 4 illustrates the successfully extracted Wavetrack CBF objects for the three events, observed at four time points, each separated by 3 minutes. Wavetrack object masks, when applied to base difference images, were visualized using a blue-green color map overlaid on the original AIA 193 Å observations in grayscale to emphasize the CBFs. Across all three events, Wavetrack adeptly delineated the extent of the CBF in consecutive time steps, demonstrating its ability to track the evolution of CBFs both on the solar disk and off the limb. This capability was maintained despite the distinct pixel distributions and intensities in these two regions. The application of Wavetrack facilitated the detailed study of the time-dependent shapes and changing intensity distributions of CBFs, separate from the broader corona. Moreover, Wavetrack effectively selected CBF objects under different coronal activity states. For instance, despite increased coronal activity on December 12, 2013, Wavetrack successfully segmented the CBF. Importantly, the segmentation of the CBF in the last event highlighted Wavetrack's capability to track multiple separate parts of the same feature.

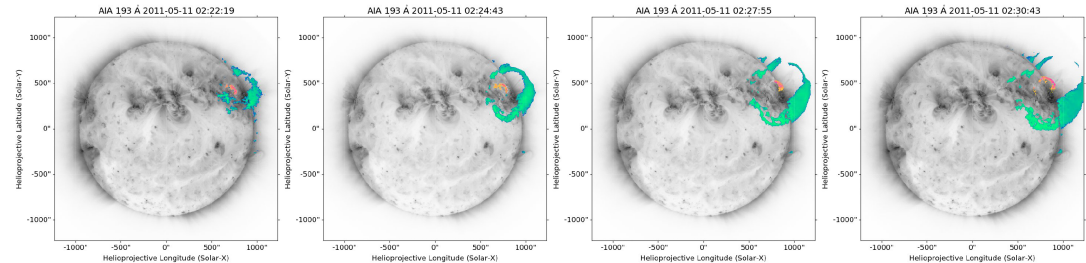


Figure 2.14: Wavetrack images showing progression of a CBF and filament on May 11, 2011. Three snapshots captured ~ 2 minutes apart track the CBF and filament over time. Credit goes to Stepanyuk et al. (2022).

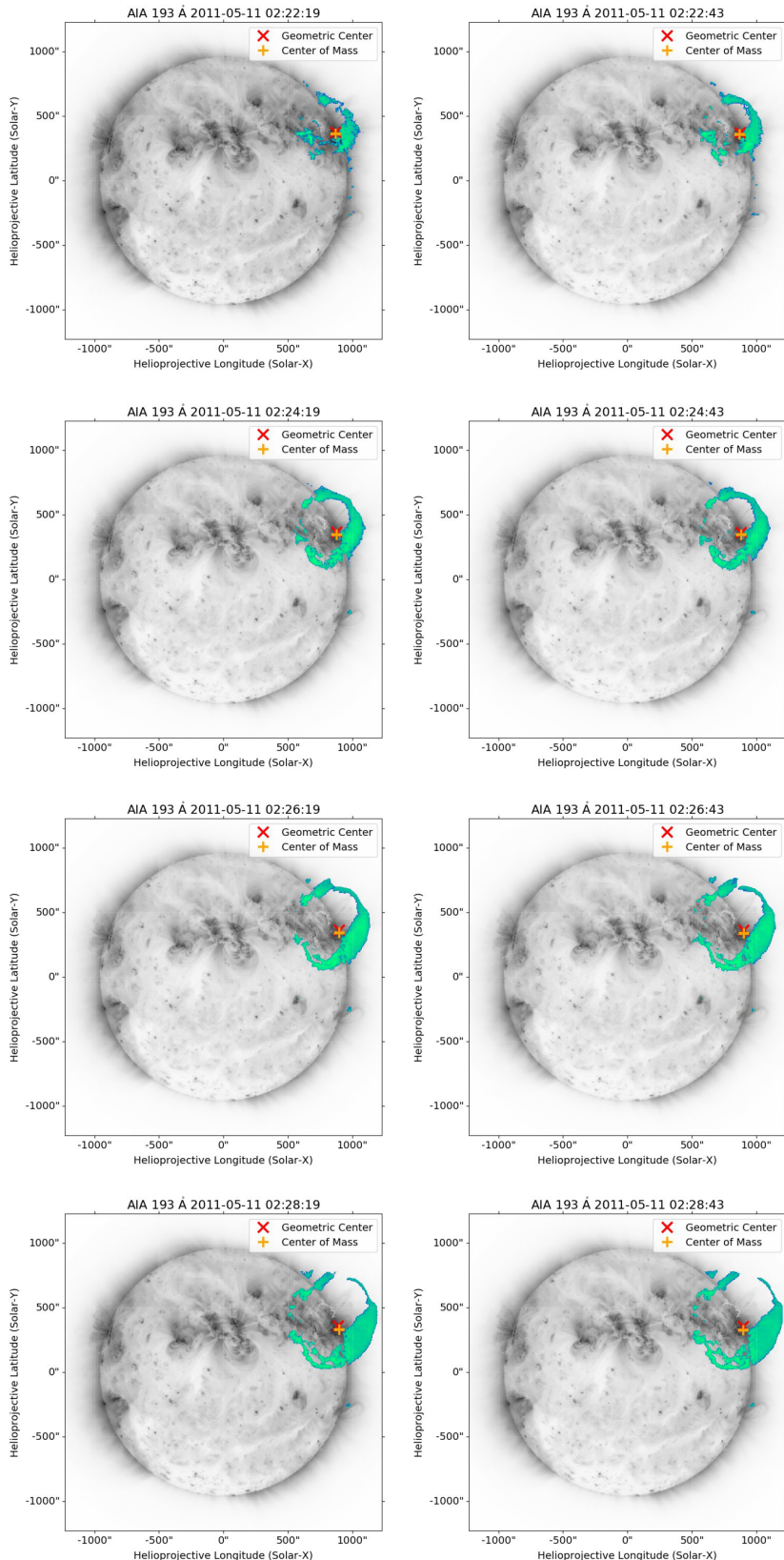


Figure 2.15: Wavetrack images of a May 11, 2011 eruption, with CBF mask applied. Four image pairs shown, separated by 2 minutes, to track CBF over time. Credit goes to Stepanyuk et al. (2022).

The Wavetrack code was further applied to isolate and study the kinematics of CBFs and filaments in detail. The Fourier Local Correlation Tracking (FLCT) method, extensively utilized for estimating horizontal flows in photospheric magnetograms, was employed for this purpose. Initially proposed as a cross-correlation technique for precise motion measurement, FLCT calculates a 2D flow field that best resembles the scalar field between two consecutive 2D maps.

Figure 2.15 displays four pairs of consecutive AIA images from the May 11, 2011 event, used as input for the FLCT algorithm. Each pair, separated by 24 seconds, is strategically chosen to observe the CBF progression over 6 minutes. The corresponding FLCT results, presented in Figure 2.16, show the instantaneous plane-of-sky direction of motion and speed of each CBF region. Notably, the results reveal the uneven expansion of the CBF from the central source. In this event, the thinnest part of the CBF, strongly driven by the erupting filament, exhibited the fastest motion compared to other regions on the disk and off the limb. This nuanced information, not discernible from intensity observations alone, underscores the value of our combined Wavetrack and FLCT approach in elucidating the dynamic behavior of coronal features.

In Figure 2.17, the kinematics of the centers of mass (CM) and geometric centers (GC) of the Coronal Bright Front (CBF) were thoroughly analyzed. The research provided detailed metrics over time, including X-axis and Y-axis positions measured from the projected solar center in solar radii, radial distances in R_{\odot} , and radial speeds of the GC and CM points in kilometers per second. The angle between the position vectors of GC and CM, denoted as $\theta(GC - CM)$, was also calculated in degrees. The results illustrated a clear split between the radial positions of GC and CM, with a noticeable shift to the south of the CM after 02:26 UT. This shift was supported by the evolution of the angle $\theta(GC - CM)$, indicating a gradual increase in the wave's thickness in the southwest of the front. Despite these positional changes, the speeds of the GC and CM points varied only slightly, ranging from 0 to 100 $km s^{-1}$. Additionally, the kinematics of the center of mass and geometric centers for the May 11, 2011 event are depicted, showcasing the X-, Y-, and R-positions, distance magnitudes, and angle variations between the two points over time. These findings offer valuable insights into the dynamic behavior and evolution of the CBF during the specified solar event.

2.7 Geomagnetic Storms: CME Speed De-Projection vs. In Situ Analysis

This study, led by Miteva et al. (2023), examines the relationship between the intensity of geomagnetic storms (GS) and parameters of solar and interplanetary phenomena. We utilize the recently developed PyThea framework to reconstruct the 3D geometry of geo-effective CMEs and compare on-sky and de-projected values, focusing on the reliability of the de-projection capabilities. Spheroid, ellipsoid, and graduated cylindrical shell models are used. We collected parameters of the GS-associated phenomena. Considerable variation in 3D de-projections of CME speeds was obtained depending on the reconstruction model chosen and subjective observations. Fast CME speeds combined with frontal magnetic structure orientation when reaching Earth's magnetosphere proved the best indicator of GS strength. More accurate estimations of geometry, direction, and de-projected speeds are critical for operational GS forecasting in space weather prediction schemes.

2.7.1 Overview

Solar eruptive events like CMEs and solar flares (SFs) can generate disturbances that propagate through interplanetary space and impact Earth's magnetosphere, leading to space weather effects (Fletcher et al. 2011; Webb & Howard 2012; Klein & Dalla 2017; Temmer 2021). The electromagnetic radiation from SFs arrives at Earth first, followed by energetic particles. The plasma clouds of CMEs take longer, from tens of hours up to a few days, to impact Earth's environment (Malandraki & Crosby 2018; Gopalswamy 2022). The temporary disruption of Earth's magnetosphere and atmosphere due to these solar events are known as geomagnetic storms (GSs) (Gonzalez et al. 1994; Saiz et al. 2013; Lakhina & Tsurutani 2016).

The coupling between solar wind plasma and Earth's magnetosphere occurs through magnetic reconnection, enabled when the interplanetary (IP) magnetic field turns southward (negative B_z component) and impacts Earth at high speed, as during CMEs (Dungey 1961; Akasofu 1981; Echer & Gonzalez 2022). This leads to increased particle injection into the magnetosphere and atmosphere, causing bright auroral displays. Drifting electrons and protons also drive the westward ring current responsible for decreases in

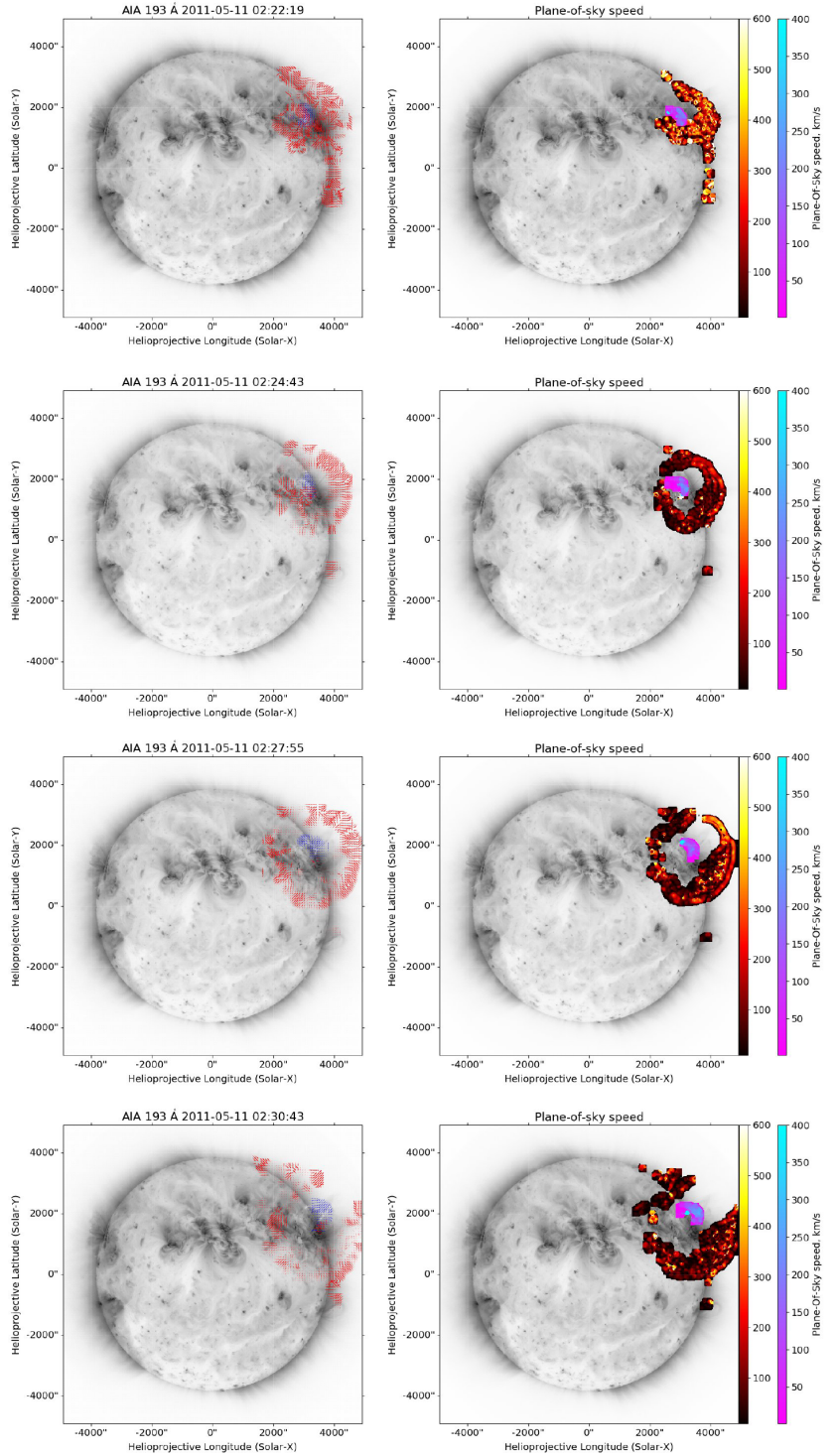


Figure 2.16: FLCT model output for four image pairs from Fig. 3. Left: the plane-of-sky velocity vectors. Right: plane-of-sky speed. Credit goes to Stepanyuk et al. (2022).

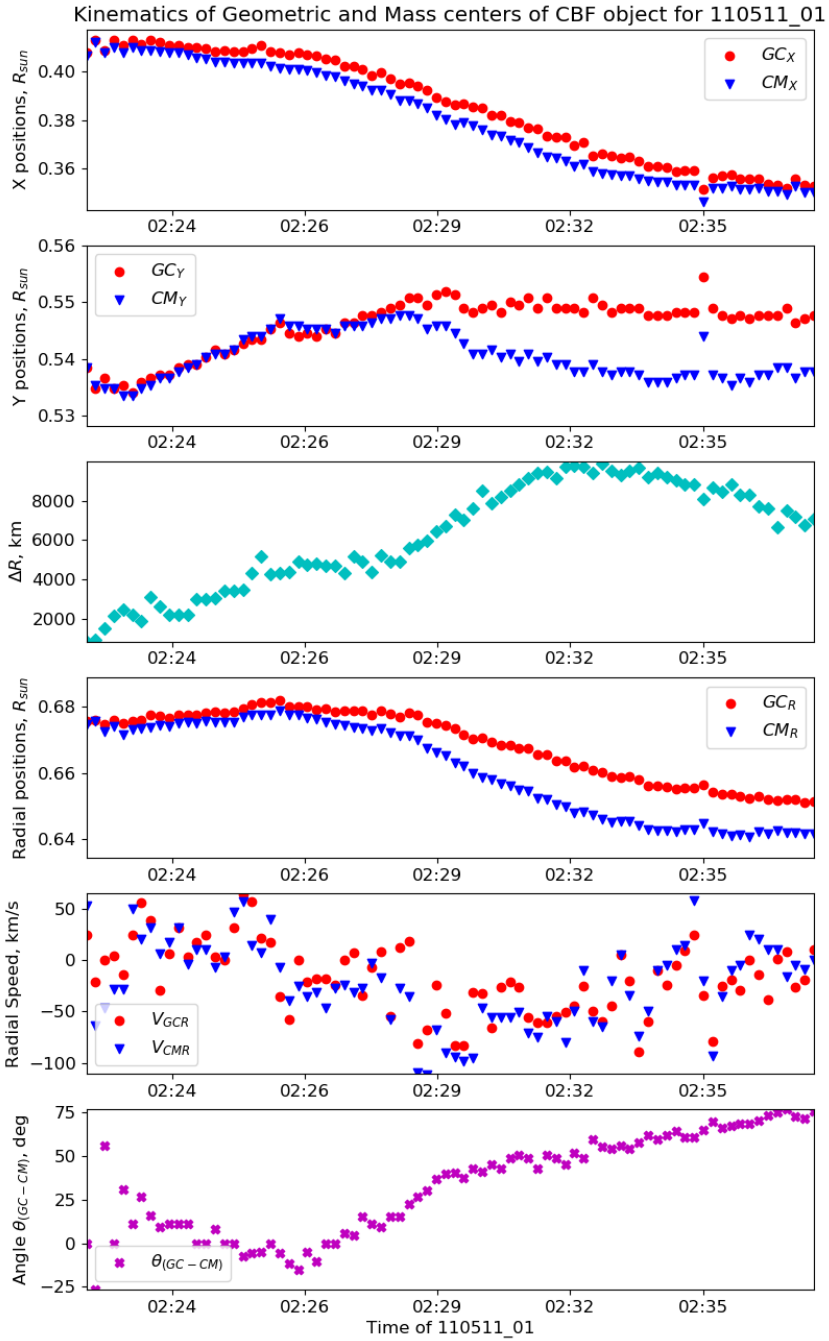


Figure 2.17: Analysis of the center of mass and geometric centers' motion during the May 11, 2011 event. The different rows present the X-, Y-, and R- positions for both GC and CM, the distance between GC and CM in kilometers, and the angle between these two points over time. Credit goes to Stepanyuk et al. (2022).

the horizontal magnetic field measured by the disturbance storm time (Dst) index (Gonzalez et al. 1994; Saiz et al. 2013; Lakhina & Tsurutani 2016).

Fast CMEs propagating through IP space (ICMEs) cause the most intense GSs, with sudden Dst decreases, compared to gradual storms from corotating interaction regions (CIRs) (Tsurutani et al. 1997; Zhang et al. 2007; Wu & Lepping 2016; Borovsky & Denton 2006). ICME shock waves and magnetic ejecta produce cascading effects in near-Earth space that can disrupt technology (Pulkkinen 2007).

Earth-directed fast ejecta with strong southward magnetic fields inside are the most geoeffective. However, single spacecraft observations are limited by projection effects, leading to uncertain CME speed estimations (Paouris et al. 2021; Kouloumvakos et al. 2022). Previous studies found no clear relationship between GS intensity and solar flare parameters or CME properties like projected speed and angular width (Samwel & Miteva 2023). Furthermore, CME magnetic structure cannot be derived from remote sensing data. Reliable solar or near-Sun measurements that provide early warnings for potential GS strength remain lacking.

Accurately predicting when an incoming disturbance will impact Earth requires determining the arrival time and speed of CMEs. Different portions of these large structures, such as the apex or flanks, can hit Earth upon arrival at 1 AU. Flank hits may only involve the CME sheath while apex hits include both sheath and ejecta, leading to different magnetospheric effects (Kay & Gopalswamy 2018). Therefore, deducing CME directionality and 3D geometry is important. To maximize forecast lead time, these parameters should be estimated as early as possible when the CME emerges in coronagraph fields of view. In images, CMEs appear as line-of-sight integrated brightness enhancements projected onto the observing plane (Vourlidas et al. 2003; Jackson et al. 2010).

Further developing reconstruction techniques to correct for projection effects can improve CME propagation understanding and impact forecasting (Thernisien et al. 2009; Mierla et al. 2010; Wood et al. 2010; Thernisien 2011). Several CME propagation models exist (Odstrcil et al. 2004; Xie et al. 2004; Vršnak et al. 2013; Pomoell & Poedts 2018). A study found 2D CME speeds underestimate 3D speeds by $\sim 20\%$ while 2D widths overestimate 3D widths (Jang et al. 2016). Another study showed observer bias in 3D modeling using graduated cylindrical shells, even for experienced observers (Verbeke et al. 2022). CME structure interpretation differs, and line-of-sight integration leads to non-unique solutions.

This study focuses on deducing CME directionality and near-Sun speeds using new tools like PyThea (Kouloumvakos et al. 2022). We analyze geo-effective cycle 24 CMEs using multiple reconstruction techniques by two team members. Comparisons are made between derived parameters and Dst. CME speed correlations with ICME and IP shock speeds evaluate 3D de-projection value for arrival forecasting. Other IP parameters are also examined, including shock speed, plasma jumps, and magnetic fields near L1. We examine the correlation between the intensity of geomagnetic storms and parameters of solar and interplanetary phenomena. More specifically, we focus on the speed and geometry of CMEs, as well as interplanetary shocks, as these factors are known to play a significant role in the occurrence and intensity of geomagnetic storms. The objective of the study is to analyze the correlations between the intensity of GS and parameters of solar and IP phenomena. The study also aims to perform 3D geometry reconstructions of geo-effective CMEs using the PyThea framework and compare the de-projected CME speeds with in situ data.

The event selection process for this investigation commenced with the identification of significant GSs within Solar Cycle 24 (SC24). These storms were characterized by a Dst index exceeding 100 nT, as per the classification outlined in Gonzalez et al. (1994). A total of 25 GSs were identified, with Dst indices ranging from 101 to 234 nT. Previous studies have explored the solar and IP origins of these GSs in SC24 (Gopalswamy et al. 2022b; Qiu et al. 2022; Besliu-Ionescu et al. 2022; Abe et al. 2023). However, the comprehensive review of all pertinent literature falls beyond the purview of this study. It is noteworthy that SC24 exhibited a reduced number of GSs in comparison to preceding solar cycles (Selvakumaran et al. 2016).

In our investigation, distinct from prior analyses, our objective was to establish a causal connection between the identified GSs and potential IP and/or solar phenomena. This approach mirrors methodologies employed by other researchers (Zhang et al. 2007; González et al. 2007; Gopalswamy et al. 2008; Echer et al. 2013; Manu et al. 2022). To delineate the solar and IP drivers, we employed an association procedure widely acknowledged in the field of Space Weather (SW) research. The methodology involves searching for the IP and solar origins of a GS storm within a specific timeframe preceding the reported GS occurrence at Earth. The sequential steps of our approach are delineated below:

1. **Temporal Association with IP and ICME Events:** We initiated the analysis with a temporal association between the GS and recorded IP shocks in the vicinity of Earth. This association was

established within a 1-day period preceding the reported minimum Dst of the GS. A parallel procedure was employed for the association with ICMEs reported in proximity to Earth. Additionally, animations from the *heliowea*ther archive⁹ (accessed on 5 April 2023) were utilized to validate potential ICME and IP shock candidates.

2. **Association with CMEs:** Subsequently, we extended the association to include CMEs within a 3-to-5 day window prior to the IP (or GS) timing. Information from available solar and IP event catalogs, as well as animations from the *heliowea*ther archive⁹ (accessed on 5 April 2023), was employed for this purpose.
3. **Completion of the Association with SFs:** The final step involved associating the GS with the identification of a SF linked to the previously associated CME. This association was based on timing (within one hour between the SF onset and CME timing) and location constraints (the SF location had to align with the solar quadrant reported in the measurement position angle, MPA, of the CME).

All utilized databases, catalogs, and publicly available lists pertinent to the analysis are summarized as follows:

- GS database (Kyoto)¹⁰ (accessed on 5 April 2023);
- SF database (GOES)¹¹ (accessed on 5 April 2023);
- CME catalog (SOHO-LASCO)¹² (accessed on 5 April 2023);
- ICME Wind database¹³ (accessed on 5 April 2023);
- ICME ACE database¹⁴ (accessed on 5 April 2023);
- IP shock database (Wind)^{15, 16} (accessed on 5 April 2023).

2.7.2 GSs and IP Phenomena

The findings pertaining to GSs and their associated ICMEs and IP shocks are succinctly presented in Table 1 in Miteva et al. (2023). The initial column designates the event number (#), a consistent reference utilized throughout this paper. Columns (2) and (3) detail the GS date, hour (mm-dd/hr), and the corresponding Dst index (in nT). Subsequently, columns (4)–(6) expound upon the ICME parameters (Nieves-Chinchilla et al. 2018), drawing from the Wind database accessible at this website¹⁷. The sheath duration (D, in hours), representing the temporal span between the initiation times of the ICME and the magnetic structure, is computed from the available timings within the plots offered by the aforementioned Wind database, and is presented in column (7). The ICME in situ measured speed is extracted from both the Wind and ACE databases, with the exception of E11 where no ICME is reported.

Column (8) integrates the minimum Bz component throughout the ICME duration, as ascertained from the data available at this website¹⁸, thereby enhancing the comprehensiveness of the dataset. In Column (9), we conduct a qualitative assessment of the ICME arrival orientation. Specifically, we visually inspect the intersection point between the ICME structure and Earth using ecliptic plane animations accessible at this website¹⁹. The orientations are denoted as either *hit* (nose) or *f* (flank) arrivals. Instances of discrepancies among diverse data sources, such as the presence of solar wind streams or CIRs visible in animations contradicting ICME arrivals identified through in situ data, are marked as ‘u’ (uncertain) in the same column. This classification signifies situations where a distinct ICME structure propagating through the IP space could not be conclusively observed. Noteworthy is the occurrence of swift solar wind flows and/or CIRs recorded near Earth during ICME and/or shock wave events. For

⁹<http://heliowea.ther.net/archive/>

¹⁰<https://wdc.kugi.kyoto-u.ac.jp/dstdir/index.html>

¹¹<http://ftp.swpc.noaa.gov/pub/warehouse/>

¹²CMEcatalog(SOHO-LASCO)

¹³https://wind.nasa.gov/ICME_catalog/ICME_catalog_viewer.php

¹⁴<https://izw1.caltech.edu/ACE/ASC/DATA/level3/icmetable2.htm>

¹⁵<http://www.ipshocks.fi/database>

¹⁶https://lweb.cfa.harvard.edu/shocks/wi_data/

¹⁷https://wind.nasa.gov/ICME_catalog/ICME_catalog_viewer.php

¹⁸<https://cdaweb.gsfc.nasa.gov/>

¹⁹<http://heliowea.ther.net/archive/>

instance, in the cases of E11 and E18, a CIR was identified as their IP origin by Qiu et al. (2022); however, in contrast to these findings, our methodology does not differentiate between ICME and sheath origins.

The final columns, (10)–(13), enumerate the properties of the IP shock, incorporating timing, speed, magnetic field, density, temperature jump at the shock interface, and the Mach number (Mms). These details are sourced from Wind satellite data, available at this website²⁰, with the exception of E24, where the median shock speed is derived from this website²¹. Notably, for E17, E18, and E25, no IP shocks are reported in either database.

2.7.3 GSs and Solar Phenomena

In the context of five cases denoted as E05, E11, E17, E18, and E22, our attempts to identify SFs or Coronal Mass Ejections (CMEs) were unsuccessful. Furthermore, in an additional six cases, the specification of SFs proved unattainable. The ensuing presentation provides details on the parameters of the remaining cases, specifically focusing on the solar origins associated with GSs, as outlined in Table 2.6.

Columns (2)–(5) of Table 2.6 elucidate the properties of the GS-associated SFs, while columns (6) to (9) furnish the parameters of the GS-associated CMEs. The identified SFs exhibit a range of magnitudes from C1.2 to X5.4 and are predominantly positioned proximate to the solar disk center, with the exception of E02 and E03. The CMEs associated with these events possess on-sky projected speeds, denoted as 2D, spanning from 126 to 2684 km s^{-1} , extracted from the SOHO-LASCO CDAW catalog. Notably, the majority of the GS-associated CMEs (15 out of 20) exhibit a halo configuration, while three others are in close proximity to halo.

It is imperative to note that events with uncertain CME origins have been excluded from the subsequent 3D analyses. Specifically, in the case of E07, the unique orientation of the double CME rendered the de-projection procedure unfeasible for the same CME structure, leading to its exclusion from the 3D analyses. Additionally, for seven other cases (E12, E14–E16, E19, E23, E25), the online tool utilized for analyses failed to retrieve data simultaneously from both spacecraft. Consequently, these cases have also been omitted from the 3D analyses.

For the remaining 12 cases, successful 3D CME speed reconstructions were achieved from each model. The mean values, based on 2 or 4 available fits (as detailed in the subsequent subsection), are presented in the concluding columns (10)–(12) of Table 2.6. This comprehensive overview provides a foundation for the subsequent analytical discussions, offering a detailed characterization of the solar events associated with the studied GSs.

2.7.4 PyThea 3D De-Projection Tool

The de-projection methodology employed in this investigation relies on the innovative PyThea online tool designed for the 3D reconstruction of CMEs and shock waves (Kouloumvakos et al. 2022). All three available models within PyThea, namely spheroid, ellipsoid, and the graduated cylindrical shell (GCS), are applied in this study. The fitting procedure is conducted independently by two observers within our team. Figure 2.18 presents an illustrative example of the fits for event E03.

Upon scrutinizing the fitting outcomes for this particular example, it becomes evident that the reconstructions exhibit a discernible bias. The observer's subjective choice of structures to align with the model introduces a level of variability. In the top row of Figure 2.18, distinct shock-related structures (manifested as the bending of streamers) are observed, upon which the idealized GCS flux rope geometry is fitted. Consequently, there is a likelihood of overestimating the CME width. Despite this bias, it is noteworthy that the overall results, including directivity and speed for event E03, are minimally impacted. However, it is acknowledged that the complexity of structure choices can lead to larger discrepancies among different observers.

This study places emphasis on deriving de-projected CME speeds based on fits conducted at two distinct time steps. For each of the three models, the initial CME longitude and latitude are manually specified, utilizing the provided locations of the CME-accompanied SFs. It is important to note that these values exhibit minimal to no substantial changes post-finalization of the fitting procedure. Consequently, the final CME directivity provided by PyThea is considered to be a relatively crude estimate. The ultimate orientations of the CME in IP space and at Earth are derived solely from qualitative information

²⁰<http://www.ipshocks.fi/database>

²¹https://lweb.cfa.harvard.edu/shocks/wi_data/

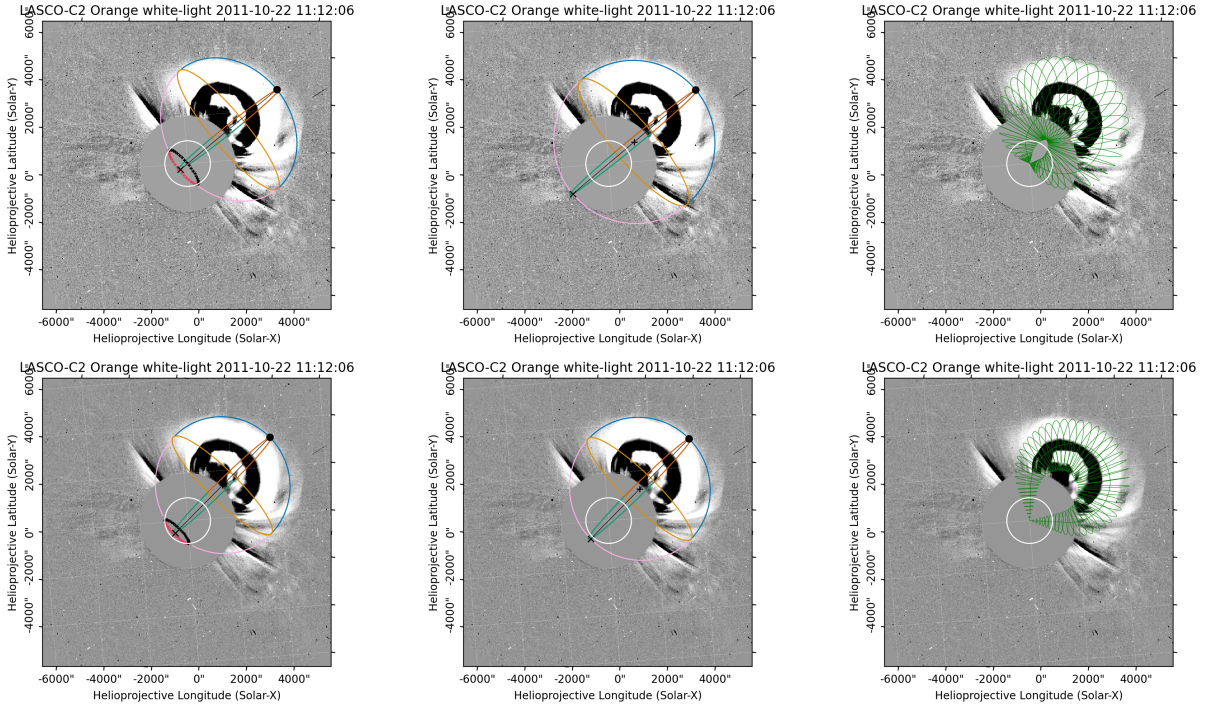


Figure 2.18: 3D reconstructions of a CME (E03) using the spheroid, ellipsoid, and GCS model from the PyThea tool performed by observers 1 and 2 (top and bottom row, respectively). Credit goes to Miteva et al. (2023).

extracted from animations available at this website²². This approach ensures a rigorous and consistent basis for evaluating the de-projected CME speeds in our analyses.

2.7.5 Results

Projection Effects

In our investigation, a fitting analysis of approximately 10 CMEs was undertaken by two designated observers within our research team, I was one of the observers. This analysis involved the utilization of all three models available in the PyThea framework, each selected based on the evaluators' individual considerations.

To elucidate, the fitting process was executed at two distinct time steps to derive a velocity parameter based on the height-time estimation. For each specific event, both observers iteratively conducted the 3D de-projection procedure twice, resulting in averaged values for the CME speeds. These values are meticulously presented in Table 2.7, rounded to the nearest tenth. The disparity between these two fitting instances is denoted as an error (or uncertainty), spanning from 10 km s^{-1} to twice the estimated speed. Additionally, Figure 2 illustrates the correlation between 3D speeds and the corresponding estimated errors for each observer. Notably, considerable variability is observed in both plots, particularly concerning the GCS model; nonetheless, a discernible positive trend emerges between the estimated error magnitude and the CME speed.

The inherent subjectivity and diverse levels of experience among observers play a crucial role in the visual fitting procedure. Noteworthy distinctions in evaluated speeds are evident not only between individual observers using the same model (e.g., spheroid fit for E06) but also between a single observer applying different models (e.g., spheroid and GCS for E13). Furthermore, variations in operating system software further contributed to differences in results. Notably, events E04, E08, and E21 were not completed by both observers due to either PyThea computing resource failures or the substantial uncertainty associated with the visual assessment of CME structures.

Our findings underscore the well-established subjectivity inherent in procedures relying on personal judgment for fit quality, where the alignment of structures with the model is subjective. A more com-

²²<http://helioweb.net/archive/>

prehensive explanation of this human-in-the-loop bias is detailed in (Verbeke et al. 2022). The specific values of CME speeds are meticulously outlined in Table 2.7, while their averaged values, categorized by model, as determined by both observers, are presented in Table 2.6. These averaged values will serve as the basis for subsequent correlation studies.

Table 2.5: Characteristics of GSs, ICMEs, and IP Shock Waves. Magnetic Obstacle (MO) categorized as Flux-rope (Fr), Small rotation flux-rope (F-), Large rotation flux-rope (F+), Complex (Cx), or Ejecta (E). The timestamp includes month (mm), day (dd), and time (UT). Dst is measured in nT, speed in km s^{-1} , Δ (duration from ICME start to MO start) in hours, B_z in nT, hit locations denoted as n (nose), f (flank), */** (fast/slow speed), u (streamer/no clear ICME). **Additional abbreviations:** X: magnetic field/plasma density/temperature; d/u: downstream/upstream side of the shock interface; M_{ms} : Mach number. Credit goes to Miteva et al. (2023).

# (1)	GS			ICME parameters					IP shock parameters				
	mm-dd/hr (2)	Dst (3)	mm-dd/time (4)	type (5)	speed (6)	Wind/ACE (7)	Δ (8)	B_z (9)	hit (10)	mm-dd/time (11)	speed (12)	X_d/X_u (13)	M_{ms}
2011													
E01	08-06/04	-115	08-06/22:00	-	-/540	-	-22.8	f*	08-05/18:41	789	2.52/1.37/2.21	3.7	
E02	09-26/24	-118	09-26/22:00	-	-/580	-	-33.6	f	09-26/11:44	544	2.35/2.56/2.64	2.4	
E03	10-25/02	-147	10-24/17:41	Cx	483/460	6.7	-24.6	f	10-24/17:40	542	2.16/2.94/4.88	2.5	
2012													
E04	03-09/09	-145	03-08/10:32	Cx	576/550	9.4	-19.2	n	03-08/10:31	1245	1.42/1.31/1.25	8.4	
E05	04-24/05	-120	04-23/02:15	F-	373/370	14.6	-15.9	f	04-23/02:15	416	2.45/2.44/1.87	1.7	
E06	07-15/17	-139	07-14/17:39	Fr	491/490	12.6	-20.0	n	07-14/17:39	617	2.08/2.53/4.29	3.3	
E07	10-01/05	-122	09-30/10:14	Cx	354/370	2.0	-21.2	f	09-30/22:19	452	2.55/2.00/2.05	2.5	
E08	10-09/09	-109	10-08/04:12	Fr	398/390	11.6	-16.0	u	10-08/04:12	445	1.96/2.01/1.63	1.7	
E09	11-14/08	-108	11-12/22:12	F+	381/380	10.2	-20.6	f	11-12/22:12	386	2.18/2.20/1.08	1.6	
2013													
E10	03-17/21	-132	03-17/05:21	Fr	529/520	8.8	-19.3	n	03-17/05:22	719	2.45/2.68/10.5	4.1	
E11	06-01/09	-124	-	-	-/-	-	-8.8	u	05-31/15:12	410	2.90/2.16/2.83	2.1	
E12	06-29/07	-102	06-27/13:51	Fr	391/-	12.5	-12.4	u	06-30/10:42	349	1.55/1.61/1.27	1.4	
2014													
E13	02-19/09	-119	02-18/05:59	Fr	421/520	9.1	-15.4	u	02-19/03:10	597	1.82/1.69/1.51	1.9	
2015													
E14	01-07/12	-107	01-07/05:38	F+	451/450	0.8	-20.4	u	01-07/05:39	494	1.70/1.73/1.89	1.2	
E15	03-17/23	-234	03-17/13:00	-	-/560	-	-26.0	f*	03-17/04:00	562	2.52/2.43/3.50	2.6	
E16	06-23/05	-198	06-22/18:07	Cx	598/610	8.3	-39.0	n	06-22/18:08	767	3.34/3.63/6.70	4.1	
E17	09-09/13	-105	09-07/13:05	F+	468/460	10.4	-12.6	u	-	-	-	-	
E18	10-07/23	-130	10-06/21:35	Fr	425/-	0	-9.2	u	-	-	-	-	
E19	12-20/23	-166	12-19/15:35	Fr	398/400	22.1	-19.0	n	12-19/15:38	563	2.49/2.25/4.87	3.0	
2016													
E20	01-01/01	-116	12-31/17:00	-	-/440	-	-16.3	n**	12-31/00:18	404	2.20/2.27/3.99	2.6	
E21	01-20/17	-101	01-19/03:31	Fr	362/370	7.9	-11.6	f	01-18/21:21	350	1.73/1.91/1.60	1.7	
E22	10-13/18	-110	10-12/21:37	F+	384/390	8.8	-6.9	u	10-12/21:16	431	1.82/2.47/4.43	1.9	
2017													
E23	05-28/08	-125	05-27/13:45	F+	318/360	9.1	-20.2	f	05-27/14:42	378	2.68/2.94/2.95	1.9	
E24	09-08/02	-122	09-07/16:17	E	683/460	8.0	-32.2	f*	09-07/22:28	718	-	-	
2018													
E25	08-26/07	-175	08-25/01:02	F+	406/410	11.0	-6.8	n	-	-	-	-	

Table 2.6: Parameters of the solar origin, SFs, and CMEs for GSs from Table 2.5. All times are in UT, speeds in $km\ s^{-1}$, AW and MPA in degrees. Credit goes to Miteva et al. (2023).

# (1)	mm-dd (2)	SF parameters			location (5)	2D CME parameters			spheroid (10)	3D CME speed		GCS (12)
		class (3)	onset (4)	time (6)		speed (7)	AW (8)	MPA (9)		elliptical (11)		
2011												
E01	08-04	M9.3	03:41	N19W36	04:12	1315	360	298	1990	1920	1780	
E02	09-24	M7.1	12:33	N10S56	12:48	1915	360	78	1570	1590	1720	
E03	10-22	M1.3	10:00	N25W77	10:24	1005	360	311	760	690	840	
2012												
E04	03-07	X5.4	00:02	N17S27	00:24	2684	360	57	2150	2460	2530	
E05				uncertain origin					-	-	-	
E06	07-12	X1.4	15:37	S15W01	16:48	885	360	158	1060	1780	1520	
E07	09-28	C3.7	23:36	N06W34	24:12	947	360	251	multiple CMEs			
E08	10-05		uncertain		02:48	612	284	202	350	360	350	
E09	11-09		uncertain		15:12	559	276	157	660	570	720	
2013												
E10	03-15	X1.1	05:46	N11S11	07:12	1063	360	112	720	1040	1110	
E11				uncertain origin					-	-	-	
E12	06-28		uncertain		02:00	1037	360	214	no SOHO images			
2014												
E13	02-16	M1.1	09:20	S11E01	10:00	634	360	227	340	690	890	
2015												
E14	01-03	C1.2	03:06	S05E21	03:12	163	153	144	no STEREO images			
E15	03-15	C9.1	01:15	S22W25	01:48	719	360	240	no STEREO images			
E16	06-21	M2.6	02:06	N12E13	02:36	1366	360	72	no STEREO images			
E17				uncertain origin					-	-	-	
E18				uncertain origin					-	-	-	
E19	12-16	C6.6	08:34	S13W04	09:36	579	360	334	no STEREO images			
2016												
E20	12-28	M1.8	11:20	S23W11	12:12	1212	360	163	820	680	1080	
E21	01-14		uncertain		23:24	191	360	234	620	440	280	
E22			uncertain	origin					-	-	-	
2017												
E23	05-23		uncertain		05:00	259	243	281	no SOHO images			
E24	09-04	M5.5	20:28	S11W16	20:36	1418	360	184	1020	1290	990	
2018												
E25	08-20		uncertain		21:24	126	120	266	no STEREO images			

Table 2.7: CME Speeds ($km\ s^{-1}$) for Observers 1 and 2. Credit goes to Miteva et al. (2023).

#	Spheroid		Ellipsoid		GCS	
	obs1	obs2	obs1	obs2	obs1	obs2
E01	2170 ± 870	1800 ± 270	2130 ± 200	1710 ± 450	1590 ± 100	1760 ± 10
E02	1780 ± 140	1350 ± 50	1880 ± 580	1310 ± 90	1780 ± 260	1630 ± 130
E03	770 ± 40	740 ± 10	640 ± 180	740 ± 180	1020 ± 170	700 ± 270
E04	-	2150 ± 140	-	2460 ± 70	-	2530 ± 630
E06	1410 ± 420	710 ± 70	1870 ± 50	1700 ± 300	1680 ± 870	1560 ± 470
E08	350 ± 90	-	360 ± 150	-	350 ± 70	-
E09	690 ± 280	630 ± 150	550 ± 170	590 ± 60	670 ± 610	710 ± 220
E10	840 ± 380	610 ± 1040	1120 ± 360	960 ± 90	1160 ± 650	1310 ± 80
E13	320 ± 90	350 ± 50	620 ± 140	750 ± 160	780 ± 80	1310 ± 700
E20	830 ± 190	800 ± 600	790 ± 90	570 ± 20	1240 ± 280	1130 ± 230
E21	620 ± 230	-	440 ± 40	-	280 ± 180	-
E24	750 ± 270	1310 ± 220	880 ± 350	2020 ± 960	950 ± 120	1560 ± 540

Correlation between GSs, Coronal and Near-Sun Parameters

In Figure 2.19, we present a scatter plot depicting the relationship between the modulus of the GS Dst index and the CME speed, as derived from the data in Table 2.6. To enhance clarity, the averaged results of the three model fits are collectively illustrated and labeled as *3D-mean* in Table 2.8. These values are juxtaposed with the 2D SOHO-LASCO CME speed. Horizontal lines, representing the error estimates from the 3D de-projections, are also included for completeness, despite the substantial overlap. For demonstrative purposes, we highlight the largest error value among the two observers, as outlined in Table 2.7.

The analysis conducted reveals no discernible trend between the Dst index and the CME speed,

irrespective of whether the 3D de-projection or the 2D CME speeds are considered. It is important to note that, due to data constraints, 3D speed de-projections were not feasible for the most robust GSs. This limitation results in a skewed distribution of the 3D speeds, impacting the overall findings. Despite the modest sample size (comprising between 10 and 20 event pairs), the quality of the fit is assessed through Pearson correlations. The correlation coefficients, reflecting the relationship between all CME speed estimations and the GS Dst index, are systematically documented in Table 2.8. These coefficients range from negligible (e.g., 0.04 for the 2D LASCO speeds) to moderate (with the highest value reaching 0.55, observed with the GCS model). Importantly, no significant correlations are identified between the Dst index and other coronal parameters, such as SF class, location, and CME AW, as inclusively presented in the same table for comprehensive evaluation.

Table 2.8: Table displaying Pearson correlation coefficients among the GS Dst index, CME speed, and various solar parameters, with the respective sample sizes indicated in parentheses. Credit goes to Miteva et al. (2023).

CME source	Dst-speed	solar parameter	Dst-solar parameter
LASCO	0.04 (20)	SF class	-0.04 (14)
3D - mean	0.49 (12)	SF latitude	-0.16 (14)
3D spheroid - mean	0.34 (12)	SF longitude	0.13 (14)
3D spheroid - obs1	0.14 (11)	CME AW	0.03 (20)
3D spheroid - obs2	0.15 (10)		
3D ellipsoid - mean	0.53 (12)		
3D ellipsoid - obs1	0.28 (11)		
3D ellipsoid - obs2	0.40 (10)		
3D GCS - mean	0.55 (12)		
3D GCS - obs1	0.49 (11)		
3D GCS - obs2	0.27 (10)		

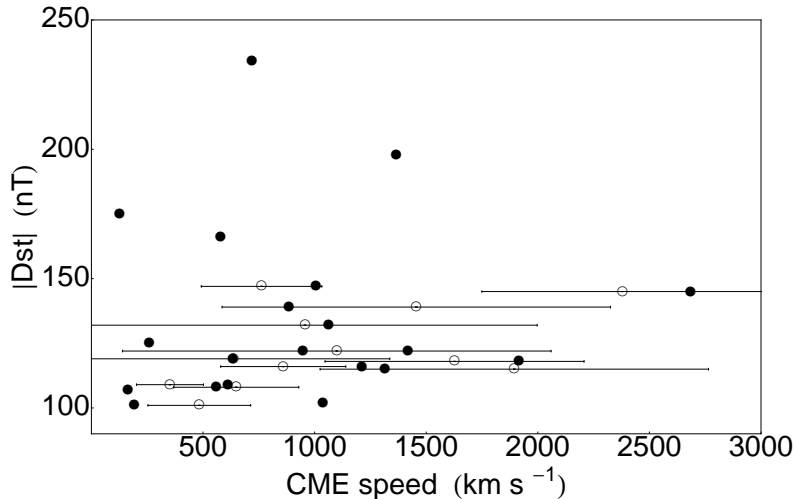


Figure 2.19: Scatter plot illustrating the relationship between the Dst index and CME speed, incorporating data from the SOHO/LASCO instrument (represented by filled circles) and 3D de-projections (depicted by empty circles). Credit goes to Miteva et al. (2023).

Correlation between GSs and IP Parameters

Here, we explore the correlations between GSs and various parameters associated with pre-selected IP phenomena. To visually represent these relationships, scatter plots are employed for specific parameter pairs. These parameters include Dst index versus ICME speed and IP shock speed, Dst versus Mach number and sheath duration, Dst versus $|B_z|$ and B_d/B_u , Dst versus T_d/T_u and N_d/N_u . Figure 2.20 shows these relationships, and the corresponding Pearson correlation values elucidating these trends are documented in Table 2.9.

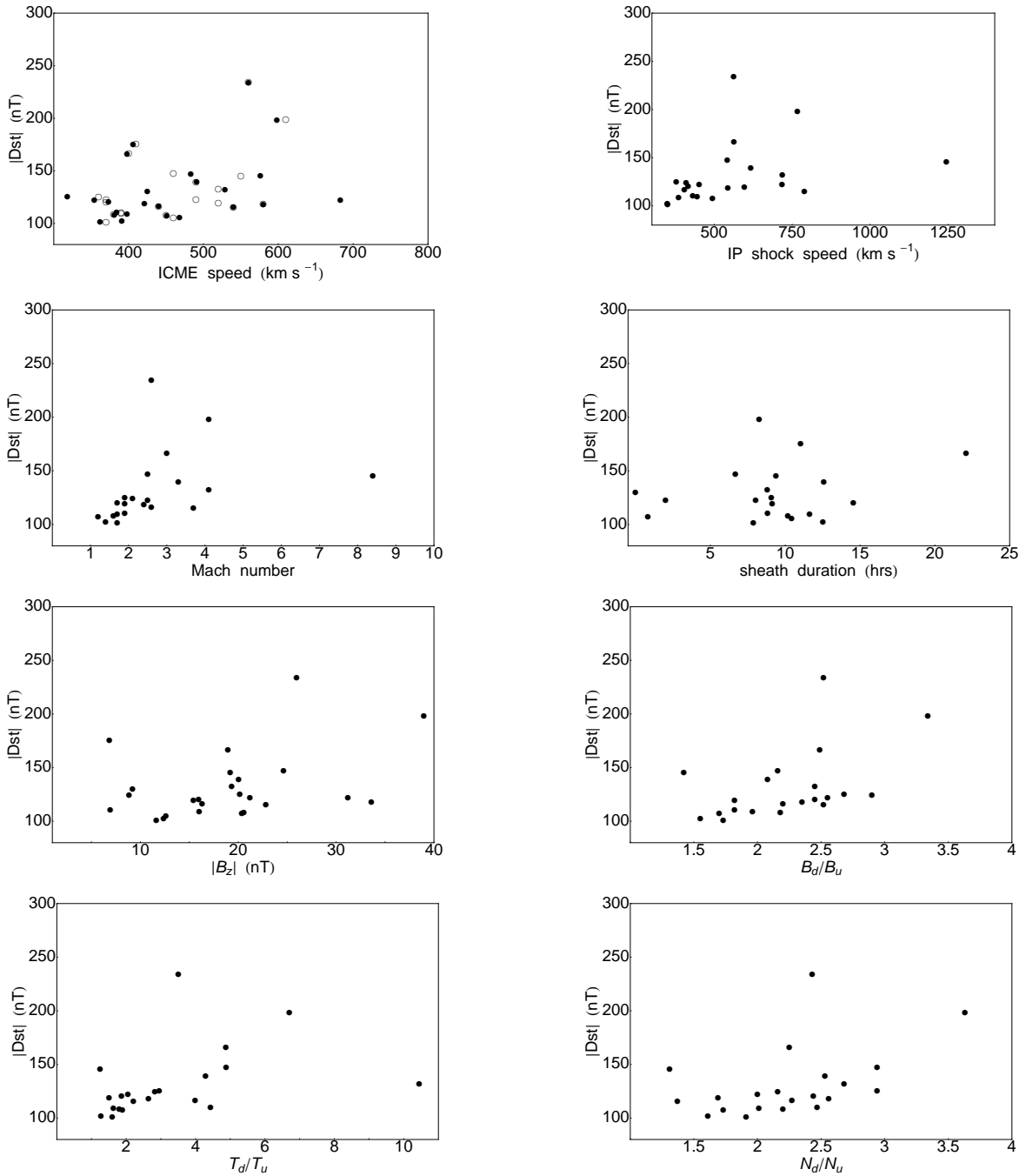


Figure 2.20: Comprehensive scatter plots illustrating the relationships between Dst index and various solar wind parameters, including Wind/ACE ICME speed, IP shock speed, Mach number, duration of sheath region, B_z , magnetic field jump, temperature jump, and density jump. Credit goes to Miteva et al. (2023).

Table 2.9: Tabular representation of Pearson correlation coefficients between the GS Dst index and various parameters of IP phenomena. The data is derived from Wind satellite measurements, unless otherwise stated, with the corresponding sample sizes indicated in parentheses. Credit goes to Miteva et al. (2023).

IP parameter	Dst–IP parameter
ICME speed	0.37 (24)
ICME speed (ACE)	0.44 (22)
IP shock speed	0.35 (22)
Mach number	0.36 (21)
sheath duration	0.22 (20)
$ B_z $	0.37 (25)
B_d/B_u	0.48 (21)
T_d/T_u	0.40 (21)
N_d/N_u	0.46 (21)
B	-0.14 (20)
V	0.19 (20)
β_u	-0.14 (21)

For the limited sample of GS storms utilized in our analyses, we observe a moderately positive trend between the Dst index and the plasma compression parameters at the shock interface (downstream to upstream ratio). Interestingly, these correlations are comparable to, or slightly larger than, those obtained when considering ICME speeds from the Wind and ACE spacecraft. Notably, the trend with $|B_z|$ is weaker (0.37 for our dataset), in contrast to the robust trend reported in previous studies. Furthermore, the correlations involving Dst and IP shock speed, Mach number, or sheath duration are relatively smaller.

Recent reports have highlighted strong correlations with different components of the electric and magnetic fields (Echer & Gonzalez 2022), although this aspect exceeds the scope of our current analyses. It is essential to exercise caution in interpreting these results, given the absence of uncertainty estimates for the correlation coefficients. The ICME and IP shock catalogs employed in our study offer additional parameters, including averaged magnetic field B , plasma speed V inside the magnetic structure, and upstream plasma beta β_u (not presented in Table 2.5). However, no robust correlations emerge between these parameters and the Dst index, with all correlation coefficients found being smaller than 0.2.

On the GS Strength Forecasting Based on Solar and IP Parameters

We examine the collective impact of magnetic obstacle type and orientation upon Earth arrival (columns 5 and 9 from Table 2.5), along with the 3D reconstructed CME speeds (columns 10–12 from Table 2.6), on the intensity of GSs, approximated in this study using the Dst index.

The most potent GSs in our compilation, arranged in descending order based on their Dst values (nT), exhibit distinctive magnetic structure parameters, including complexity, orientation of arrival, and speed at Earth (refer to Tables 2.5 and 2.6):

- E15 (-234): Magnetic obstacle type undefined, fast speed (f), no 3D speed estimation;
- E16 (-198): Complex (Cx) structure, nose-like (n) orientation, no 3D speed estimation;
- E25 (-175): Flux-rope (Fr) structure, nose-like (n) orientation, no 3D speed estimation;
- E19 (-166): Flux-rope (Fr) structure, nose-like (n) orientation, no 3D speed estimation;
- E03 (-147): Complex (Cx) structure, fast speed (f), reduced 3D speed compared to 2D;
- E04 (-145): Complex (Cx) structure, nose-like (n) orientation, similar 3D speed compared to 2D;
- E06 (-139): Flux-rope (Fr) structure, nose-like (n) orientation, larger 3D speed compared to 2D;
- E10 (-132): Flux-rope (Fr) structure, nose-like (n) orientation, similar 3D speed compared to 2D.

Upon scrutiny of these cases, it becomes apparent that the most intense GSs are linked to magnetic obstacles characterized by a nose-like (n) orientation upon arrival, coupled with either a complex (Cx) or

flux-rope (Fr) structure. Exceptions include instances of fast speed flank hits or flank hits in combination with a complex (Cx) structure. It has been established that sheath duration does not serve as a decisive ordering parameter. Other GSs of lesser intensity (refer to Table 2.5) predominantly result from flank hits or exhibit uncertain configurations, possibly influenced by fast solar wind streams or CIRs. Notably, E20 is an exception, resulting from a nose hit; however, the IP structure associated with it has a notably low speed, as observed in the examined animations.

It is crucial to acknowledge that the IP shock speed provided by the Wind and ACE satellites represents a single point sample within the entire structure. In contrast, animations offer a global speed distribution. Therefore, our interpretation considers information from both sources — speed reconstructions and in situ measurements — to enhance the robustness of our analysis.

2.8 Discussion

The eruption on May 11, 2011, presented a complex set of solar phenomena, including a fast partial-halo CME, a weak solar flare, an eruptive filament, and a type II radio burst. The interplay of these events and their effects on the solar and interplanetary environment provides valuable insights into the dynamic nature of solar processes.

2.8.1 CME Kinematics and Coronal Shockwave Characteristics

The CME associated with the eruption exhibited notable characteristics, such as a linear speed of 745 km s^{-1} , an acceleration of 3.3 m s^{-2} , and an angular width of 225° . The shockwave generated by the CME displayed intricate kinematics, as analyzed in both the low and middle/outer corona.

In the low corona, the shockwave was asymmetric, with differences observed in the time-dependent evolution between the left and right flanks. The aspect ratio evolution from elongation to symmetry and subsequent flattening revealed the dynamic nature of the shockwave geometry. The lateral directions exhibited differences in thickness, speed, and acceleration, indicating a complex interaction with the coronal environment. The right flank demonstrated over six times the sheath thickness observed on the left, emphasizing lateral expansion over radial propagation.

Further analysis segmented the shock surface into the Cap zone, Zone 1, and Zone 2. The shock speed at the flanks exceeded that at the Cap zone, suggesting variations in shock characteristics along its surface. The shock density jump remained consistent across the segments, indicating a relatively homogeneous magnetic structure.

In the middle/outer corona, the height-time profile of the CME leading edge provided by SOHO/LASCO measurements showcased the dynamic evolution of the EUV wave. The Gallagher model fitting captured the early stages of the event near the Sun, emphasizing the importance of a comprehensive approach in combining AIA and LASCO measurements.

The wave's rapid acceleration and subsequent speed decrease within a distance of $5 R_\odot$ from the Sun highlighted the intricate interplay between the CME and the surrounding medium. The fluctuations in acceleration and speed over time further underscored the complexity of the coronal shockwave dynamics.

2.8.2 Statistical Study and Correlations

The statistical analysis of coronal wave events in the AIA and LASCO FOVs revealed intriguing patterns. Waves in the radial direction exhibited higher speeds, acceleration, lower mean intensities, and lower thickness compared to the lateral direction, indicating early elongation near the Sun.

Cumulative dynamic spectra illustrated the decline in shock speed and intensity with increasing distance, aligning with expectations of decreasing momentum and plasma densities in the solar environment.

The investigation into plasma parameters and shock characteristics over 26 events demonstrated correlations between various pairs of parameters. Noteworthy correlations included those between the shock-field θ_{BN} angle and magnetic field amplitude, as well as between shock density jump and magnetic field magnitude.

Power fits were identified as suitable models, laying the groundwork for developing parameterizations in the subsequent phases of the project.

2.8.3 Unveiling Dynamic Coronal Features with Wavetrack

In this study, Stepanyuk et al. (2022) applied the Wavetrack methodology to investigate eruptive solar events, focusing particularly on the May 11, 2011 event associated with a prominent CBF. The analysis encompassed two additional events, occurring on June 7, 2011, and December 12, 2013, showcasing Wavetrack's versatility in tracking various solar features both on the solar disk and off the limb.

The Wavetrack algorithm efficiently delineated the evolving CBFs across consecutive time steps for the May 11, 2011 event, as depicted in Figure 2.14. Notably, the algorithm's adaptability was evident despite variations in pixel distributions and intensities on the solar disk and near the limb. This capability allowed for a detailed exploration of the time-dependent shapes and changing intensity distributions of CBFs, distinct from the broader corona.

The segmentation of the CBF during the December 12, 2013 event underscored Wavetrack's efficacy in tracking multiple separate parts of the same feature, even under heightened coronal activity. This highlights the potential of Wavetrack as a valuable tool for studying complex solar phenomena with varying activity states.

To further probe the kinematics of CBFs and filaments, we employed the FLCT method. The results, presented in Figure 2.16, revealed the instantaneous plane-of-sky direction and speed of different regions within the CBF during the May 11, 2011 event. Intriguingly, the uneven expansion of the CBF from the central source was evident, with the thinnest part driven by the erupting filament exhibiting the fastest motion. This nuanced information, not discernible from intensity observations alone, underscores the complementary nature of the Wavetrack and FLCT approach in elucidating the dynamic behavior of coronal features.

2.8.4 Coronal Bright Front (CBF) Kinematics

The highest speeds observed during the event were consistently in the direction away from the Sun, above the erupting filament driver. The continued compression by the driving filament caused a thinner wavefront region and higher speeds there. The study calculated the plane-of-sky velocities of the erupting filament driver, showing that the region of highest speeds in the rising filament was directly below the region of highest speeds in the CBF.

2.8.5 Geometric Centers (GC) and Centers of Mass (CM)

The Wavetrack method provided the geometric centers and centers of mass for the May 11, 2011 event. The GC is defined as the geometric center of all Wavetrack mask pixels at a given time, while the CM includes a weighting based on the AIA 193 Å channel's base difference intensity. The study presented the kinematics of the center of mass and geometric centers for this event, showing the X-axis and Y-axis positions, radial distances, radial speeds, and the angle between the two position vectors over time.

These results provide insights into the dynamics and characteristics of the May 11, 2011 solar eruption event, highlighting the movement and speeds of key features such as the CBF and the erupting filament driver.

2.8.6 Projection Effects: The Challenge of Subjectivity in CME Speed Determination

Our investigation into CMEs reveals a nuanced landscape marked by the inherent subjectivity in the fitting and de-projection procedures. The analysis of approximately 10 CMEs, employing three models from the PyThea framework, underscores the considerable variability in results. Two designated observers within our research team, accounting for individual considerations, conducted fitting analyses. The iterative 3D de-projection procedure led to averaged CME speeds, documented in Table 2.7. The associated errors, ranging from 10 km s^{-1} to twice the estimated speed, highlight the challenges and uncertainties in this process.

The observed disparities among observers, even using the same model, and the impact of different models and operating systems on results emphasize the subjective nature of visual fitting procedures. Technical limitations, such as PyThea computing resource failures and uncertainty in visual assessments, further contributed to incomplete data for specific events. Our findings echo the well-established subjectivity inherent in procedures relying on personal judgment for fit quality, aligning with the broader discussion presented by Verbeke et al. (2022).

The averaged CME speed values, categorized by model and determined by both observers, serve as the foundation for subsequent correlation studies. Despite the challenges posed by subjectivity, these averaged values provide a basis for further analysis.

2.8.7 Correlation between GSs, Coronal, and Near-Sun Parameters

Our exploration of the correlation between GSs and various parameters, such as the GS Dst index, CME speed, and 2D LASCO CME speed, unfolds in Figure 2.19 and Table 2.8. Despite the modest sample size, the analysis reveals no discernible trend between the Dst index and CME speed, irrespective of the 3D de-projection or the 2D CME speeds. The absence of 3D speed de-projections for the most robust GSs introduces a limitation in the distribution of 3D speeds, impacting overall findings.

Pearson correlation coefficients, systematically documented in Table 2.8, range from negligible to moderate, indicating diverse relationships between CME speed estimations and the GS Dst index. Notably, no significant correlations are identified between the Dst index and other coronal parameters, such as SF class, location, and CME AW. The complexities in these relationships highlight the need for cautious interpretation, given the data constraints and uncertainties associated with the correlation coefficients.

2.8.8 Correlation between GSs and IP Parameters

The examination of correlations between GSs and IP parameters unfolds in scatter plots in Figure 2.20, accompanied by Pearson correlation values in Table 5. Noteworthy trends include a moderately positive correlation between the Dst index and plasma compression parameters at the shock interface, comparable to correlations with ICME speeds. However, caution is advised in interpreting results due to the absence of uncertainty estimates for correlation coefficients.

Additional parameters from ICME and IP shock catalogs, including averaged magnetic field B , plasma speed V , and upstream plasma β_u , exhibit no robust correlations with the Dst index. The complexities in these relationships underline the multifaceted nature of GS-IP parameter associations.

2.8.9 GS Strength Forecasting: Unraveling Magnetic Structures

Our analysis of the collective impact of magnetic obstacle type, orientation, and 3D reconstructed CME speeds on Geospace Storms (GSs) sheds light on intriguing patterns. The most potent GSs, based on descending Dst values, exhibit distinctive magnetic structure parameters, such as complexity, orientation of arrival, and speed at Earth. Notably, nose-like (n) orientation, coupled with a complex (Cx) or flux-rope (Fr) structure, characterizes the most intense GSs. Exceptions include instances of fast-speed flank hits or flank hits in combination with a complex (Cx) structure.

The interplay of magnetic obstacle characteristics, orientation, and 3D CME speeds provides valuable insights into the factors influencing GS intensity. However, it is crucial to acknowledge the limitations of single-point IP shock speed measurements and the need for a comprehensive interpretation that considers both speed reconstructions and in situ measurements.

2.9 Conclusions

I have conducted a comprehensive study focusing on the characterization of 26 historical CME-driven CBFs in the low solar corona. These events were accompanied by type III radio bursts, and SEP events near Earth and were observed by the AIA instrument onboard the SDO spacecraft in the EUV 193 Å band. To achieve this, we utilized the SPREAdFAST framework, which encompasses physics-based and data-driven models to estimate the coronal magnetic field, dynamics of coronal shock waves, energetic particle acceleration, and SEP propagation in the heliosphere.

Our analysis relied on sequences of base-difference images obtained from the AIA instrument. These images served as the primary input data for our investigation. We employed these data to generate annulus plots and J-maps to estimate the kinematic measurements in both the radial and lateral directions for the EUV waves.

In order to obtain a thorough understanding of the CBFs, we computed various time-dependent and distance-dependent kinematic parameters. These included shock speed, acceleration, intensity, and thickness of the front, peak, and back edges of the waves, as well as the major and minor axes and the rate of change of the waves' aspect ratios. To augment our analysis based on AIA observations, we

incorporated LASCO measurements up to $17 R_{\odot}$. This additional data is important in improving the characterization of the SEP spectra near the Sun.

The analysis of kinematic measurements played a pivotal role in our study as they enabled us to generate time-dependent 3D geometric models of wavefronts. In addition, these measurements provided valuable insights for deriving time-dependent plasma diagnostics by incorporating the outcomes of the MHD and DEM models.

To accurately represent the shocks, we employed shock kinematic measurements to fit a geometric spheroid surface model for each measured time step. This approach allowed us to capture the intricate characteristics of the shocks with precision.

In order to gain a deeper understanding of the phenomenon, we explored the parametrized relationships between the modeled plasma parameters. Through this analysis, we aimed to identify potential connections and interdependencies, shedding light on the complex dynamics at play.

Overall, our findings in this study and in Kozarev et al. (2022) as well as Stepanyuk et al. (2022) contribute to a nuanced understanding of shock kinematics and shock plasma parameters.

Moving forward, our future investigations will focus on examining SEP acceleration near the Sun, as well as investigating the transport of coronal and interplanetary particles using the insights gained from our models. Additionally, we aim to refine the methods of shock and coronal parameters characterization, which will contribute to enhancing the accuracy and reliability of the results.

In the study led by Stepanyuk et al. (2022), we introduce Wavetrack, an innovative approach designed for the automated identification and monitoring of dynamic coronal phenomena. Employing wavelet decomposition, feature enhancement, filtering, and ultimate object recombination, Wavetrack generates time-dependent masks for feature pixels. These masks can be applied to integral or base-difference images, yielding comprehensive feature maps. Notably, Wavetrack excels in tracing pixels associated with faint, large-scale features, such as coronal bright fronts/EUV waves in AIA observations, and has demonstrated efficacy in tracking eruptive filaments. Operable for both on-disk and off-limb features, Wavetrack adeptly follows features that evolve into distinct components over time. Implemented as a versatile, object-oriented framework in Python, Wavetrack is freely accessible for download and utilization.

The application of Wavetrack to four distinct events, with emphasis on three – the CBFs occurring on May 11 and June 07, 2011, and December 12, 2013 – reveals its proficiency in tracking complete CBF pixel maps. These model results, when integrated with the FLCT method for calculating plane-of-sky speeds, unveil the dynamic evolution of driven and non-driven regions within CBFs, as well as their correlation with eruptive filament drivers. Our findings indicate that drivers induce a compression effect, causing CBF thinning and increased speed, aligning with theoretical models. However, the brightness of CBFs in the driven regions, as observed in AIA data, does not necessarily exhibit a significant increase.

Furthermore, Wavetrack facilitates the tracking of temporal changes in feature regions by computing the time-dependent vector between the pixel geometric center and the center of mass, determined by weighing the observed pixel intensities. This proves particularly valuable for large-scale features like CBFs, providing a straightforward metric in the form of a one-dimensional time series for characterizing feature evolution.

While the method demonstrates widespread applicability to various solar dynamic features and observational data, it currently relies on human input for the segmentation of specific feature types, particularly dim ones. Manual setting of object criteria, including threshold intervals and recombination weight coefficients, is necessary. In instances of base difference imaging, precise selection of the base image is crucial to prevent contamination of input data with spurious features. Additionally, parameter fine-tuning through trial and error may be required for specific events. These limitations are acknowledged, and future work will address them to enhance the model's versatility.

The methodology holds promise for extensive application across diverse solar dynamic features and observational datasets. Subsequent research endeavors will extend its use to in-depth studies of filament evolution and coronagraph data. The objective is to refine our comprehension of how large-scale eruptive fronts manifest variations across distinct observational contexts, spanning the low and middle corona.

In the study led by Miteva et al. (2023), we conduct post-event analyses of all geo-effective storms observed during solar cycle 24 with the aim of identifying distinct and reliable predictors for GS intensity. The overarching objective is to derive dependable solar or near-Sun parameters from remote sensing image data that can be effectively utilized for early warnings regarding potential GS onsets and their strength. Our approach involves the integration of solar, near-Sun, and interplanetary parameters, primarily sourced from catalogs but also subject to our analysis using space-related databases. Notably, we incorporate the results obtained from a novel tool for CME speed de-projection, termed PyThea,

which is employed for the first time alongside well-established parameters in space weather and geophysics research.

Among the solar and near-Sun phenomena considered, certain selected parameters exhibit a positive correlation with the Dst index. Notably, the correlation coefficient, when comparing the observed projected CME speed, experiences an improvement from 0.04 (as obtained from LASCO) to a range of 0.34–0.55, achieved through various geometrical models provided by the PyThea software package, combining LASCO and STEREO data. However, our exploration of different CME geometry reconstruction techniques reveals a susceptibility to large speed errors, particularly in the case of fast CMEs. This aligns with findings from prior studies focusing on CME arrival time and speed forecasts for Earth, suggesting a potential overestimation of CME launch speed for fast events, likely attributable to the increased complexity in discerning coronal structures due to the rapid expansion of the magnetic structure associated with the CME.

Moreover, our examination indicates that fast halo CMEs may exhibit significant deviations, stemming from the overlap in shock and magnetic structure components, thereby strongly impacting the reconstruction quality. Consequently, we assert that the derived near-Sun 3D parameters continue to possess limited forecasting potential for predicting GS strength. In contrast, most selected IP parameters derived from in situ measurements display moderate positive correlations with GS strength, in line with expectations. However, the B_z parameter (southward component of the magnetic field) shows a relatively low correlation coefficient of 0.37, possibly influenced by the limited event sample used in our study.

Other IP parameters, such as ICME and IP shock speeds, along with their derivative parameters (e.g., Mach number), exhibit a positive trend with the Dst index, featuring correlation coefficients of 0.35–0.45. Nevertheless, none of these parameters emerge as predominant, and their reliance on single-point in situ observation raises considerations about their comprehensive predictive capability. Discrepancies in ICME speed values between ACE and Wind measurements prompt further investigation, with slightly stronger correlation coefficients (0.4–0.5) observed when utilizing different shock parameters. However, averaged values of magnetic field and speed within the magnetic structure, plasma beta in the upstream region, or duration of the sheath region show no correlation with GS strength.

Among the multitude of considered solar, near-Sun, and IP parameters, only the combination of speed and orientation (nose-like) of the magnetic obstacle appears to exert a positive influence on GS strength, as indicated by qualitative results obtained from animations accessible at *helioweaether*. Consistent with earlier studies, de-projected CME speeds emerge as imperative for enhancing modeling accuracy when predicting CME propagation through the IP space. However, a notable observation is the apparent lack of direct impact of 3D de-projected CME speed on GS intensity. Consequently, an accurate estimation of the ICME speed distribution over the entire ICME structure upon arrival at Earth assumes significant importance. We emphasize the imperative need for permanent stereoscopic observations, exemplified by the upcoming ESA Vigil mission situated at Lagrange point L5. Future research endeavors should aim for a more comprehensive disentanglement of distinct CME structures, thereby enabling more reliable 3D reconstructions of CME geometries for a nuanced estimation of 3D speed and directivity.

The identified correlations and statistical patterns provide a foundation for the ongoing project. Further work will focus on refining parameterizations and establishing synoptic MHD parameters corresponding to measured shock parameters. The ultimate goal is to enhance the representation of shock parameters in the *S3M* synoptic model, contributing to a more comprehensive understanding of solar dynamics and space weather forecasting.

Our findings emphasize the significance of integrating advanced tracking methodologies like Wave-track with kinematic analyses such as FLCT. This synergistic approach enables a more comprehensive understanding of the intricate dynamics involved in eruptive solar events, shedding light on the complexities of CBF evolution and its correlation with eruptive features. As we continue to refine and expand such methodologies, our ability to decipher the underlying mechanisms governing solar phenomena will undoubtedly advance, contributing to the broader field of Heliophysics.

In conclusion, our findings underscore the complexity and subjectivity inherent in studying CMEs and their impact on Geospace Storms. The integration of observational data, model outputs, and correlation analyses offers a comprehensive perspective, laying the groundwork for further investigations into the dynamic interplay between solar and interplanetary phenomena in shaping space weather events.

Chapter 3

Solar Radio Observations: Integrating Space-based and Ground-based Data for Coronal Diagnostics

In this chapter, I focus on multi-wavelength observations of solar type III radio bursts, as well as modeling studies of plasma parameters and coronal magnetic fields, to gain insights into the mechanism of solar radio emission during quiet times and the coronal conditions influencing the propagation and detection of these bursts. First, I briefly introduce the characteristics of solar type III radio bursts. I then present the data I have worked with, detailing the multiple processing stages I undertook. Finally, I present my outputs and interpret their meaning.

3.1 Introduction

Type III radio bursts are manifestations of transient energetic electron beams injected into the solar corona, propagating along the interplanetary magnetic field (IMF) lines Ergun et al. (1998); Pick (2006); Reid (2020). As these beams traverse the corona, they trigger plasma waves (also known as Langmuir waves) that are then transformed into radio emission at the local plasma frequency or its harmonic components Melrose (2017). In the radio spectrograms, type III bursts are usually observed as intense emissions that drift in frequency over timescales of several seconds to minutes and over a wide range of frequencies, from metric to decametric wavelengths Wild & McCready (1950); Lecacheux et al. (1989); Bonnin et al. (2008), making them detectable by ground-based instruments on Earth and various spacecraft within the heliosphere. The frequency of the radio emission is directly related to the plasma density, making type III bursts a valuable diagnostic tool for examining the inner heliosphere and the processes that drive solar active phenomena, such as solar flares and coronal mass ejections Reid & Ratcliffe (2014); Kontar et al. (2017).

The electron beams follow open magnetic field lines and can persist well beyond 1 astronomical unit (AU) (e.g., Dulk et al. (1985); Boudjada et al. (2020)), offering in situ insights into the burst and ambient conditions of the heliosphere, including electron density, radio frequency drift, speed of the electron beams and even potential direct detection of Langmuir waves (see Gurnett & Anderson (1976, 1977) and Reid & Ratcliffe (2014) and references within). In addition, tracing the path of type III bursts provides a map of the density structure of the heliosphere, serving as a foundation for developing and testing density models. Since radio observations below ~ 10 MHz cannot be accomplished from the ground, it is important to combine high- and low-frequency observations from ground-based and space-borne instruments. In this work, I perform a study of several type III radio bursts that occurred in close succession on April 3, 2019. I use remote observations of type III radio bursts detected by the Low-Frequency Array (van Haarlem et al. 2013, LOFAR) ground-based radio telescope and the Parker Solar Probe (Fox et al. 2016, PSP) spacecraft during Encounter 2 to study the sources of these radio emissions and to investigate the physical conditions responsible for their generation. Additionally, I incorporate results of two steady-state models of the solar corona: the potential field source surface (PFSS) model Altschuler & Newkirk

(1969); Schatten et al. (1969) and the magnetohydrodynamic algorithm outside a sphere (MAS) model Mikić et al. (1999), to gain a better understanding of the coronal magnetic environment and its role in the acceleration of electrons. The ground-based LOFAR imaging observations provide valuable insight into the actual location of the burst sources. This research aims to expand upon current knowledge of the electron beams responsible for triggering type III radio bursts and the coronal conditions they experience. Gaining a deeper insight into this aspect is vital in comprehending other solar phenomena, such as solar energetic particles and solar wind, and how they influence the near-Earth space environment.

A number of recent studies investigate the physical mechanisms responsible for the generation of solar type III radio bursts. For example, Chen et al. (2013) investigated the association of type III bursts with flaring activities in February 2011, via combined multi-wavelength observation from the Solar Dynamic Observatory (SDO) instruments, as well as Wind/WAVE and ground-based instruments. They found that the SDO measurements indicated that type III emission was correlated with a hot plasma (7 MK) at the extreme ultraviolet (EUV) jet's footpoint. By using a triangulation method with the Wind and the twin STEREO spacecraft, Bonnin et al. (2008) reported the first measurements of the beaming characteristics for two type III bursts between 2007-2008, assuming the source was located near the ecliptic plane (see also Reiner et al. (2009)). They concluded that the individual type III bursts have a broad beaming pattern that is roughly parallel to the Parker spiral magnetic field line at the source. Saint-Hilaire et al. (2012) conducted a study on almost 10,000 type III bursts observed by the Nançay Radioheliograph between 1998 and 2008. Their analysis revealed discrepancies in the location of type III sources that may have been caused by a tilted magnetic field. Additionally, they found that the average energy released during type III bursts throughout a solar cycle could be comparable to the energy produced by non-thermal bremsstrahlung mechanisms in nano-flares. Morosan & Gallagher (2017) utilized LOFAR data to investigate the statistical characteristics of over 800 type III radio bursts within an eight-hour period on July 9, 2013. They discovered that the drift rates of type III bursts were twice that of type S bursts and plasma emission was the primary emission mechanism for both types.

Pulupa et al. (2020) introduced a statistical overview of type III radio bursts during the first two PSP solar encounters. While the first encounter in November 2018 revealed a small number of bursts, the second encounter in April 2019 exhibited frequent type III bursts, including continuous occurrences during noise storms. They reported the characteristics of type III bursts with spectral and polarization analysis.

Krupar et al. (2020) performed a statistical survey of 30 type III radio bursts detected by PSP during the second encounter in April 2019 and estimated their decay times, which were used to estimate the relative electron density fluctuations in the solar wind. They localized radio sources using a polarization-based-radio triangulation technique, which placed the sources near the modeled Parker spiral rooted in the active region AR12738 behind the plane of the sky as seen from Earth.

Cattell et al. (2021) explored correlations between type III radio bursts and EUV emission in the solar corona. Using coordinated observations from PSP, SDO, and Nuclear Spectroscopic Telescope Array (NuSTAR) on April 12, 2019, they identified periodicities in EUV emission correlated with type III burst rates. The findings suggested impulsive events causing heating and cooling in the corona, possibly nano-flares, despite the absence of observable flares in X-ray and EUV data, which implies periodic non-thermal electron acceleration processes associated with small-scale impulsive events.

Harra et al. (2021) explored the origin of the type III radio bursts I am tackling in this paper and found that electron beams that triggered radio bursts may have emanated from the periphery of an active region that showed significant blue-shifted plasma. More recently, Badman et al. (2022) observed a distinct type III radio burst using the PSP and LOFAR between 0.1 and 80 MHz on April 9, 2019, around 12:40 UT, six days after the occurrence of the event analyzed in our study. While no detectable flare activity was linked with the event, a type III noise storm was ongoing during the PSP encounter 2. The authors determined the type III trajectory and reconstructed its source using observations from Wind and STEREO spacecraft, as well as measuring related electron enhancement *in situ*.

In the last few years, I have witnessed the emergence of modern instruments, such as LOFAR and PSP, that have allowed for the observation of solar radio emissions with higher sensitivity from a better vantage point. Although type III bursts have been extensively studied Dabrowski et al. (2021), there are still some unresolved issues regarding the exact mechanism of type III emissions. For example, it is not yet clear how the electrons are accelerated to the high energies required to generate type III radio bursts or what role the coronal magnetic field plays in this process. Furthermore, there are inconsistencies between the observations and the models, which need to be resolved in order to gain a more complete understanding of the dynamics of the solar corona. Examples of these inconsistencies are the origin of the type III radio bursts and the discrepancy between the estimated plasma densities from the models

and the observations. This paper aims to address these unresolved challenges by using new observations from LOFAR and PSP and models of the solar corona to study the physical mechanisms responsible for the generation of type III bursts. The data analysis includes a combination of radio spectroscopy and imaging techniques to study the frequency, temporal and spatial variations of the radio bursts.

This chapter is organized as follows. In Section 3.2, I describe the observations of type III radio bursts made with LOFAR and PSP. In Section 3.3 I explain the data analysis and modeling techniques used to study these events. In Section 3.4, I present the results of our analysis, including an investigation of the potential physical mechanisms responsible for the generation of type III radio bursts and a comparison of the observations with models of the solar corona. Finally, in Section 3.5, I summarize our findings and discuss their implications.

3.2 Observations

A number of studies focused on observing the solar radio emissions during the second encounter of the PSP in late 2019 Krupar et al. (2020); Pulupa et al. (2020); Cattell et al. (2021); Harra et al. (2021); Badman et al. (2022). In this study, our primary emphasis is directed towards investigating a set of type III radio bursts that took place on April 3, 2019, during the time interval spanning from \sim 12:10 to 12:50 UT. This period coincided with the presence of two distinct active regions (ARs) on the Sun, denoted as AR12737 and AR12738. AR12737 was situated on the Sun’s near side at coordinates E12°N06°. Notably, this region had eight sunspots and exhibited a β magnetic configuration according to the Hale magnetic classification Hale et al. (1919). On the other hand, AR12738 was positioned on the solar far side at coordinates E140°N02°. Due to its remote location, detailed observations of the magnetic configuration and activity within AR12738 were unattainable in this time frame.

I observed a group of intense type III radio bursts by four instruments (Wind/WAVES, PSP/FIELDS, STEREO-A/SWAVES, and LOFAR/LBA) via a regular survey. In Figure 3.1, I show the first type III burst within the time of this study as observed by the four instruments. By taking the second derivative of the light curve at a specific frequency channels, I determined the start time of the burst, which is denoted by the vertical red dashed line. The frequency bands used for obtaining the start time at each instrument are as follows: 6.97 MHz (Wind), 7.03 MHz (STEREO), 5.03 MHz (PSP), and 40.16 MHz (LOFAR).

I checked the relative orientations of the instruments with respect to Earth (Fig. 3.2). Since the PSP and STEREO spacecraft were almost aligned (close in an angular sense) with the Sun, the STEREO/EUVI image could be taken as what PSP would see (Fig. 3.3). Figure 3.3 shows how the solar disk looks like from the Earth perspective (using the SDO/AIA instrument) and from the eastern side where the PSP and STEREO were located at that time (using the STEREO/EUVI instrument). The right panel shows a closer view of AR12737 with the contours of the photospheric magnetic field obtained from the Helioseismic and Magnetic Imager (HMI) on board SDO. From the GOES-15/XRS and SDO/EVE instruments in the panels below, they also confirm that there is no flaring activity at that time.

The solar disk was quiet, including only one AR that is visible with no X-rays and no EUV transient emissions over this period. Nevertheless, the very sensitive LOFAR telescope detected a number of bursts close to noon. I checked PSP data, and I found bursts there as well. Meanwhile, from the EUVI and AIA images, I see that there are numerous small localized regions of relatively higher intensity (i.e., likely small-scale coronal brightenings spots or campfires; see Young et al. (2018); Madjarska (2019); Berghmans et al. (2021)). In the next subsections, I introduce the PSP and LOFAR instruments and their observations of the radio bursts.

3.2.1 PSP Observations

Parker Solar Probe (PSP) is a pioneering spacecraft with cutting-edge technologies, launched on August 12, 2018, aimed at helping to resolve key questions about solar corona and solar wind (Fox et al. 2016). To study the radio bursts, I used the level-2 data of the radio dynamic spectrum obtained from the FIELDS instrument suite (Bale et al. 2016; Pulupa et al. 2017), which can be downloaded from this website¹. The data file is in CDF format and the unit of the data values is converted from V^2/Hz to dB units using the formula

$$I_{dB} = 10 \times \log_{10}(I/10^{-16}) \quad (3.1)$$

¹PSP FIELDS data products: <http://research.ssl.berkeley.edu/data/psp/data/sci/fields/>

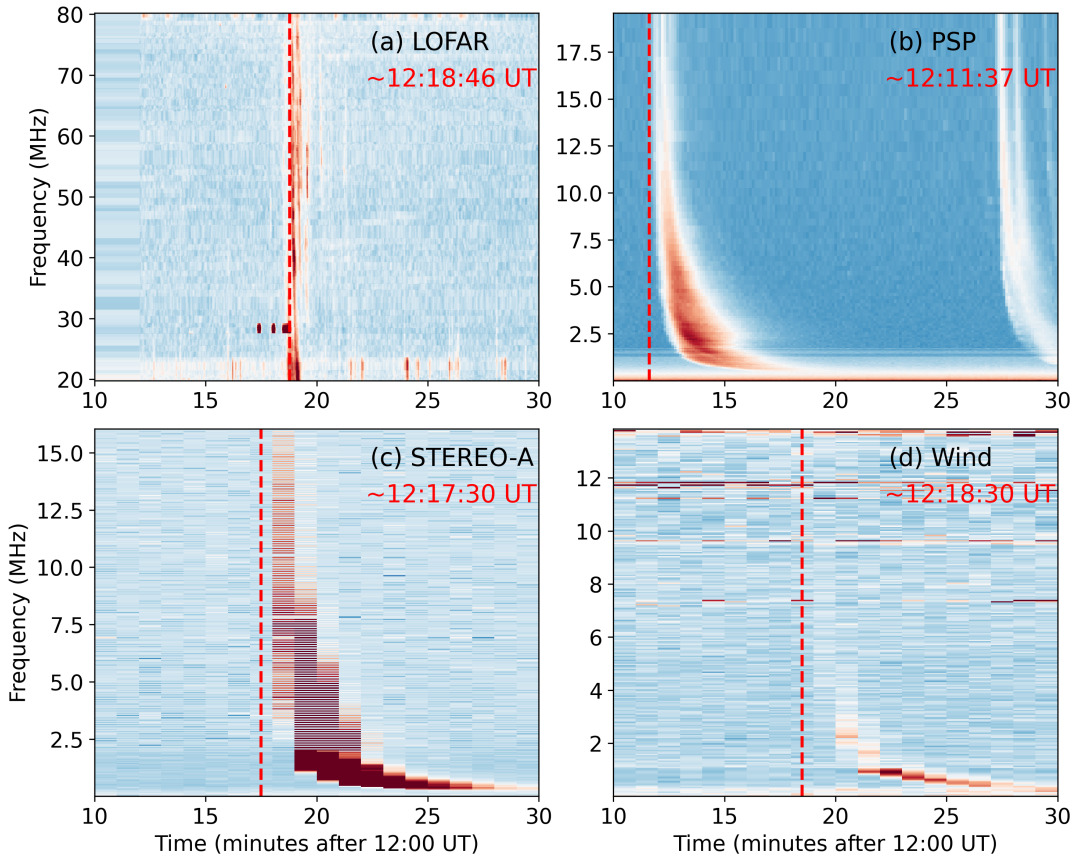


Figure 3.1: Radio dynamic spectra for a single burst obtained from multiple instruments. The top-left panel is from the LOFAR/LBA instrument, the top-right is from the PSP/FIELDS instrument, the bottom-left is from the STEREO/SWAVES instrument, and the bottom-right is from the Wind/WAVES. The vertical red dashed line denotes the start time of the burst.

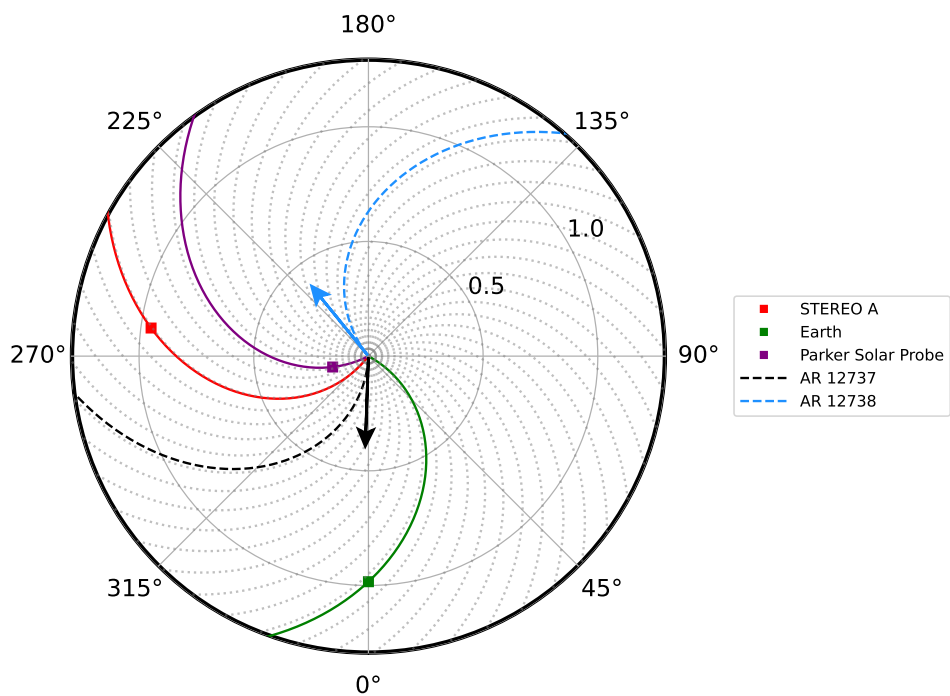


Figure 3.2: Top view of the spacecraft positions in the ecliptic plane at 12:15 UT on April 3, 2019, with the Sun-Earth line as the reference point for longitude. The Earth's location is representative of the positions of LOFAR, Wind/WAVES, and GOES-15/XRS instruments. The spacecraft were connected back to the Sun by a 400 km/s reference Parker Spiral. The black arrow represents the longitude of AR12737 and the blue arrow represents the longitude of the AR12738. The gray dotted lines are the background Parker spiral field lines. The black dashed spiral shows the field line connected to the AR12737, and the blue dashed spiral is connected to the AR12738. The figure is generated using the Solar MAgnetic Connection Haus (Solar-MACH) tool (Gieseler et al. 2023).

The minimum power spectral density (PSD) of $10^{-16} V^2/Hz$ is used as a threshold for radio bursts according to Pulupa et al. (2020) for converting to decibels. Then, both the High-Frequency Receiver (HFR: 1.3 – 19.2 MHz) and the Low-Frequency Receive (LFR: 10.5 kHz – 1.7 MHz) data are combined into a single dynamic spectrum as shown in Figure 3.4 with a full frequency range between 10.5 kHz – 19.2 MHz. The mean intensity value at each timestep over the full frequency range is subtracted from each frequency channel to clean the spectrum and minimize the noise level.

3.2.2 LOFAR Observations

The Low Frequency ARray (LOFAR) radio telescope (van Haarlem et al. 2013) is a powerful tool for studying the Sun at low radio frequencies ranging between 10 and 240 MHz. Its high sensitivity and high time resolution have enabled the detection of various solar phenomena, including radio bursts and CMEs, and the study of dynamic processes in the solar atmosphere on timescales of milliseconds. The LOFAR dynamic spectrum from the beamformed radio observations is obtained by the Low-Band Antenna (LBA: 10 – 90 MHz) and can be downloaded from the LOFAR long-term archive (LTA)². The High-Band Antenna (HBA: 110 – 190 MHz) data are not available for that timeframe. For this day under study, the LOFAR data are available between 11:42 – 13:27 UT. To clean the spectrum, background subtraction is performed, which flattens the sensitivity (response) with the frequency of the LBA antennas. Basically, the mean spectrum along each frequency band is calculated and subtracted from the whole frequency band, the same applied to the PSP spectrum. This operation effectively removes the constant background from the spectrum. Then a Gaussian smoothing filter is applied to the spectrum using the `scipy.ndimage.gaussian_filter` function with a sigma value of 1.5, which helps to reduce noise and variations in the data. After that, the PSP and LOFAR spectra are combined together in a single plot within the same time interval. The bursts' signals observed by the PSP occur earlier than those at LOFAR. This is due to the fact that the PSP spacecraft is much closer to the Sun and hence it detects the radio emissions earlier than LOFAR because of the shorter travel time of radio signals from the Sun. Therefore, the PSP dynamic spectrum must be shifted with respect to the LOFAR observations based on a calculation of the relative time travel of the radio emission from the Sun to PSP and to LOFAR. In addition, the time cadence of the PSP observations changes according to its distance from the Sun. On that day, the PSP data cadence was 7 seconds, while LOFAR's is 1 second. Therefore, the LOFAR dynamic spectrum was down-sampled to 7 seconds to match the time resolution of the PSP. Figure 3.4 shows the resulting combined LOFAR-PSP spectrum on a logarithmic y-axis. The LOFAR LBA frequency ranges between 19.82 – 80.16 MHz and for the PSP is 10.55 kHz – 19.17 MHz.

In order to detect the type III radio bursts automatically from the combined dynamic spectrum, I applied the Zhang et al. (2018) algorithm based on the probabilistic Hough transformation that detects vertical bright edges in images, within a certain degree of deviation from the vertical direction.

3.3 Methods

3.3.1 Imaging of radio sources

As part of our task, I developed an automated pipeline consisting of several modules that not only preprocessed and calibrated the LOFAR interferometric data to produce cleaned images of the Sun in the radio band (Zhang et al. 2022a), but also utilized the resulting data to find the trajectory of the radio sources and sample the magnetic field and plasma parameters at their respective locations through modeling and simulations in subsequent modules.

First, I ran the burst detection algorithm (Zhang et al. 2018)³ on the combined dynamic radio spectrum of LOFAR and PSP (Fig. 3.4) to find the characteristics of each type III burst. I converted the spectrum into a binary map to isolate the bursts from the background. Then I applied the Hough transformation to get line segments of the features. For each type III burst, the line segments are grouped together into one group. To account for the interplanetary component within radio dynamic spectra, I employed the Parker electron-density model (Parker 1960) assuming a fundamental emission. This model enabled mapping between the time and frequency indices for each type III burst and subsequently converted electron densities into radial distances. Finally, a least-squares fitting method was applied to derive both the frequency drifts and the speed of the electron beams.

²LOFAR LTA: <https://lta.lofar.eu/>

³Detection algorithm repository: <https://github.com/peijin94/type3detect>

After this step, I did the same for the LOFAR dynamic spectrum only (Fig. 3.5) to find the (f, t) pairs for every type III burst. Then I took snapshot frequencies for each burst defined by a list of 60 central frequencies between $\sim 20 - 80$ MHz from LOFAR LTA for the interferometric imaging. I obtained the interferometric data from LOFAR core and remote stations at the snapshot frequencies for all type III bursts. I used the concurrent observations of the radio source Tau-A to calibrate the interferometric observations. For that, I used the default preprocessing pipeline (van Diepen et al. 2018, DP3) for preliminary processing and calibrating the measurement sets (MS). Finally I obtained the cleaned images of the radio sources by using *w*-stacking clean (WSClean) algorithm (Offringa et al. 2014) only at the time indices in the MS files that are equivalent to the snapshot frequencies.

Table 3.1: Characteristics of the type III bursts detected via the automatic algorithm from the combined spectrum.

Burst ID	Start Time (UT)	End Time (UT)	Start Frequency (MHz)	End Frequency (MHz)	Frequency Drift (MHz s ⁻¹)	Beam Speed (c)
1	12:18:45	12:22:42	76.44	1.57	0.892	0.044
2	12:34:05	12:36:31	41.24	0.86	0.241	0.119
3	12:34:40	12:34:56	54.44	26.54	3.992	0.046
4	12:37:14	12:38:09	66.03	10.02	4.006	0.046
5	12:38:17	12:40:54	76.92	1.57	0.77	0.066
6	12:39:34	12:40:11	78.86	11.93	3.192	0.062
7	12:40:28	12:40:40	45.34	22.9	3.21	0.067
8	12:41:39	12:43:06	78.21	2.13	1.555	0.093
9	12:43:53	12:44:15	59.07	42.13	2.424	0.013

After processing and cleaning the interferometric measurements of LOFAR, I explored the observations of each burst individually. Out of the 60 frequency bands in the LOFAR LTA, I chose 54 frequency bands that have unique integer numeric, between 19.92 - 80.08 MHz. For each burst, at each timestamp, the nearest frequency of the fit model to the list of chosen frequencies is picked as the snapshot frequency at that particular timestamp. This process was repeated for all the 16 type III bursts detected in the LOFAR dynamic spectrum in order to obtain snapshot images for each type III burst (Fig. 3.6). For each type III burst, I applied persistence imaging in order to create a continuous display of the radio emissions (Thompson & Young 2016).

Persistence imaging enables the creation of a clearer and more informative image. In the context of a time-ordered series of images, a method of persisting pixel values can be employed as follows: for each image, compare the value of each pixel to its corresponding value in the previous persistence image in the series. If the pixel value in the current image is brighter than its corresponding pixel in the previous image, replace the previous value with the current one; otherwise, retain the previous value. This process generates a new image, referred to as the current persistence image, which serves as the basis for the subsequent evaluation of the next image in the series. This evaluation involves a pixel-by-pixel comparison between the current image and its associated persistence image, allowing for the identification of any changes or patterns that may have occurred over time. The mathematical background is explained in Appendix A.2.

In order to estimate the locations of the type III sources in 3D space, I combined observations with modeling. I used magnetogram data from the Global Oscillation Network Group project (GONG) (Harvey et al. 1996). I constructed a grid of footpoints on the GONG map over two longitudinal belts around the two active regions AR12737 and AR12738, which are the two potential candidates source regions for the group of type III bursts under study. These points are used as the seed points for tracing the coronal magnetic field lines using pfsspy python package⁴, which is a robust implementation in python of the PFSS model developed by Stansby et al. (2020). Using the major and minor axes of the beam size, I estimated the radius of the radio source using Equation 3.2, which was used to approximate the source size. Since I already obtained the (x, y) positions of the type III sources in the plane of the sky (POS) through LOFAR observations, now it is necessary to determine their corresponding z position to have an overall understanding of their spatial distribution. Therefore, I employed Badman et al. (2022)'s approach here, assuming that the type III bursts were from harmonic emission. Firstly, I found the radial distance of the radio source from the Sun in the POS (Eq. 3.3). Secondly, I calculated the sources' radial distance (r_{model}) using the $2.5 \times$ Newkirk electron-density model (Newkirk 1961, 1967). The 2.5 fold factor is taken to incorporate the effects of scattering and overdensity (streamers) beyond

⁴Pfsspy tool: <https://pfsspy.readthedocs.io/>

the nominal Newkirk quiet Sun model. The MAS model results (Fig. 3.8) show streamers above the eastern limb, supporting the inclusion of such a factor. Lastly, I estimated the z location of the type III sources (Eq. 3.4). I proceeded with the $+z$ solution because the theory precludes emission behind POS in this region of high-density gradients (i.e., the emission would be absorbed by passing through the high-density regions of the corona). More details are explained in Appendix A.3.

$$r_{source} = \sqrt{(b_{major}^2 + b_{minor}^2)}, \quad (3.2)$$

$$r_{pos} = \sqrt{(x^2 + y^2)}, \quad (3.3)$$

$$z = \sqrt{(r_{model}^2 - r_{pos}^2)}. \quad (3.4)$$

The result of the deprojection of the type III sources for the sixth burst are shown in Figure 3.7 with 70% contours made for ten frequencies on the extrapolated magnetic field lines. The red dashed line is a spline fitting curve that represents the trajectory of the centroids of the radio sources. The black arrow points toward the Earth's line of sight (LOS). It is worth to mention that the axes direction in the POS of LOFAR images are different in the 3D space. The (x, y) coordinates in the POS are translated into (y, z) in the 3D space, and z in the POS is translated into x in the 3D space.

3.3.2 Modeling

To explore the characteristics of the coronal plasma environment during the studied events, I used the Predictive Science Inc. (PSI) standard coronal solutions from magnetohydrodynamic (MHD) simulations originating from the MAS code (Mikić et al. 1999). The data are available on the PSI's data archive⁵. I obtained the PSI MAS coronal solution (a thermodynamic-with-heating MHD model) on April 3, 2019, at 12:00 UT, with the following simulation result ID⁶. Initially, I calculated the angle between the burst's source radial vector and the LOS. Moreover, I calculated the complement angle, which is the separation angle between the burst's radial vector and POS from the Earth's perspective. Subsequently, I utilized the complement angle to derive the Carrington longitude (Thompson, W. T. 2006), facilitating the extraction of a longitudinal segment from the MAS datacube, as if it were in the POS. Following this, the selected data slice was fed into the FORWARD model, a toolset responsible for generating synthetic coronal maps of observable quantities describing the plasma state. For extracting the longitudinal slices from the MAS data, I utilized the psipy python package⁷. The MAS datacube is specifically defined on a spherical grid and represents a steady-state MHD model. Owing to the inherent attributes of this datacube, the utilization of the FORWARD toolset proves more practical and advantageous for our objective. In Figure 3.8 I show the first radio contour of the sixth type III burst on top of the equivalent 2D maps for six plasma parameters, as an example. The plasma parameters are, from left to right and from the top to bottom: plasma density, plasma temperature, magnetic field strength, plasma beta parameter, the total plasma pressure, and the Alfvén speed. By taking the value of these physical plasma quantities at the centroids' coordinates of the type III sources at each frequency band, I obtained estimates of local plasma conditions shown in Figure 3.9 for the sixth type III burst, as an example.

3.4 Results and discussion

3.4.1 Detection and characterization of type III radio bursts

I found that the radio waves arrived at STEREO one minute before they arrived at Wind (Fig. 3.1). However, the difference between the $+z$ and $-z$ positions of the burst this close to the Sun in terms of light travel time is ~ 10 seconds ($\sim 4 R_\odot$), which is within the time resolution of the observations (1 min time resolution). Thus, I cannot confidently conclude whether the emission arrived at one spacecraft first and the other second.

Figure 3.4 shows the combined dynamic spectrum from both LOFAR and PSP. The free parameters of the auto-detection algorithm do not have the same values as for detection the type III bursts in the LOFAR spectrum alone. Upon visual examination, I observed that the detection algorithm effectively identified type III bursts in the LOFAR dynamic spectrum (Fig. 3.5), but it had limitations in terms of

⁵Predictive Science Inc.: <https://www.predsci.com/mhdweb/home.php>

⁶Simulation result ID: hmi_med-cor-thermo2-std01_med-hel-poly-std01

⁷PsiPy repository: <https://github.com/predsci/PsiPy>

detecting type III bursts in the combined spectrum of the LOFAR and PSP, as well as missing segments of the detected bursts and a few bursts entirely. This could be due to the increased frequency drift and dispersion of the radio bursts at lower frequencies, which made it a challenging task for the detection algorithm. I captured nine type III bursts from the combined dynamic spectrum and their characteristics are reported in Table 3.1. However, the detection algorithm performed better on the LOFAR dynamic spectrum only and I traced 16 type III bursts.

3.4.2 Imaging of radio emission sources

Figure 3.6 shows the persistence imaging for the 16 type III bursts in the LOFAR dynamic spectrum (Fig. 3.5). The observation frequencies and timestamps of the snapshot images used to produce the persistence image are shown at the top-right corner of each image. From a visual inspection of Figure 3.6, it seems that all the type III emissions originated from the same quadrant in the images (south-east direction on the solar disk), although there was no active region presented at that location except for a single active region nearby the central meridian (Fig. 3.3). Based on the imaging data presented in Figure 3.6, I chose one representative type III burst (No. 6) for a single-burst analysis in this paper, as it shares similarities in extent and location with other bursts.

To determine the spatial connection between the sources of radio emissions and the coronal magnetic field, a three-dimensional (3D) projection of the radio source contours onto the extrapolated coronal magnetic field via the PFSS model was employed (Fig. 3.7). The result indicates a discernible south-eastward propagation of the radio sources relative to the Earth's perspective, with no open field line crossing the radio sources. In Figure 3.7, I performed an extrapolation only over the two active regions presented on the solar surface at that time. However, when I extrapolated the magnetic field over the entire solar surface, I noticed that the radio sources are aligned with the lower part of large-scale closed field lines and are placed onto the open field lines emanating from the southern coronal hole. No open field lines crossing the radio sources are observed. I note that the PFSS modeling is limited by the fact that AR12738 is behind the limb on April 3 as observed from Earth. Consequently, the magnetic data available to us could be around two weeks old or more. This might limit the reliability of PFSS extrapolation for that region during that specific timeframe.

From Figure 3.7, the results suggest several potential origins of these type III radio emissions: 1) they could be triggered in a closed-field lines structure such as large-scale coronal loops, given that the radio sources are aligned to closed-field lines geometry in the southern hemisphere; 2) they could be triggered by electron beams that are accelerated from an open-field active region (Kong et al. 2018). However, from the PFSS model, I found no evidence for magnetic connectivity from both ARs on the Sun at that time; 3) they may result from electron beams that are accelerated in the corona due to expanding magnetic fields from plasma upflows in the active region (Del Zanna et al. 2011; Harra et al. 2021). Our findings indicate a notable inverse relationship between imaging quality and the level of solar radio emission brightness (e.g., for type III bursts 10 and 13, for instance). This observation is due to the leakage of solar radio emission into the side lobes of the calibrator beam, which disrupts the accuracy of calibration solutions.

3.4.3 Plasma diagnostics and magnetic field analysis

Considering the observed alignment of radio sources in Figure 3.7 and the case depicted in Figure 3.8, it becomes evident that radio sources at higher frequencies (indicating proximity to the Sun) align with a streamer-like structure near the equator within the coronal model. This structure is characterized by elevated plasma beta, reduced coronal temperature, and diminished Alfvén speed. The coronal plasma density was relatively homogeneous with no prominent structures, probably due to the model resolution.

The location of radio sources of all the bursts were in the same quadrant as seen from Earth. Therefore, I assumed that the former description applies for all bursts. I also found that the radio sources were confined between the equatorial sheet and the southern coronal hole and moving along that boundary. Figure 3.9 shows the variability of the coronal plasma quantities at the radio sources' centroids, taken from FORWARD maps in Figures 3.8, at different frequencies for the sixth burst. To estimate the error bars, I initialized random centroids, within the limits of the 70%-contours of the radio emissions, to sample the plasma quantities at those locations. Then the standard error (SE) is calculated using Equation 3.5, where σ is the standard deviation, and n is the number of points.

$$SE = \frac{\sigma}{\sqrt{n}} \quad (3.5)$$

The coronal temperature was increasing with radial distance, which implies there may have been some heating locally. The behavior of the coronal magnetic field, the plasma total dynamic pressure, and the Alfvén speed were decreasing over distance as expected. Finally the value of plasma beta parameter started increasing sharply around 40 MHz, which implies that the plasma pressure became more dominant than the magnetic pressure around that distance from the Sun (for a $2.5 \times$ Newkirk model, it is $1.89 R_\odot$ assuming a fundamental emission, or $2.57 R_\odot$ assuming a harmonic emission).

The top-left panel of Figure 3.9 shows a comparison between the density profiles of the MAS model, the $2.5 \times$ Newkirk model and the theoretical expected density profiles under the fundamental and harmonic assumptions. Although the Newkirk density model provided a useful approximation for determining the height of radio sources in the corona, it is not entirely accurate due to a number of its underlying assumptions; for instance, the assumption of a steady state and the spherical symmetry of the corona, which do not always apply. Therefore, I tried to use the MAS density values to estimate the depth along the LOS of the radio source, since it is supposed to give a more realistic result. I found that the plasma density obtained from the MAS and FORWARD modeling results were significantly lower compared with the $2.5 \times$ Newkirk density model and the theoretical expected density obtained from the classical relation in Equation 3.6, where f_p is the plasma frequency (in MHz) and n_e is the electron density (in cm^{-3}):

$$n_e = \left(\frac{f_p}{8.98 \times 10^{-3}} \right)^2 \quad (3.6)$$

The required density from the fitted Newkirk model is much higher (about ten times) than what is obtained from the MAS model, even after accounting for the $2.5 \times$ enhancement already applied to the standard Newkirk model. This implies the discrepancy cannot be fully explained by the density enhancement factor alone. Furthermore, the imaging places the radio sources near a streamer which is an overdense region in the MAS model, so it seems unlikely the source's apparent location in the model is wrongly attached to a less dense feature, as there are not denser options available. The apparent source positions from the imaging are likely too high, possibly due to scattering effects (Kontar et al. 2019, 2023; Chen et al. 2023), which could lead to fitting an overly dense Newkirk model. Another potential explanation is that there could be a stealth CME that pushed the coronal magnetic field outward, allowing the plasma to follow it to be perceived as having a higher density than expected, and there was not enough time for the magnetic field relaxation to occur (private communication with J. Magdalenić). However, scattering alone does not seem to fully explain the large density discrepancy. While further investigation is certainly needed regarding scattering and propagation effects on the radio waves, it is interesting to report this significant discrepancy between the model and observations, as it highlights limitations in the current modeling and suggests the need for additional physics to properly characterize the density distribution. Resolving this discrepancy could lead to important insights into the true nature of the corona.

3.5 Summary and conclusions

In this work I analyze the characteristics of a series of type III bursts that occurred on April 3, 2019, during the second near-Sun encounter period of PSP. The bursts were observed in dynamic spectra taken with the PSP/FIELDS (2.6 kHz – 19 MHz) instrument, as well as in interferometric imaging with the LOFAR (20 – 80 MHz) ground-based telescope, as part of a coordinated observing campaign. The series of 16 separate weak bursts were observed over the span of ~ 20 minutes, during an otherwise relatively quiet period. The solar disk as observed from Earth was dominated by a single active region near its center. I combined the dynamic spectra for the LOFAR frequency range and the PSP frequency range to study the solar radio emissions within the frequency range of 2.6 kHz – 80 MHz.

For the study, I developed a semi-automated pipeline, which allowed us to obtain the exact times and frequencies of the bursts. These I used to align the PSP to the LOFAR observations and to generate interferometric images between 20 and 80 MHz. I performed data pre-processing of the PSP and LOFAR dynamic spectra to resample and shift the data based on the relative location of the spacecraft with respect to the Sun and Earth, and found an excellent temporal match between the two sets of observations. Thus I automatically traced the type III bursts in the dynamic spectra algorithmically and estimated frequency drift and the electron beam speeds. I found that frequency drifts remained relatively uniform between the high-frequency (LOFAR) and low-frequency (PSP) observations, as well as among the bursts, suggesting that they are related.

In addition, I imaged the type III emission at multiple frequency bands using the interferometric observations from LOFAR to determine the locations of the sources in the solar corona. The type III emissions observed were all found to occur in the same general region off the southeast limb of the Sun, leading us to conclude that they shared a single source of electron beams low in the corona. The potential origins of these emissions are varied and include: 1) small-scale impulsive events such as nanoflares (ish 2017; Che 2018; Chhabra et al. 2021); 2) plasma upflows from the active region (Harra et al. 2021); 3) coronal closed-loop structures (Wu et al. 2002); 4) electron beams accelerated from interchange reconnection (Gopalswamy et al. 2022a); 5) high-frequency Alfvén waves and/or magnetic reconnection in the outer corona (Morton et al. 2015; Alielden & Taroyan 2022).

Our magnetic extrapolation shows that there is no open potential field to either AR12737 or AR12738, which is consistent with Cattell et al. (2021). Our findings are in line with the conclusions of Harra et al. (2021), who proposed that the likely origin of these type III bursts is the AR12737 region. The type III radio bursts in Harra et al. (2021) occurred between April 1 and 4, are temporally aligned with the emergence of AR12737 near the eastern limb of the solar disk.

While potential field source surface models provide valuable insight into the large-scale magnetic topology, their reliability decreases near active regions where the field can deviate significantly from a potential configuration. Therefore, the lack of open field connectivity directly to AR12737 suggested by the PFSS model should be viewed with some caution.

This work (Nedal et al. 2023b) complements those results by precisely locating the burst sources in the middle of the corona. I used the Newkirk density model to estimate the height of the radio sources from the Sun of one of the type III bursts as representative of all. Combining this with PFSS magnetic modeling, I found good agreement between the centroids of the radio sources and the location of the southern open field lines in the corona, which would be required to produce radio emissions at interplanetary wavelengths in general. On the other hand, this location does not seem to be well connected to the AR itself, according to the PFSS model.

I attempted to correct the radial distance of the radio sources from the Sun by replacing the Newkirk model with more realistic MHD results from the MAS model, but I found that there is a significant discrepancy between the Newkirk model profile fitted to the observations and the MAS density. This could result from scattering lensing the apparent burst location to a higher altitude, thus, overestimating the height of radio sources in the corona. The presence of type III radio sources at relatively high distances in the corona, with plasma density higher than expected from the MAS model, suggests that there may be missing information in the modeling. One possibility is the existence of a stealth CME that pushed the coronal magnetic field outward, causing the plasma to appear denser than expected (see Dumbović et al. (2021)) — or other non-obvious changes in large-scale coronal magnetic topology. These findings demonstrate that scattering and propagation effects play a significant role in determining the location and directionality of solar radio bursts (Kontar et al. 2019, 2023; Chen et al. 2023). Therefore, the discrepancy between the observed and modeled density profiles could potentially be attributed to scattering and lensing effects that make the radio sources appear higher in the corona than their true location. Further investigation is required to disentangle these effects from limitations in the density models themselves. Overall, accounting for scattering and refraction will likely lead to improved modeling of the corona and solar radio bursts. In future work, I will also employ the time delay of arrival (TDoA) technique (Zhang et al. 2019) to estimate the radio burst source positions from multi-instrument observations and compare that with the current methodology in this paper. Solar Orbiter observations shall also be included.

High-fidelity interferometric radio imaging in metric-decametric wavelengths provides a powerful method to characterize solar eruptive events. It is also becoming increasingly important for studying relatively quiet periods, during which there may be elevated levels of in situ particle fluxes. The ability to observe and image faint radio bursts such as those presented in this work, which may be related to episodes of reconnection on the solar surface, and potentially to episodes of solar wind release, is a testament to LOFAR’s power as a space weather instrument. In a future work, I will automate and use our method for studying hundreds of faint bursts observed with LOFAR and will investigate their relation to small-scale activity on the solar surface.

Through a novel combination between the LOFAR imaging and MAS model results, I found that the type III radio bursts experienced a weakening background magnetic field, decreasing solar wind dynamic pressure and Alfvén speed, increasing plasma beta and coronal temperature, and plasma rarefaction. The radio sources appeared at larger radial distances than the models predicted, which suggests scattering and density fluctuations are important when attempting to interpret the actual burst trajectory. The discrepancies between the observed and modeled radial distances of the radio sources suggest refinements are needed in the models to fully explain the radio imaging and modeling results. Overall, comparing the

LOFAR imaging and MAS modeling for these type III bursts motivates further analysis on additional radio bursts to improve our understanding of the physical conditions that influence the propagation of radio emissions in the corona.

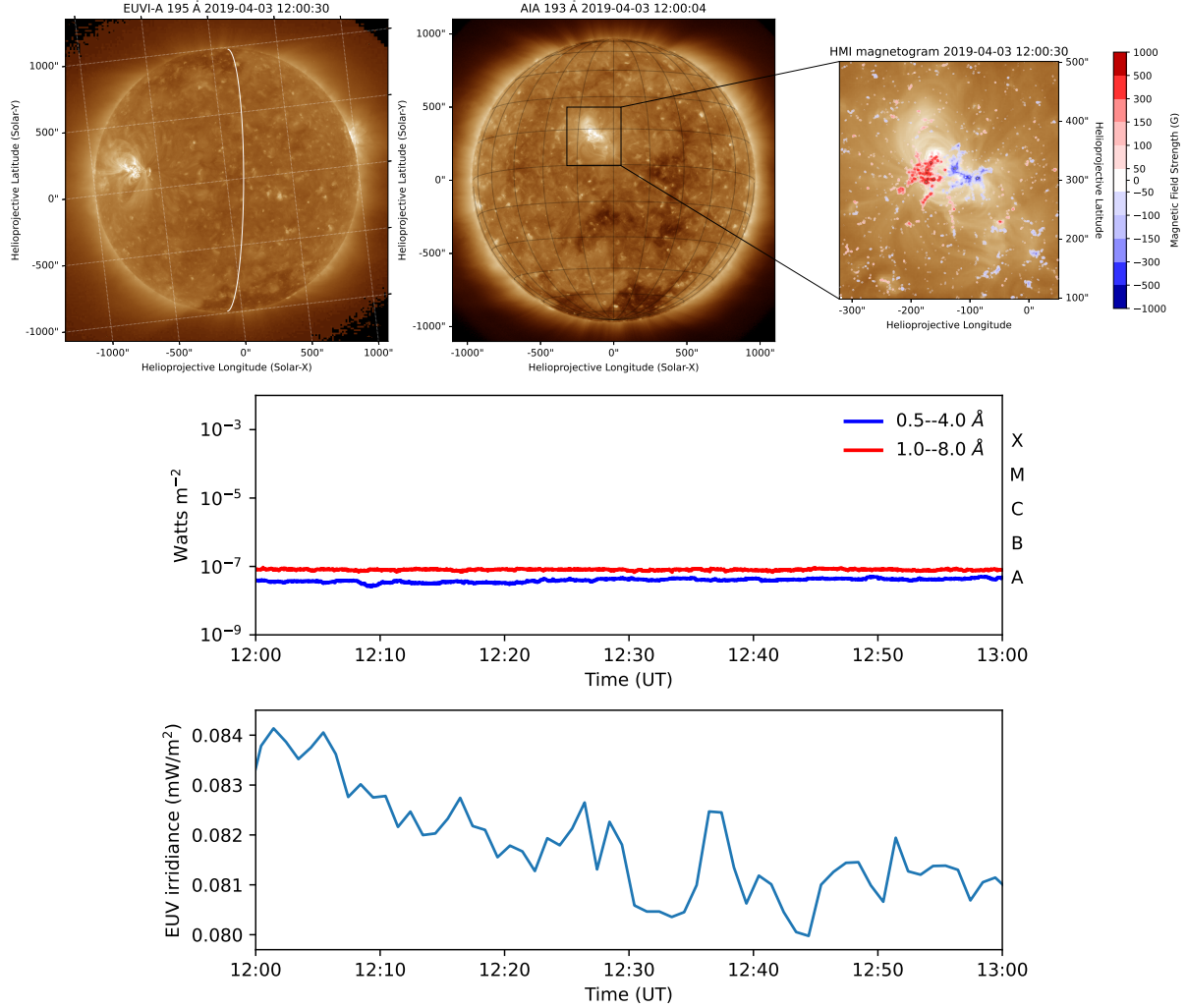


Figure 3.3: Exploring the X-ray and extreme ultraviolet (EUV) emissions from the Sun. The top panel showcases a cutout region of the SDO/AIA 193 Å image of the solar disk along with the STEREO-A EUVI 195 Å point of view. The white curve is the limb of the solar disk as seen by AIA from the right side. The red and blue colors are the contours of the line-of-sight magnetogram from the SDO/HMI instrument. The levels are (50, 100, 150, 300, 500, 1000) Gauss. The middle panel shows the X-ray flux from the GOES-14 spacecraft shows minimum activity. The bottom panel shows the time series of the ESP Quad band from the SDO/EVE instrument, which shows the solar irradiance in the extreme ultraviolet (EUV) band.

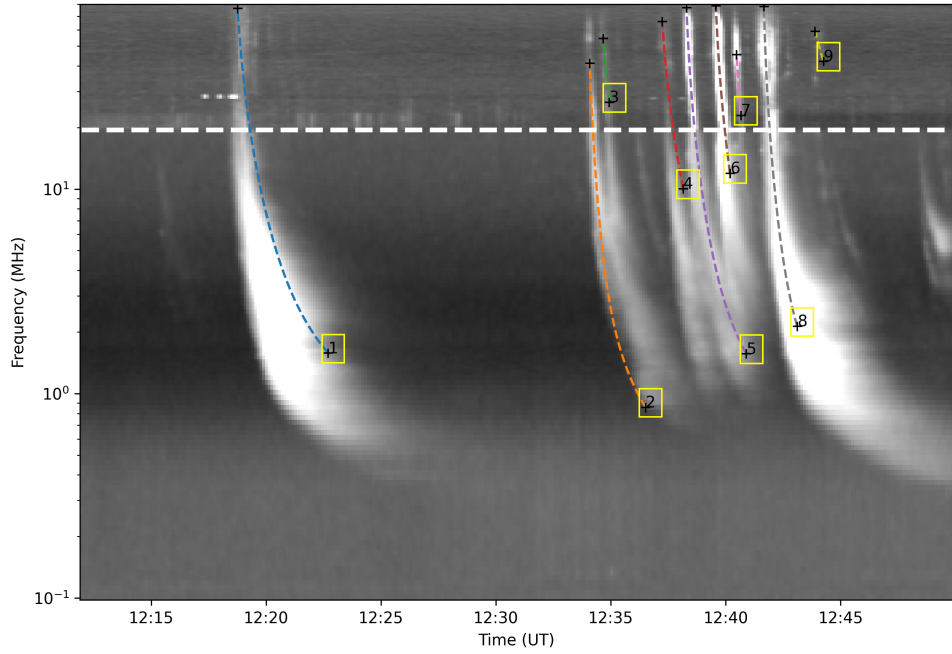


Figure 3.4: Automatic detection of type III radio bursts from the combined radio dynamic spectrum of LOFAR and PSP instruments. The dashed horizontal lines separates the LOFAR frequency range (top) and the PSP frequency range (bottom).

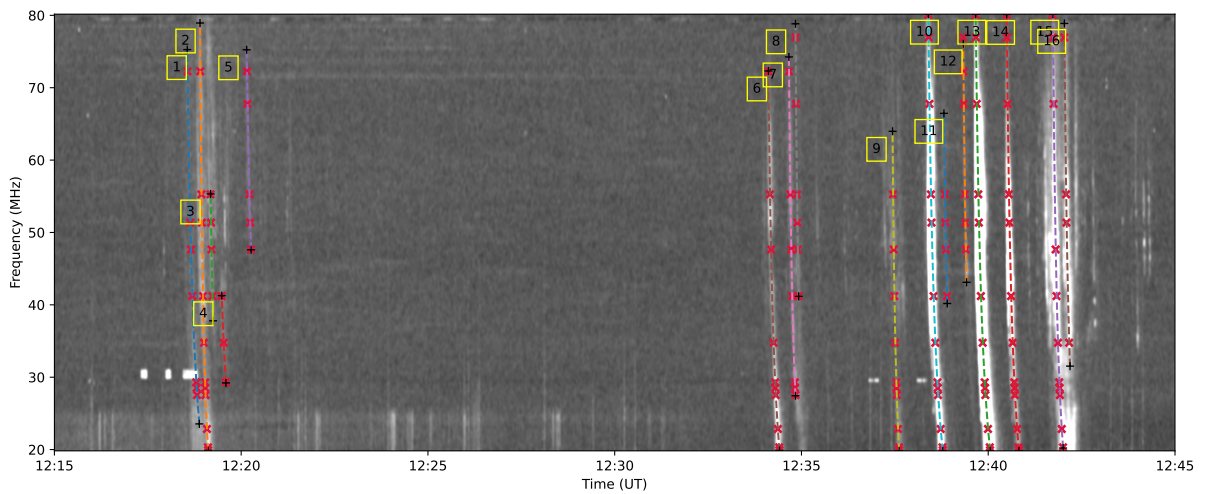


Figure 3.5: Automatic detection of type III bursts observed by LOFAR. The red symbols along the fit lines are the (f, t) coordinates of the image snapshots shown in Figure 3.6.

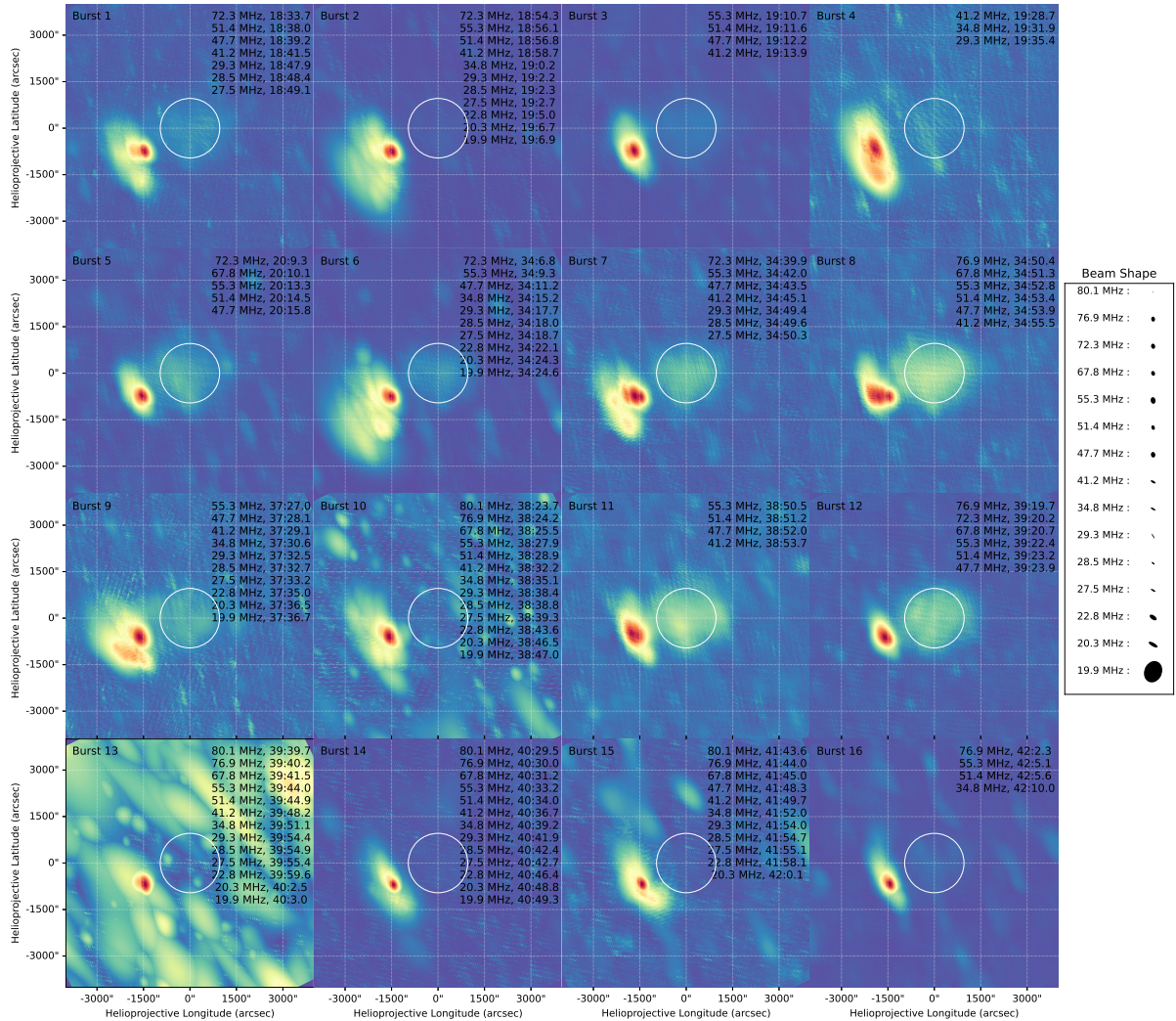


Figure 3.6: Persistence imaging for the 16 type III bursts detected in the LOFAR dynamic spectrum. The label shows the observation frequencies in MHz and times in (minutes:seconds from 12:00:00 UT). Here, the color coding is not absolute, but rather each panel has its own color code.

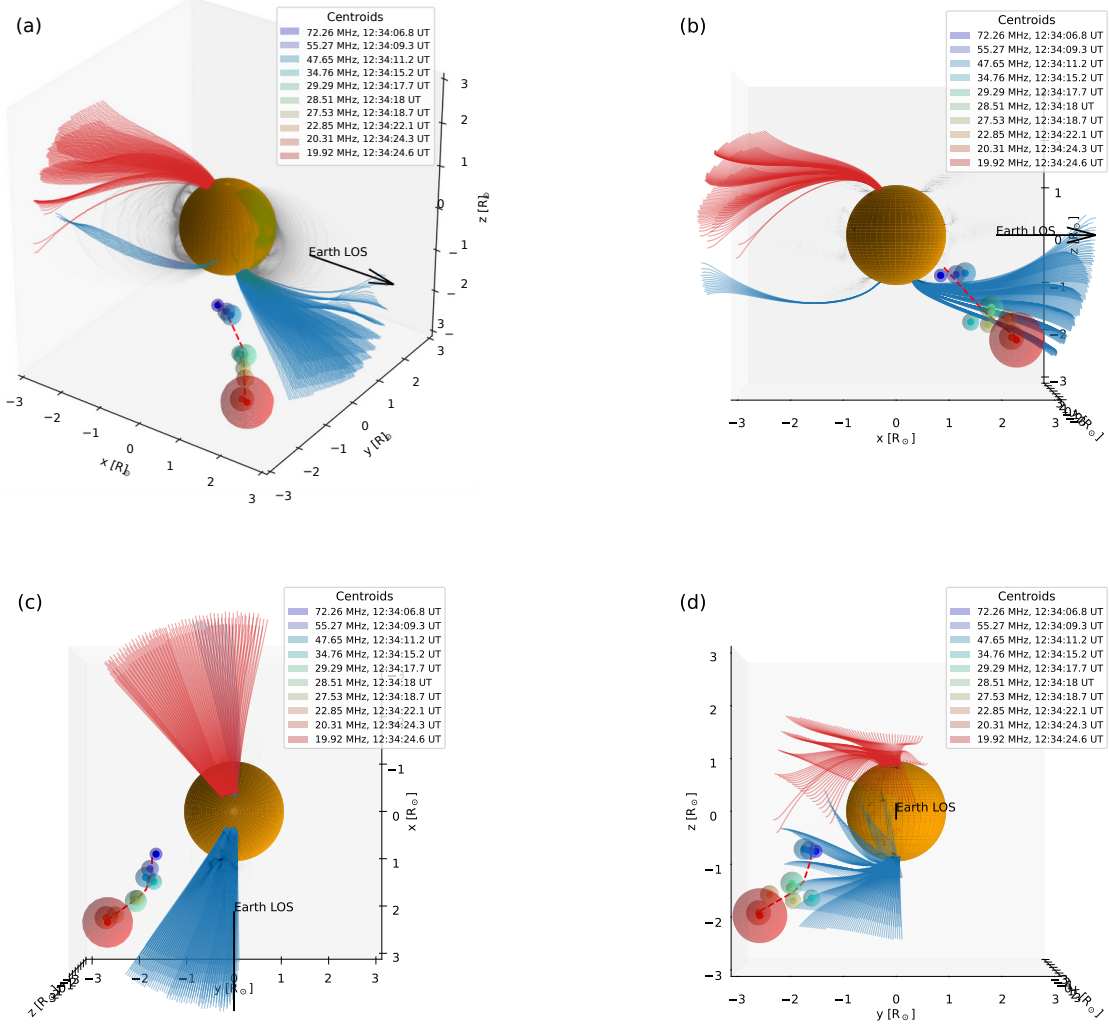


Figure 3.7: Different viewing angles for the deprojection of the radio sources of the sixth burst using the $2.5 \times$ Newkirk electron-density model on the PFSS solution. The black arrow points toward the Earth's LOS. The yz plane is the POS as seen from the Earth. The red dashed line is a spline curve fit for the sources' centroids. The red, black, and blue curves are the open northern, closed, and open southern field lines, respectively. The opacity of the closed field lines is decreased for better visualization.

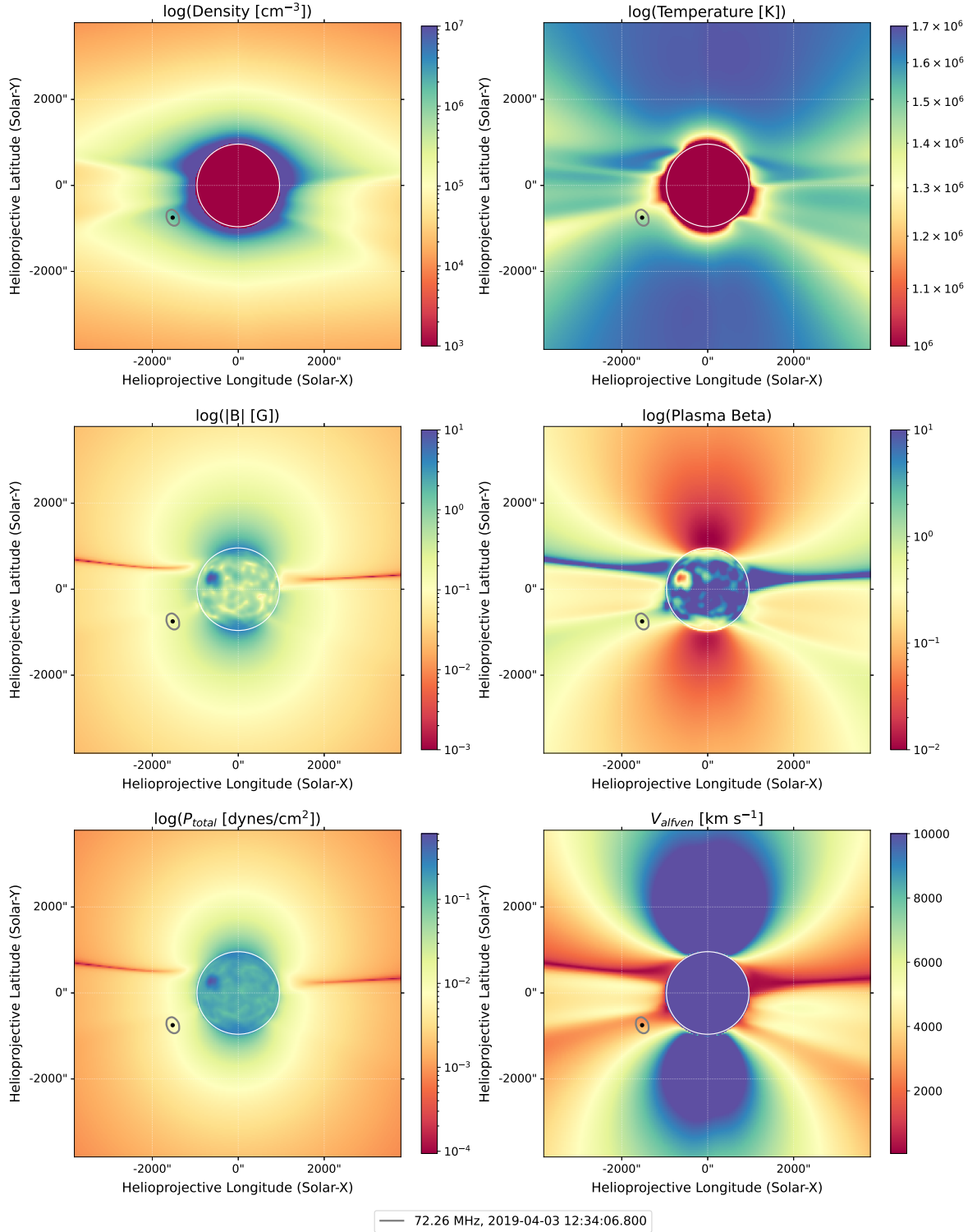


Figure 3.8: Synthesized maps of plasma parameters obtained using the FORWARD toolset, with the 70%-contour of radio emission of the sixth burst at the first timestamp (12:34:06.8 UT) at the frequency of 72.26 MHz depicted on top of the 2D POS cuts. The left column represents, from top to bottom, plasma density, magnetic field, and the total plasma dynamic pressure. The right column represents, from top to bottom, the temperature, plasma beta, and the Alfvén speed.

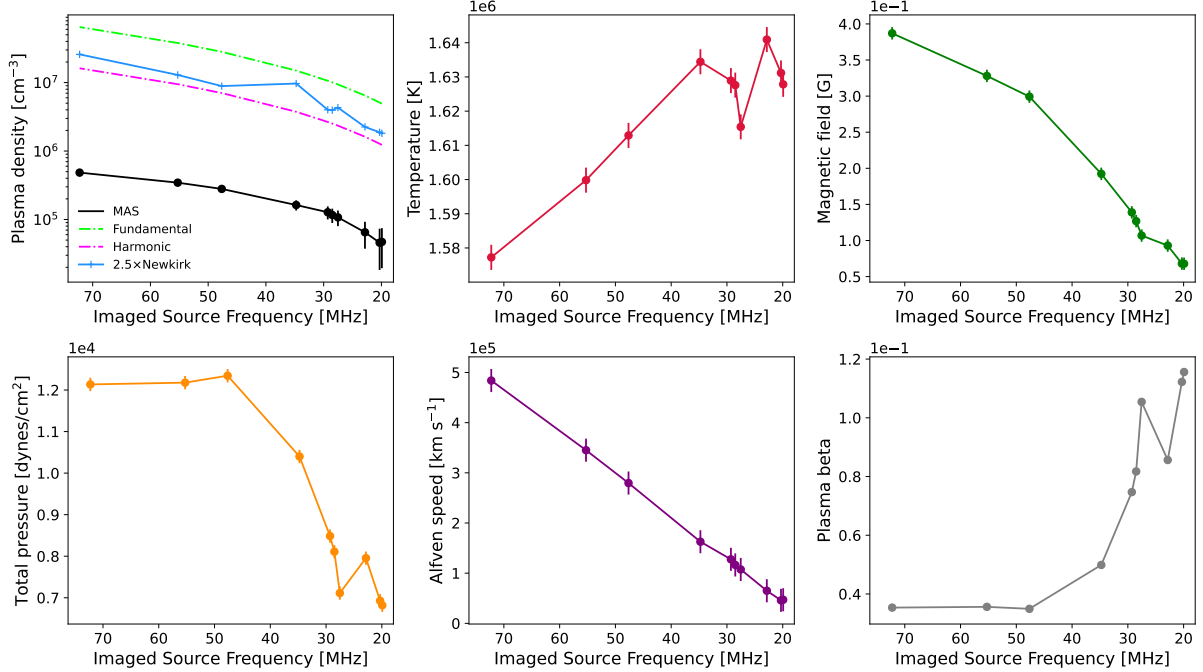


Figure 3.9: Coronal plasma parameters sampled from the 2D maps by the source centroids. The top panel shows (from left to right) the plasma density profiles from the MAS model, $2.5 \times$ Newkirk model, and the theoretical densities under the fundamental and harmonic assumptions, plasma temperature, and magnetic field. The bottom panel shows, from left to right, the total plasma dynamic pressure, Alfvén speed, and plasma beta. The x-axis is inverted to demonstrate a progression of increasing radial distance from the Sun as the observer moves towards the right.

Chapter 4

Modeling and Forecasting of Solar Energetic Protons (SEP)

This chapter has two parts. In the first part, I describe a modeling study that we conducted on energetic proton acceleration and propagation from the solar corona to 1 AU. For this modeling, we employ the physics-based approach utilized in the first chapter, including the 3D coronal models and a 3D MAS-MHD model run. With these models, we use the EPREM model to find the fluxes and spectra of energetic protons at 1 AU. We then compare the modeling results with in-situ measurements. In the second part, I describe a deep learning approach that I developed to forecast the integral flux of energetic protons in three energy channels across three different forecasting horizons.

4.1 Introduction

CMEs represent significant phenomena in solar physics, captivating attention due to their prominent role in solar activity. Traditionally, CMEs have been identified through white light observations, providing valuable insights into their characteristics (Vourlidas et al. 2003; Zhang & Dere 2006; Bein et al. 2011). However, a comprehensive understanding of these eruptions requires examination across multiple wavelengths, including ultraviolet and radio bands, where observations reveal additional facets of their dynamics (Bastian et al. 2001; Veronig et al. 2010). Notably, EUV observations, facilitated by instruments like the AIA on the Solar Dynamics Observatory, have become instrumental in capturing the early stages of CMEs (Lemen et al. 2012; Pesnell et al. 2012).

CMEs, in their trajectory through the solar corona, can give rise to shock waves when their propagation speeds surpass the local fast magnetosonic speed, observable as EUV waves or CBFs (Thompson et al. 1998; Long et al. 2011). These shock waves are crucial in the context of SEP acceleration. While solar flares also contribute to SEP production, recent advancements in observations and numerical modeling have reshaped the prevailing understanding. It is now recognized that, especially in their early stages (below $5\text{--}10 R_{\odot}$), CMEs often drive shocks capable of accelerating SEPs to energies exceeding 100 MeV/n (Ontiveros & Vourlidas 2009; Gopalswamy & Yashiro 2011; Battarbee et al. 2013; Kozarev et al. 2013; Schwadron et al. 2014; Kong et al. 2017).

Previous research has primarily focused on characterizing the dynamics of CMEs and their associated shocks within the solar corona, utilizing advanced observations spanning white light, EUV, and radio wavelengths (Vourlidas et al. 2003; Zhang & Dere 2006; Bein et al. 2011). The relationship between CMEs and shock waves, particularly CBFs, has been a subject of in-depth investigation. Notably, Kozarev et al. (2019) conducted a comprehensive study of nine distinct western CBF events, employing the Diffusive Shock Acceleration (DSA) model proposed by Kozarev & Schwadron (2016). Their findings revealed variations in SEP production among events, coupled with evolving patterns over the course of each event. Moreover, the acceleration efficiency demonstrated a strong dependence on the diverse coronal environments traversed by the propagating shock waves.

Building upon the groundwork laid by Kozarev et al. (2019), this present study extends its scope by modeling the dynamics of CBF-related shock/compression waves and particle acceleration up to $10 R_{\odot}$. This advancement involves integrating outcomes with a comprehensive numerical particle transport model, allowing for comparisons with in situ observations. This marks a significant enhancement in our methodology, representing the first validated extension of Sun-to-Earth physics-based modeling for

SEP acceleration and transport within our current understanding of solar physics (Kozarev et al. 2022).

In the quest to understand the mechanisms through which SEPs are produced by coronal shocks throughout the inner heliosphere, considerable progress has been made. Traditionally, the prevailing assumption was that SEP acceleration primarily occurred in interplanetary space, driven by in situ measurements of Energetic Storm Particle (ESP) fluxes during encounters with interplanetary shocks by spacecraft. However, recent advancements in observations and numerical modeling have reshaped this understanding.

CMEs emerge as the principal contributors to the generation of SEPs, encompassing ions and electrons with energies several orders of magnitude beyond the thermal coronal plasma (Reames 1999). While solar flares also contribute to SEP production during solar eruptions, CMEs predominantly facilitate SEP generation within the magnetized shock waves they instigate and in plasma compressions resulting from their expansive forces. The prevailing assumption that the majority of SEP acceleration transpired in interplanetary space has been challenged by the revelation that, particularly in their initial stages (below $5\text{--}10 R_{\odot}$), CMEs frequently induce shocks capable of accelerating SEPs to energies surpassing 100 MeV/n (Ontiveros & Vourlidas 2009; Gopalswamy & Yashiro 2011; Battarbee et al. 2013; Kozarev et al. 2013; Schwadron et al. 2014; Kong et al. 2017).

Efforts have been directed towards characterizing the dynamics of CMEs and the accompanying shocks within the solar corona, employing increasingly sophisticated observations spanning white light, EUV, and radio wavelengths. This exploration aims to deduce early-stage SEP production in the solar corona (Kozarev et al. 2013; Schwadron et al. 2015). In a notable contribution, Kozarev et al. (2019) conducted an in-depth study of nine distinct western CBF events, utilizing the Diffusive Shock Acceleration (DSA) model proposed by Kozarev & Schwadron (2016). Their findings highlighted variations in SEP production among events, along with evolving patterns over the duration of each event. Importantly, the acceleration efficiency exhibited a strong dependence on the diverse coronal environments traversed by the propagating shock waves.

This study, led by Kozarev et al. (2022), advances the work of Kozarev et al. (2019) by extending the modeling of CBF-related shock/compression wave dynamics and particle acceleration to $10 R_{\odot}$. Our approach involves coupling these results with a global numerical particle transport model and comparing the outcomes to in situ observations. This represents a significant enhancement in our methodology, marking the first validated extension of Sun-to-Earth physics-based modeling for SEP acceleration and transport within our current understanding of solar physics.

Several models are available, or under development, for forecasting SEP, which use diverse approaches and serve different objectives. These models comprise computationally complex physics-based models, quick and simple empirical models, Machine Learning (ML)-based models, and hybrid models that combine different approaches and produce different types of outputs, including deterministic, probabilistic, categorical, and binary. Deterministic models always generate the same output without any randomness or stochastic components, such as predicting the SEP flux at a specific moment or the arrival time of SEP. On the other hand, probabilistic models provide a probability value that reflects the likelihood of an SEP event occurring. However, replicating SEP fluxes at a specific time is still a significant challenge for current models.

An excellent review on SEP models and predictive efforts was recently published by Whitman et al. (2023), which summarizes the majority of the existing models. For instance, Papaioannou et al. (2022) introduced the Probabilistic Solar Particle Event Forecasting (PROSPER) model, which is incorporated into the Advanced Solar Particle Event Casting System (ASPECS)¹. The PROSPER model utilizes a Bayesian approach and data-driven methodology to probabilistically predict SEP events for 3 integral energy channels >10 , >30 , and >100 MeV. The model's validation results indicate that the solar flare and CME modules have hit rates of 90% and 100%, respectively, while the combined flare and CME module has a hit rate of 100%. Bruno & Richardson (2021) developed an empirical model to predict the peak intensity and spectra of SEP at 1 AU between 10 and 130 MeV, using data from multiple spacecraft. The model is tested on 20 SEP events and shows good agreement with observed values. The spatial distribution of SEP intensities was reconstructed successfully, and they found a correlation between SEP intensities and CME speed.

Hu et al. (2017) extended the Particle Acceleration and Transport in the Heliosphere (PATH) model to study particle acceleration and transport at CME-driven shocks. They showed that the model can be used to obtain simultaneous calculations of SEP characteristics such as time-intensity profiles, instantaneous particle spectra, and particle pitch angle distributions at multiple heliospheric locations. Overall, results resemble closely those observed in situ near the Earth but also yield results at other places of interest,

¹ ASPECS: <http://phobos-srv.space.noaa.gov/>

such as Mars, making it of particular interest to Mars missions. SPREAdFAST (Kozarev et al. 2017, 2022) is a physics-based, data-driven framework that utilizes EUV observations and models to simulate SEP fluxes at 1 AU and to estimate energetic particle acceleration and transport to various locations in the inner heliosphere. It generates time-dependent histograms and movies distributing them through an online catalog. The accuracy and efficiency of the model were encouraging, but the highest energy fluxes showed disagreement with in situ observations by the SOHO/ERNE instrument. However, the framework has great potential for space weather science and forecasting.

In Aminalragia-Giamini et al. (2021), they used neural networks to provide probabilities for the occurrence of SEP based on soft X-rays data from 1988 to 2013. They obtained >85% for correct SEP occurrence predictions and >92% for correct no-SEP predictions. Lavasa et al. (2021) described a consistent approach to making a binary prediction of SEP events using ML and conventional statistical techniques. The study evaluated various ML models and concluded that random forests could be the best approach for an optimal sample comprising both flares and CMEs. The most important features for identifying SEP were found to be the CME speed, width, and flare soft X-ray fluence. Kasapis et al. (2022) employed ML techniques to anticipate the occurrence of a SEP event in an active region that generates flares. They utilized the Space-Weather MDI Active Region Patches (SMARP) dataset, which comprises observations of solar magnetograms between June 1996 and August 2010. The SMARP dataset had a success rate of 72% in accurately predicting whether an active region that produces a flare would result in a SEP event. Moreover, it provided a competitive lead time of 55.3 min in forecasting SEP events.

Engell et al. (2017) introduced the Space Radiation Intelligence System (SPRINTS), a technology that uses pre- and post-event data to forecast solar-driven events such as SEP. It integrates automatic detections and ML to produce forecasts. Results show that SPRINTS can predict SEP with an 56% probability of detection and 34% false alarm rate. Nevertheless, the HESPERIA REleASE tools provide real-time predictions of the proton flux at L1 by using near-relativistic electrons as a warning for the later arrival of protons and have been set to operation (Malandraki & Crosby 2018). Historical data analysis indicates high prediction accuracy, with a low false alarm rate of approximately 30% and a high probability of detection of 63% (Malandraki & Crosby 2018).

Forecasting SEP is a critical task that serves operational needs and provides insight into the broader field of space weather science and heliophysics. As emphasized in previous works, a high precision forecasting model is urgently required to predict SEP flux within a period of time, given the risks associated with these events. This highlights the critical requirement for a dependable forecasting system that can mitigate the risks associated with SEP.

Scientists have been using physics-based and empirical models for decades to forecast SEP. However, these models have certain limitations. Physics-based models require accurate input data and underlying physical assumptions. In addition, the complexity of the physics involved and incorrect parameters may introduce uncertainties that can lead to inaccurate predictions. On the other hand, empirical models rely on historical data to make predictions. While they can be accurate sometimes, they may be unable to account for changes in physical conditions related to the acceleration and propagation of SEP, which can influence prediction accuracy. ML models, however, provide a different approach to SEP forecasting. These models can analyze vast amounts of data, learning patterns from the data that are used, and connections that may not be obvious to experts. Additionally, ML models can adapt to changes in underlying physical conditions, resulting in more accurate predictions as more data is collected; they also provide relatively rapid forecasts, which allows for incorporation into a real-time forecasting workflow.

In the upcoming sections, I will explore the limitations in accuracy that arise from dealing with an imbalanced dataset and low-resolution data. Specifically, the presence of intrinsic outliers in the time series data pertaining to SEP flux poses a significant challenge in modeling. These outliers correspond to occurrences of SEP events and, consequently, have an impact on the accuracy of predictions. Notably, they often lead to an underestimation of the SEP fluxes, primarily due to the predominance of relatively low values throughout the majority of the time interval.

In the first part, we extend the work in Chapter 2 on the kinematics of CBFs and expand on previous relevant investigations by modeling CBF-related shocks and particle acceleration up to $10 R_{\odot}$. Our modeling approach incorporates coupling to a numerical model of particle transport throughout the heliosphere, with validation against in-situ spacecraft measurements. Our study implements, for the first time, an extensive physics-based model linking CME-driven shock acceleration with the propagation of SEPs from the Sun to Earth. In the second part, I present advanced deep learning models to forecast the daily integral flux of SEP over a 3-day forecasting window by using bi-directional long short-term memory (BiLSTM) neural networks, for 3 energy channels (>10 , >30 , and >60 MeV). Our models can

forecast the time-dependent development of SEP events in different energy domains, which can be used to model the space radiation profiles using frameworks such as BRYNTRN Wilson et al. (1988) and GEANT4 (Truscott et al. 2000).

4.2 Early-Stage SEP Acceleration by CME-Driven Shocks

4.2.1 Overview

CMEs stand out as one of the most prevalent expressions of solar activity, attracting considerable attention in solar physics. Traditionally defined through white light observations (Vourlidas et al. 2003; Zhang & Dere 2006; Bein et al. 2011), these eruptions reveal diverse facets when examined across ultraviolet and radio bands (Bastian et al. 2001; Veronig et al. 2010). Particularly noteworthy is their observation in EUV light, a realm where telescopes like the AIA onboard SDO (Lemen et al. 2012; Pesnell et al. 2012) excel in capturing the early stages of CMEs.

CMEs, in their dynamic journey through the solar corona, can generate shock waves if their propagation speeds surpass the local speed of information, typically the fast magnetosonic speed. These shock waves manifest prominently in EUV observations as EUV waves or, more specifically, as CBFs (Thompson et al. 1998; Long et al. 2011). The intricate relationship between CMEs and these shock waves forms a crucial aspect of solar physics.

As the primary contributors to SEPs, CMEs play a pivotal role in the energization of ions and electrons to levels significantly exceeding the thermal coronal plasma (Reames 1999). Flares also contribute to SEP production during solar eruptions. The acceleration of SEPs in CMEs predominantly occurs within the magnetized shock waves they propel, as well as in plasma compressions induced by the CMEs. While historical perspectives inferred the bulk of SEP acceleration in interplanetary space from in situ observations of energetic storm particle (ESP) fluxes during the traversal of interplanetary shocks by spacecraft, recent advancements in observations and numerical models have reshaped this understanding.

Over the past fifteen years, sophisticated observations and modeling techniques have revealed that, in their early stages (below $5\text{--}10 R_{\odot}$), CMEs often drive shocks (Ontiveros & Vourlidas 2009; Gopalswamy & Yashiro 2011). These shocks, in turn, exhibit the capability to accelerate SEPs to energies exceeding 100 MeV/n (Battarbee et al. 2013; Kozarev et al. 2013; Schwadron et al. 2014; Kong et al. 2017). Consequently, recent research has focused on characterizing the dynamics of CMEs and the associated shocks in the solar corona, employing advanced observations spanning white light, EUV, and radio wavelengths.

Building upon this foundation, efforts have been made to estimate the early-stage SEP production in the corona (Kozarev et al. 2013; Schwadron et al. 2015). In a notable contribution, Kozarev et al. (2019) conducted an in-depth study of nine distinct western CBF events. Utilizing the diffusive shock acceleration (DSA) model proposed by Kozarev & Schwadron (2016), they simulated particle acceleration in the very early stages, while the CMEs were still below $1.5 R_{\odot}$. Their findings highlighted variations in SEP production among events, along with evolving patterns over the event's duration. Importantly, the acceleration efficiency exhibited a strong dependence on the diverse coronal environments traversed by the shock waves.

This study, led by Kozarev et al. (2022), advances the work of Kozarev et al. (2019) by extending the modeling of CBF-related shock/compression wave dynamics and particle acceleration to $10 R_{\odot}$. Our approach involves coupling these results with a global numerical particle transport model and comparing the outcomes to in situ observations. This represents a significant enhancement in our methodology, marking the first validated extension of Sun-to-Earth physics-based modeling for SEP acceleration and transport within our current understanding of solar physics. In order to analyze particle fluxes at 1 AU and compare them with observational data, we employ the SPREAdFAST framework that is explained in Chapter 2.

The purpose of the SPREAdFAST framework is to model and analyze the particle fluxes from the Sun to Earth, specifically focusing on SEP events. The project combines detailed observations of CBFs with modeling of the coronal plasma and the resulting SEP production and interplanetary transport. The SPREAdFAST framework utilizes physics-based modeling to simulate the evolution of the plasma upstream of the coronal shock associated with CBFs and the subsequent acceleration and transport of protons from the Sun to 1 AU. It incorporates various components such as EUV observations, shock dynamics, particle acceleration, and interplanetary transport. The project aims to provide a better understanding of the processes involved in SEP events and improve forecasting capabilities for these events. By modeling a large number of events and comparing the model results with in situ observations, the

SPREAdFAST project contributes to the advancement of Sun-to-Earth physics-based modeling of SEP acceleration and transport. Overall, the SPREAdFAST project is a comprehensive effort to study and simulate the complex phenomena associated with SEP events, with the goal of enhancing our knowledge and predictive capabilities in this field.

The SPREAdFAST framework includes the following components:

1. CBF Kinematics and Geometric Modeling: This component characterizes the kinematics of CBFs using observations from the AIA instrument. It estimates the CBF kinematics, including the front, peak, and back edge positions over time, as well as the mean intensity and thickness of the CBFs.
2. Coronal Shock and Particle Acceleration Modeling: This component models the evolution of the plasma immediately upstream of the coronal shock associated with CBFs. It incorporates the physics of coronal shock waves and the process of particle acceleration through diffusive shock acceleration.
3. Interplanetary Particle Transport Modeling: This component simulates the transport of accelerated particles from the corona to 1 AU, which is the distance between the Sun and Earth. It takes into account the interplanetary magnetic field and other factors that influence particle propagation.
4. Comparison with Observations: The framework compares the modeled particle fluxes and fluences at 1 AU with observations from instruments like the SOHO and the Energetic and Relativistic Nuclei and Electron (ERNE) instrument. It evaluates the accuracy of the model predictions by calculating metrics such as the Mean Squared Logarithmic Error (MSLE).

Overall, the SPREAdFAST framework combines detailed observations, physics-based modeling of coronal shocks and particle acceleration, and interplanetary transport modeling to analyze and forecast SEP events from the Sun to Earth.

4.2.2 Event Selection

Our study focuses on a carefully selected set of solar events to ensure the robustness of our analysis. We initiated the event selection process by identifying proton events within the energy range of 17–22 MeV, as observed by the Solar and Heliospheric Observatory/Energetic and Relativistic Nuclei and Electron (SOHO/ERNE) instrument during the period spanning 2010–2017. This initial screening yielded a total of 216 events.

To refine our dataset and concentrate on events with clear solar signatures, we excluded proton events lacking associated flares, CMEs, and those devoid of EUV waves before the onset of SEP events. This step resulted in the exclusion of 39 events, leaving us with 177 events for further consideration.

Further narrowing our focus, we excluded cases where EUV waves were absent or where EUV data was not available, even if flares or CMEs had been identified. This decision aligns with the requirements of the SPREAdFAST model, which necessitates the presence of an EUV wave for accurate analysis. Consequently, this step reduced the dataset to 105 events.

In the interest of precision and relevance, we removed several events with uncertain EUV waves, deeming them more appropriate for investigations related to different solar eruptions. This additional refinement brought the total down to 99 events.

A meticulous examination of the remaining dataset revealed 62 events with measurable near-limb or off-limb CBFs, aligning with the capabilities of our analytical framework. These 62 events constitute our final selection for in-depth analysis and interpretation, as outlined in Table ??.

For comprehensive reference, Table 1 provides detailed information for each event, including the date, start and end times, and class of the associated flare. Additionally, it includes the source location on the solar disk specified in helioprojective Cartesian coordinates. These key details were sourced from the Heliophysics Events Knowledge Base, ensuring accurate and standardized information for each event in our study.

4.2.3 Coronal SEP Acceleration

Having established plasma parameters along individual shock-crossing field lines, our study employs the coronal DSA model (Kozarev & Schwadron 2016; Kozarev et al. 2019) to calculate proton acceleration dynamics from the low corona to $10 R_{\odot}$. Specifically designed to utilize remote solar observations and data-driven model output from the CASHeW framework, this model solves for the large-scale acceleration of charged particles induced by CME-driven shocks.

The model incorporates time-dependent estimates of shock speed (V_{shock}), density jump ratio (r), magnetic field strength ($|B|$), and shock angle (θ_{BN}) for multiple shock-crossing field lines. Using these parameters, the model computes the minimum shock injection momenta for particles. It takes as input a particle distribution function and produces time-dependent distribution function spectra or fluxes as output. The obtained solution (Equations 8–11 in cKozarev & Schwadron (2016)) provides both the first distribution function (f_1) and momentum (p_1) values for an initial momentum (p_0). The model iteratively solves for subsequent values (f_i and p_i) at time steps separated by the observational cadence δt of the instrument (in this case, SDO/AIA). The model is executed for each individual shock-crossing field line, based on observed and calculated parameters at a single shock-crossing point along it. Flux spectra at each time step are then computed, and the model’s validity has been confirmed through its application in the analysis of several SEP events.

4.2.4 Input Data and Spectral Fitting

The model relies on input data derived from observations-based suprathermal proton spectra obtained from 1 AU fluxes recorded by the SOHO/ERNE instrument (Torsti et al. 1995). These spectra are acquired during the 24-hour period of quiet time preceding each SEP event. Power laws are fitted to each suprathermal spectrum within the energy range of 0.056–3.0 MeV and scaled to a distance of $1.05 R_\odot$, assuming a simple inverse square dependence on radial distance to conserve flux. While the current implementation does not consider adiabatic cooling or other particle transport effects, acknowledging their significance, a comprehensive exploration of these effects will be conducted in future studies to determine general trends for forecasting.

The time-independent power law input spectra generated for the DSA model represent the suprathermal spectrum calculated for $1.05 R_\odot$. These spectra are injected at all shock positions and distances without modification to account for changing shock locations in the current model implementation. This approach allows for a detailed examination of proton acceleration dynamics and flux evolution under the influence of CME-driven shocks in the solar corona.

4.2.5 Transport of Accelerated SEPs and Comparison with ERNE Observations

The culmination of our modeling chain involves the transport of accelerated SEPs to 1 AU, followed by a comprehensive comparison with particle observations obtained through the ERNE instrument. This final phase is executed by utilizing the averaged fluxes derived from the entire event, exemplified here with the illustrative case of the May 11, 2011 event.

To achieve this, we employ a modified version of the Energetic Particle Radiation Environment Module (EPREM) model (Schwadron et al. 2010). The modified EPREM model facilitates the transport of fluxes through a Parker-type static interplanetary medium. The particle injection from the DSA model into EPREM is sustained throughout the duration of the coronal shock event. This model incorporates essential effects such as pitch-angle scattering, adiabatic focusing and cooling, convection, streaming, and stochastic acceleration.

The solver demands inner boundary conditions, with no initial conditions imposed. It features a dynamic simulation grid where computational nodes are carried away from the Sun with the solar wind, naturally adopting the shape of a three-dimensional interplanetary magnetic field. EPREM employs an interplanetary magnetic field model, incorporating radial and azimuthal field components that fall off with radial distance and a constant latitudinal component—the Parker spiral model.

The spatial grid structure is organized in nested cubes, subdivided into square arrays of square cells, representing the propagation pathway of energetic particles. The inner boundary surface rotates with the solar rotation rate and is expelled outward at the solar wind speed. At each time step, a new shell of cells is created at the inner boundary, initiating its outward propagation. The inner boundary for the EPREM simulation is fixed at $1.05 R_\odot$, while the outer boundary varies for individual field lines due to dynamic conditions, consistently exceeding 1 AU. The model’s credibility has been extensively validated through its application in Solar Energetic Particle studies (Kozarev et al. 2010; Schwadron et al. 2014).

For the EPREM model runs conducted on the 62 events in this study, standardized input parameters were employed. These parameters include a mean free path (λ_0) of 0.1 AU at 1 AU and 1 GV magnetic rigidity, a constant solar wind speed (V_{sw}) of 500 km s^{-1} , proton number density (n) at 1 AU set at 5.0 cm^{-3} , and a magnetic field magnitude ($|B|$) at 1 AU of $5.0 \times 10^{-5} \text{ G}$. The mean free path is additionally scaled with proton rigidity and radial distance from the Sun to incorporate the magnetic turbulence

spectrum and its radial dependence (Zank et al. 1998; Li et al. 2003; Sokolov et al. 2004; Verkhoglyadova et al. 2009), providing the parallel mean free path for the simulation.

An energy grid with 20 points, logarithmically spaced between 1 and 200 MeV, and a 4-point pitch-angle grid were utilized. A simulation time-step of 0.5 AU/c (approximately 4 minutes) with 30 sub-steps allowed for accurate calculation of SEP propagation among nodes. These baseline simulations encompassed all effects of diffusive transport, including adiabatic cooling/heating, adiabatic focusing, pitch-angle scattering, convection with the solar wind, and streaming. Subsequent work will incorporate the effects of perpendicular diffusion and particle drifts. The simulations were concluded at 9.6 hours from the onset of the event at the Sun for all events, focusing on modeling their initial stages.

We used a combination of telescopic observations and dynamic physical models to simulate the acceleration of SEPs in global coronal shock events. We first observed off-limb CBFs and studied their interaction with the coronal plasma using synoptic MHD simulations. Based on these observations and simulations, we then employed an analytical DSA model to simulate the SEP acceleration. The simulated fluxes obtained from the DSA model were used as time-dependent inner boundary conditions for modeling the particle transport to 1 AU. This approach allowed us to study the early-stage acceleration and transport of SEPs from the Sun to 1 AU.

The criteria used to select the events for analysis in the study of the SPREAdFAST framework were as follows:

1. Proton events in the energy range of 17-22 MeV observed by the SOHO/ERNE instrument from 2010 to 2017 were initially identified.
2. Events without identified flares and coronal mass ejections (CMEs) and without EUV waves preceding the SEP event were excluded.
3. Events without EUV waves or no EUV data, even if they had identified flares/CMEs, were also excluded.
4. Uncertain EUV waves that were not relevant to the specific solar eruption were dropped.
5. Events with measurable near-limb or off-limb Coronal Bright Fronts (CBFs) that could be analyzed with the SPREAdFAST framework were selected.

In total, 62 events met the selection criteria and were included in the analysis.

The kinematics of CBFs are characterized using the methodology of the CASHeW framework. This framework estimates the CBF kinematics by following the leading edge of the front on consecutive images. It calculates the kinematics of the front, peak, and back edge of the CBFs over time, allowing for the estimation of their time-dependent mean intensity and thickness. The kinematics are determined using time-height maps (J-maps) generated with the CASHeW code for each event. The radial and lateral wave front positions are measured in these J-maps, providing information on the radial and lateral positions, speeds, accelerations, mean wave intensities, and wave thickness of the CBFs.

The methodology used to characterize the kinematics of CBFs is based on the CASHeW framework. This framework involves analyzing observations from the AIA instrument on board the SDO. The kinematics of CBFs are determined by tracking the leading edge of the front on consecutive images. Time-height maps, also known as J-maps, are created by stacking columns of pixels in a desired direction from a solar image. The shape of the track on these J-maps depends on the direction and speed of the CBF. The CASHeW code identifies the radial and lateral wave front positions over time in the J-maps, allowing for the estimation of the CBF kinematics, including speeds, accelerations, mean wave intensities, and wave thickness. A three-dimensional geometric model, known as the Synthetic Shock Model (S2M), is then created based on the measured front positions, which describes the shock surface at regular intervals. This model is propagated through the solar corona using a synoptic coronal MHD model, providing information on the relevant parameters for coronal shock acceleration of SEPs.

In the SPREAdFAST DSA model, the shock-crossing field lines are modeled by dividing the shock surface into three regions: the *nose* of the shock model, which consists of model points on the spheroidal cap; and two flanks or zones, divided by a plane parallel to the Sun-Earth line. The plasma parameters at the points on these three surfaces are examined separately. The model calculates the proton acceleration along these shock-crossing field lines based on time-dependent estimates of shock speed, density jump ratio, magnetic field strength, and shock angle. The model solves for the coronal charged particle acceleration by large-scale CME-driven shocks and provides time-dependent distribution function spectra or fluxes as output.

The method used to compare the modeled and observed proton fluences is by analyzing scatter plots of the fitted power indices of the proton fluences from the EPREM model and the ERNE observations. The power law indices are compared between the two sets, and the onset hours for the proton events are also compared. The comparison helps evaluate the performance of the modeling framework in predicting the proton fluxes. Additionally, histograms and Mean Squared Logarithmic Error (MSLE) are used to assess the agreement between the modeled and observed fluence spectra and onset times.

4.2.6 Results and Discussions

The study's findings have important implications for understanding and predicting solar particle radiation. By modeling the dynamics of shock waves and particle acceleration in the solar corona, the study provides valuable insights into the factors that influence the efficiency of particle acceleration. The results highlight the significant role of the coronal environment in shaping the acceleration and transport of SEPs from the Sun to Earth. One key implication is that the overlying coronal structure and the particle energy play a crucial role in determining where SEPs are produced during CME-driven shock and compressive waves. The study shows that the large gradients in plasma parameters between neighboring streamers, quiet-Sun areas, and coronal holes lead to continuous changes in the acceleration process. This knowledge can help improve our understanding of the spatial distribution of SEPs and their energy dependence. Furthermore, the study's findings contribute to the development of physics-based models for forecasting SEP events. The SPREAdFAST framework used in the study demonstrates the potential for accurately simulating the evolution of SEPs from the Sun to 1 AU. This framework can be further refined and utilized for early-stage forecasting of SEP events, providing valuable information for space weather prediction and mitigation efforts. Overall, the study enhances our understanding of the complex processes involved in solar particle radiation and provides a foundation for improving our ability to predict and mitigate the impacts of these events on space weather.

The main discrepancies between the modeled and observed fluxes in the study are primarily seen at higher energies. Above 15 MeV, there is a discrepancy in the time profile, with the observed proton fluxes rising approximately 1 hour before the simulation. Additionally, the fluxes at the highest energies show the most disagreement, mainly due to the slope of the increase and the onset times. These discrepancies indicate the need for further improvements and refinements in the modeling framework to better match the observations.

4.2.7 Conclusions

This study represents a pioneering multi-event exploration, presenting a comprehensive examination of Sun-to-1 AU SEP simulations grounded in detailed coronal diffusive shock acceleration and interplanetary propagation—a unique endeavor within the current body of knowledge. Investigating 62 distinct eruptive events, each characterized by an EUV CBF and notable enhancements in 1 AU proton fluxes, our approach utilized the SPREAdFAST framework. This framework, originally designed for forecasting early-stage SEP events, demonstrated its efficacy in the analysis of this extensive event set.

The input spectra for coronal proton acceleration were derived from quiet-time suprathermal spectra averaged over one to three days preceding each event. These averages were then scaled back to the Sun, assuming a simple inverse square proportionality to heliospheric distance. Utilizing an energy-independent mean free path for coronal proton acceleration in the diffusive shock acceleration model, we observed significant influences of solar corona conditions on proton acceleration. The gradients in plasma parameters among neighboring streamers, quiet-Sun regions, and coronal holes induced continuous changes in the θ_{BN} angle along the shock wave surface, as well as in density and density enhancements.

The results from the DSA model, serving as time-dependent input to the interplanetary transport EPREM model, were compared with in situ observations by the SOHO/ERNE instrument at 1 AU. The overall alignment between model predictions and observations is promising, affirming the efficiency and accuracy of the SPREAdFAST model chain. Nevertheless, discrepancies, particularly at the highest energies, were observed, mainly attributed to variations in the slope of increase and onset times.

To address these discrepancies and enhance model precision, future work will delve into more realistic modeling of events. This includes exploring time-dependent injection of source spectra at the inner boundary of the EPREM simulation to better match observed decay rates. Acknowledging the importance of three-dimensional transport effects in realistic interplanetary magnetic fields, perpendicular transport will be incorporated in subsequent investigations. Furthermore, introducing location-dependent output to accommodate varying connectivity between the source and observer will be explored.

The integration of geometric shock models with existing and novel observations of CME evolution in the middle corona is anticipated to reduce uncertainties in the results. Ongoing efforts involve comparing near-Sun in situ observations of quiet-time suprathermal populations from the Parker Solar Probe and Solar Orbiter with 1 au fluxes, aiming to refine the estimation of input spectra. This holistic approach contributes to advancing our understanding of SEP dynamics, paving the way for more accurate modeling and forecasting capabilities in the realm of solar-terrestrial physics.

4.3 Solar Proton Flux Forecasting with Deep Learning Models

4.3.1 Data preparation

In this section, I describe the physical quantities, the types of inputs and their sources, as well as the outputs I am forecasting. Some of the technical terms used in this study are explained further in the appendices.

In order to capture the variability of solar activity, which modulates the SEP flux, I selected input physical quantities that describe both the interplanetary medium and solar activity. These input features can be categorized into two groups: remote signatures and in-situ measurements. The remote signatures consist of the F10.7 index, as well as the long-wavelength (X_L) and short-wavelength (X_S) x-ray fluxes. The F10.7 index represents the flux of solar radio emission at a wavelength of 10.7 cm, measured in solar flux units (sfu). To obtain the x-ray fluxes, I utilized 1- and 5-minute averaged data from the GOES database², specifically at long wavelengths (1 - 8 Å) and short wavelengths (0.5 - 4.0 Å).

The in-situ measurements encompass the near-Earth solar wind magnetic field and plasma parameters. These include the solar wind speed (in km s⁻¹), average IMF strength (in nT), and the integral SEP fluxes at three energy channels: >10, >30, and >60 MeV, which correspond to the GOES channels (in 1/cm² sec ster). These SEP fluxes were obtained from multiple spacecraft stationed at the first Lagrange point (L1) throughout the study period. In particular, the IMF and plasma data in the OMNI database are obtained from the IMP, Wind, and ACE missions, while the energetic particle fluxes are obtained from the IMP and GOES spacecraft³.

To ensure a comprehensive dataset, I acquired hourly-averaged data covering a timeframe from December 1976 to July 2019, which spans the past four solar cycles. These data were sourced from the Space Physics Data Facility (SPDF) OMNIWeb database⁴, hosted by the Goddard Space Flight Center. This database provides a wealth of information, including integral proton fluxes, as well as an extensive range of solar wind plasma and magnetic field parameters. Lastly, the daily data on sunspot numbers were obtained from the Sunspot Index and Long-term Solar Observations (SILSO) archive⁵, maintained by the World Data Center.

Figure 4.1 shows a plot for the timeseries data of all features. The top 3 panels are the logarithms of the SEP integral flux at the 3 energy channels (log_PF10, log_PF30, and log_PF60), then the sunspot number, the F10.7 index (F10_idx), the logarithms of the x-ray fluxes (log_Xs and log_Xl), the solar wind speed (Vsw), and the average magnitude of the IMF (avg_IMF). Throughout this paper, I adopt the convention that "log" refers to the common logarithm with a base of 10. The gray shades refer to the timespan of solar cycles. The blue, orange, and gold colors refer to the training, validation, and test sets, respectively. The data split method will be explained shortly.

Since the input SEP data have been compiled from various spacecraft, it may have artifacts even after processing. In particular, there are occasional jumps in the background level. There are also several day-long gaps in the OMNI solar wind parameters from the early 1980s to mid-1990s where only IMP 8 data are available and this spacecraft spent part of each orbit in the magnetosphere. I am reasonably confident that these issues do not influence the overall analysis significantly.

In deep learning applications, the dataset is split into 3 sets; namely the training set, the validation set, and the test set. The training set is usually the largest chunk of data that is used to fit the model. The validation set is a smaller chunk of data used to fine-tune the model and evaluate its accuracy to ensure it is unbiased. The test set is the out-of-sample data exclusively used to assess the final model when performing on unseen data (Ripley 1996).

After inspecting the correlation between the solar wind indices and the SEP integral fluxes in the OMNIWeb database, I chose the top-correlated features with the SEP flux. The correlations were made

²GOES SXR Database: <https://satdat.ngdc.noaa.gov/sem/goes/data/avg/>

³OMNIWeb Data Documentation: https://omniweb.gsfc.nasa.gov/html/ow_data.html

⁴OMNI Database: <https://omniweb.gsfc.nasa.gov>

⁵Sunspot Number Dataset: <https://www.sidc.be/silso/home>

between the SEP fluxes and the individual parameters. Hence I took only timeseries of logarithms of the protons' integral flux at 3 energy channels (>10 , >30 , and >60 MeV), the timeseries of logarithm of the X-ray fluxes, the F10.7 index, the sunspot number, the solar wind speed, and the average strength of the IMF as input parameters to our model. The log of the SEP flux was used across the whole study. The correlation matrices for the training, validation, and test sets are shown in Figure 4.2. The X-ray and proton fluxes were converted into the logarithmic form because it was more convenient than the original form of data since the time series data were mostly quiet and had numerous sharp spikes, which correspond to solar events. Based on a previous experience with NNs (Nedal et al. 2019), I found that training separate models for each target (output) feature can lead to better results. This is because a dedicated model for each output feature can more easily learn the interrelationships between input features and make more accurate predictions. Therefore, in our current study, I trained 3 separate models, each one targeting the logarithm of the protons integral flux at a specific energy channel.

In order to ensure consistency across all features, all durations of the time series data of the physical quantities were matched to be within the same time range. Subsequently, the dataset was resampled to obtain daily averaged data, resulting in a significant reduction of the dataset size by a factor of 24. This reduction facilitated expeditious training and yielded prompt results.

There were missing data values in the original dataset; for the B_{avg} ($\sim 10.7\%$), V_{sw} ($\sim 10.5\%$), F10.7-index ($\sim 0.08\%$), short-band x-ray flux ($\sim 8\%$), long-band x-ray flux ($\sim 9.8\%$), and proton fluxes ($\sim 4.3\%$). The data gaps were linearly interpolated.

In timeseries forecasting, it is a common practice to take a continuous set of data points from the main dataset to be the validation set and another smaller chunk of data to be the test set, for instance in Pala & Atici (2019); Benson et al. (2020); ?; Zhu et al. (2022). From our experiments, I got descent results when I applied the same data split method, but the results were a bit biased toward the end of the solar cycle 24 and the testing set was biased towards a quiet period. So, I adopted the 9-2-1 strategy, that is taking from each year 9 months to be added in the training set, 2 months to be added in the validation set, and 1 month to be added in the test set. This is applied over the ~ 43 years of data (Fig. 4.1), which yields 74.29% of the data for the training set, 16.2% for the validation set, and 9.51% for the testing set. By doing so, I eliminated the need to do cross-validation and hence, made the training more efficient. It is worth to mention that the timeseries data must not be shuffled as that will break temporal and logical order of measurements, which must be maintained.

4.3.2 Method

In this section, I introduce the data analysis methods used in this work. I start with explaining the model selection phase, followed by a discussion of the bidirectional long-short-term memory (BiLSTM) neural network architecture. The technical terminologies are described in the appendices.

The Bi-LSTM Model

Recurrent neural networks (RNNs) that support processing input sequences both forward and backward are known as Bidirectional Long Short-Term Memory (BiLSTM) neural networks (Schuster & Paliwal 1997). Regular RNNs (Hochreiter & Schmidhuber 1997; Kolen & Kremer 2001) depend on the prior hidden state and the current input to determine the output at a given time. The output of a BiLSTM network, on the other hand, is dependent on the input at a given moment as well as the previous and future hidden states. As a result, the network is able to make predictions using contexts from the past as well as the future. Hence, accuracy is improving. Each BiLSTM layer consists of two LSTM layers; a forward layer that processes the input sequences from the past to future, and a backward layer that processes the input sequences from the future to the past, as illustrated in Figure 4.3, to capture information from both past and future contexts. The output from each layer is concatenated and fed to the next layer, which can be another BiLSTM layer or a fully connected layer for final prediction.

BiLSTM networks are advantageous than traditional LSTM networks in a variety of aspects (Graves & Schmidhuber 2005; Ihianle et al. 2020; Alharbi & Csala 2021). First, as I demonstrate in this study, they are excellent for tasks like timeseries forecasting, as well as speech recognition and language translation (Wöllmer et al. 2013; Graves & Jaitly 2014; Sundermeyer et al. 2014; Huang et al. 2018; Nammou et al. 2022) because they can capture long-term dependencies in the input sequence in both forward and backward directions. Second, unlike feedforward networks, BiLSTM networks do not demand fixed-length input sequences, thus being able to handle variable-length sequences better. Furthermore, by taking into account both past and future contexts, BiLSTM networks can handle noisy data. However, BiLSTM networks are computationally more expensive than regular LSTM networks due to the need

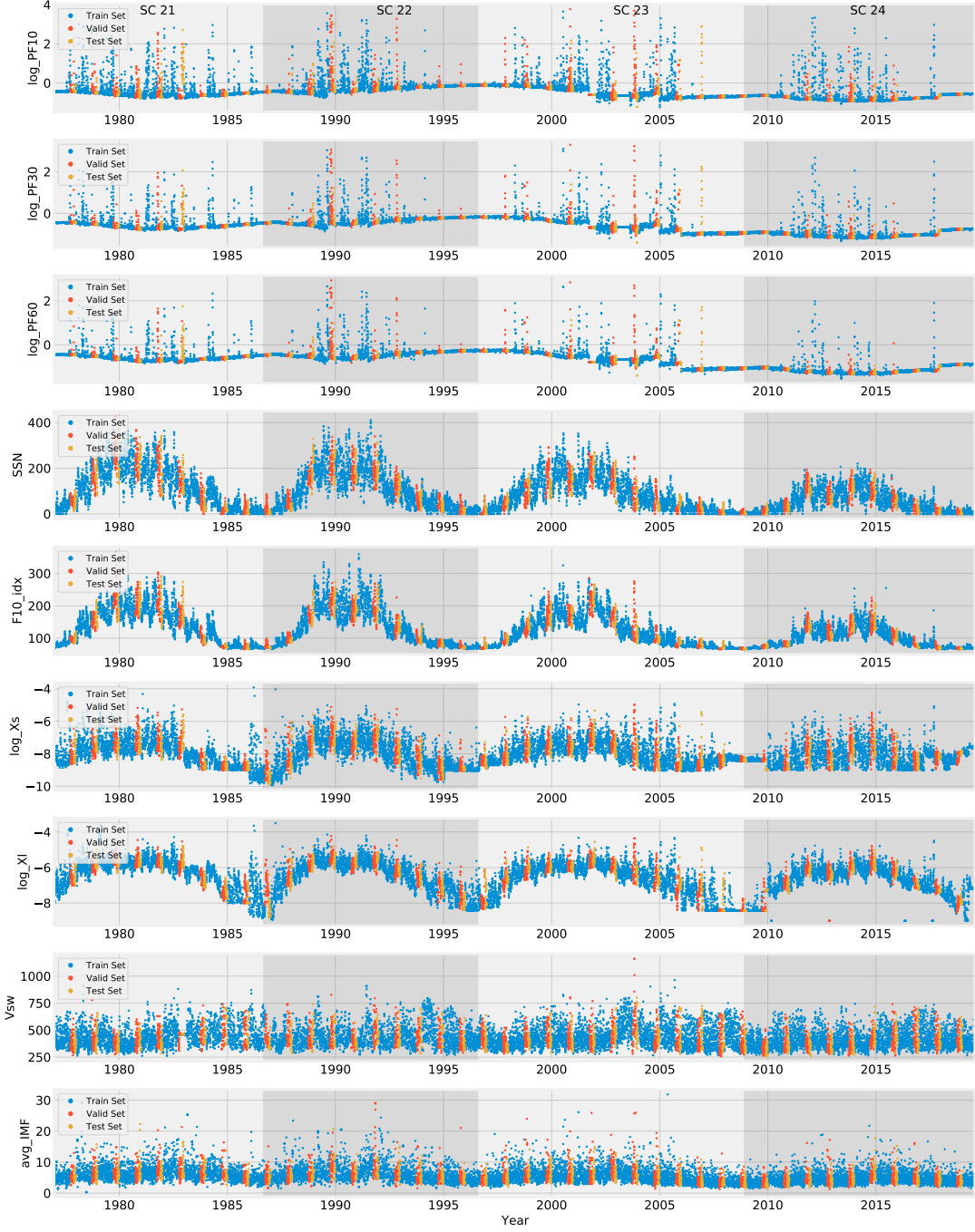


Figure 4.1: Data splitting for all input features, showing the training, validation, and testing sets. Daily data from 1976-12-25 00:00 to 2019-07-30 00:00. The gray shading labels the solar cycles from SC21 to SC24.

for processing the input sequence in both directions. They also have a higher number of parameters and require more training data to achieve good performance.

The final dataset has 7 features, including the target feature, from December 25th 1976 to July 30th 2019, with a total of 15,558 samples (number of days). The training set has 11,558 samples, the validation set has 2,520 samples, and the test set has 1,480 samples.

The input horizon of 270 steps (30 days \times 9 months) was used. A data batch size of 30 was used, which is the number of samples processed that result in one update to the model's weights (Appendix A.4.1). The model consists of 4 BiLSTM layers with 64 neurons each, and an output dense layer with 3 neurons, representing the output forecasting horizon. The total number of trainable parameters is 333,699. The number of training epochs was set to 50 because from experiments, the model stopped improving

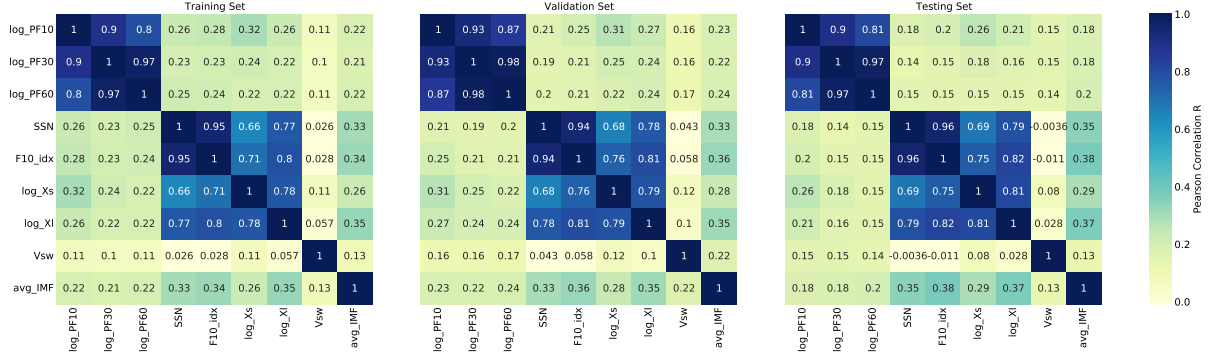


Figure 4.2: Correlation matrices show the correlation between the features in the training, validation, and test sets.

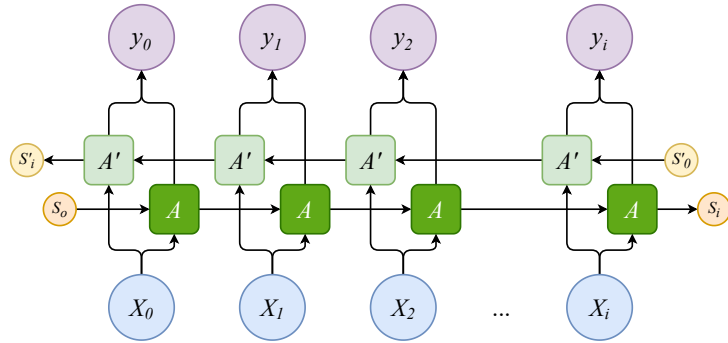


Figure 4.3: Architecture of a single BiLSTM layer. The blue circles at the bottom labeled by $(x_0, x_1, x_2, \dots, x_i)$ are the input data values at multiple time steps. The purple circles, on the other hand, are the output data values at multiple time steps labeled by $(y_0, y_1, y_2, \dots, y_i)$. The dark green and light green boxes are the activation units of the forward layer and the backward layer, respectively. The orange and yellow circles are the hidden states at the forward layer and the backward layer, respectively. Both the forward and backward layers compose a single hidden BiLSTM layer. The figure is adopted from Olah (2015)

remarkably after almost 50 epochs. Thus, there was no need to waste time and computational resources to train the model for more than 50 epochs.

The *ModelCheckpoint* callback function was used to register the model version with the minimal validation loss. The *EarlyStopping* callback function was used to halt the model run when detecting overfitting, with a *patience* parameter of 7. *ReduceLROnPlateau* callback function was used to reduce the learning rate when the validation loss stops improving, with a *patience* parameter of 5, a reduction factor of 0.1 and minimal learning rate of $1e^{-6}$.

Model Selection

To determine the most suitable model for our objective and provide justifiable reasons, I conducted the following analysis. First I examined the naive (persistence) model, which is very simplistic and assumes that the timeseries values will remain constant in the future. In other words, it assumes that the future value will be the same as the most recent historical value. That was the baseline. Next I examined the moving-average model, which calculates the future values based on the average value of historical data within a specific time widow. This gives a little bit lower error.



Figure 4.4: Illustration of the sliding window technique for a sample of 10 timesteps, where each number denotes a distinct time step. As an example here, the input horizon (blue color) length is 4 timesteps and the output horizon length is 3 timesteps. The input window slides 1 time step at a time across the entire data sequence to generate 4 distinct input and forecast horizon pairs. The purple, orange, and green colors of the output horizon represent 1-day, 2-day, and 3-day ahead forecasting, respectively. The timesteps of 1-day ahead forecasting across the data sequences are then concatenated into a single timeseries list that is called 1-day ahead prediction. The same for 2-day and 3-day ahead.

After that, I went towards the machine learning (ML)-based models. For all the ML models, I chose the Adaptive moment estimation (Adam) optimizer (Kingma & Ba 2015) as the optimization algorithm due to its minimal memory requirements and high computational efficiency as it is well-suited for applications that involve large number of parameters or large datasets. As a rule of thumb, I set the optimizer's learning rate to be 0.001 as it is usually recommended (?).

In order to prepare the data in a readable format to the ML models, I created a windowed dataset with an input horizon of 365 steps representing 1 year of data and an output horizon of 3 steps representing the forecast window of three days. I call this windowing method as Multi-Input Multiple Output (MIMO) strategy, in which the entire output sequence is predicted in one shot. The MIMO strategy adopts the sliding window method that was mentioned in Benson et al. (2020) in which each sequence is shifted by one step with respect to the previous sequence until reaching the end of the available data (Fig. 4.4). This approach minimized the imbalance of active days, with high SEP fluxes, and quiet days.

After experiments with different loss functions and evaluate their performance on our dataset, I chose the Huber function A.9a as the loss function and the Mean Absolute Error (MAE) is used as the metric function to monitor the model performance. I used the Huber function because it is robust and combines the advantages of both Mean Squared Error (MSE) and MAE loss functions. It is less sensitive to outliers than MSE, while still being differentiable and providing gradients, unlike MAE. Since our data is noisy and contains outliers that may negatively impact the model's performance, the Huber loss function is a good choice.

I examined various neural network models to determine the optimal architecture for our task. Initially, I started with a simple linear model comprising of a single layer with a single neuron. However, this model did not yield satisfactory results. I then explored a dense ML model consisting of two hidden layers, each with 32 neurons and a *ReLU* activation function. Next, I experimented with a simple RNN model with the same number of hidden layers and neurons. To find the optimal learning rate, I utilized the

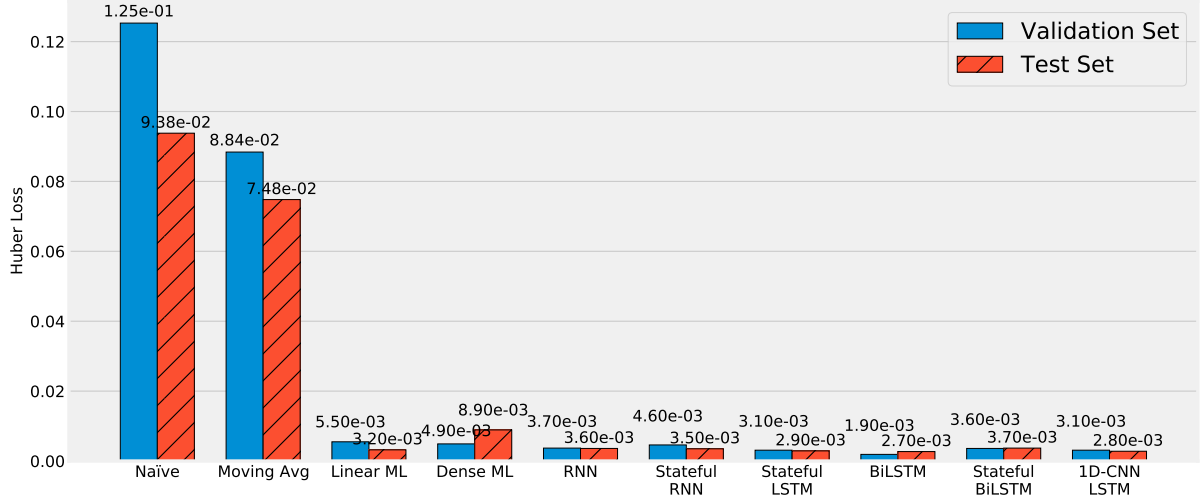


Figure 4.5: Benchmarking of 10 models, shows the Huber loss for the validation and test sets.

LearningRateScheduler callback function and discovered that a rate of $1.58e^{-4}$ under the basic settings minimized the loss. I proceeded to examine stateful versions of RNN, LSTM, and BiLSTM models with three hidden layers, each with 32 neurons and a learning rate of $1.58e^{-4}$. In addition, I explored a hybrid model that consisted of a 1-dimensional convolutional layer with 32 filters, a kernel size of 5, and a *ReLU* activation function. I combined this with a two-hidden layer LSTM network with 32 neurons each and a learning rate of $1.58e^{-4}$. I experimented with *Dropout* layers but did not observe any significant improvement in the results. Finally, I evaluated a BiLSTM model with five hidden layers, 64 neurons each, and a learning rate of 0.001. Based on the evaluation of all the models on both the validation and test sets (Fig. 4.5 and Table A.2), I selected the BiLSTM model for further refinement. More details on the final model architecture and hyperparameters are explained in the Appendix A.5. Figure 4.5 presents a comparative analysis of the Huber loss within the validation and testing sets across the ten aforementioned models. I used several evaluation measures to assess our models since each metric provides valuable insights into the accuracy and performance of the forecasts (Appendix A.4.2), helping to identify areas for improvement and adjust the forecasting models accordingly.

4.3.3 Results and discussion

Long-term forecasting

The benchmarking in Figure 4.5 showed that, in general, the ML-based methods were not much different. On the other hand, the persistence model and moving average model resulted in the highest errors compared with the ML-based models, and their results were close to some extent. As I see, the BiLSTM model performed the best over both the validation and test sets compared with the other models.

I developed and trained 3 BiLSTM models to forecast the integral flux of SEP, one model per energy channels. After the training was completed, I evaluated the performance of the models from the loss curve (Fig. 4.6) using the Huber loss (the left panel) and the metric MAE (the middle panel). During the training, the learning rate was reduced multiple times via the *LearningRateScheduler* callback function (the right panel). The left panel quantifies the discrepancy between the model's predictions and the true values over time. It shows how the Huber loss function changes during the training iterations (Epochs) for the training and validation sets for the three energy channels so that each channel has one color. The middle panel shows how the model's metric MAE changes with training epochs. It is used to evaluate the performance of the trained model by measuring the average absolute difference between the model's predictions and the true values, providing a single numerical value that indicates the model's error at a given epoch. The right panel shows how the learning rate of the model's optimizer changes with epochs via the *LearningRateScheduler* callback function, which changes the learning rate based on a predefined schedule to improve training efficiency and convergence. The learning rate refers to the rate at which the model's parameters are updated during the training process. I noticed that at the epochs where the learning rate has changed, there were bumps in the loss curves across all the energy channels, which is expected. This highlights the boundaries within which the learning rate yields better performance.

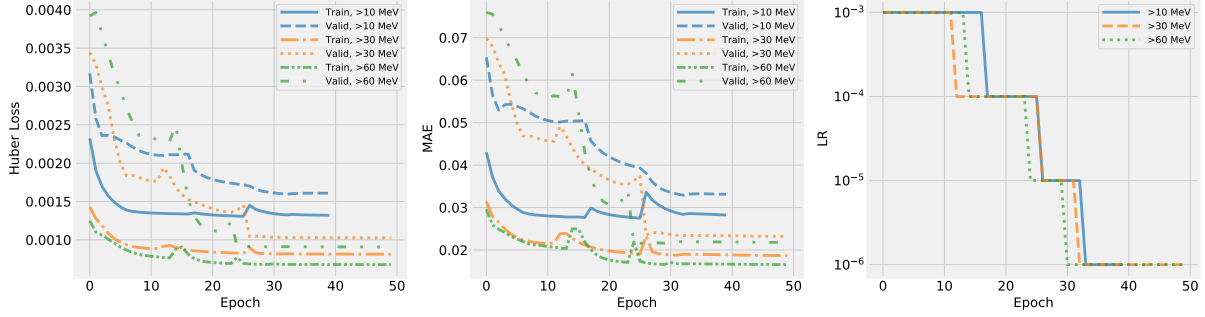


Figure 4.6: *Left Panel* - The Huber loss vs. the number of training epochs for the BiLSTM model for the validation and test sets, for the 3 energy channels. *Middle Panel* - The mean absolute error (MAE); the model’s metric vs. the number of training epochs. *Right Panel* - Shows how the learning rate of the Adam optimizer changes over the number of epochs.

From experimentation, I found that the batch size and the optimizer learning rate are the most important hyperparameters that have a strong influence on the overall model’s performance (Greff et al. 2016). In addition, adding *dropout* layers as well as varying the number of hidden layers and hidden neurons resulted in only marginal improvements to the final model performance, while substantially increasing training time and requiring greater computational resources.

The term *batch size* refers to the number of data sequences processed in one iteration during the training of a ML model (Goodfellow et al. 2016). Initially, a batch size of 64 was selected, however, I observed that the model produced better results when a batch size of 30 was used instead. This could be related to the Carrington rotation, which lasts for ~ 27 days. There were ~ 570 Carrington rotations between December 25th 1976 and July 30th 2019. Therefore, updating the model’s weights after every Carrington rotation could be a reasonable choice for improving its performance. Figure 4.7 shows how good the model predictions are (on the y-axis) compared with the observations of the validation set (on the x-axis). The blue, orange, and gold colors refer to 1-day, 2-day, and 3-day ahead predictions, respectively. The top panel is for the >10 MeV channel, the middle panel is for the >30 MeV channel, and the bottom panel is for the >60 MeV channel. The left column is for the entire validation set, while the right column is for the observations points ≥ 10 proton flux units (pfu). That is the threshold value of proton flux as measured by the National Oceanic and Atmospheric Administration (NOAA) GOES spacecraft to indicate severity of space weather events caused by SEP.

I found that, overall, the models performed very well. The R correlation was >0.9 for all points of the validation set across the forecasting windows for the 3 energy channels. The R correlation was >0.7 for the observations points ≥ 10 pfu as well. However, the correlation between the modeled data and the observations exhibited a decline as the forecast horizon increased, in accordance with the anticipated result. To confirm the validity of the models, I performed the same correlation analysis between the modeled data and the observations of the out-of-sample test set (Fig. 4.8), which was not given to the model. Again, I found a high correlation across the forecasting windows for the 3 energy channels. The points were more dispersed between 1 and 1.5 on the x-axis, which reflected in a bit lower correlation. This might be a limitation in the current version of the model between that range of SEP fluxes since the models underestimated the flux values within that range across all energy channels, possibly due to the relatively smaller training samples with fluxes above 10 pfu compared with the majority of the data.

In order to see the temporal variation of the correlation between the modeled data and the observations, I applied a rolling window of 90 steps (3 months \times 30 days/month = 1 season) that shows the seasonal variation of the correlation, as shown in Figure 4.9. Here, I show only the 1-day ahead predictions for the test set, for the 3 energy channels. I observe drops in the correlation factor synchronized with the transition between solar cycles (e.g., particularly between ~ 1995 -2000, which represents the declining phase of the solar cycle 22 and the rising phase of the solar cycle 23). This could be related to the fact that the low SEP fluxes during quiet times are more random and thus more difficult to forecast (Feynman et al. 1990; Gabriel et al. 1990; Rodriguez et al. 2010; Xapsos et al. 2012).

During periods of low solar activity, the forecasting of low SEP fluxes becomes more challenging due to their increased randomness. This difficulty arises from the reduced occurrence of conventional SEP drivers, such as solar flares and CMEs. Studies have suggested that the most significant solar eruptions tend to happen shortly before or after the solar cycle reaches its maximum (Švestka 1995).

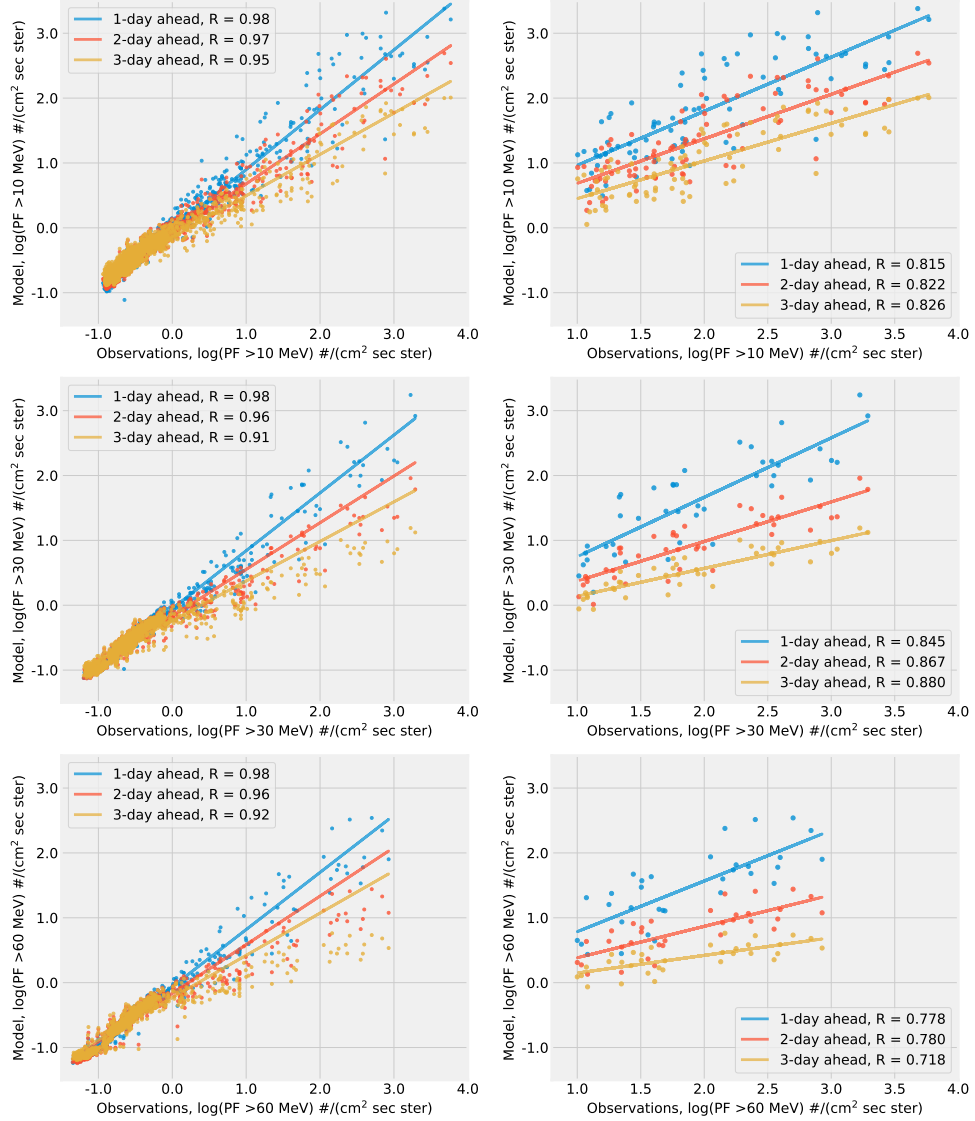


Figure 4.7: Correlation between the model predictions and observations for 1-day, 2-day, and 3-day ahead for >10 MeV (top panel), >30 MeV (middle panel), and >60 MeV (bottom panel). The panels in the left column represent all the points of the validation set, those in the right column represent all the observations points with daily mean flux ≥ 10 pfu.

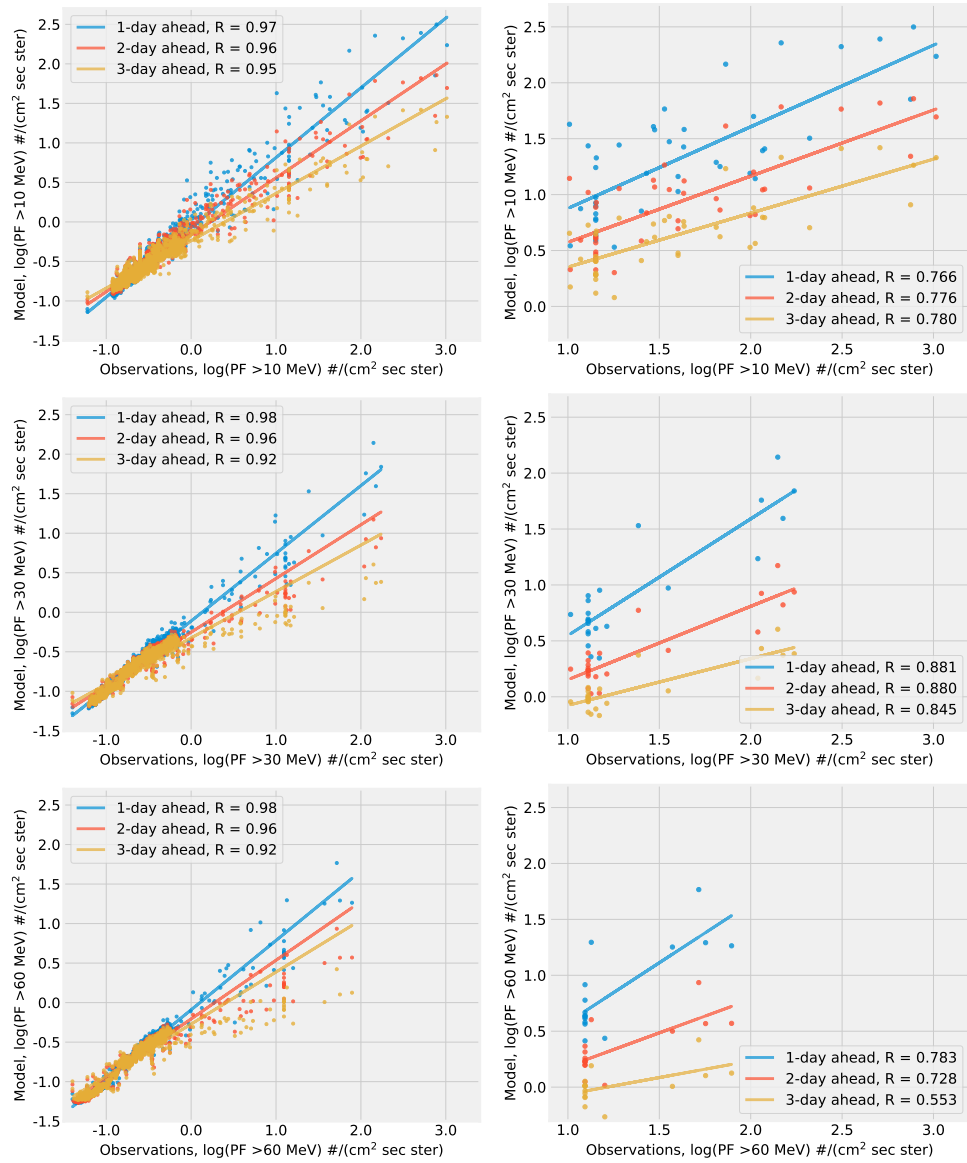


Figure 4.8: Same as Figure 4.7 but for the test set.

Additionally, sporadic increases in solar activity have been observed (Kane 2011), which might contribute to the diminished correlations observed in our research. There is clearly some factor that is influencing the correlation during certain periods where there are no or only weak SEP events. However, it is not obvious which physical phenomena are the cause rather than, for instance, some artifact of the data. Understanding the interplay between these factors and their influence on SEP fluxes during periods of reduced solar activity remains a critical area of research. It would be interesting to find what is reducing the correlations, thus more investigation is needed.

Overall, the modeled data was correlated the most with observations at >60 MeV, then the second rank was for the >10 MeV channel, and the third rank was for the >30 MeV channel. That could be related to the relatively larger extent of drops in correlation at the >30 MeV channel. The decline in correlation at the >30 MeV channel is consistent with the findings of Le & Zhang (2017). A summary of the performance results of the models for both the validation set and test set is presented in Table 4.1.

From the visual inspection of the test set examples (Fig. 4.10, 4.11, and 4.12), I found that the predicted onset time, the peak time, and end times of SEP events were highly correlated with those of the observations, which implies that the model captured the temporal variations, as well as the trends in SEP flux.

Table 4.1: Summary of the performance results of the models for the validation and test sets.

Validation Set									
	log PF >10 MeV			log PF >30 MeV			log PF >60 MeV		
Model Loss	0.0016			0.0010			0.0009		
Model Metric	0.0329			0.0232			0.0218		
	1-Day	2-Day	3-Day	1-Day	2-Day	3-Day	1-Day	2-Day	3-Day
MAE	0.061	0.091	0.125	0.053	0.079	0.098	0.052	0.069	0.086
MSE	0.013	0.028	0.054	0.010	0.031	0.055	0.009	0.027	0.047
RMSE	0.114	0.168	0.233	0.098	0.176	0.234	0.097	0.164	0.217
MAPE	22.156	28.104	34.721	13.039	18.590	22.735	10.036	13.994	16.731
Test Set									
	log PF >10 MeV			log PF >30 MeV			log PF >60 MeV		
Model Loss	0.0014			0.0011			0.0010		
Model Metric	0.0333			0.0283			0.0250		
	1-Day	2-Day	3-Day	1-Day	2-Day	3-Day	1-Day	2-Day	3-Day
MAE	0.072	0.099	0.125	0.053	0.088	0.107	0.045	0.066	0.081
MSE	0.015	0.030	0.050	0.009	0.029	0.048	0.007	0.020	0.034
RMSE	0.121	0.172	0.224	0.094	0.170	0.218	0.082	0.141	0.184
MAPE	30.135	37.498	48.139	20.599	34.300	40.803	12.358	20.504	25.305

To get further insight into the model's performance, I conducted an assessment of various skill scores, including True Positive (TP), True Negative (TN), False Positive (FP), and False Negative (FN). Additionally, skill score ratios such as Probability of Detection (POD), Probability of False Detection (POFD), False Alarm Rate (FAR), Critical Success Index (CSI), True Skill Statistic (TSS), and Heidke Skill Score (HSS). Detailed descriptions of these skill scores can be found in Appendix A.6. To extract individual SEP events from the test dataset, I implemented a threshold-based clustering algorithm. This algorithm uses the NOAA/SWPC warning threshold value of 10 pfu for the $E \geq 10$ MeV channel. Upon analysis, I identified the number of detected SEP events for each output forecasting window and calculated the skill scores (Table 4.2). In the true test set, I identified 12 SEP events.

The evaluation of the model revealed notable trends as the length of the output forecasting window increased. The POD and CSI exhibited a declining pattern, indicating a reduced ability of the model to accurately detect and capture positive events (SEP occurrences) as the forecasting horizon extended further into the future. This suggests that the model's performance in identifying and capturing true positive instances diminishes with longer forecasting windows. Moreover, the POFD demonstrated an increasing trend, indicating an elevated rate of false positive predictions as the forecasting horizon lengthened. The model's propensity to generate false alarms rose with the lengthening forecasting window, leading to incorrect identification of non-events as positive events. Consequently, the TSS and HSS exhibited decreasing values, signifying a deterioration in the model's overall skill in accurately capturing and distinguishing between positive and negative instances. Overall, our skill scores are comparable with those reported by previous studies (Table 4.3). Although the UMASEP model does better than ours

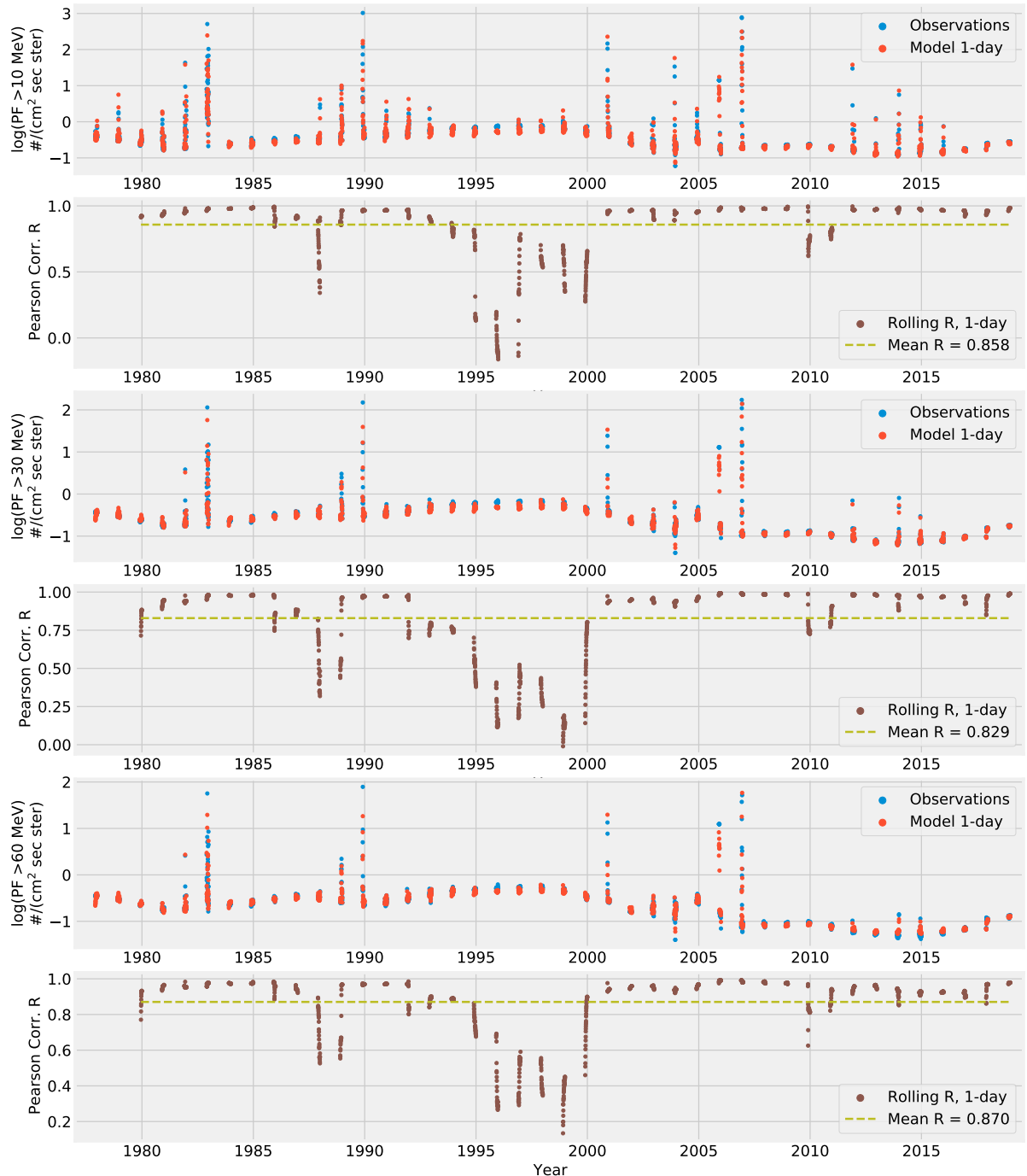


Figure 4.9: Comparison between the model outputs and observations of the test set for the 3 energy channels. In addition to the rolling-mean window correlation for 1-day ahead predictions.

(i.e., has a higher POD), our FAR is much lower, thus, making fewer false alarms than the UMASEP model.

Short-term forecasting

This work focuses on improving the prediction accuracy of the SEP integral flux, a critical aspect for mitigating the potential hazards posed by high-energy protons originating from the Sun. Expanding on previous work (Nedal et al. 2023a), the study utilizes a BiLSTM NN model, incorporating high-resolution hourly-averaged data for four standard integral GOES channels.

So far, the forecasting models, developed with 6-hour forecast window, integrate key input parameters

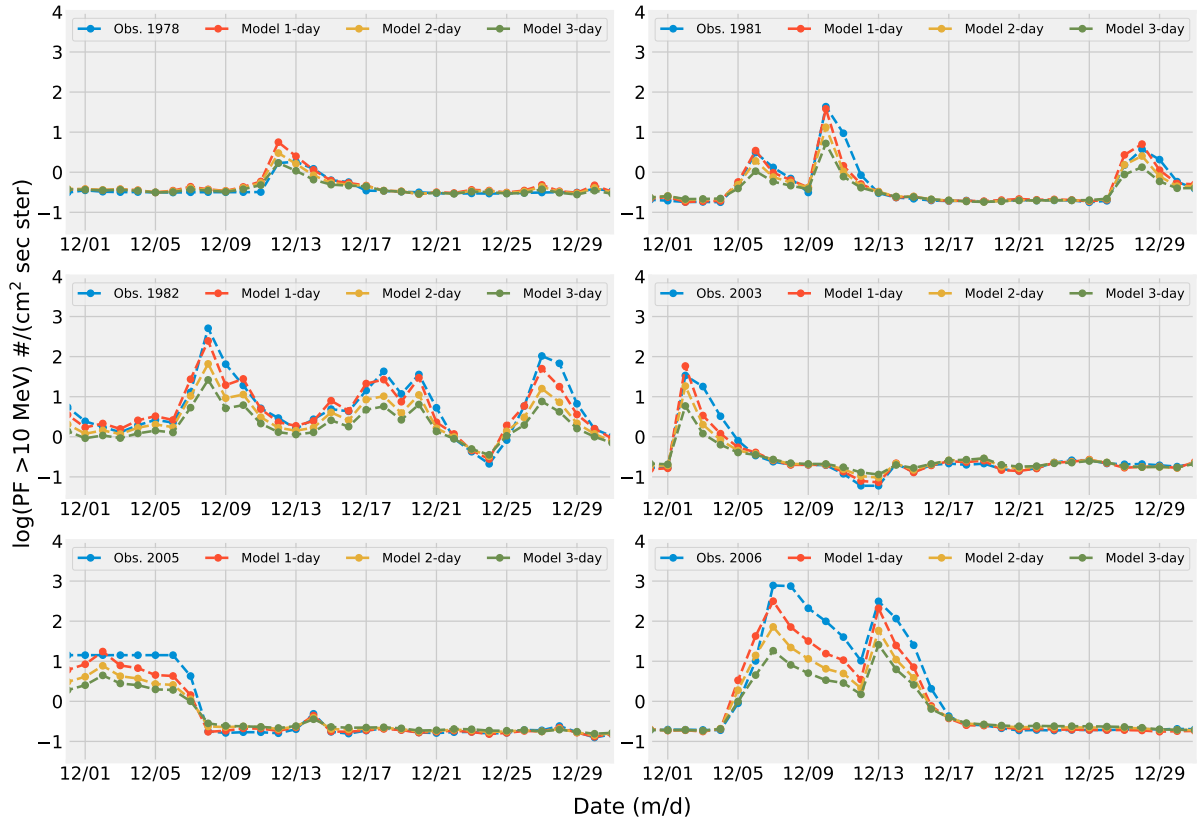


Figure 4.10: The model's forecasts for the out-of-sample testing set for the >10 MeV channel are shown at forecast horizons of 1 day, 2 days, and 3 days ahead, using samples of data from December in selected years mentioned in the top-left side of the plots.

Table 4.2: Confusion matrix for the energy channel ≥ 10 MeV predictions in the test set.

E >10 MeV	No. events	TP	TN	FP	FN
1-day ahead	15	21	1441	2	13
2-day ahead	13	14	1441	2	20
3-day ahead	5	5	1443	0	29

Table 4.3: Comparing the skill scores with previous models. The dashed entries mean the data is unavailable (Whitman et al. (2023) for more details).

Model	POD	FAR	TSS	HSS	POFD	CSI	Accuracy	Precision
Our BiLSTM model	0.618	0.087	0.531	0.732	0.001	0.583	0.99	0.913
	0.412	0.125	0.287	0.553	0.001	0.389	0.985	0.875
	0.147	0	0.147	0.252	0	0.147	0.980	1
UMASEP-10 (Núñez 2011)	0.822	0.219	—	—	—	—	—	—
PCA (Papaioannou et al. 2018)	0.587	0.245	—	0.65	—	—	—	—
SPARX (Dalla et al. 2017)	0.5	0.57	—	—	0.32	0.3	—	—
SPRINTS (Engell et al. 2017)	0.56	0.34	—	0.58	—	—	—	—
REleASE (Malandraki & Crosby 2018)	0.63	0.3	—	—	—	—	—	—

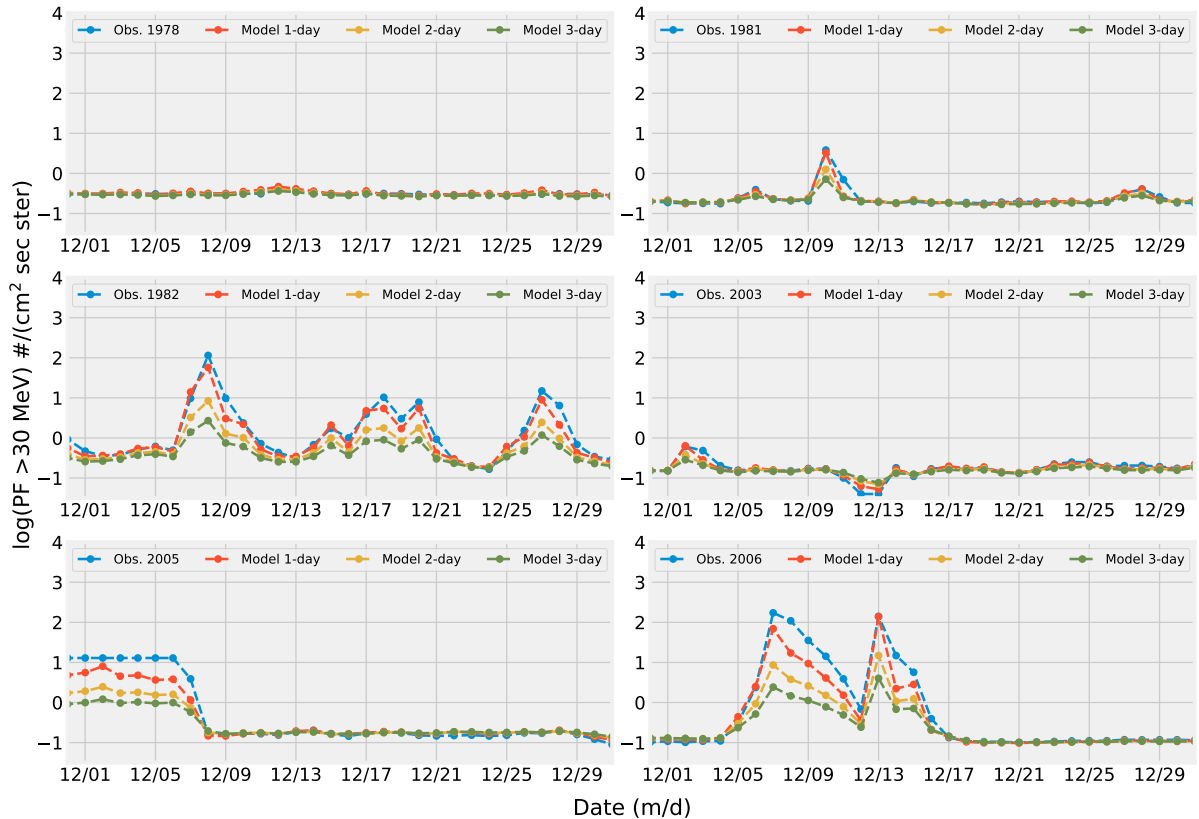


Figure 4.11: The model's forecasts for the out-of-sample testing set for the >30 MeV channel are shown at forecast horizons of 1 day, 2 days, and 3 days ahead, using samples of data from December in selected years mentioned in the top-left side of the plots.

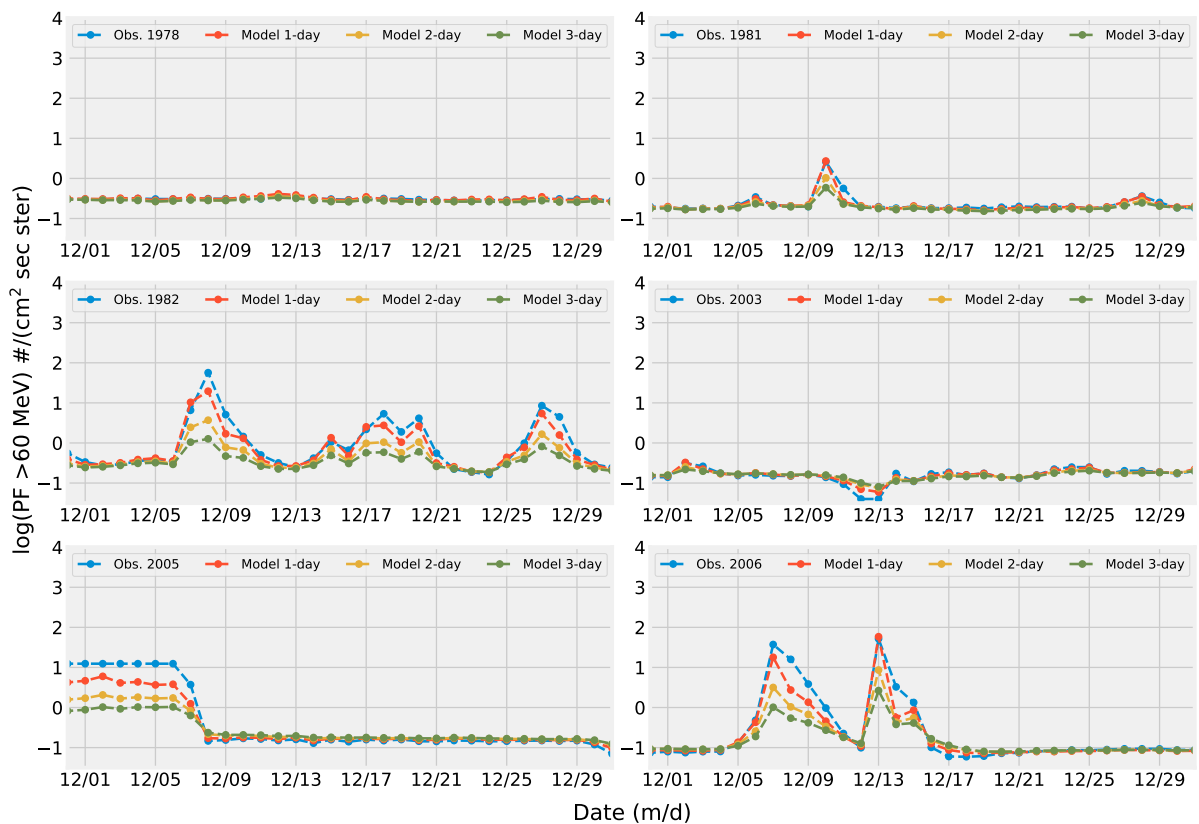


Figure 4.12: The model's forecasts for the out-of-sample testing set for the >60 MeV channel are shown at forecast horizons of 1 day, 2 days, and 3 days ahead, using samples of data from December in selected years mentioned in the top-left side of the plots.

such as the F10.7 index, sunspot number, x-ray flux, solar wind speed, and IP magnetic field strength, obtained from the OMNIWeb and GOES databases, spanning two solar cycles. Additional features, including the location of active regions obtained from the NOAA daily reports, are introduced to enhance predictive capabilities.

Rigorous evaluation involves independent out-of-sample testing, quantifying the impact of different features on prediction results, and benchmarking against existing approaches. This comprehensive approach contributes to advancing our ability to forecast SEP flux and better understand its implications for space weather.

I employed the 9-2-1 strategy to partition the data, allocating 9 months to the training set, 2 months to the validation set, and 1 month to the test set for each year. This approach spans the 23-year period from January 1996 to December 2018, resulting in 73.99% of the data for the training set, 16.44% for the validation set, and 9.57% for the testing set. To facilitate model training, we formatted the data using the MIMO strategy, predicting the entire output sequence in one iteration (Benson et al. 2020). The model forecasts the logarithm of the integral proton flux, encompassing various energy channels. However, for clarity in our poster, I specifically present results for the >10 MeV channel.

Figure 4.13 illustrates the temporal correlation across six future windows, with Figure 4.14 providing a visual representation through a scatter plot. Additionally, Figure 4.15 showcases the variation in prediction errors across these windows. For a more detailed examination, Figure 4.16 compares our model's 1-hour predictions with observations specifically for two sample SEP events in the >10 MeV channel.

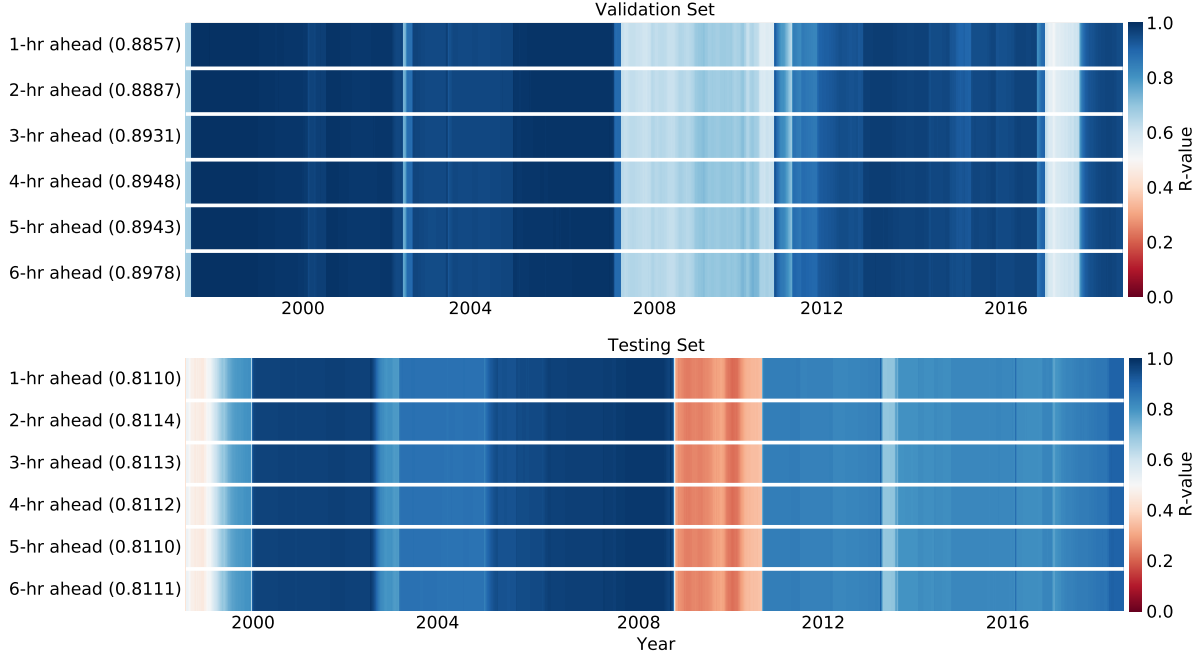


Figure 4.13: Temporal heatmap shows a comparison between the model outputs and observations for the rolling-mean window correlation of the integral >10 MeV proton flux at six predicting windows. The top panel represents the validation set and the bottom panel represents the testing set. The numbers on the y-axis are the mean R values.

Table 4.4: The MSE/MAE for the validation and test sets over six forecasting windows.

	1-hr	2-hr	3-hr	4-hr	5-hr	6-hr
Valid. Set	0.078/0.238	0.086/0.254	0.091/0.263	0.098/0.273	0.102/0.280	0.115/0.299
Test Set	0.012/0.080	0.012/0.079	0.012/0.080	0.011/0.079	0.011/0.080	0.011/0.079

Predicting SEPs remains a complex task due to their non-linear nature. This study, however, demonstrates promise by utilizing BiLSTM NNs. These models effectively captured the intricate patterns within SEP data, leading to successful hourly-averaged integral flux predictions across various energy channels. The model exhibited robust performance with low MSE values ranging from 0.011 to 0.012

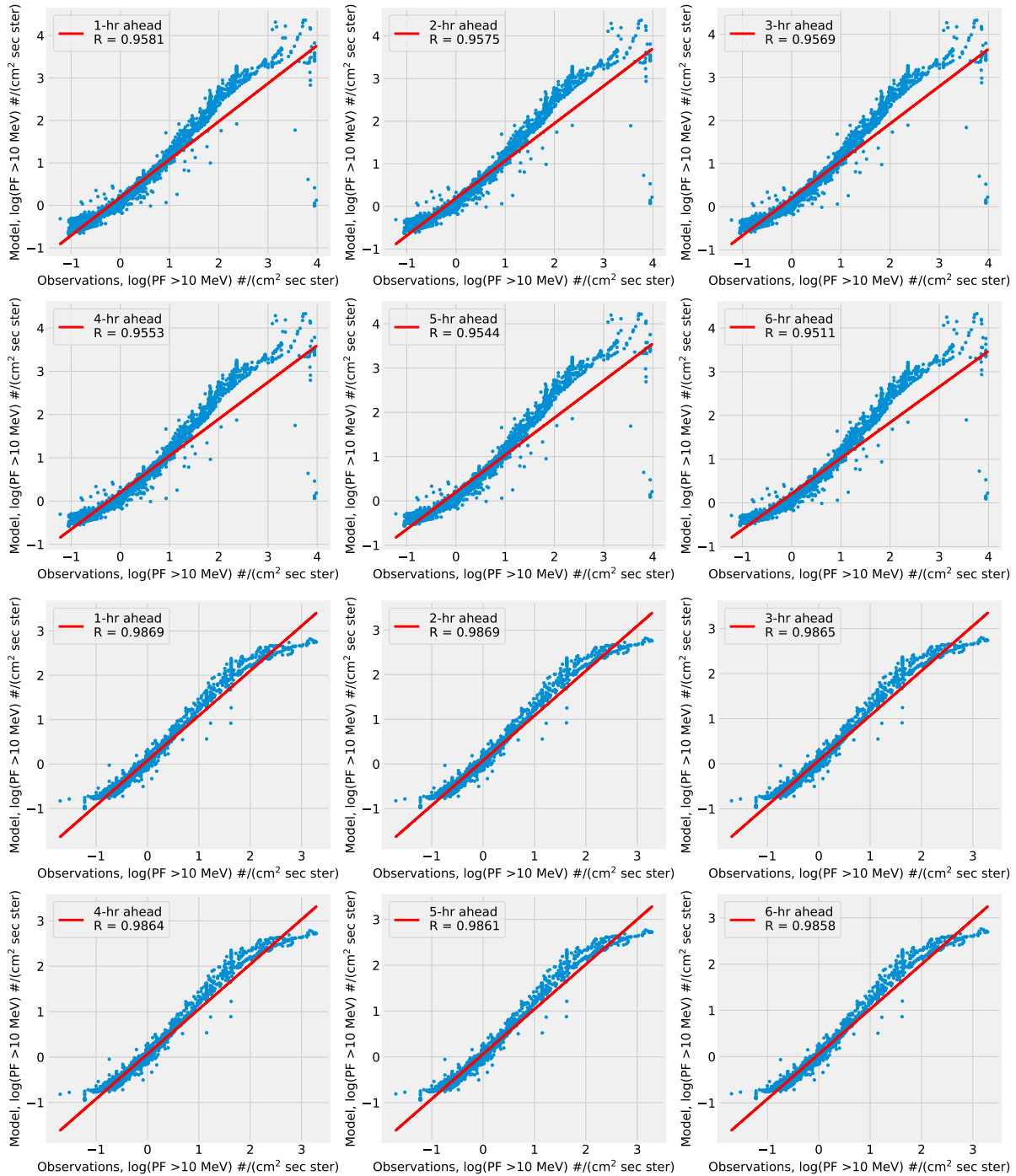


Figure 4.14: Correlation between model predictions and observations for the integral >10 MeV proton flux of the validation (top two rows) and testing (bottom two rows) sets.

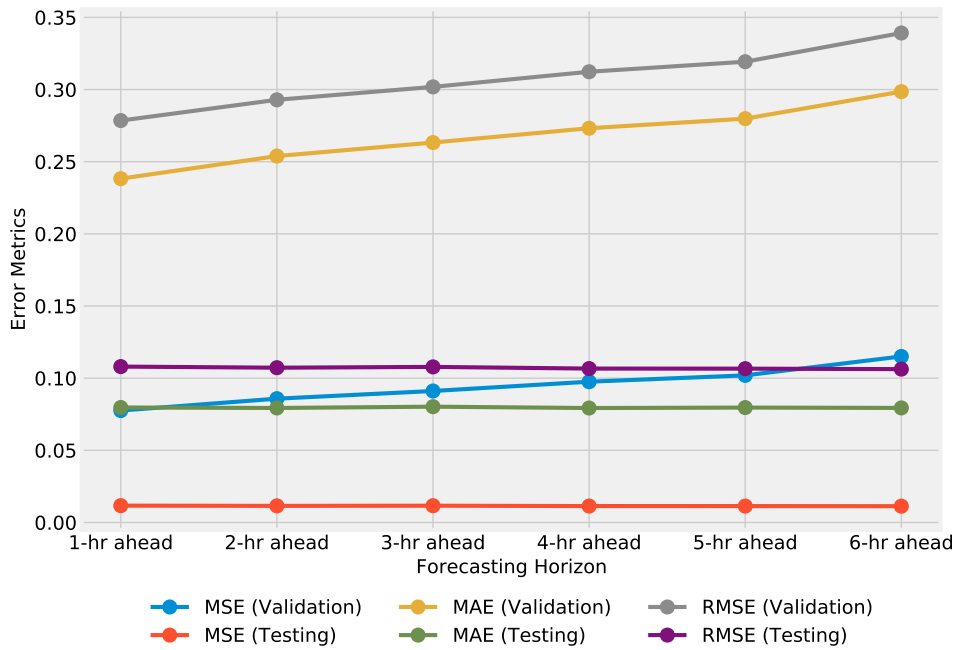


Figure 4.15: Correlation between model predictions and observations for the integral >10 MeV proton flux of the testing set.

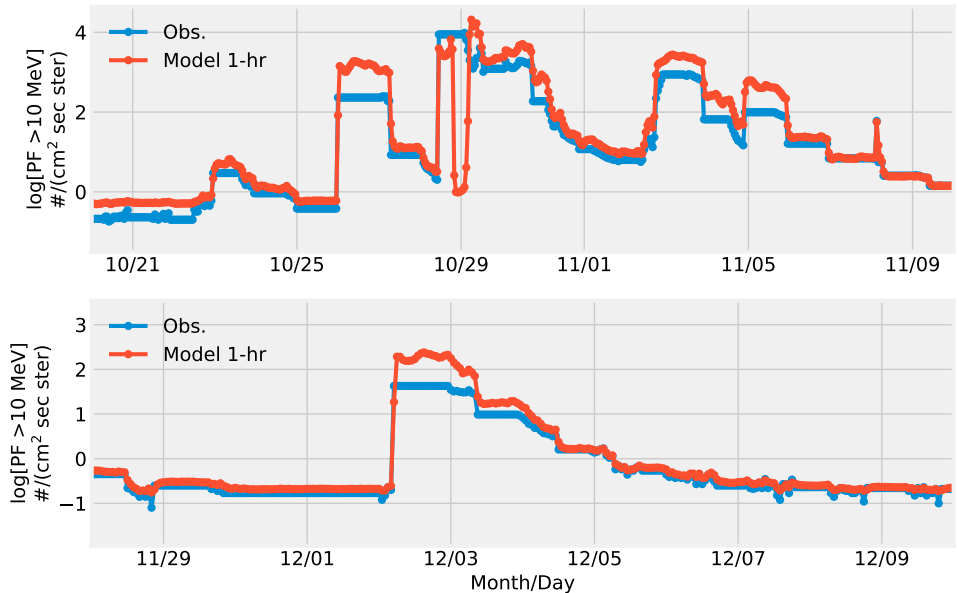


Figure 4.16: Comparison between the model's forecast and the observations for the integral >10 MeV proton flux at forecast horizon of 1 hour ahead. The top panel represents a sample of the validation set and the bottom panel represents a sample of the testing set.

in the test set. However, challenges remain, particularly during solar minimum phases, highlighting the inherent complexity of SEP prediction. Despite this, BiLSTM networks showcase significant potential for time series forecasting in heliophysics, especially when considering sequential data. Moving forward, we aim to optimize the model by fine-tuning parameters and benchmarking it against established methods. Additionally, extending the forecasting window and incorporating more energy channels with differential energy forecasting will offer a more comprehensive analysis and improve model interpretability.

4.3.4 Conclusions

Forecasting the SEP flux is a crucial task in heliophysics since it affects satellite operations, astronaut safety, and ground-based communication systems. It is a challenging task due to its non-linear, non-stationary, and complex nature. Machine learning techniques, particularly neural networks, have shown promising results in predicting SEP flux. In this study, I developed and trained BiLSTM neural network models to predict the daily-averaged integral flux of SEP at 1-day, 2-day, and 3-day ahead, for the energy channels >10 MeV, >30 MeV, and >60 MeV. I used a combination of solar and interplanetary magnetic field indices from the OMNIWeb database for the past 4 solar cycles as input to the model. I compared the models with baseline models and evaluated them using the Huber loss and the error metrics in Appendix A.4.2.

The data windowing method I used, based on the MIMO strategy, eliminates the need to feed the output forecast as input back into the model and that allows to do forecasting relatively far into the future while maintaining decent results (e.g., the MSE is ranging between 0.007 and 0.015 for 1-day forecasting in the test set, compared to an MSE of 0.236 for a persistence model. See Table 4.1). The results show that the model can make reasonably accurate predictions given the difficulty and complexity of the problem. The MSE was ranged between 0.009 and 0.055 for the validation set, and between 0.007 and 0.05 for the test set. The correlations between the observations and predictions were >0.9 for the validation and test sets (Fig. 4.7 and Fig. 4.8). Nevertheless, the mean temporal correlation was ~ 0.8 for the test set (Fig. 4.9). Although our models performed well, I observed a relatively large discrepancy between the predictions and the observations in the >30 MeV energy band.

The findings of this study underscore the challenges encountered by the forecasting model in accurately predicting SEP data over longer time periods. As the length of the output forecasting window increased, the model's ability to detect true positives and its overall skill in differentiating positive and negative instances diminished. Additionally, the model displayed an elevated rate of false negative predictions, indicating an increased tendency to generate misses as the forecasting horizon extended. These results highlight the importance of carefully considering the appropriate forecasting window length for SEP data to ensure the model's optimal performance. Our skill scores generally align with those from previous works (Table 4.3). There are variations in the metrics' values across different studies, highlighting the complexities and nuances associated with each study. Nevertheless, it is important to acknowledge that the statistical significance of the results in this study is limited due to data averaging. Future studies should consider incorporating hourly data, as this is likely to result in a greater number of identified events. The model can provide short-term predictions, which can be used to anticipate the behavior of the near-Earth space environment. These predictions have important implications for space weather forecasting, which is essential for protecting satellites, spacecraft, and astronauts from the adverse effects of solar storms.

Multiple techniques exist for identifying the optimal combination of hidden layers and neurons for a given task such as empirical methods, parametric methods, and the grid search cross-validation method, which I will explore in future work. The observed reduction in correlation necessitates further investigation to determine its origin, whether stemming from tangible causal factors or potential aberrations within the model or data. I plan to expand upon this work by performing short-term forecasting using hourly-averaged data. This extension will involve integrating additional relevant features such as the location and area of active regions and coronal holes on the Sun.

BiLSTM networks are particularly useful for tasks involving sequential data such as timeseries forecasting. Given their capacity to handle input sequences in both directions in time and capture long-term dependencies, they are valuable in a broad range of applications. Nonetheless, one should carefully consider their data requirements and computational complexity before adopting them. Our results emphasize that the use of deep learning models in forecasting tasks in heliophysics are promising and encouraging, as pointed out by Zhang et al. (2022b).

This work is a stepping stone towards real-time forecasting of SEP flux based on the public-available datasets. As an extension, I am currently working on developing a set of models that deliver near-real

time prediction of SEP fluxes at multiple energy bands, multiple forecasting windows, with hourly-averaged data resolution, with a more sophisticated model architecture, as well as more features that address the state of solar activity more comprehensively. I plan to extend the analysis to include more recent data from solar cycle 25, in order to improve the accuracy of the models. In conclusion, our study highlights the potential of using BiLSTM neural networks for forecasting SEP integral fluxes. Our models provide a promising approach for predicting the near-Earth space environment too, which is crucial for space weather forecasting and ensuring the safety of our space assets. Our findings contribute to the growing body of literature on the applications of deep learning techniques in heliophysics and space weather forecasting.

Chapter 5

Summary

In this final chapter, I present a comprehensive summary of the key findings from the dissertation's chapters, providing insights into the analysis of EUV waves, solar type III bursts, and SEP modeling and forecasting. The exploration of CBFs and the introduction of the Wavetrack tool have significantly contributed to our nuanced understanding of solar dynamics. As we look towards the future, the extension of the CBF dataset promises deeper insights into their kinematics, while the utilization of multi-wavelength observations from LOFAR, PSP, and Solar Orbiter aims to unravel the origin and evolution of energetic particles in the solar corona. Furthermore, the development of interpretable deep learning models, driven by higher resolution data, holds the key to advancing SEP forecasting capabilities. These future endeavors underscore the commitment to refining models, incorporating advanced data analysis techniques, and leveraging cutting-edge observational tools to unlock new dimensions in our comprehension of space weather phenomena.

Chapter 2 centered on the analysis of base-difference images obtained from the SDO/AIA instrument to investigate EUV waves. Key kinematic parameters, including shock speed, acceleration, intensity, and thickness, were computed. SOHO/LASCO measurements up to $17 R_{\odot}$ were incorporated to enhance the understanding of shock plasma parameters. Kinematic measurements played a pivotal role in generating 3D geometric models of wavefronts and informing plasma diagnostics using MHD and DEM models. The use of shock kinematic measurements facilitated the fitting of geometric spheroid surface models. Parametrized relationships between plasma parameters were explored to uncover connections and interdependencies. The study also introduced Wavetrack, an automated tool for identifying and monitoring dynamic coronal phenomena. Its application to CBF events revealed proficiency in tracking complete pixel maps, aiding in understanding CBF evolution. Limitations were acknowledged, and future work will address them for enhanced versatility. The methodology holds promise for extensive application in solar dynamic features and observational datasets.

Chapter 3 delved into the analysis of type III bursts during the second near-Sun encounter period of PSP. Sixteen separate radio bursts were observed using the PSP/FIELDS instrument and LOFAR ground-based telescope. A semi-automated pipeline facilitated data analysis, alignment, and interferometric imaging. Uniform frequency drifts among bursts suggested related origins. Interferometric observations located type III emissions off the southeast limb of the Sun, hinting at a single source of electron beams low in the corona. Magnetic extrapolation favored the active region AR12737 as the source, aligning with previous studies. However, caution was advised regarding potential deviations in magnetic field configurations near active regions. The study also explored discrepancies in observed and modeled density profiles, attributing them to scattering and propagation effects. Future work will integrate TDoA technique and Solar Orbiter observations for a more comprehensive analysis of solar radio bursts.

The pioneering multi-event exploration in Chapter 4 focused on Sun-to-Earth SEP simulations, investigating 62 eruptive events with EUV CBFs. The SPREAdFAST framework was employed to analyze coronal diffusive shock acceleration and interplanetary propagation. Input spectra for coronal proton acceleration were derived from quiet-time suprathermal spectra, exhibiting influences of solar corona conditions on proton acceleration. Comparison with in situ observations demonstrated overall alignment, validating the efficiency of the SPREAdFAST model. Discrepancies at the highest energies were noted, prompting future work to refine modeling and incorporate three-dimensional transport effects. The study also introduced a BiLSTM neural network model for forecasting SEP integral flux at 1 AU, showcasing promising results for short-term predictions with implications for space weather forecasting.

In conclusion, the dissertation contributions include a nuanced understanding of EUV waves, an automated tool for tracking coronal phenomena, insights into type III bursts and their sources, and advancements in SEP simulations and forecasting using deep learning. Future directions involve addressing limitations, refining models, and incorporating more recent data for a comprehensive understanding of solar dynamics and space weather forecasting.

5.1 Future Work

Future work will expand our understanding of CBFs by extending the list of observed events, aiming for a more comprehensive analysis of their kinematics and early-stage evolution within the complex coronal environment. Leveraging multi-wavelength remote-sensing observations from LOFAR and Solar Orbiter will be instrumental in probing the origin and evolution of energetic particles in the solar corona. The integration of high-resolution data from these sources will provide a more detailed and accurate representation of the dynamic processes involved. Additionally, future research endeavors will focus on developing interpretable deep learning models for SEP forecasting. These models, built with higher resolution data, aim to enhance the precision and reliability of predictions, contributing to the advancement of space weather forecasting capabilities. The incorporation of advanced methodologies and diverse observational datasets is essential for refining our comprehension of solar dynamics and improving the accuracy of predictive models.

5.2 Definitions and Acronyms

Some of the key technical terms and acronyms used in this thesis are listed below:

- SEP – Solar Energetic Particles/Protons
- CME – Coronal Mass Ejection
- EUV – Extreme Ultra-Violet
- CBF – Coronal Bright Front
- SOHO – Solar and Heliospheric Observatory
- LASCO – Large Angle and Spectrometric COronagraph
- SDO – Solar Dynamics Observatory
- AIA – Atmospheric Imaging Assembly
- EIT – Extreme ultraviolet Imaging Telescope
- TRACE – Transition Region and Coronal Explorer
- GOES – Geostationary Operational Environmental Satellite
- PSP – Parker Solar Probe
- MHD - Magneto-Hydro-Dynamic
- AU - Astronomical Unit
- IMF – Interplanetary Magnetic Field
- LOFAR – Low-Frequency Array
- SN – Sunspot Number
- SPREAdFAST – Solar Particle Radiation Environment Analysis and Forecasting–Acceleration and Scattering Transport
- CASHeW – Coronal Analysis of SHocks and Waves
- DEM – Differential Emission Measure
- AI – Artificial Intelligence
- BiLSTM – Bi-directional Long short-term Memory
- NN – Neural Network
- MIMO – Multi-Input Multiple Output
- MSE – Mean Squared Error
- MAE – Mean Absolute Error

This provides definitions of the major domain-specific terms and measurement concepts used. Additional terminology is introduced as required in the respective chapters.

Appendix A

A.1 Kinematics of the CBFs in the Middle/Outer Corona

Here I present the extended measurements of the 26 EUV waves in the SOHO/LASCO FOV, up to $\sim 30 R_\odot$, and fitted with two CME kinematics models by Gallagher et al. (2003) and Byrne et al. (2013). Overall, the Gallagher fitting model accommodated both AIA and LASCO measurements very well and proved the model's proficiency in capturing the early stages of the solar event, particularly in the lower corona.

A.2 Persistent Imaging Technique

Persistent imaging is a technique used in medical imaging, particularly ultrasound imaging, to create a continuous, real-time display of the anatomy being imaged (see Pysz et al. 2011, and references within). The core idea of persistent imaging is to use persistence, or the ability of the human eye to retain an image for a brief moment after it has disappeared to create a more informative and visually clear image (Fredkin et al. 1995; Thompson & Young 2016).

At every image in a time-ordered series, the technique keeps the old pixel value if it is brighter than the current pixel value, else it takes the current pixel's value. The result is saved as the current persistence image. Then, the next image in the series is evaluated by comparing it pixel by pixel with respect to the previous persistence image. The resulting image emphasizes the changes between the current image and the previous persistent image, making them more visible to the human eye.

The persistent imaging technique can be described mathematically by a set of equations. If we let $I(t, x, y)$ be the intensity at time t and pixel coordinates (x, y) , and let $P(t, x, y)$ be the persistence image at time t and pixel coordinates (x, y) , then the persistence image at time t is computed as:

$$P(t, x, y) = \max\{I(t, x, y), P(t - 1, x, y)\}, \quad (\text{A.1})$$

where **max** represents the maximum of its two arguments. The current image at time t is then evaluated with respect to the previous persistence image as follows:

$$I'(t, x, y) = \max\{I(t, x, y) - P(t - 1, x, y), 0\}, \quad (\text{A.2})$$

The resulting image $I'(t, x, y)$ is a modified version of the current image that emphasizes the differences from the previous persistence image.

The persistent imaging technique has been shown to improve the visual quality of ultrasound images and other medical imaging modalities, and is commonly used in clinical practice. In this work, I utilize the persistent imaging technique to improve the visualization of the solar radio sources of type III emissions (Fig. 3.6).

A.3 Resolving the radio emission location ambiguity

In this part, we show that the -Z solution of Equation 3.4 is highly unlikely in our case. Figure A.26 shows the positive and negative solutions of Equation 3.4. I take the innermost and outermost coronal radio sources at R_1 and R_2 , respectively, as an example. r_1 and r_2 are the projections of R_1 and R_2 on the POS, respectively. Harmonic radio emission from R_1 will theoretically be absorbed by a region along the LOS with plasma frequency (and corresponding density) equal to or higher than the harmonic

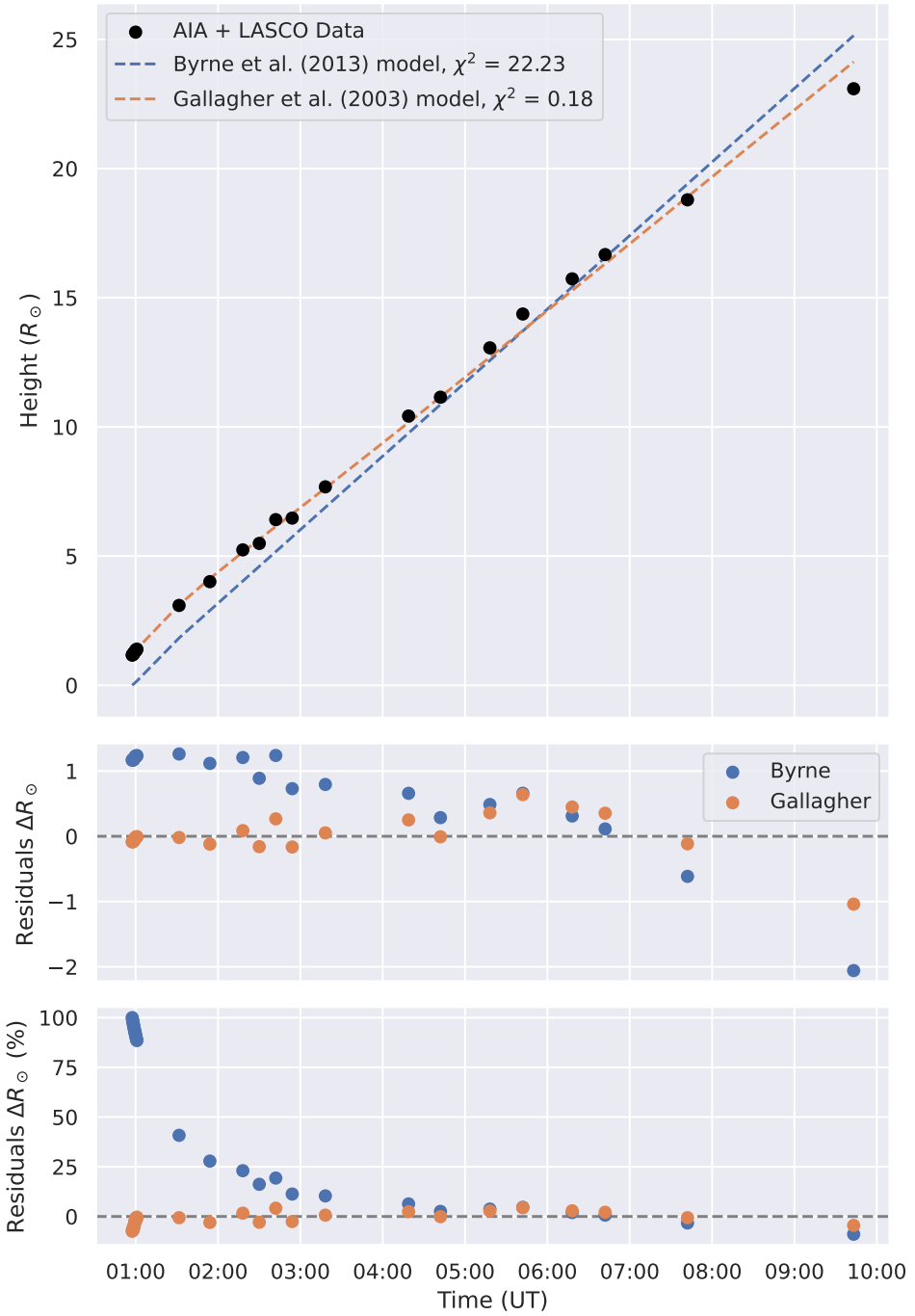


Figure A.1: Top panel: Height-time profile on June 12, 2010, using AIA and LASCO data, fitted with two CME kinematics models. Middle panel: Fitting vs. real observation difference. Bottom panel: Relative residuals in %.

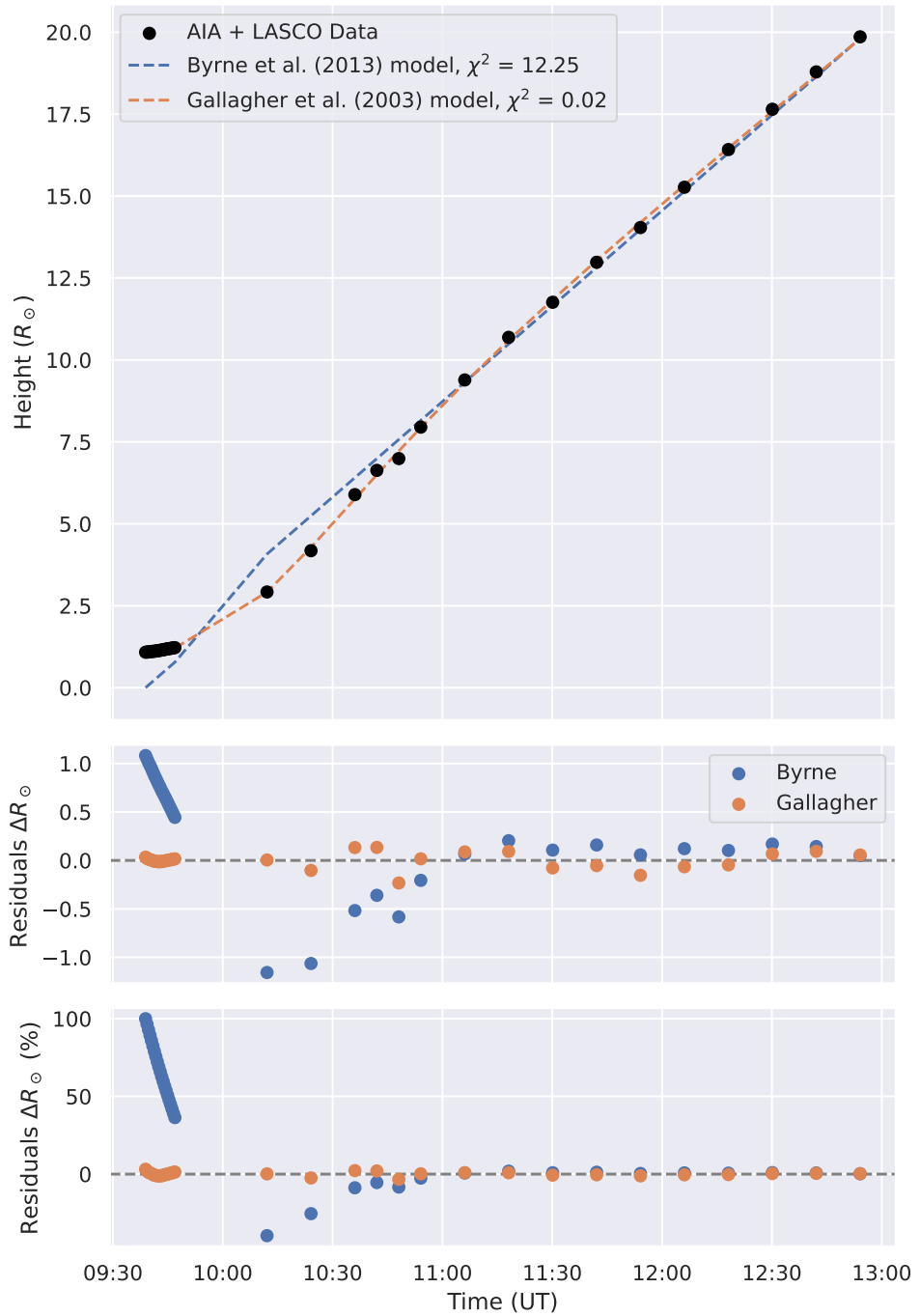


Figure A.2: Same for the event on August 14, 2010.

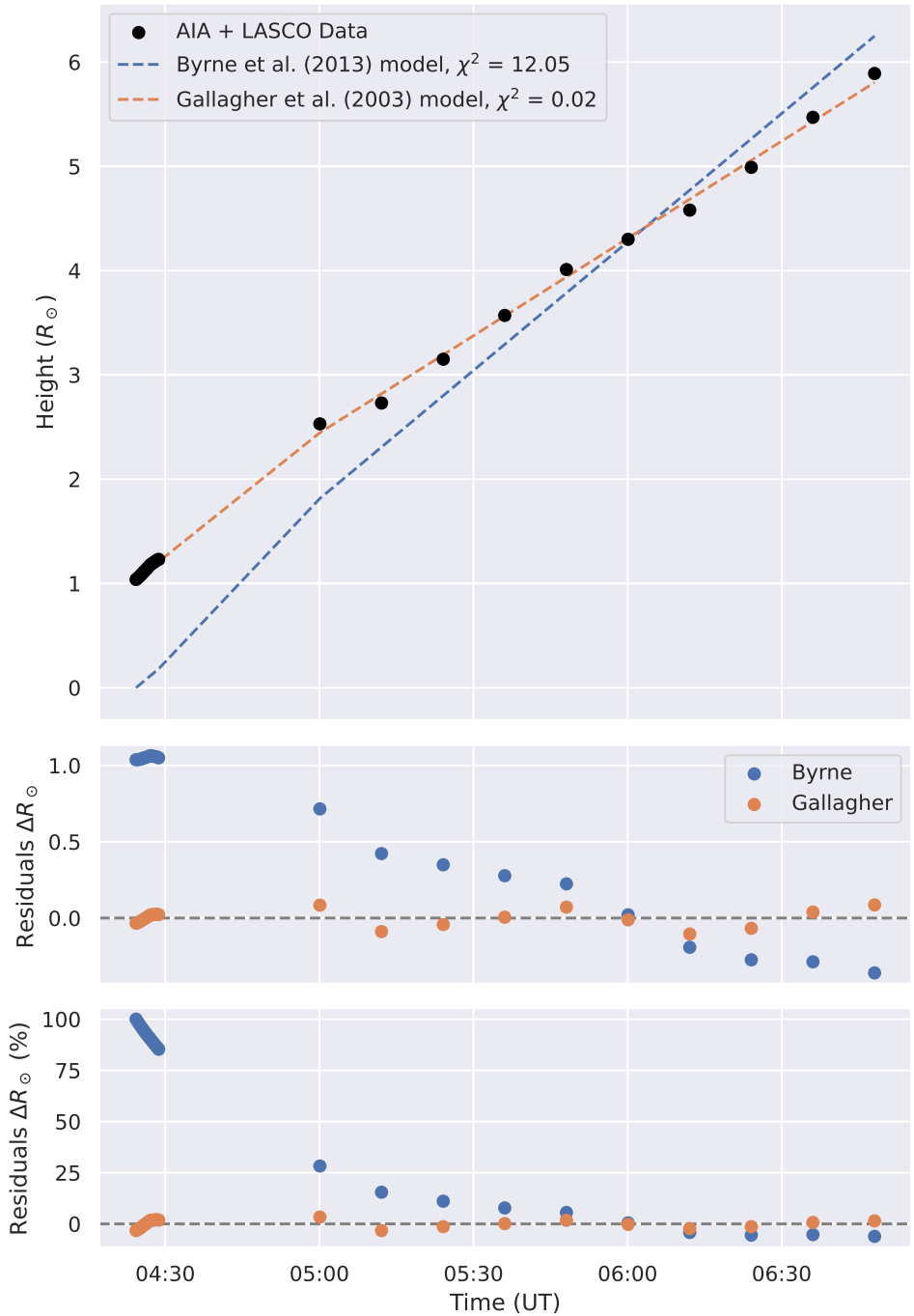


Figure A.3: Same for the event on December 31, 2010.

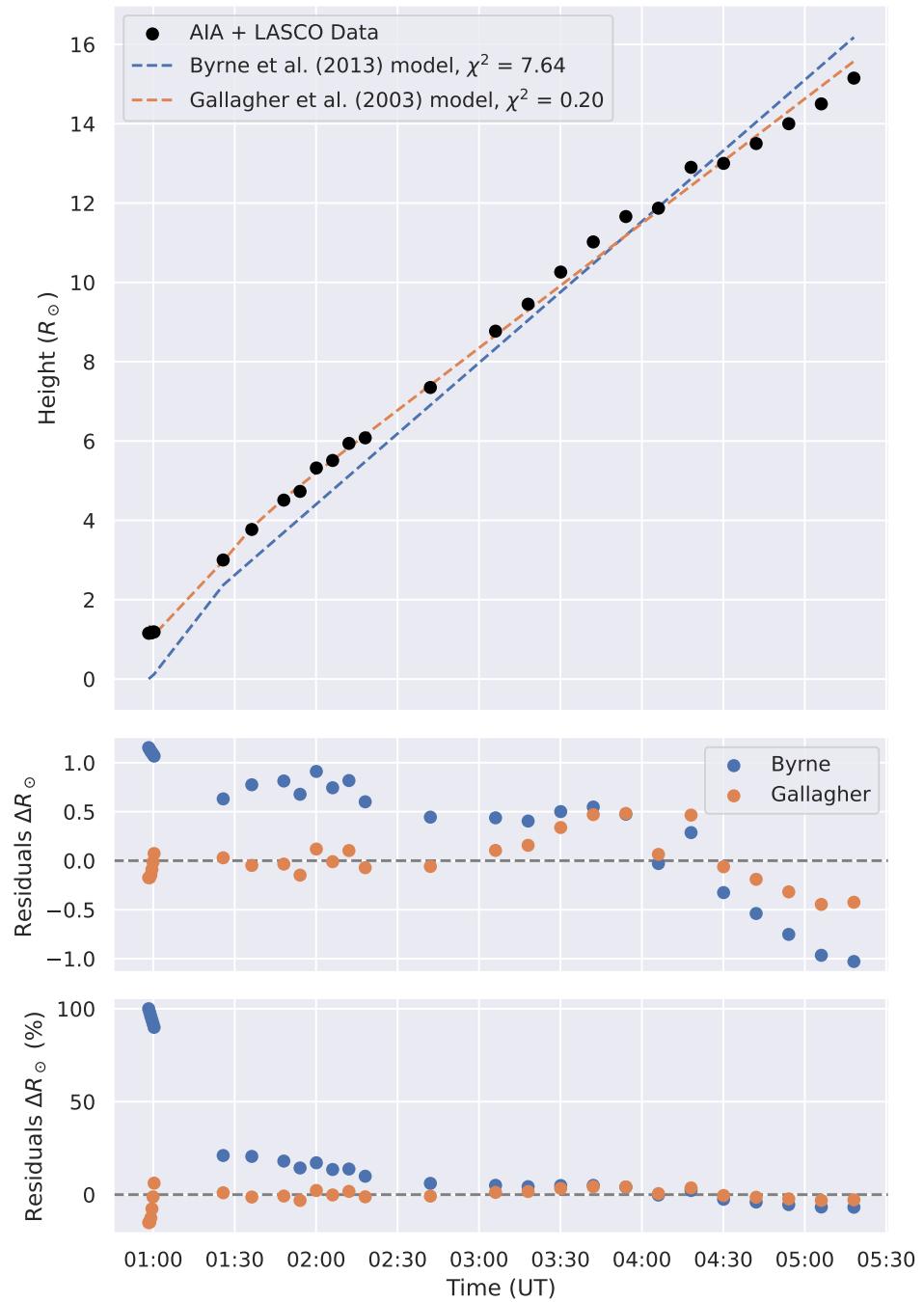


Figure A.4: Same for the event on January 28, 2011.

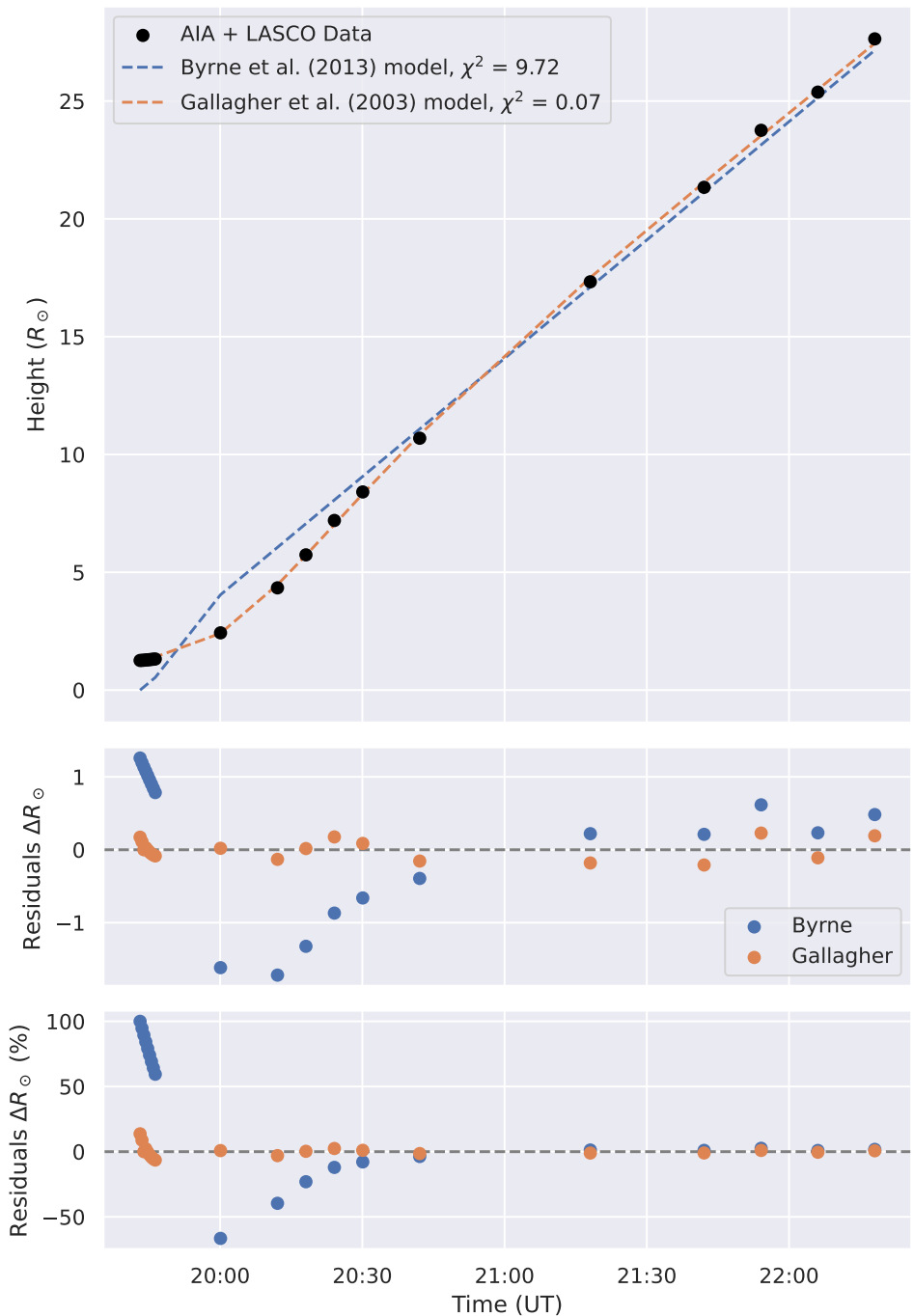


Figure A.5: Same for the event on March 7, 2011.

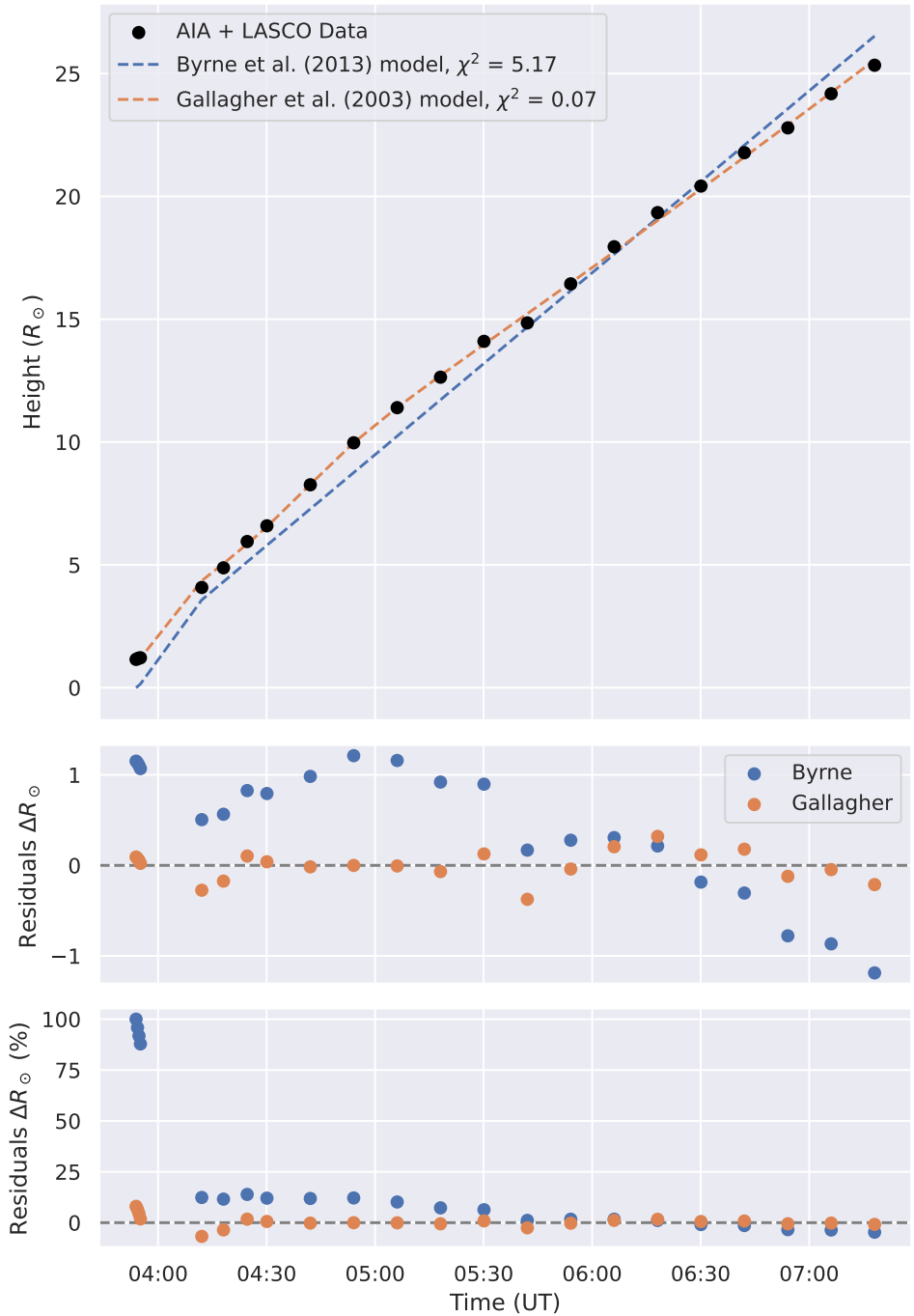


Figure A.6: Same for the event on August 4, 2011.

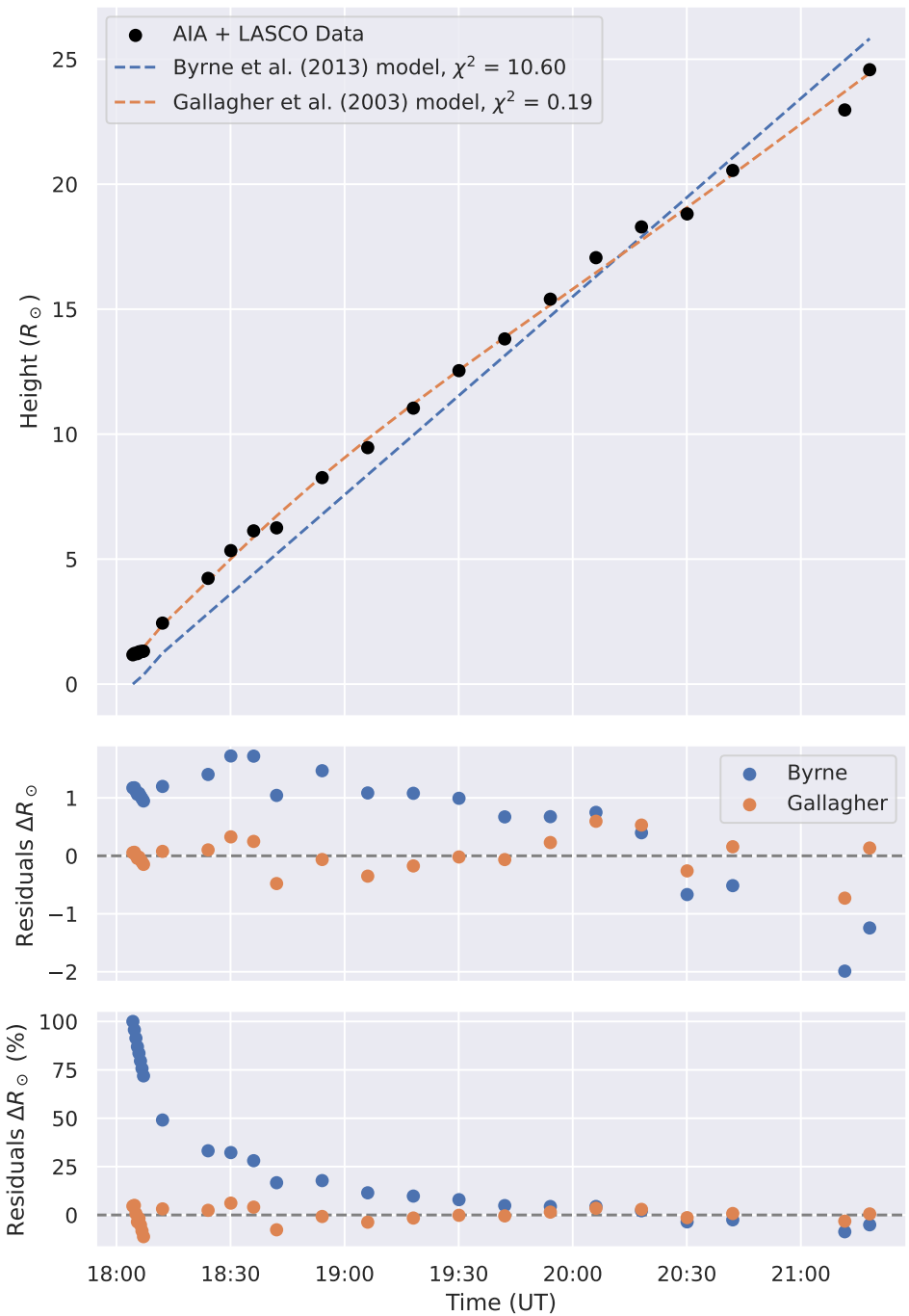


Figure A.7: Same for the event on August 8, 2011.

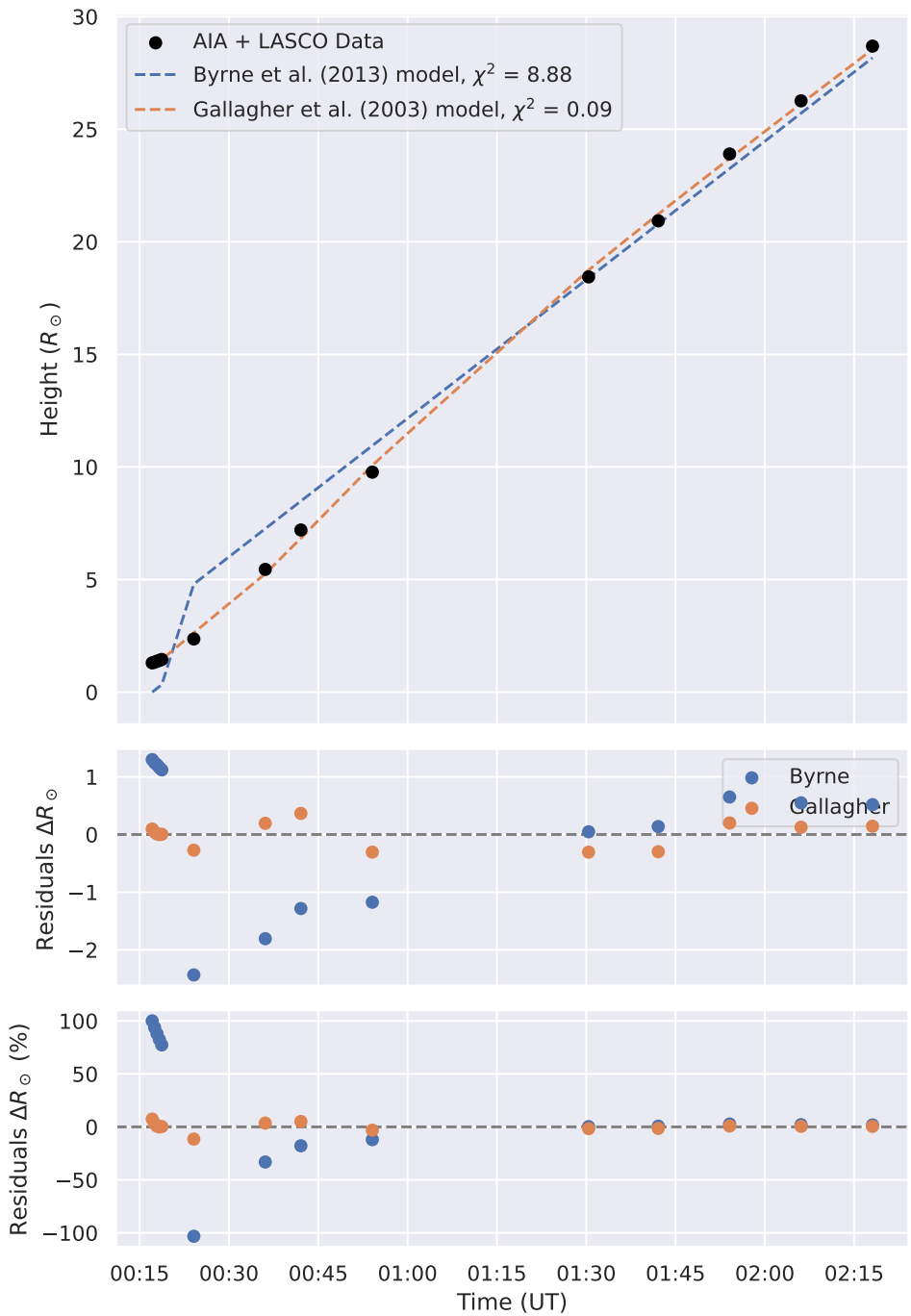


Figure A.8: Same for the event on March 7, 2012.

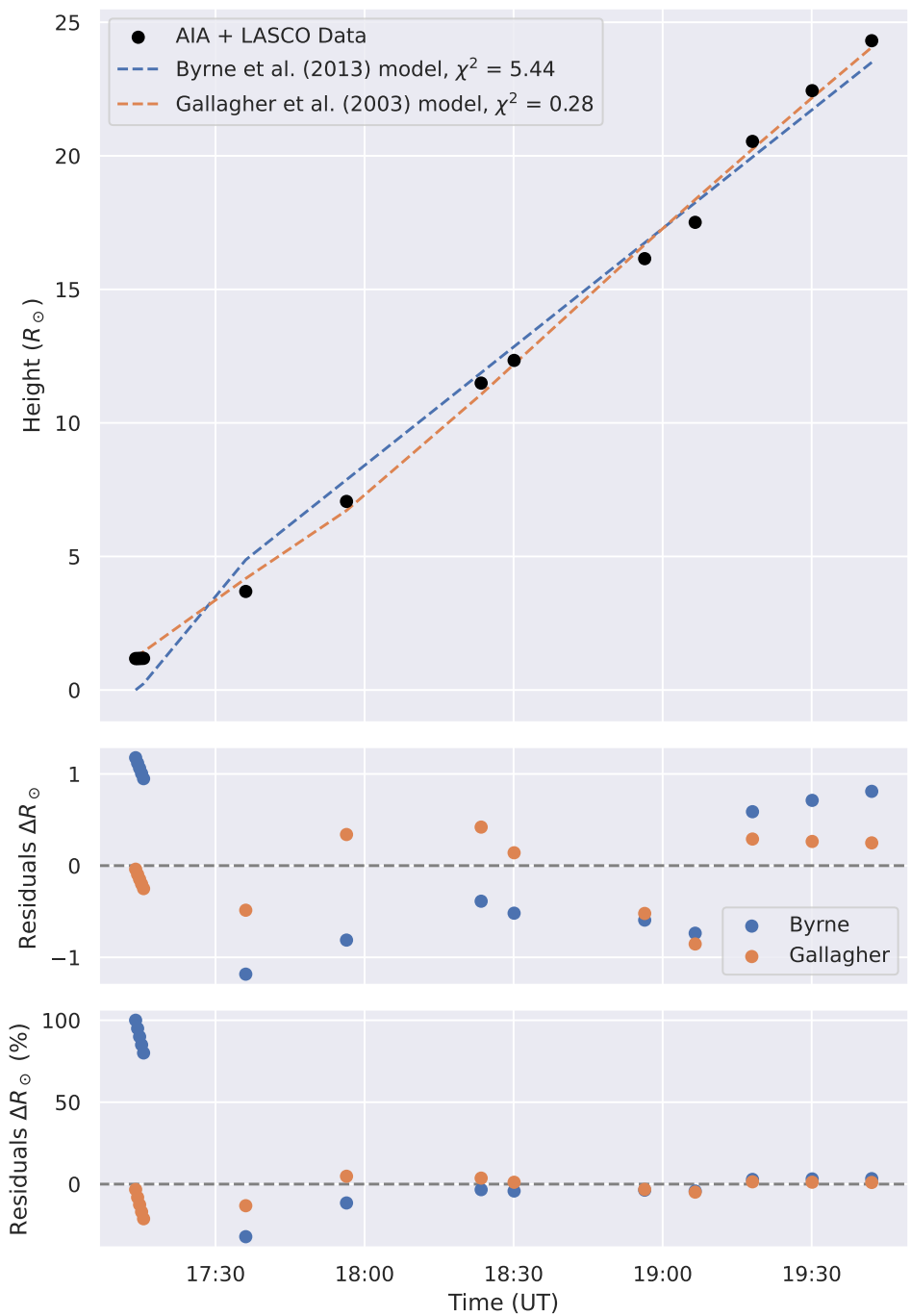


Figure A.9: Same for the event on March 13, 2012.

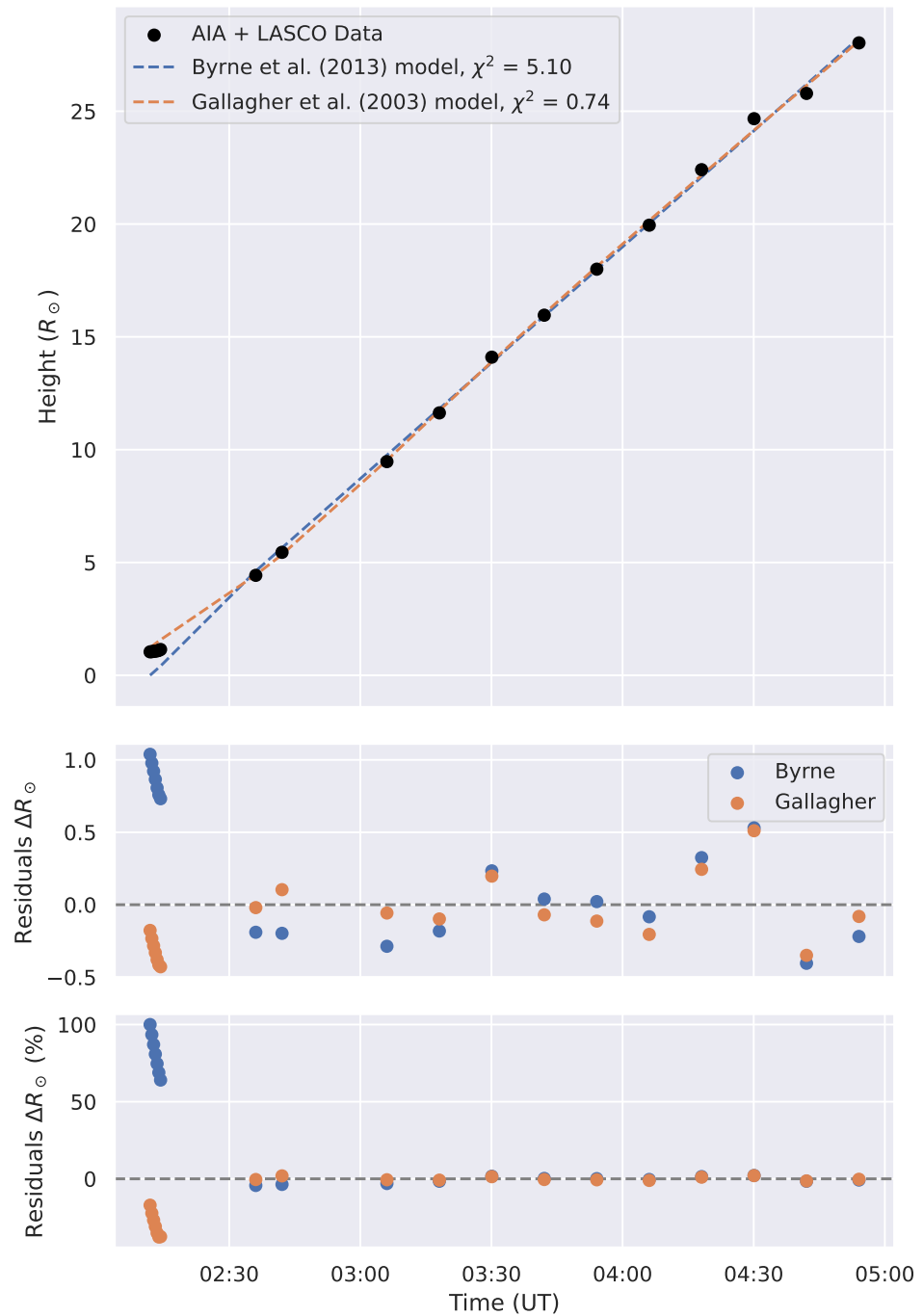


Figure A.10: Same for the event on July 23, 2012.

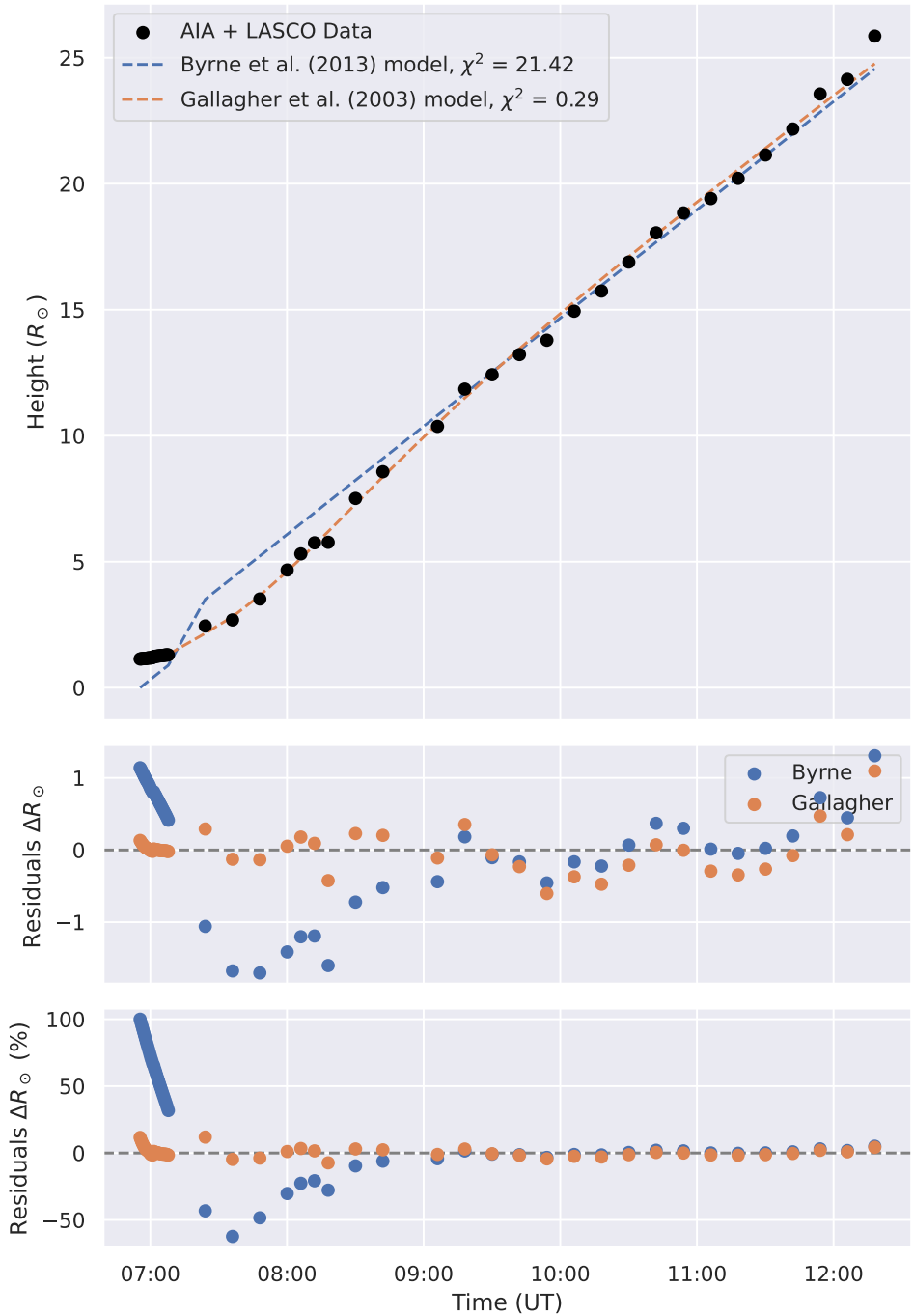


Figure A.11: Same for the event on April 21, 2013.

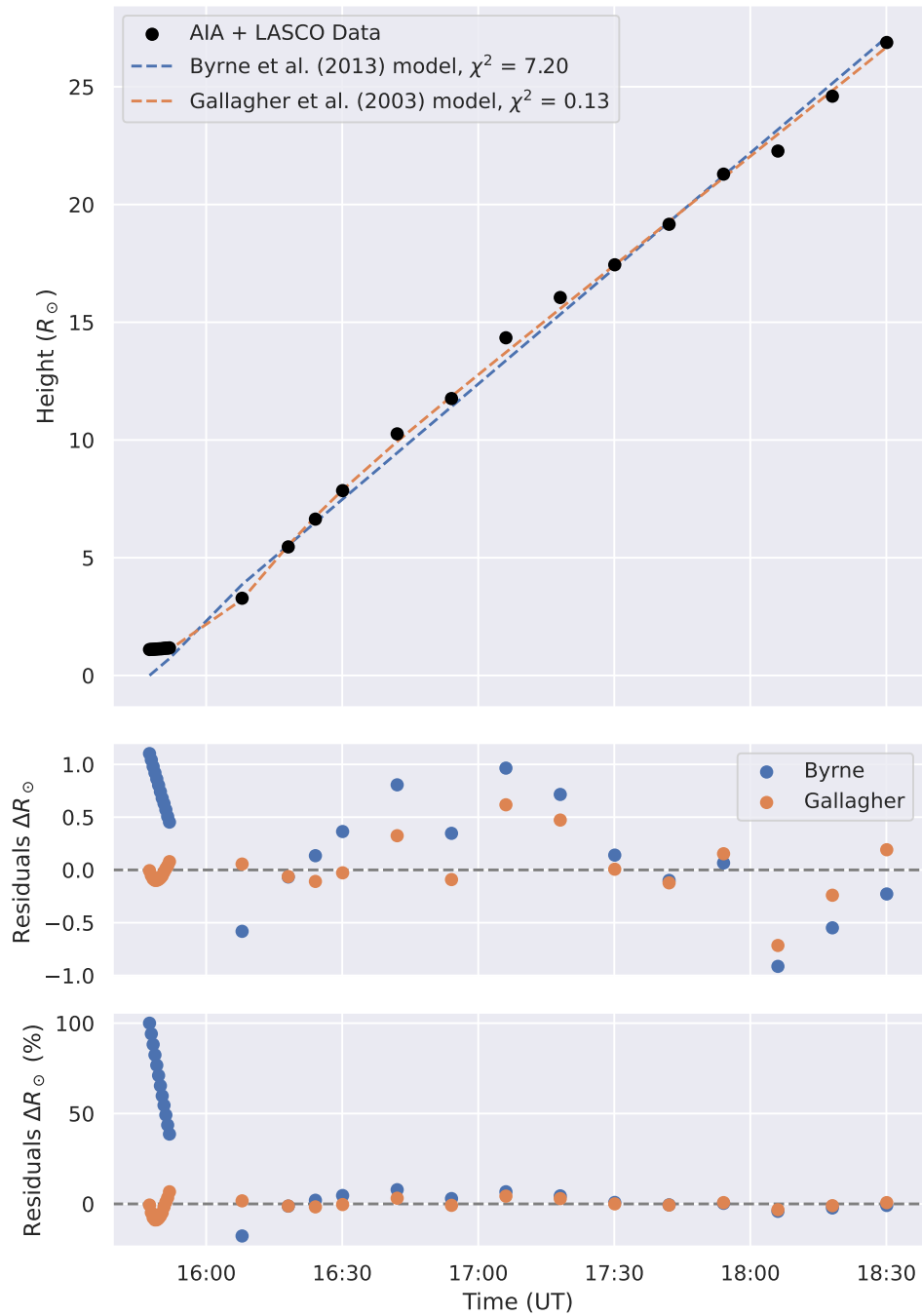


Figure A.12: Same for the event on May 13, 2013.

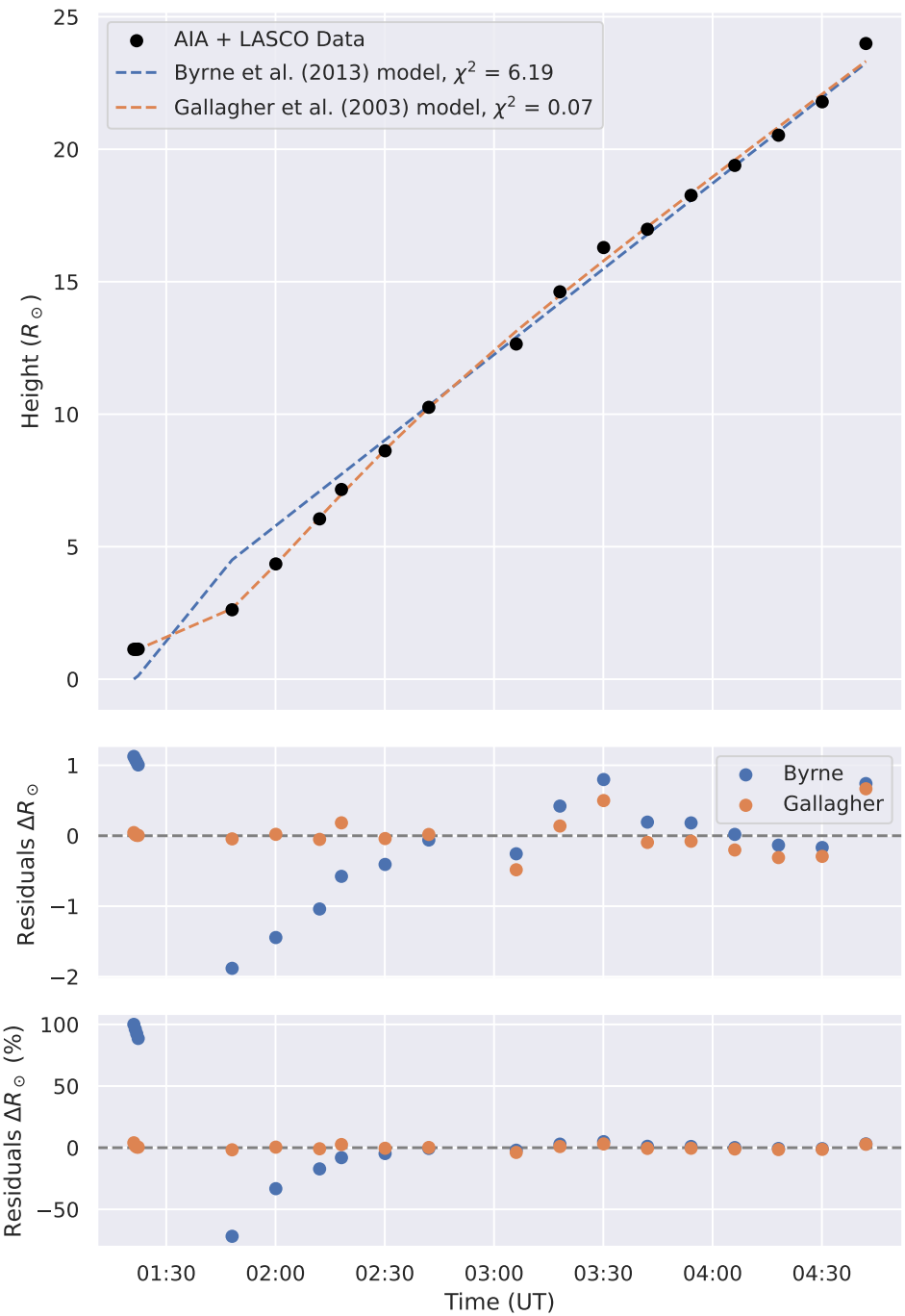


Figure A.13: Same for the event on May 15, 2013.

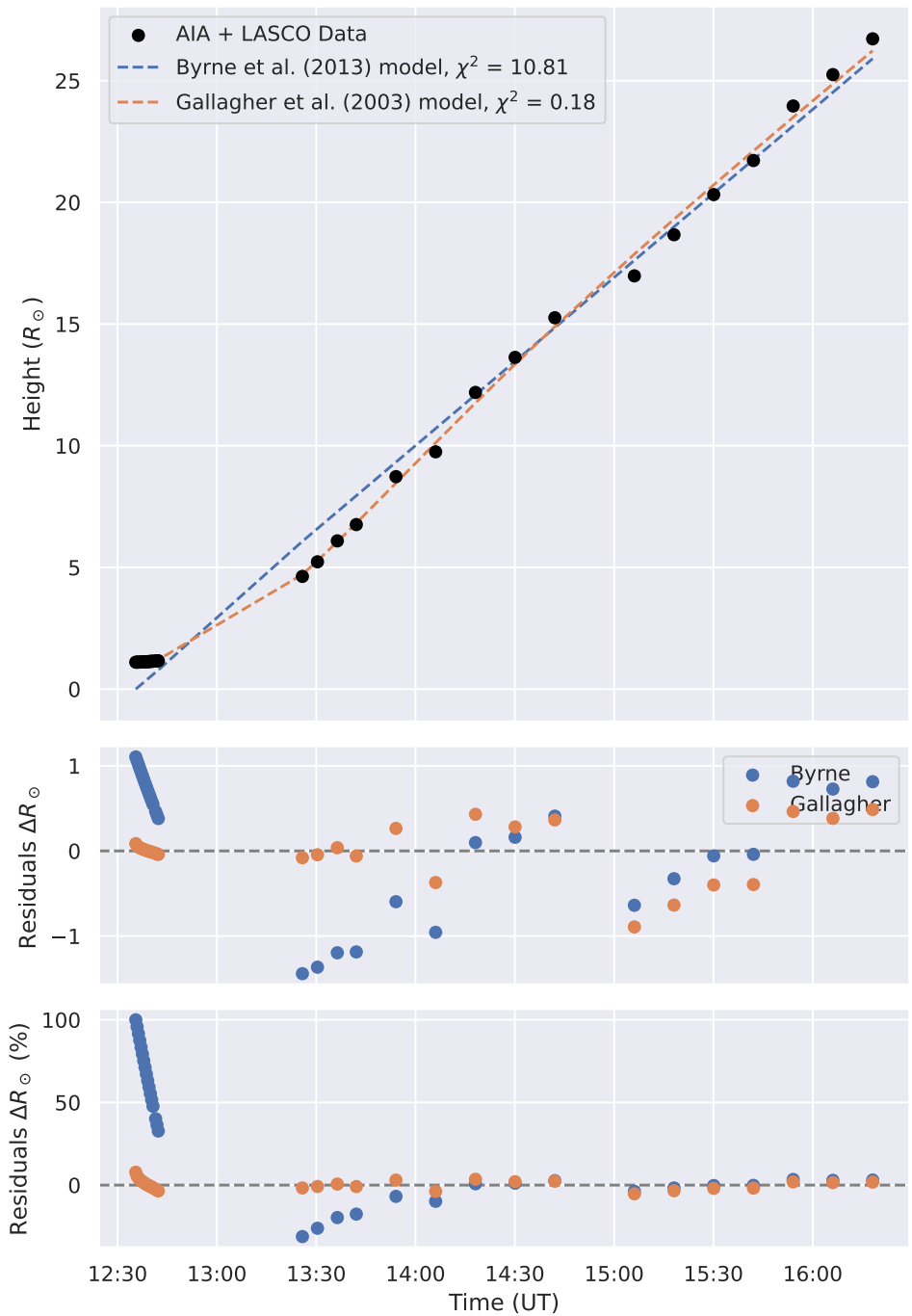


Figure A.14: Same for the event on May 22, 2013.

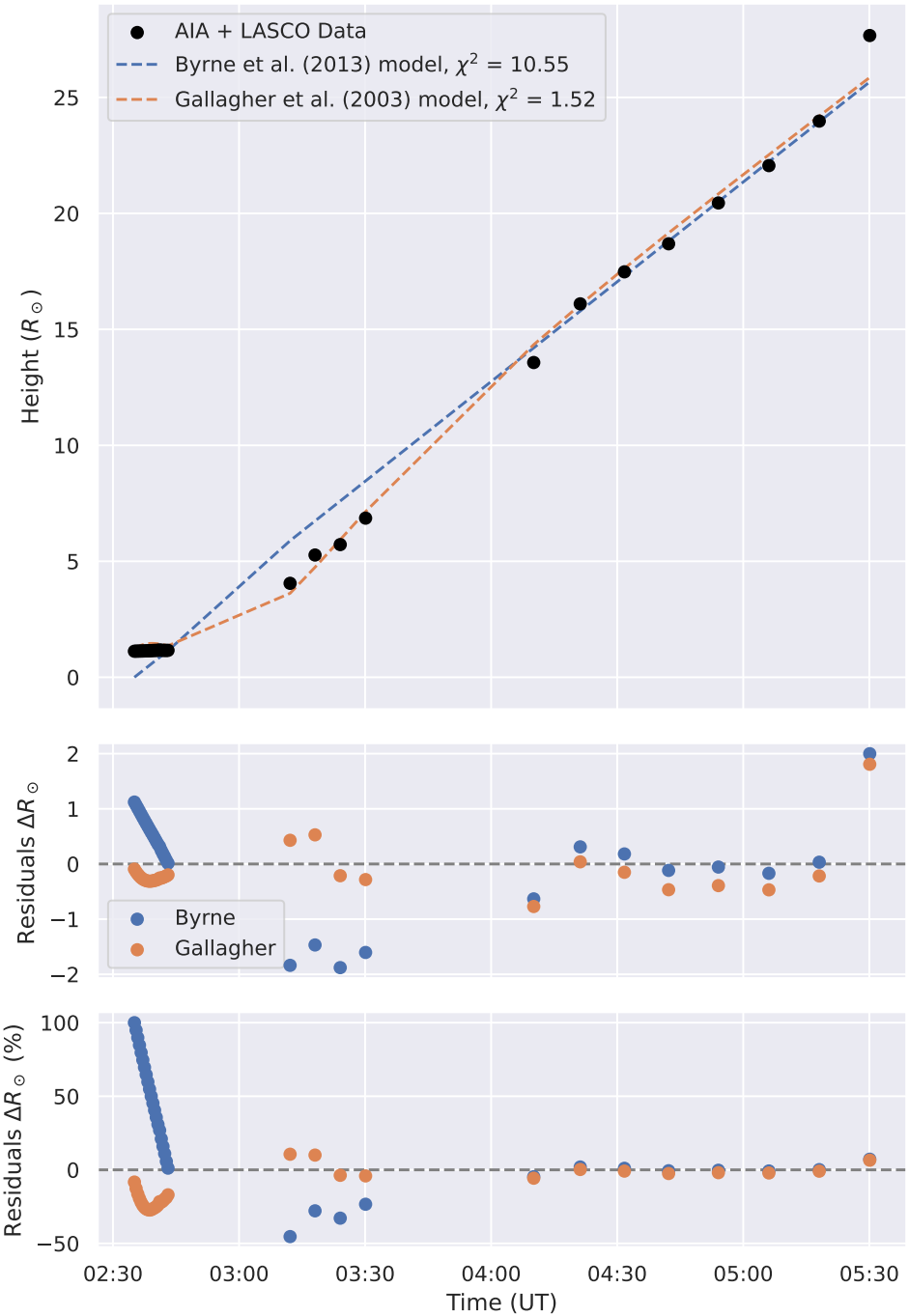


Figure A.15: Same for the event on June 21, 2013.

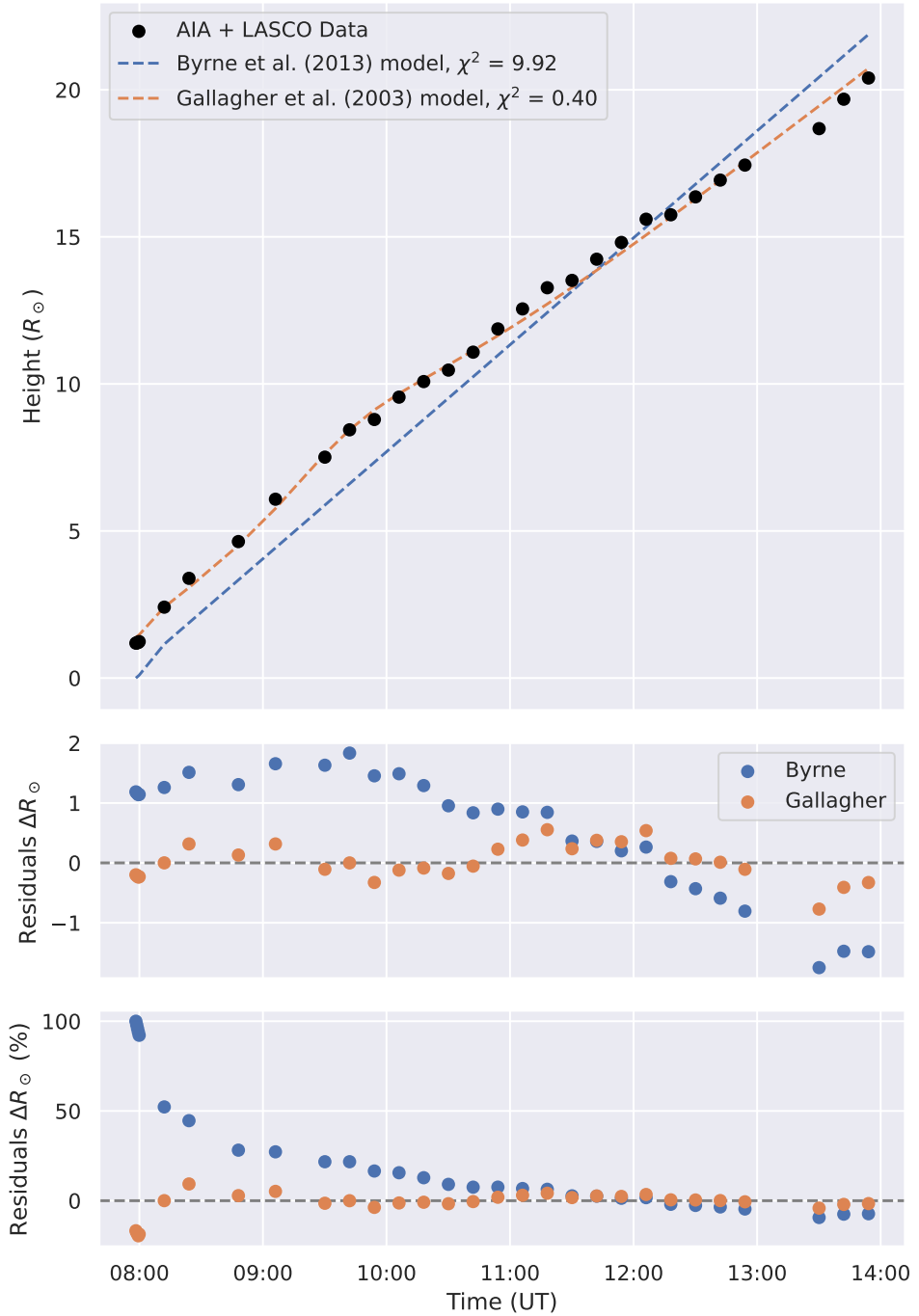


Figure A.16: Same for the event on October 25, 2013.

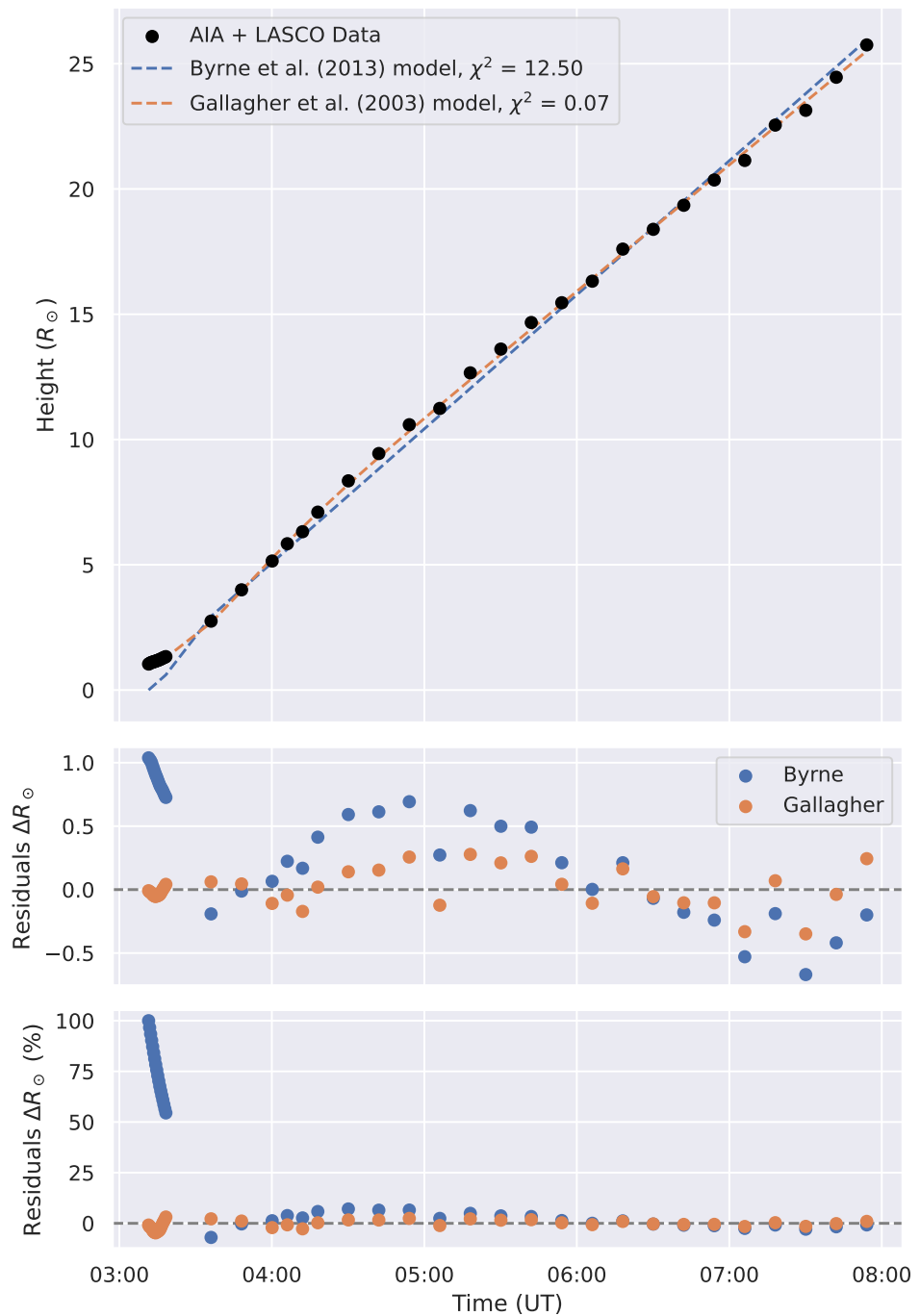


Figure A.17: Same for the event on December 12, 2013.

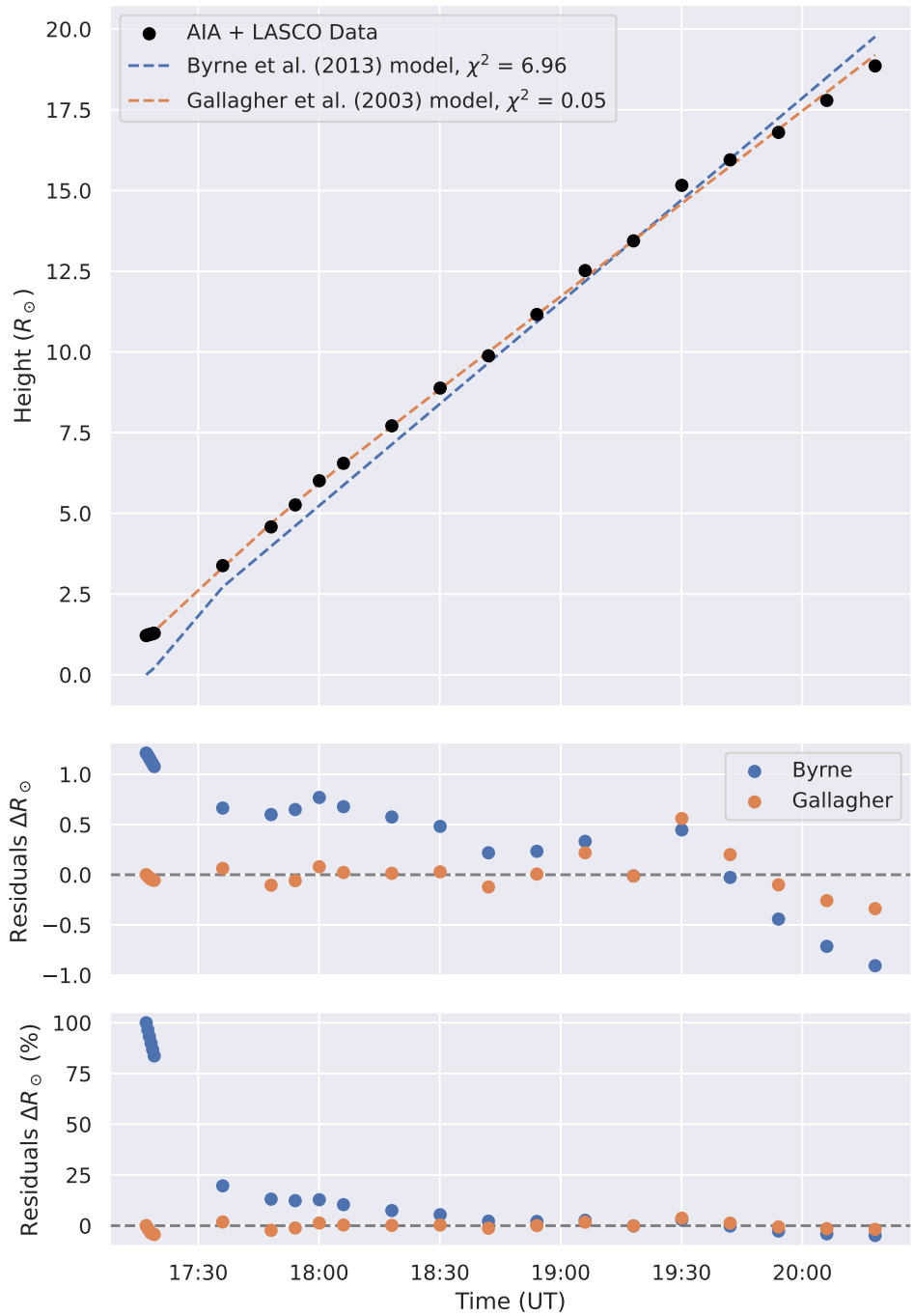


Figure A.18: Same for the event on December 28, 2013.

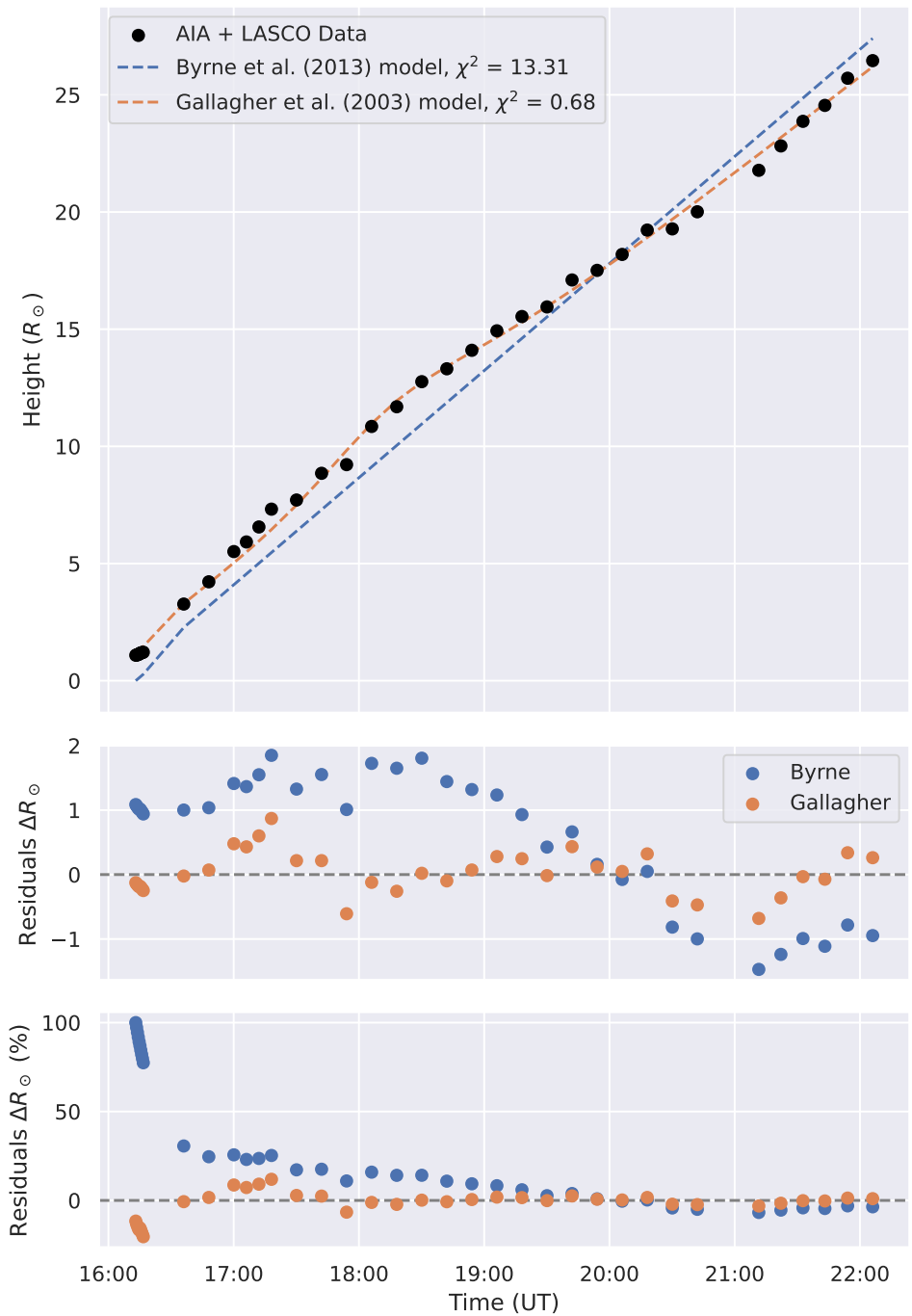


Figure A.19: Same for the event on July 8, 2014.

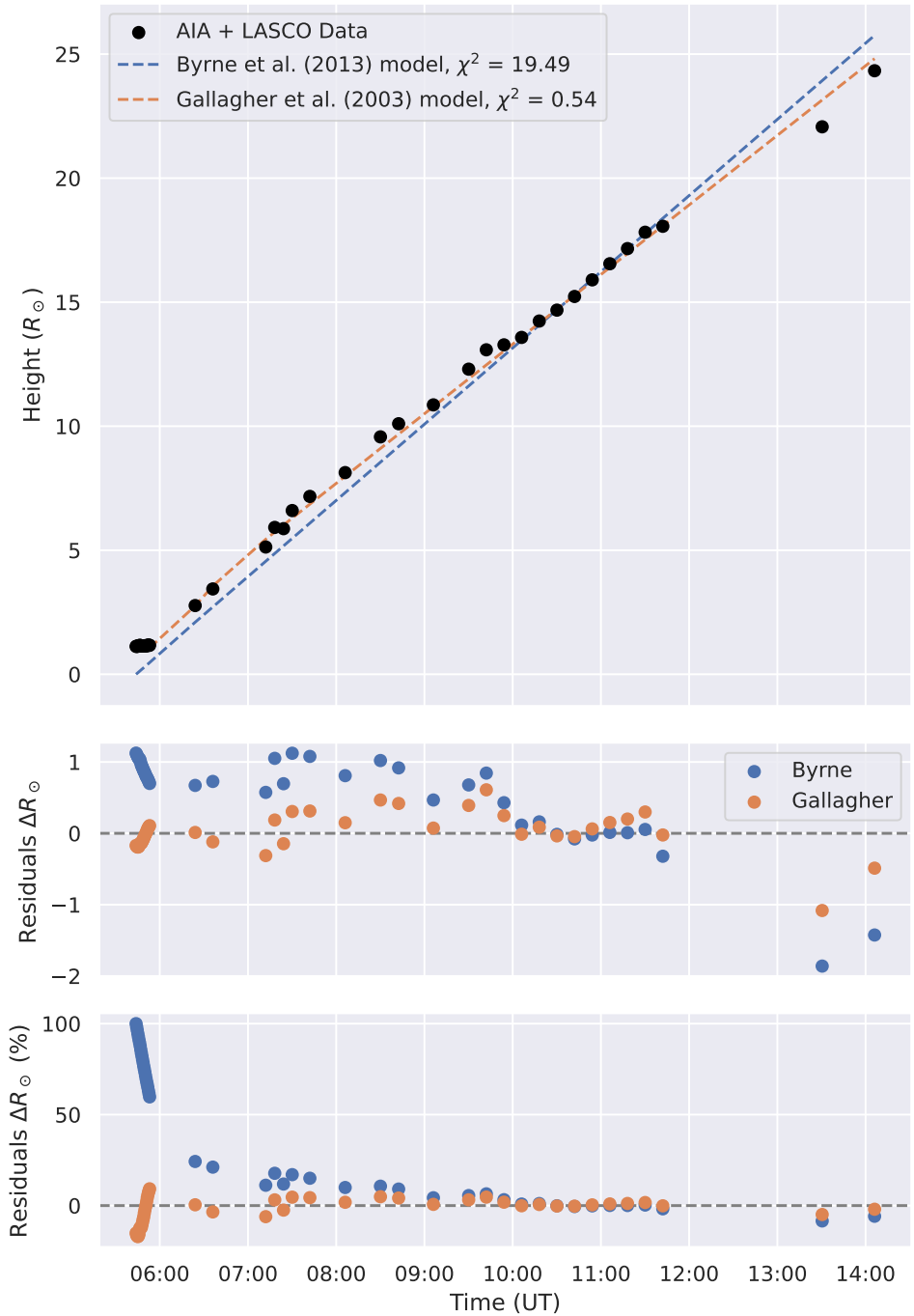


Figure A.20: Same for the event on December 5, 2014.

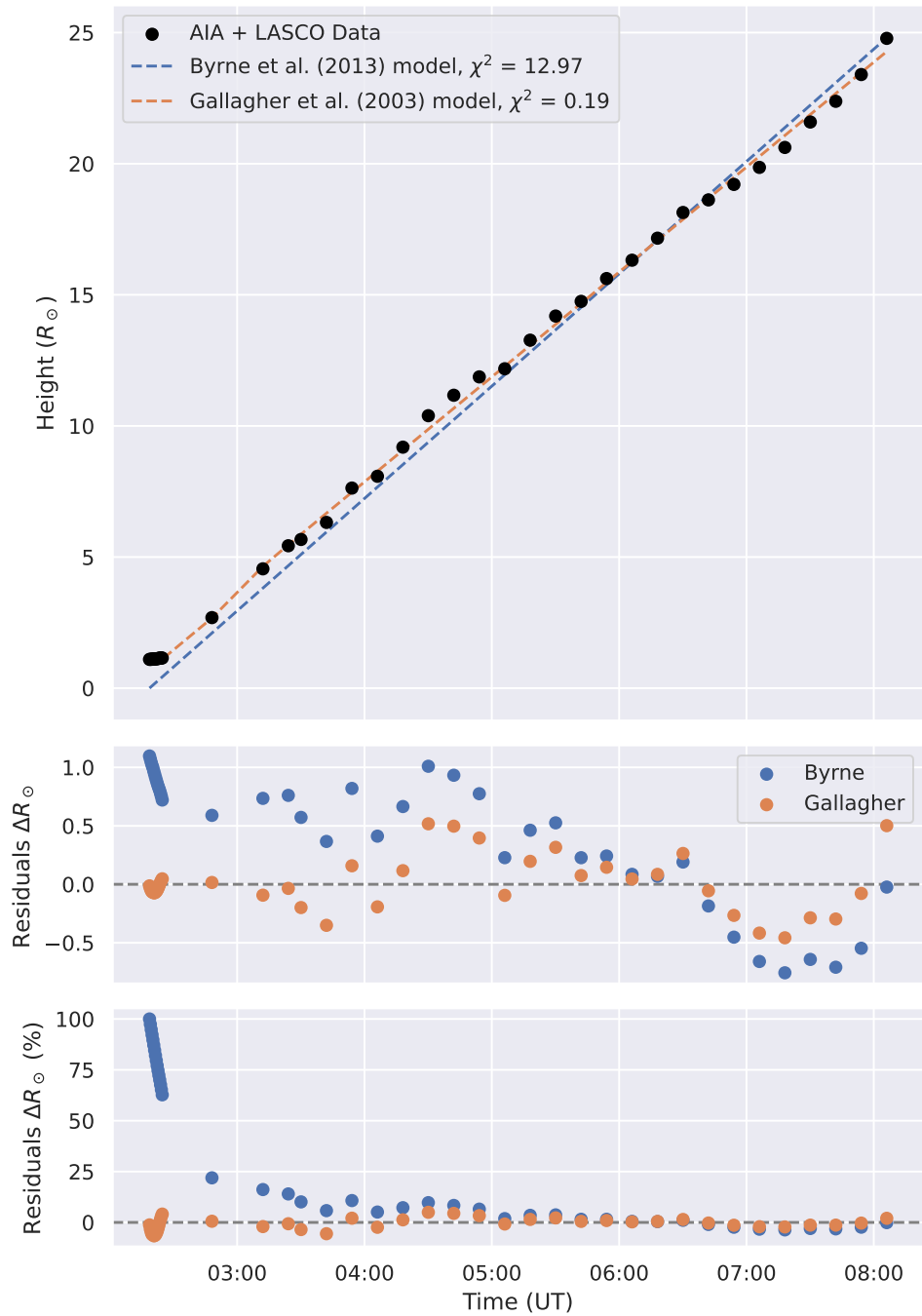


Figure A.21: Same for the event on May 12, 2015.

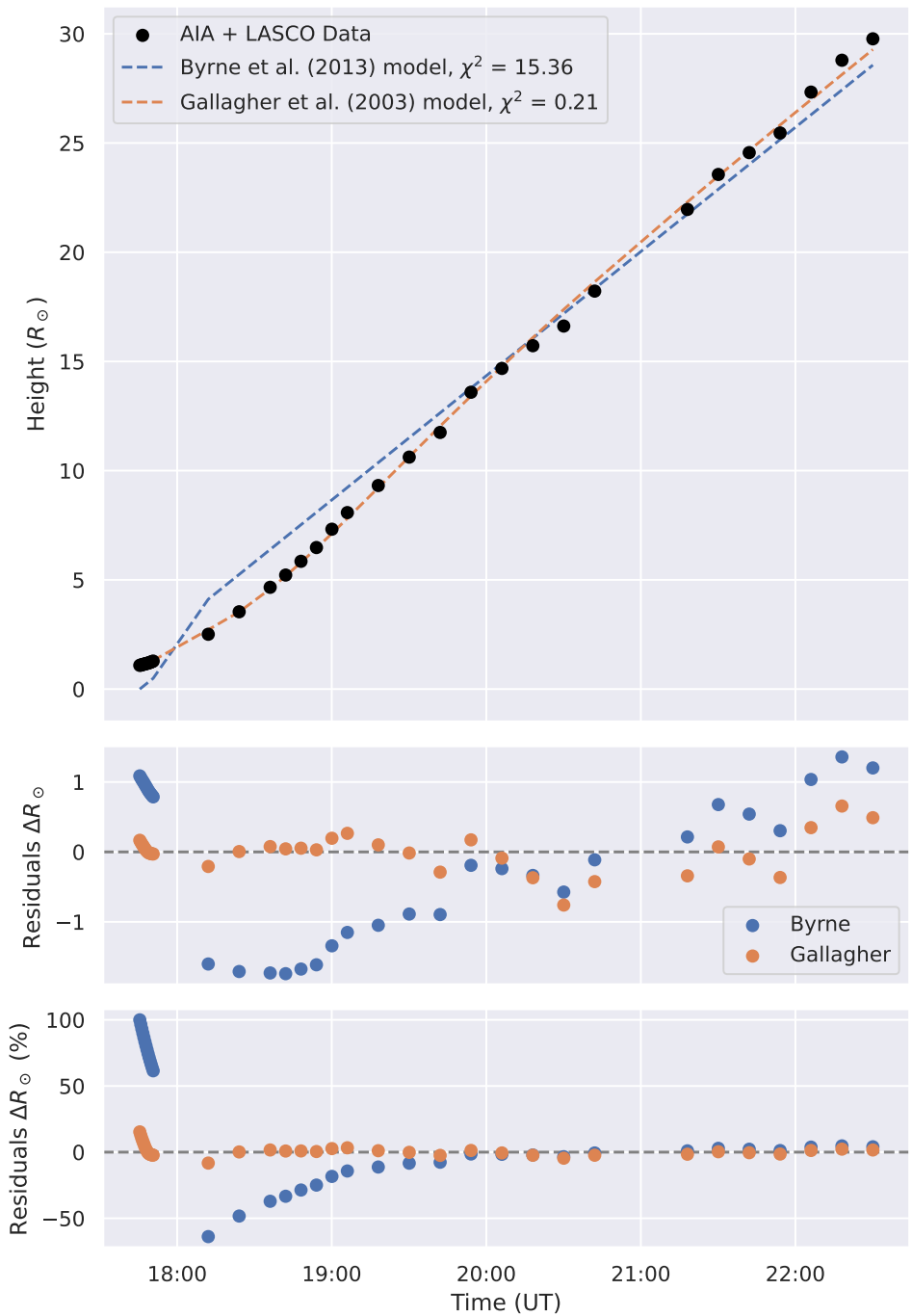


Figure A.22: Same for the event on September 20, 2015.

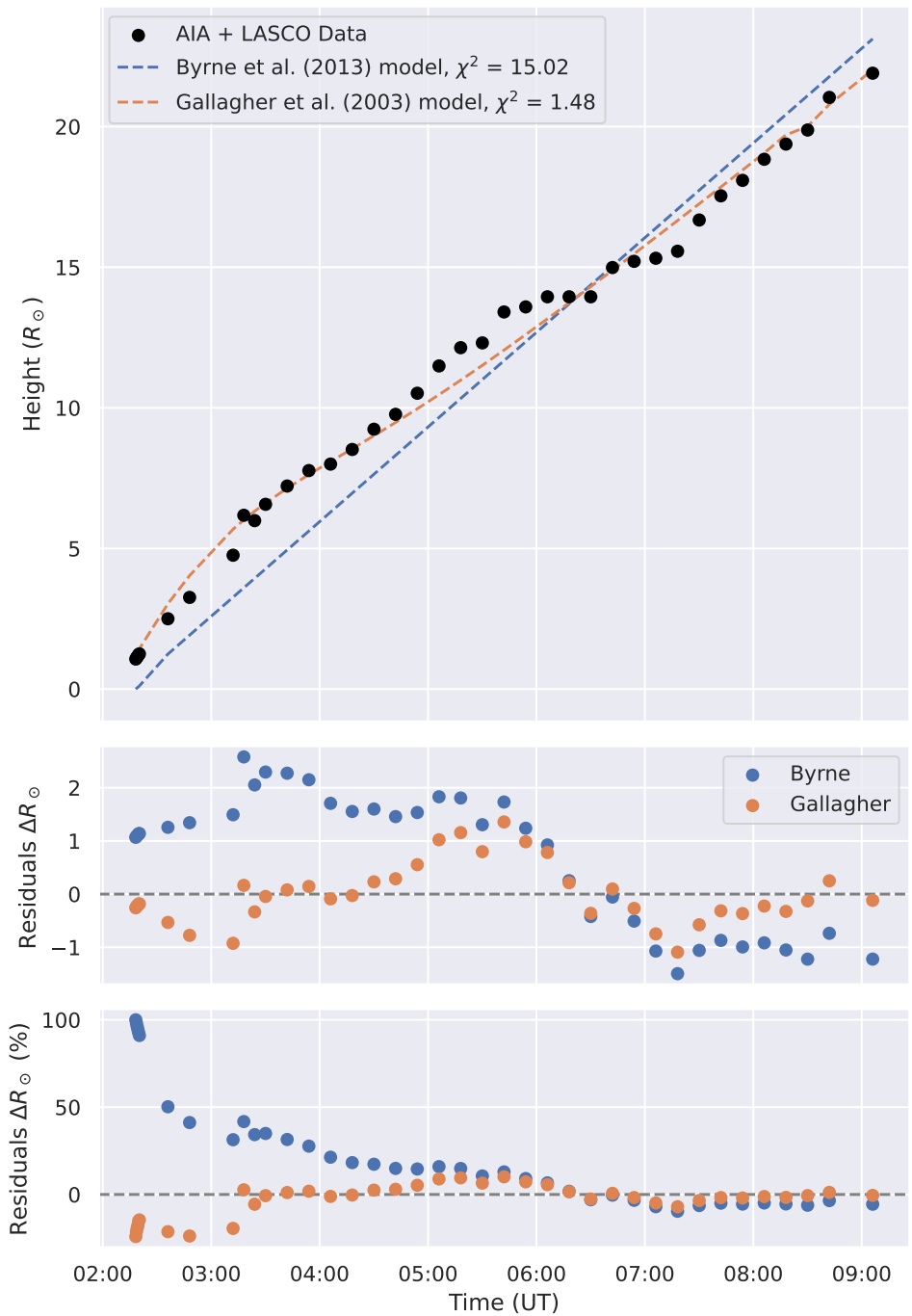


Figure A.23: Same for the event on October 29, 2015.

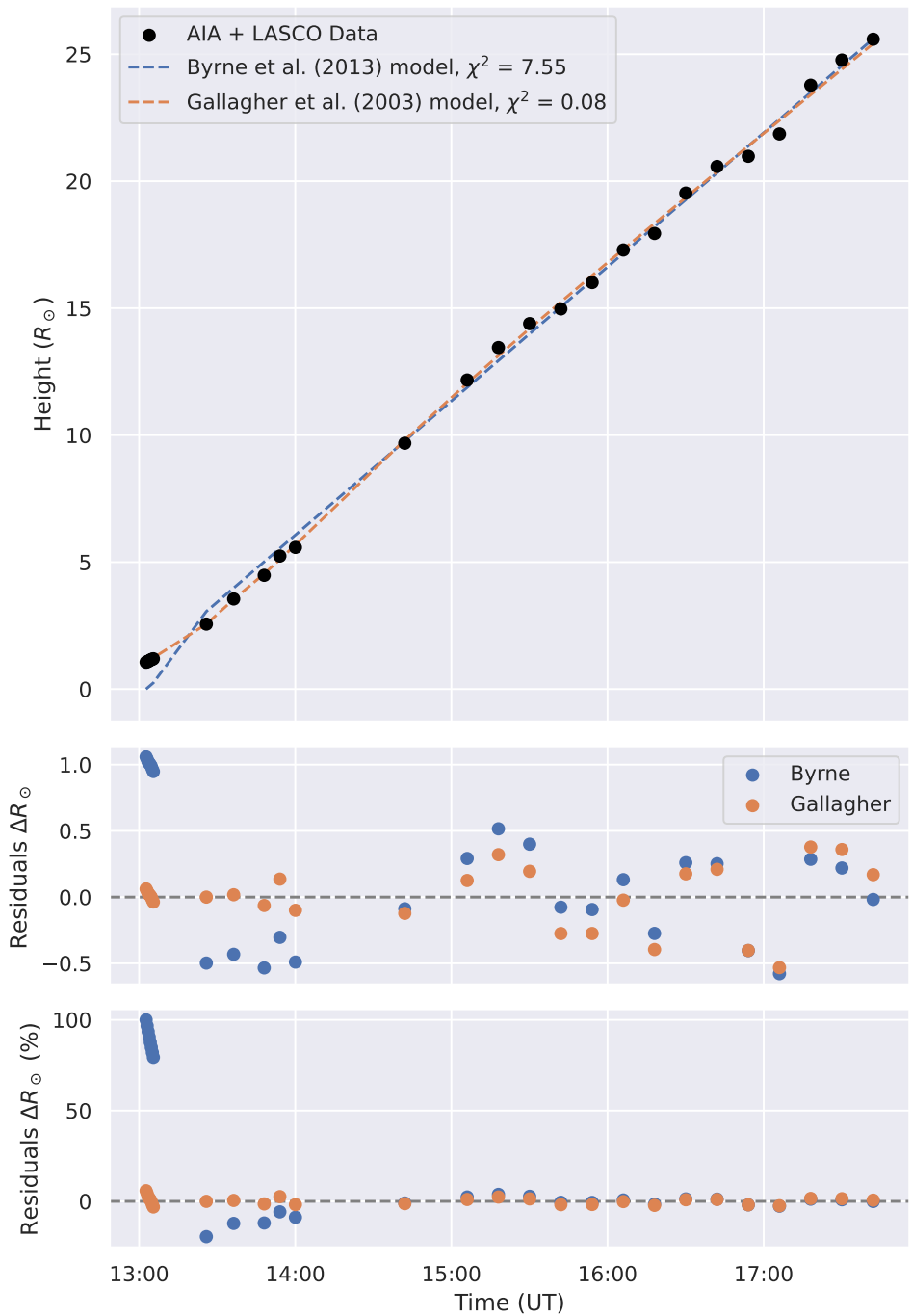


Figure A.24: Same for the event on November 9, 2015.

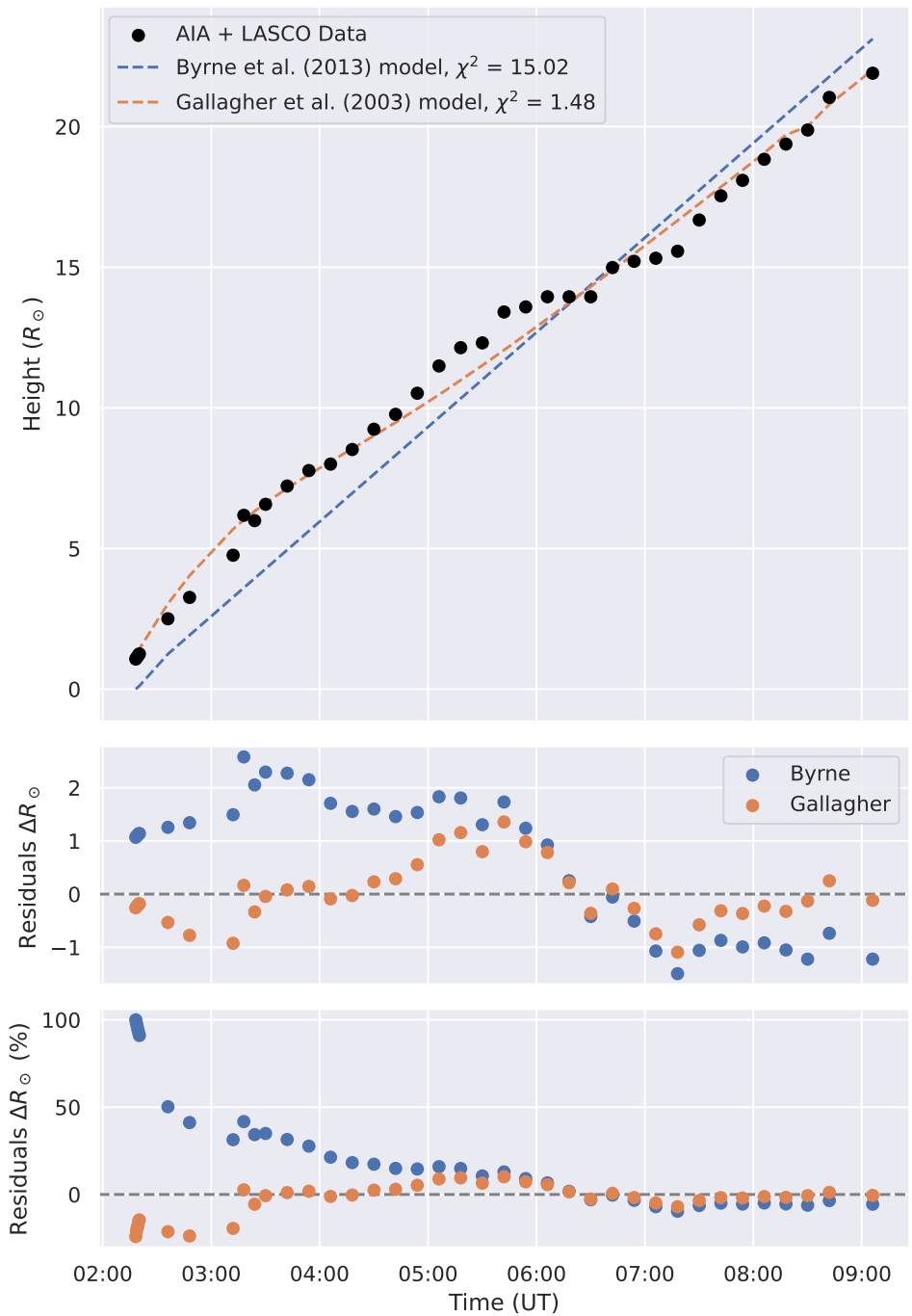


Figure A.25: Same for the event on April 1, 2017.

emission frequency at R_1 . In the case of the spherically symmetric Newkirk model, the highest density location the emission from R_1 could pass through is r_1 on the POS. Thus, for harmonic radio emission from behind the POS ($-Z$, where $Z = 0$ is defined at the center of the Sun and positive Z is towards the observer) to be observed at the Earth, it must satisfy the following condition:

$$2f_{R_1} > f_{r_1}, \quad (\text{A.3})$$

where f_{R_1} is the plasma frequency of radio emission that occurred behind the POS, and f_{r_1} is the plasma frequency at the projected location of r_1 on the POS. The relation between the local plasma frequency and the electron density is defined by the equation:

$$f[\text{MHz}] = 8.93 \times 10^{-3} \sqrt{n[\text{cm}^{-3}]} \quad (\text{A.4})$$

The Newkirk electron-density model (Newkirk 1961, 1967) describes the typical densities in the outer part of the corona according to the following equation:

$$n[\text{cm}^{-3}] = \alpha 4.2 \times 10^4 10^{4.32 \frac{R_\odot}{r}}, \quad (\text{A.5})$$

where α is the fold number (i.e., a multiplicative factor that accounts for the density variations based on the degree of solar activity), and r is the radial distance from the Sun in solar radii. By substituting Equations A.4 and A.5 into Equation A.3, we obtain

$$\frac{n_{r_1}}{n_{R_1}} = \frac{10^{4.32 \frac{R_\odot}{r_1}}}{10^{4.32 \frac{R_\odot}{R_1}}} < 4. \quad (\text{A.6})$$

After reduction we obtain the final formula that must be satisfied under these assumptions in order for radio emission behind the POS to pass through the corona and reach the Earth:

$$\frac{r_1}{R_\odot} < \left(\frac{\log 2}{2.16} + \frac{R_\odot}{R_1} \right)^{-1}. \quad (\text{A.7})$$

From Figure A.26, r_1 and r_2 will always be smaller than R_1 and R_2 , respectively. The Newkirk model requires that the density at r_1 and r_2 be significantly higher than the density at R_1 and R_2 , respectively (Table A.1). Additionally, from the geometric representation in Figure A.26, we find that the electron density at r_1 is higher than at R_1 , hence the radio emission cannot reach the Earth from that point behind the POS (Mann, G. et al. 2018).

From Table A.1, the assumption of Equation A.6 is not satisfied. Thus, the $-Z$ solution is invalid in our case. This implies that the harmonic emission from behind the POS will not reach the Earth. Thus, the $+Z$ assumption is the valid solution.

Table A.1: Radial distances and densities at the first (R_1) and last (R_2) radio sources were obtained from the $2.5 \times$ Newkirk model, as well as their impact parameters r_1 and r_2 , respectively.

Point	Radial distance (R_\odot)	Density (cm^{-3})	Ratio (n_r/n_R)
r_1	1.58	5.69×10^7	
R_1	1.81	4.82×10^6	11.81
r_2	2.6	2.59×10^7	
R_2	3.49	1.82×10^6	14.23

Furthermore, I analyzed the time difference of arrival of the radio emission at interplanetary wavelengths in Figure A.27. Specifically, we compared the timing of peak signals at a low frequency between two spacecraft, Wind and STEREO. This analysis was conducted under the assumption of two possible scenarios:

- one in which the radio emission source follows a trajectory that is roughly equidistant between Wind and STEREO – if the $+Z$ assumption is true.
- the trajectory implies significantly longer travel times from the source to Wind compared to STEREO – if the $-Z$ assumption is true.

Examining the data, I selected the frequency channel 700 kHz observed by Wind and its nearest counterpart 675 kHz for STEREO. Interestingly, the difference in the arrival times of these signals was merely one minute, which is within the bounds of the time resolution of the instrument. This negligible difference in arrival times supports the $+Z$ assumption for the beam trajectory, meaning it travels approximately at an equal distance between the two spacecraft.

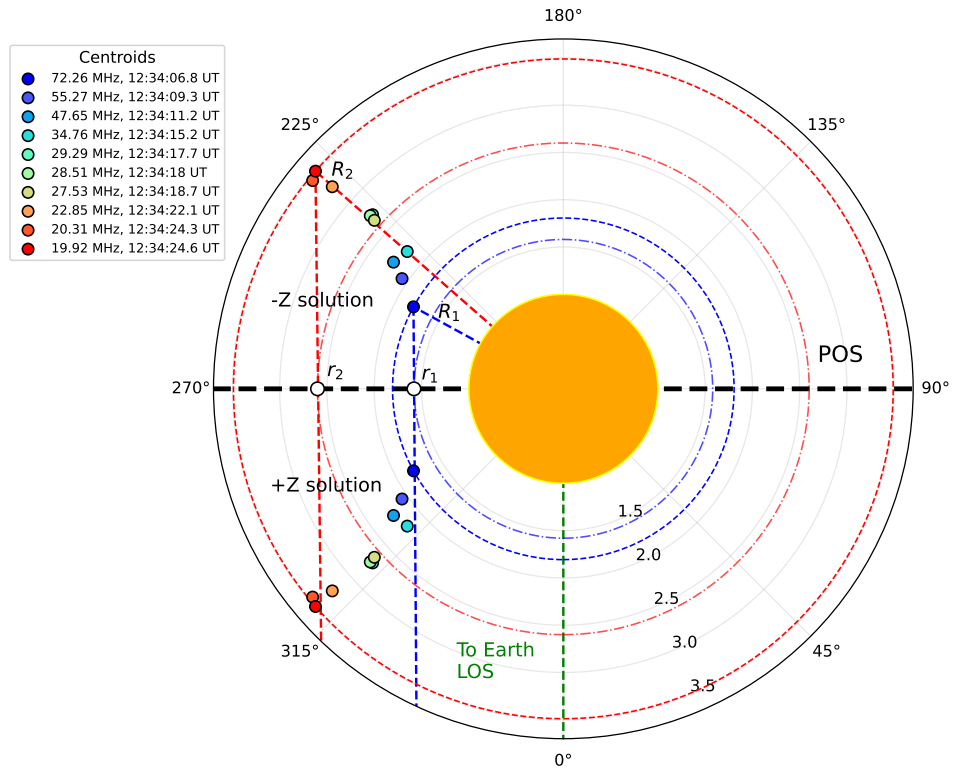


Figure A.26: Schematic shows the locations of the radio sources for the $+Z$ and $-Z$ solutions of Equation 3.4. The Sun is located in the middle as an orange circle, with a horizontal dashed black line representing the POS. The vertical dashed green line represents the Sun-Earth LOS. The dashed blue and red circles represent the plasma spheres of density equivalent to the observation frequencies of the innermost and outermost radio sources at R_1 and R_2 , respectively, under the Newkirk model assumption of spherically-symmetric density distribution. The impact parameters r_1 and r_2 are the projection of R_1 and R_2 on the POS. The dot-dashed blue and red circles are the circles passing through the impact parameters r_1 and r_2 , respectively.

A.4 Machine Learning Terminologies

In this section, I introduce the main concepts related to machine learning which are presented in the dissertation.

- **Cross-validation:** A technique used to evaluate the performance of a machine learning model by dividing the data into subsets and assessing the model on different combinations of these subsets.
- **Input Horizon:** The number of previous time steps considered as input to a model for time series forecasting. It represents the length of the historical sequence used for predictions.
- **Batch Size:** The number of samples processed together in a single iteration of the training algorithm. It affects training speed and memory requirements.
- **Updating the Model's Weights:** The process of adjusting the parameters of a neural network based on training data to minimize the difference between predicted and true outputs. The model's weights represent the parameters that are learned during the training process.
- **Loss:** A function that quantifies the difference between predicted and actual outputs. It guides the optimization process during training.
- **Minimum Validation Loss:** The lowest value achieved by the loss function on a validation dataset during training. It indicates the most accurate predictions on unseen data.
- **Overfitting:** When a model performs well on training data but fails to generalize to unseen data due to memorizing training examples instead of learning underlying patterns.

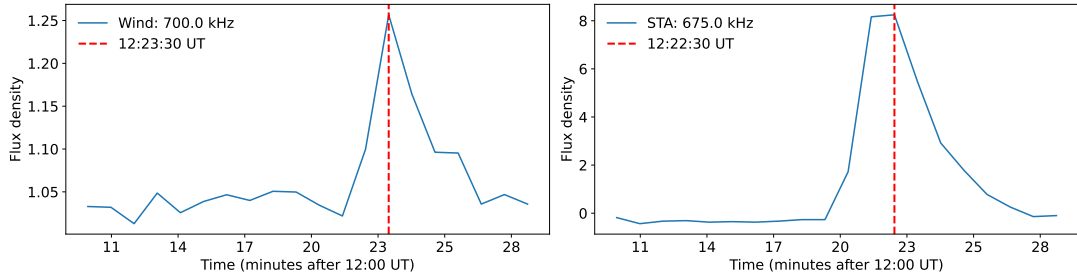


Figure A.27: Cut of the flux density at 700 kHz observed by Wind (left panel) and STEREO-A (right panel). Note: for STEREO-A, there is no exact frequency channel at 700 kHz; therefore we selected the nearest one (675 kHz).

- **Learning Rate:** A hyperparameter that determines the step size at each iteration of the optimization algorithm during training. It affects learning speed and convergence. A high learning rate can cause the training process to converge quickly, but it may also result in overshooting the optimal solution or getting stuck in a suboptimal solution. On the other hand, a very low learning rate can make the training process slow, and may struggle to find the optimal solution.
- **Reducing the learning rate when the validation loss stops improving:** This concept involves adjusting the learning rate dynamically during the training process. When the validation loss reaches a plateau or stops improving, it indicates a suboptimal point. By reducing the learning rate, the model can take smaller steps in weight space, potentially finding a better solution. This technique, known as learning rate scheduling or learning rate decay, is commonly used to fine-tune the model's performance.
- **Patience:** A parameter used in training to determine the number of epochs to wait for an improvement in validation loss before stopping the training process.
- **Patience Parameter of 7:** In the context of early stopping, training will be stopped if the validation loss does not improve for 7 consecutive epochs.
- **Adam Optimizer:** A popular optimization algorithm in deep learning that combines Adaptive Gradient Algorithm (AdaGrad) and Root Mean Square Propagation (RMSprop) to achieve efficient optimization.
- **Optimal Architecture:** The best configuration of a neural network, including the number of layers, neurons, and other choices, for optimal performance on a specific task.
- **Hyperparameters:** Parameters set before training a model that control the learning algorithm's behavior, such as learning rate, batch size, and activation functions.
- **Layer:** A building block of a neural network that performs specific operations on input data. Includes input, hidden, output, fully connected, convolutional, recurrent, activation, and dropout layers. Here is a description for each layer:
 - **Input Layer:** The first layer of a neural network that receives raw input data. It passes the input to subsequent layers for further processing. The number of nodes in the input layer is determined by the dimensionality of the input data.
 - **Hidden Layers:** Intermediate layers between the input and output layers. They perform computations on the input data and capture higher-level representations or abstractions. Hidden layers are not directly exposed to the input or output.
 - **Output Layer:** The final layer of a neural network that produces model predictions or outputs based on computations from preceding layers. The number of neurons in the output layer depends on the problem being solved, such as regression or classification.
 - **Fully Connected Layer (Dense Layer):** Each neuron in this layer is connected to every neuron in the previous layer. It allows information flow between all neurons, enabling complex relationships to be learned.

- **Convolutional Layer:** Commonly used in Convolutional Neural Networks (CNNs) for analyzing grid-like data, such as images. It applies convolution operations using filters or kernels to learn spatial patterns or features.
- **Recurrent Layer:** Used in Recurrent Neural Networks (RNNs) to process sequential data. These layers have feedback connections that allow information to be passed from one step to the next, capturing temporal dependencies and maintaining memory of past inputs.
- **Activation Layer:** Applies a non-linear function to the output of a layer, introducing non-linearity into the neural network. Activation functions like Sigmoid, Hyperbolic Tangent (\tanh), or Rectified Linear Unit (ReLU) determine neuron outputs based on weighted inputs.
- **Dropout Layer:** A regularization technique commonly used in deep learning models. It randomly sets a fraction of outputs from the previous layer to zero during training, preventing overfitting and improving generalization.

Layers play a crucial role in the information processing and learning capabilities of neural networks. The arrangement and combination of different layers determine the network's architecture and ultimately its ability to solve specific tasks.

- **Stateful:** A property of Recurrent Neural Networks (RNNs) where the hidden state is preserved between consecutive inputs, allowing the network to have memory.
- **Neuron:** A computational unit in a neural network that receives input, applies weights, and passes the result through an activation function to produce an output.
- **Hidden Neuron:** A neuron in a hidden layer of a neural network that performs intermediate computations.
- **Callback Function:** A function used during model training to perform specific actions at certain points or conditions, such as saving the best model, adjusting learning rates, or early stopping.
- **LearningRateScheduler Callback Function:** A function used in training to dynamically adjust the learning rate at specific points based on a predefined schedule or function. It improves training efficiency and convergence by allowing the model to make finer adjustments as it approaches the optimal solution.

A.4.1 Mathematical Representation of the LSTM NN Model

The computations inside one LSTM cell can be described by the following formulas (Ihianle et al. 2020):

$$f_t = \sigma(W_f x_t + U_f h_{t-1} + b_f) \quad (\text{A.8a})$$

$$i_t = \sigma(W_i x_t + U_i h_{t-1} + b_i) \quad (\text{A.8b})$$

$$\tilde{C}_t = \tanh(W_c x_t + U_c h_{t-1} + b_c) \quad (\text{A.8c})$$

$$C_t = f_t \odot C_{t-1} + i_t \odot \tilde{C}_t \quad (\text{A.8d})$$

$$o_t = \sigma(W_o x_t + U_o h_{t-1} + b_o) \quad (\text{A.8e})$$

$$h_t = o_t \odot \tanh(C_t) \quad (\text{A.8f})$$

where x_t is input data at time t . The input gate i_t determines which values from the updated cell states (candidate values) \tilde{C}_t should be added to the cell state. It also takes into account the current input x_t and the previous output h_{t-1} , and is passed through a sigmoid activation function. \tilde{C}_t represent the candidate values that are added to the cell state at time t . The forget gate activation vector f_t at time step t , which determines how much of the previous cell state should be retained. The cell state C_t at time t is updated based on the forget gate, input gate, and candidate values. The output gate o_t at time t determines how much of the cell state should be output. The output vector h_t at time t is calculated based on the cell state and the output gate values. h_{t-1} is the output vector at the previous time step $t - 1$. W_f, W_i, W_c, W_o are the weight matrices for the input vector x_t . U_f, U_i, U_c, U_o are the weight matrices for the output vector h_{t-1} . b_f, b_i, b_c, b_o are the bias vectors. The symbol \odot denotes a pointwise multiplication. The sigmoid function σ is used as the activation function for the gate vectors, and the hyperbolic tangent function \tanh is used for the candidate values and the output vector.

A.4.2 Evaluation Metrics

To evaluate the model performance, we used the following equations:

$$L_\delta(y, \hat{y}) = \begin{cases} \frac{1}{2}(y - \hat{y})^2, & \text{if } |y - \hat{y}| \leq \delta, \\ \delta(|y - \hat{y}| - \frac{1}{2}\delta), & \text{otherwise} \end{cases} \quad (\text{A.9a})$$

$$MSE = \frac{1}{N} \sum_{i=1}^N (y_i - \hat{y}_i)^2 \quad (\text{A.9b})$$

$$MAE = \frac{1}{N} \sum_{i=1}^N |y_i - \hat{y}_i| \quad (\text{A.9c})$$

$$RMSE = \sqrt{\frac{\sum_{i=1}^N (y_i - \hat{y}_i)^2}{N}} \quad (\text{A.9d})$$

$$MAPE = \frac{1}{N} \sum_{i=1}^N \left| \frac{y_i - \hat{y}_i}{\hat{y}_i} \right| \quad (\text{A.9e})$$

$$R = \frac{\sum_{i=1}^n (y_i - \bar{y})(\hat{y}_i - \bar{\hat{y}})}{\sqrt{\sum_{i=1}^n (y_i - \bar{y})^2} \sqrt{\sum_{i=1}^n (\hat{y}_i - \bar{\hat{y}})^2}} \quad (\text{A.9f})$$

where y is the true value, \hat{y} is the predicted value, and δ is a threshold in the Huber loss function that controls the trade-off between the mean squared error (MSE) and the mean absolute error (MAE). In this paper, it was set to 0.1, which was selected based on several experiments.

MSE is the mean squared error, which measures the difference between predicted and actual values by calculating the average of squared differences. It provides a measure of the average squared magnitude of the errors in your forecasts, which can be useful in penalizing larger errors more heavily than smaller errors.

MAPE is the mean absolute percentage error, which measures the difference between predicted and actual values by calculating the average of absolute differences. It provides a measure of the average magnitude of the errors, allowing to evaluate the overall accuracy of your forecasts.

RMSE is the root mean squared error, which measures the difference between predicted and actual values by taking the square root of the average of squared differences. It provides a measure of the accuracy of the forecasts in the same units as the original data, allowing to evaluate the magnitude of errors in the same scale as the data.

MAPE is the mean absolute percentage error, which measures the accuracy of a forecast by calculating the average of absolute percentage errors. It provides a measure of the accuracy of the forecasts in percentage terms, allowing to evaluate the magnitude of errors relative to the actual values. MSE, MAE, RMSE, and MAPE are often used in regression analysis to assess the accuracy of the model's predictions.

Finally, R is the Pearson correlation coefficient, which measures the strength and direction of the relationship between two continuous variables, and can provide an indication of the extent to which changes in one variable may be related to changes in the other.

A.5 Deep Learning Model Configuration

The configurations for the ML models shown in Figure 4.5 and their performance on the validation set and the test set for the SEP integral flux ≥ 10 MeV are presented in Table A.2. The batch size was set to be 64 and the number of training epochs was set to be 100. The *EarlyStopping* callback function, with a *patience* of 10, is used to help prevent overfitting during the training process by stopping training when the monitored metric has stopped improving for a certain number of epochs. The *patience* parameter controls how many epochs the training will continue without improvement before it is stopped. This is useful because if the validation loss stops getting better, the model has probably overfitted the training data and is not generalizing effectively to new data. By stopping the training early, we can avoid wasting time and resources on further training that is unlikely to improve the model's performance.

I used the *ModelCheckpoint* callback function to save the best weights of the model during training so that they can be reused later. The *LearningRateScheduler* callback function allows to dynamically adjust the learning rate of the model during training using a function passed to it that will be called at the beginning of each epoch, and it should return the desired learning rate for that epoch. It can be

useful when training deep neural networks, as it allows for a higher learning rate in the early stages of training when the model is still far from convergence, and a lower learning rate as the model approaches convergence, which can help it to converge more accurately. The downside might be the longer training time.

Table A.2: Configuration of the ML model. (1) refers to the error value for 1-day forecasting. Same for (2) refers to 2-day forecasting, and (3) for 3-day forecasting. *In the 1D-CNN layer, 32 filters, a kernel size of 5, and strides of 1 were used.

Model Architecture	No. of Hidden Layers	No. of Hidden Neurons	Activation Function	Batch Size	Learning Rate	Epochs	Callbacks Functions	Validation Set				Testing Set			
								MAE	MSE	RMSE	MAPE	MAE	MSE	RMSE	MAPE
Linear	-	-	-	64	0.001	100	EarlyStopping	0.312	0.141	0.376	87.883	0.143	0.045	0.211	60.689
Dense ML	2	32	ReLU	64	0.001	100	EarlyStopping	0.262 (1)	0.118 (1)	0.344 (1)	132.580 (1)	0.400 (1)	0.281 (1)	0.530 (1)	238.898 (1)
Simple RNN	2	32	Tanh	64	0.001	100	EarlyStopping ModelCheckpoint	0.275 (2)	0.138 (2)	0.372 (2)	132.004 (2)	0.395 (2)	0.286 (2)	0.535 (2)	234.704 (2)
Stateful RNN	3	32	Tanh	64	1.58e-4	100	LearningRateScheduler EarlyStopping	0.290 (3)	0.166 (3)	0.407 (3)	129.288 (3)	0.392 (3)	0.294 (3)	0.542 (3)	230.896 (3)
Stateful LSTM	3	32	Tanh	64	1.58e-4	100	EarlyStopping	0.143 (1)	0.035 (1)	0.187 (1)	70.994 (1)	0.178 (1)	0.052 (1)	0.228 (1)	69.624 (1)
Stateful Bi-LSTM	3	32	Tanh	64	1.58e-4	100	EarlyStopping	0.171 (2)	0.063 (2)	0.251 (2)	68.694 (2)	0.171 (2)	0.071 (2)	0.265 (2)	78.075 (2)
1D-CNN LSTM	3	32 (5.1)*	ReLU Tanh	64	1.58e-4	100	EarlyStopping	0.264 (3)	0.118 (3)	0.343 (3)	72.505 (3)	0.200 (3)	0.084 (3)	0.289 (3)	67.416 (3)
								0.203 (1)	0.060 (1)	0.244 (1)	56.393 (1)	0.155 (1)	0.039 (1)	0.197 (1)	59.988 (1)
								0.305 (2)	0.131 (2)	0.362 (2)	81.028 (2)	0.223 (2)	0.079 (2)	0.281 (2)	71.679 (2)
								0.349 (3)	0.173 (3)	0.416 (3)	82.819 (3)	0.223 (3)	0.084 (3)	0.289 (3)	64.159 (3)
								0.095 (1)	0.021 (1)	0.146 (1)	40.335 (1)	0.098 (1)	0.020 (1)	0.141 (1)	41.781 (1)
								0.151 (2)	0.048 (2)	0.220 (2)	48.937 (2)	0.134 (2)	0.042 (2)	0.205 (2)	57.860 (2)
								0.174 (3)	0.076 (3)	0.275 (3)	55.662 (3)	0.166 (3)	0.071 (3)	0.267 (3)	68.025 (3)
								0.149 (1)	0.043 (1)	0.207 (1)	58.151 (1)	0.170 (1)	0.049 (1)	0.221 (1)	71.169 (1)
								0.190 (2)	0.074 (2)	0.272 (2)	60.154 (2)	0.211 (2)	0.090 (2)	0.300 (2)	92.727 (2)
								0.249 (3)	0.120 (3)	0.347 (3)	67.984 (3)	0.229 (3)	0.108 (3)	0.329 (3)	87.049 (3)
								0.108 (1)	0.027 (1)	0.165 (1)	41.164 (1)	0.098 (1)	0.023 (1)	0.151 (1)	51.732 (1)
								0.146 (2)	0.051 (2)	0.226 (2)	47.512 (2)	0.138 (2)	0.047 (2)	0.217 (2)	68.376 (2)
								0.177 (3)	0.078 (3)	0.279 (3)	53.087 (3)	0.156 (3)	0.067 (3)	0.259 (3)	69.338 (3)

All the calculations and model runs were implemented under the framework of TensorFlow 2.3.0 (Singh et al. 2020) in Python 3.6.13. The models were executed on Ubuntu 20.04.1 LTS OS with 4 × GPUs (NVIDIA GeForce RTX 2080 Ti, 11019 MiB, 300 MHz). According to the Keras API guide (Ketkar & Ketkar 2017), the requirements to use the cuDNN implementation are the activation function must be set to *tanh* and the recurrent activation must be set to *sigmoid*. I also set the seed number to 7 across all the model runs to maintain reproducibility.

Stateful RNNs can be difficult to work with when using callbacks in Keras because their hidden state must be manually managed across mini-batch updates. When training a stateful RNN in Keras, the hidden state is carried over from the previous epoch and can cause problems with certain callbacks, such as *EarlyStopping* or *ModelCheckpoint*. To work around this issue, one can use stateless RNNs or manually reset the hidden state at the end of each epoch, but this can be complex and prone to errors.

A.6 Description of Skill Scores

Skill scores and ratios are commonly used in evaluating the performance of classification models, particularly in binary classification tasks. They provide insights into the model’s ability to correctly predict positive and negative instances. Here is a brief description of each skill score and ratio, along with their formulas:

- **True Positive (TP):** The number of data points or intervals correctly identified as positive by the model. It represents instances where both the model and the ground truth indicate the presence of an event.
- **True Negative (TN):** The number of intervals correctly identified as negative by the model. It represents instances where both the model and the ground truth indicate the absence of an event.
- **False Positive (FP):** The number of intervals incorrectly identified as positive by the model. It occurs when the model predicts an event, but the ground truth indicates its absence.
- **False Negative (FN):** The number of intervals incorrectly identified as negative by the model. It occurs when the model fails to detect an event that the ground truth indicates its presence.
- **Accuracy:** Represents the proportion of correct predictions out of total predictions.

$$\text{Accuracy} = \frac{TP + TN}{TP + TN + FP + FN} \quad (\text{A.10})$$

- **Precision:** Represents the proportion of positive predictions that are actually positive.

$$\text{Precision} = \frac{TP}{TP + FP} \quad (\text{A.11})$$

- **Probability of Detection (POD) or Recall:** Represents the model's ability to correctly identify positive instances.

$$POD = \frac{TP}{TP + FN} \quad (\text{A.12})$$

- **Probability of False Detection (POFD):** Measures the model's tendency to falsely predict positive instances when the ground truth indicates their absence.

$$POFD = \frac{FP}{FP + TN} \quad (\text{A.13})$$

- **False Alarm Rate (FAR):** Indicates the ratio of false positive predictions to the total number of positive instances.

$$FAR = \frac{FP}{FP + TP} \quad (\text{A.14})$$

- **Critical Success Index (CSI):** Measures the model's ability to correctly predict both positive and negative instances.

$$CSI = \frac{TP}{TP + FP + FN} \quad (\text{A.15})$$

- **True Skill Statistic (TSS):** Takes into account both the model's ability to detect positive instances and its ability to avoid false alarms.

$$TSS = POD - FAR \quad (\text{A.16})$$

- **Heidke Skill Score (HSS):** Evaluates the model's performance by comparing it with random chance. It takes into account the agreement between the model's predictions and the observed data, considering both true positive and true negative predictions.

$$HSS = \frac{TP + TN - C}{T - C} \quad (\text{A.17})$$

where

$$T = TP + TN + FP + FN$$

$$C = \frac{(TP + FP)(TP + FN) + (TN + FP)(TN + FN)}{T}$$

Bibliography

- 2017, Nature Astronomy, 1, 771
- Abe, O., Fakomiti, M., Igboama, W., et al. 2023, Advances in Space Research, 71, 2240
- Akansu, A. N. 1991, Optical Engineering, 30, 912
- Akasofu, S. I. 1981, Space Science Reviews, 28, 121
- Alharbi, F. R. & Csala, D. 2021, in 2021 International Conference on Electrical, Communication, and Computer Engineering (ICECCE), IEEE, 1–6
- Alieldén, K. & Taroyan, Y. 2022, The Astrophysical Journal, 935, 66
- Altschuler, M. D. & Newkirk, G. 1969, Solar Physics, 9, 131
- Amari, T., Canou, A., & Aly, J.-J. 2014, Nature, 514, 465
- Aminalragia-Giamini, S., Raptis, S., Anastasiadis, A., et al. 2021, Journal of Space Weather and Space Climate, 11, 59
- Aran, A., Sanahuja, B., & Lario, D. 2006, Advances in Space Research, 37, 1240
- Aschwanden, M. J. 2002, Space Science Reviews, 101, 1
- Aschwanden, M. J. 2010, Solar Physics, 262, 235
- Badman, S. T., Carley, E., Cañizares, L. A., et al. 2022, The Astrophysical Journal, 938, 95
- Bale, S., Goetz, K., Harvey, P., et al. 2016, Space science reviews, 204, 49
- Bastian, T., Pick, M., Kerdraon, A., Maia, D., & Vourlidas, A. 2001, The Astrophysical Journal, 558, L65
- Battarbee, M., Vainio, R., Laitinen, T., & Hietala, H. 2013, Astronomy & Astrophysics, 558, A110
- Bein, B. M., Berkebile-Stoiser, S., Veronig, A. M., et al. 2011, apj, 738, 191
- Benson, B., Pan, W. D., Prasad, A., Gary, G. A., & Hu, Q. 2020, Solar Physics, 295, 65
- Benz, A. & Thejappa, G. 1988
- Benz, A. O. 2017, Living reviews in solar physics, 14, 1
- Berghmans, D., Auchère, F., Long, D. M., et al. 2021, Astronomy & Astrophysics, 656, L4
- Besliu-Ionescu, D., Maris Muntean, G., & Dobrica, V. 2022, Solar Physics, 297, 65
- Biesecker, D., Myers, D., Thompson, B., Hammer, D., & Vourlidas, A. 2002, The Astrophysical Journal, 569, 1009
- Bonnin, X., Hoang, S., & Maksimovic, M. 2008, Astron. Astrophys., 489, 419
- Borovsky, J. E. & Denton, M. H. 2006, Journal of Geophysical Research: Space Physics, 111
- Boudjada, M. Y., Abou el Fadl, A., Galopeau, P. H., Al-Haddad, E., & Lammer, H. 2020, Advances in Radio Science, 18, 83

- Brewer, D. A., Barth, J. L., Label, K. A., Kauffman, W. J., & Giffin, G. 2002, *Acta Astronautica*, 51, 609
- Bruno, A. & Richardson, I. G. 2021, *Solar Physics*, 296, 36
- Byrne, J., Long, D., Gallagher, P., et al. 2013, *Astronomy & Astrophysics*, 557, A96
- Camporeale, E. 2019, *Space weather*, 17, 1166
- Cane, H. V., Erickson, W., & Prestage, N. 2002, *Journal of Geophysical Research: Space Physics*, 107, SSH
- Cattell, C., Glesener, L., Leiran, B., et al. 2021, *Astron. Astrophys.*, 650, A6
- Che, H. 2018, *Journal of Physics: Conference Series*, 1100, 012005
- Chen, N., Ip, W.-H., & Innes, D. 2013, *Astrophys. J.*, 769, 96
- Chen, P. 2016, *Low-Frequency Waves in Space Plasmas*, 379
- Chen, P. F., Wu, S. T., Shibata, K., & Fang, C. 2002, *The Astrophysical Journal*, 572, L99
- Chen, X., Kontar, E. P., Chrysaphi, N., et al. 2023, arXiv e-prints, arXiv:2306.09160
- Cheung, M. C., Boerner, P., Schrijver, C., et al. 2015, *The Astrophysical Journal*, 807, 143
- Chhabra, S., Klimchuk, J. A., & Gary, D. E. 2021, *The Astrophysical Journal*, 922, 128
- Cohen, C. & Mewaldt, R. 2018, *Space Weather*, 16, 1616
- Curto, J. J., Blanca, M., & Martínez, E. 2008, *Solar Physics*, 250, 411
- Dabrowski, B., Flisek, P., Mikuła, K., et al. 2021, *Remote Sensing*, 13, 148
- Dalla, S., Swalwell, B., Battarbee, M., et al. 2017 in (Cambridge University Press), 268–271
- Debrunner, H., Flückiger, E., Grädel, H., Lockwood, J., & McGuire, R. 1988, *Journal of Geophysical Research: Space Physics*, 93, 7206
- Del Zanna, G., Aulanier, G., Klein, K.-L., & Török, T. 2011, *Astronomy & Astrophysics*, 526, A137
- Delannée, C. & Aulanier, G. 1999, *Solar Physics*, 190, 107
- Desai, M. & Giacalone, J. 2016, *Living Reviews in Solar Physics*, 13, 3
- Dierckxsens, M., Tziotziou, K., Dalla, S., et al. 2015, *Solar Physics*, 290, 841
- Domingo, V., Fleck, B., & Poland, A. I. 1995, *Solar Physics*, 162, 1
- Dulk, G., Steinberg, J.-L., Lecacheux, A., Hoang, S., & MacDowall, R. J. 1985, *Astronomy and Astrophysics*, 150, L28
- Dumbović, M., Veronig, A., Podladchikova, T., et al. 2021, *Astronomy & Astrophysics*, 652, A159
- Dungey, J. 1961, *Journal of Geophysical Research*, 66, 1043
- Eastwood, J., Nakamura, R., Turc, L., Mejnertsen, L., & Hesse, M. 2017, *Space Science Reviews*, 212, 1221
- Echer, E. & Gonzalez, W. 2022, *Advances in Space Research*, 70, 2830
- Echer, E., Tsurutani, B., & Gonzalez, W. 2013, *Journal of Geophysical Research: Space Physics*, 118, 385
- Efron, B. 1979, *The Annals of Statistics*, 7, 1
- Engell, A., Falconer, D., Schuh, M., Loomis, J., & Bissett, D. 2017, *Space Weather*, 15, 1321
- Ergun, R., Larson, D., Lin, R., et al. 1998, *The Astrophysical Journal*, 503, 435

- Feynman, J., Armstrong, T., Dao-Gibner, L., & Silverman, S. 1990, Solar Physics, 126, 385
- Fletcher, L., Dennis, B. R., Hudson, H. S., et al. 2011, Space science reviews, 159, 19
- Florios, K., Kontogiannis, I., Park, S.-H., et al. 2018, Solar Physics, 293, 28
- Fox, N., Velli, M., Bale, S., et al. 2016, Space Science Reviews, 204, 7
- Fredkin, D. R., Rice, J. A., Colquhoun, D., & Gibb, A. 1995, Philosophical Transactions of the Royal Society of London. Series B: Biological Sciences, 350, 353
- Gabriel, S., Evans, R., & Feynman, J. 1990, Solar physics, 128, 415
- Gallagher, P. T., Lawrence, G. R., & Dennis, B. R. 2003, The Astrophysical Journal Letters, 588, L53
- Gieseler, J., Dresing, N., Palmroos, C., et al. 2023, Frontiers in Astronomy and Space Sciences, 9, 384
- Gonzalez, W., Joselyn, J.-A., Kamide, Y., et al. 1994, Journal of Geophysical Research: Space Physics, 99, 5771
- González, W. D., Echer, E., Clua-Gonzalez, A., & Tsurutani, B. T. 2007, Geophysical research letters, 34
- Goodfellow, I., Bengio, Y., & Courville, A. 2016, Deep learning (MIT press)
- Gopalswamy, N. 2022, Atmosphere, 13, 1781
- Gopalswamy, N., Akiyama, S., Yashiro, S., Michalek, G., & Lepping, R. 2008, Journal of Atmospheric and Solar-Terrestrial Physics, 70, 245
- Gopalswamy, N., Mäkelä, P., Yashiro, S., et al. 2017in , IOP Publishing, 012009
- Gopalswamy, N., Mäkelä, P., Yashiro, S., Akiyama, S., & Xie, H. 2022a, in 2022 3rd URSI Atlantic and Asia Pacific Radio Science Meeting (AT-AP-RASC), 1–4
- Gopalswamy, N. & Yashiro, S. 2011, apjl, 736, L17
- Gopalswamy, N., Yashiro, S., Akiyama, S., et al. 2022b, Journal of Geophysical Research: Space Physics, 127, e2022JA030404
- Graves, A. & Jaitly, N. 2014in (Beijing, China: PMLR), 1764–1772
- Graves, A. & Schmidhuber, J. 2005, Neural networks, 18, 602
- Greff, K., Srivastava, R. K., Koutník, J., Steunebrink, B. R., & Schmidhuber, J. 2016, IEEE transactions on neural networks and learning systems, 28, 2222
- Guo, F. & Giacalone, J. 2013, The Astrophysical Journal, 773, 158
- Gurnett, D. A. & Anderson, R. R. 1976, Science, 194, 1159
- Gurnett, D. A. & Anderson, R. R. 1977, Journal of Geophysical Research, 82, 632
- Hale, G. E., Ellerman, F., Nicholson, S. B., & Joy, A. H. 1919, Astrophys. J., 49, 153
- Harra, L., Brooks, D. H., Bale, S. D., et al. 2021, Astronomy & Astrophysics, 650, A7
- Harvey, J. W., Hill, F., Hubbard, R. P., et al. 1996, Science, 272, 1284
- Hochreiter, S. & Schmidhuber, J. 1997, Neural computation, 9, 1735
- Holman, G. D., Aschwanden, M. J., Aurass, H., et al. 2011, Space science reviews, 159, 107
- Holschneider, M., Kronland-Martinet, R., Morlet, J., & Tchamitchian, P. 1989, in Wavelets. Time-Frequency Methods and Phase Space, ed. J.-M. Combes, A. Grossmann, & P. Tchamitchian (Springer-Verlag), 286
- Hu, J., Li, G., Ao, X., Zank, G. P., & Verkhoglyadova, O. 2017, Journal of Geophysical Research: Space Physics, 122, 10

- Huang, X., Tan, H., Lin, G., & Tian, Y. 2018, 2018 International Conference on Artificial Intelligence and Big Data (ICAIBD), 185
- Ihianle, I. K., Nwajana, A. O., Ebenuwa, S. H., et al. 2020, IEEE Access, 8, 179028
- Ireland, J., Inglis, A. R., Shih, A. Y., et al. 2019, Solar Physics, 294, 158
- Jackson, B., Hick, P., Buffington, A., et al. 2010in , American Institute of Physics, 659–662
- Jang, S., Moon, Y.-J., Kim, R.-S., Lee, H., & Cho, K.-S. 2016, The Astrophysical Journal, 821, 95
- Kahler, S., Cliver, E., Cane, H., et al. 1987, in Proceedings of the 20th International Cosmic Ray Conference Moscow, Volume 3, p. 121
- Kahler, S., Kazachenko, M., Lynch, B., & Welsch, B. 2017in , IOP Publishing, 012011
- Kahler, S., Sheeley Jr, N., Howard, R., et al. 1984, Journal of Geophysical Research: Space Physics, 89, 9683
- Kahler, S. W., Cliver, E. W., & Ling, A. G. 2007, Journal of Atmospheric and Solar-Terrestrial Physics, 69, 43
- Kane, R. 2011, Indian Journal of Radio & Space Physics, 40, 7
- Kasapis, S., Zhao, L., Chen, Y., et al. 2022, Space Weather, 20, e2021SW002842
- Kay, C. & Gopalswamy, N. 2018, Journal of Geophysical Research: Space Physics, 123, 7220
- Ketkar, N. & Ketkar, N. 2017, Deep learning with python: a hands-on introduction, 97
- Kim, T., Park, E., Lee, H., et al. 2019, Nature Astronomy, 3, 397
- Kingma, D. P. & Ba, J. 2015, International Conference on Learning Representations (ICLR), San Diego
- Klassen, A., Karlický, M., & Mann, G. 2003a, Astronomy & Astrophysics, 410, 307
- Klassen, A., Pohjolainen, S., & Klein, K.-L. 2003b, Solar Physics, 218, 197
- Klein, K.-L. & Dalla, S. 2017, Space Science Reviews, 212, 1107
- Kolen, J. F. & Kremer, S. C. 2001, Gradient Flow in Recurrent Nets: The Difficulty of Learning LongTerm Dependencies (IEEE), 237–243
- Kong, D., Pan, G., Yan, X., Wang, J., & Li, Q. 2018, The Astrophysical Journal Letters, 863, L22
- Kong, X., Guo, F., Giacalone, J., Li, H., & Chen, Y. 2017, The Astrophysical Journal, 851, 38
- Kontar, E. P., Chen, X., Chrysaphi, N., et al. 2019, The Astrophysical Journal, 884, 122
- Kontar, E. P., Emslie, A. G., Clarkson, D. L., et al. 2023, arXiv preprint arXiv:2308.05839
- Kontar, E. P., Yu, S., Kuznetsov, A., et al. 2017, Nature communications, 8, 1515
- Kóta, J., Manchester, W., Jokipii, J., De Zeeuw, D., & Gombosi, T. 2005in , American Institute of Physics, 201–206
- Kouloumvakos, A., Rodríguez-García, L., Gieseler, J., et al. 2022, Frontiers in Astronomy and Space Sciences, 9, 974137
- Kozarev, K., Nedal, M., Miteva, R., Dechev, M., & Zucca, P. 2022, Frontiers in Astronomy and Space Sciences, 9, 34
- Kozarev, K., Schwadron, N., Dayeh, M., et al. 2010, Space Weather, 8
- Kozarev, K. A., Davey, A., Kendrick, A., Hammer, M., & Keith, C. 2017, Journal of Space Weather and Space Climate, 7, A32
- Kozarev, K. A., Dayeh, M. A., & Farahat, A. 2019, The Astrophysical Journal, 871, 65

- Kozarev, K. A., Evans, R. M., Schwadron, N. A., et al. 2013, *The Astrophysical Journal*, 778, 43
- Kozarev, K. A., Korreck, K. E., Lobzin, V. V., Weber, M. A., & Schwadron, N. A. 2011, *The Astrophysical Journal*, 733, L25
- Kozarev, K. A., Raymond, J. C., Lobzin, V. V., & Hammer, M. 2015, *The Astrophysical Journal*, 799, 167
- Kozarev, K. A. & Schwadron, N. A. 2016, *apj*, 831, 120
- Krucker, S., Hudson, H. S., Jeffrey, N. L. S., et al. 2011, *The Astrophysical Journal*, 739, 96
- Krupar, V., Szabo, A., Maksimovic, M., et al. 2020, *Astrophys. J. Suppl.*, 246, 57
- Kwon, R.-Y., Zhang, J., & Olmedo, O. 2014, *The Astrophysical Journal*, 794, 148
- Laitinen, T. & Dalla, S. 2017, *The Astrophysical Journal*, 834, 127
- Lakhina, G. S. & Tsurutani, B. T. 2016, *Geoscience Letters*, 3, 1
- Lanzerotti, L. J. 2001, Washington DC American Geophysical Union Geophysical Monograph Series, 125, 11
- Laurenza, M., Cliver, E., Hewitt, J., et al. 2009, *Space Weather*, 7
- Lavasa, E., Giannopoulos, G., Papaioannou, A., et al. 2021, *Solar Physics*, 296, 107
- Le, G.-M. & Zhang, X.-F. 2017, *Research in Astronomy and Astrophysics*, 17, 123
- Lecacheux, A., Steinberg, J. L., Hoang, S., & Dulk, G. A. 1989, *Astron. Astrophys.*, 217, 237
- Lemen, J. R., Akin, D. J., Boerner, P. F., et al. 2011, in *The solar dynamics observatory* (Springer), 17–40
- Lemen, J. R., Title, A. M., Akin, D. J., et al. 2012, *Solar Physics*, 275, 17
- Li, B. & Cairns, I. H. 2012, *The Astrophysical Journal*, 753, 124
- Li, G., Shalchi, A., Ao, X., Zank, G., & Verkhoglyadova, O. 2012, *Advances in Space Research*, 49, 1067
- Li, G., Zank, G., & Rice, W. 2003, *Journal of Geophysical Research: Space Physics*, 108
- Li, R. & Zhu, J. 2013, *Research in Astronomy and Astrophysics*, 13, 1118
- Lilensten, J., Coates, A. J., Dehant, V., et al. 2014, *The Astronomy and Astrophysics Review*, 22, 1
- Lin, R. 2005, *Advances in Space Research*, 35, 1857
- Lin, R. 2011, *Space science reviews*, 159, 421
- Liu, W. & Ofman, L. 2014, *Solar Physics*, 289, 3233
- Long, D. M., Bloomfield, D. S., Chen, P.-F., et al. 2017, *Solar physics*, 292, 1
- Long, D. M., Bloomfield, D. S., Gallagher, P. T., & Pérez-Suárez, D. 2014, *Solar Physics*, 289, 3279
- Long, D. M., DeLuca, E. E., & Gallagher, P. T. 2011, *apjl*, 741, L21
- Ma, S., Raymond, J. C., Golub, L., et al. 2011, *The Astrophysical Journal*, 738, 160
- MacDowall, R., Lara, A., Manoharan, P., et al. 2003, *Geophysical research letters*, 30
- Madjarska, M. S. 2019, *Living Reviews in Solar Physics*, 16, 2
- Magdalenić, J., Marqué, C., Zhukov, A. N., Vršnak, B., & Žic, T. 2010a, *Astrophys. J.*, 718, 266
- Magdalenić, J., Marqué, C., Zhukov, A. N., Vršnak, B., & Žic, T. 2010b, *Astrophys. J.*, 718, 266
- Malandraki, O. E. & Crosby, N. B. 2018, *Solar particle radiation storms forecasting and analysis: the HESPERIA HORIZON 2020 project and beyond*

- Mann, G., Klassen, A., Aurass, H., & Classen, H.-T. 2003, *Astronomy & Astrophysics*, 400, 329
- Mann, G., Breitling, F., Vocks, C., et al. 2018, *A&A*, 611, A57
- Manu, V., Balan, N., Zhang, Q.-H., & Xing, Z.-Y. 2022, *Journal of Geophysical Research: Space Physics*, 127, e2022JA030747
- Markwardt, C. B. 2009, in *Astronomical Society of the Pacific Conference Series*, Vol. 411, *Astronomical Data Analysis Software and Systems XVIII*, ed. D. A. Bohlender, D. Durand, & P. Dowler, 251
- Melrose, D. 1980, *Space Science Reviews*, 26, 3
- Melrose, D. 2017, *Reviews of Modern Plasma Physics*, 1, 1
- Mierla, M., Inhester, B., Antunes, A., et al. 2010in , *Copernicus GmbH*, 203–215
- Mikić, Z., Linker, J. A., Schnack, D. D., Lionello, R., & Tarditi, A. 1999, *Physics of Plasmas*, 6, 2217
- Miteva, R., Klein, K.-L., Malandraki, O., & Dorrian, G. 2013, *Solar Physics*, 282, 579
- Miteva, R., Nedal, M., Samwel, S. W., & Temmer, M. 2023, *Universe*, 9, 179
- Miteva, R., Samwel, S., Costa-Duarte, M., & Danov, D. 2016, in *Proceedings of the Eighth Workshop” Solar Influences on the Magnetosphere, Ionosphere and Atmosphere*, Vol. 30, 27–30
- Miteva, R., Samwel, S., Costa-Duarte, M., & Malandraki, O. 2017, *Sun Geoph*, 12
- Moore, R. L., Sterling, A. C., Hudson, H. S., & Lemen, J. R. 2001, *The Astrophysical Journal*, 552, 833
- Morosan, D. E. & Gallagher, P. T. 2017, in *Planetary Radio Emissions VIII*, ed. G. Fischer, G. Mann, M. Panchenko, & P. Zarka, 357–368
- Morton, R., Tomczyk, S., & Pinto, R. 2015, *Nature Communications*, 6, 7813
- Muhr, N., Veronig, A. M., Kienreich, I. W., et al. 2014, *Solar Physics*, 289, 4563
- Nammous, M. K., Saeed, K., & Kobojeck, P. 2022, *Journal of King Saud University - Computer and Information Sciences*, 34, 764
- Nedal, M., Kozarev, K., Arsenov, N., & Zhang, P. 2023a, *J. Space Weather Space Clim.*, 13, 26
- Nedal, M., Kozarev, K., Zhang, P., & Pietro, Z. 2023b, *A&A*, 680, A106
- Nedal, M., Mahrous, A., & Youssef, M. 2019, *Astrophysics and Space Science*, 364, 161
- Newkirk, G. 1967, *Annual Review of Astronomy and Astrophysics*, 5, 213
- Newkirk, Gordon, J. 1961, *Astrophys. J.*, 133, 983
- Ng, C. K., Reames, D. V., & Tylka, A. J. 2012in , *American Institute of Physics*, 212–218
- Nieves-Chinchilla, T., Vourlidas, A., Raymond, J. C., et al. 2018, *Solar Physics*, 293, 1
- Nindos, A., Alissandrakis, C. E., Hillaris, A., & Preka-Papadema, P. 2011, *Astron. Astrophys.*, 531, A31
- Nindos, A., Aurass, H., Klein, K. L., & Trottet, G. 2008, *Sol. Phys.*, 253, 3
- Nitta, N. V., Mason, G. M., Wang, L., Cohen, C. M. S., & Wiedenbeck, M. E. 2015, *The Astrophysical Journal*, 806, 235
- Nitta, N. V., Schrijver, C. J., Liu, W., et al. 2013, *The Astrophysical Journal*, 776, 58
- Nymmk, R. 2007, *Advances in Space Research*, 40, 321
- Núñez, M. 2011, *Space Weather*, 9
- Odstrcil, D., Riley, P., & Zhao, X. 2004, *Journal of Geophysical Research: Space Physics*, 109
- Offringa, A. R., McKinley, B., Hurley-Walker, N., et al. 2014, *Mon. Not. R. Astron. Soc.*, 444, 606

- Ofman, L. & Thompson, B. 2002, *The Astrophysical Journal*, 574, 440
- Olah, C. 2015, Neural Networks, Types, and Functional Programming, [Blog post]
- Olmedo, O., Vourlidas, A., Zhang, J., & Cheng, X. 2012, *The Astrophysical Journal*, 756, 143
- Ontiveros, V. & Vourlidas, A. 2009, *The Astrophysical Journal*, 693, 267
- Ontiveros, V. & Vourlidas, A. 2009, *apj*, 693, 267
- Oughton, E. J., Skelton, A., Horne, R. B., Thomson, A. W., & Gaunt, C. T. 2017, *Space Weather*, 15, 65
- Pala, Z. & Atici, R. 2019, *Solar Physics*, 294, 50
- Paouris, E., Vourlidas, A., Papaioannou, A., & Anastasiadis, A. 2021, *Space Weather*, 19, e2020SW002617
- Papaioannou, A., Anastasiadis, A., Kouloumvakos, A., et al. 2018, *Solar Physics*, 293, 1
- Papaioannou, A., Vainio, R., Raukunen, O., et al. 2022, *Journal of Space Weather and Space Climate*, 12, 24
- Park, J., Innes, D. E., Bucik, R., & Moon, Y.-J. 2013, *The Astrophysical Journal*, 779, 184
- Parker, E. N. 1960, *Astrophysical Journal*, 132, 821
- Patsourakos, S. & Vourlidas, A. 2009, *The Astrophysical Journal*, 700, L182
- Patsourakos, S. & Vourlidas, A. 2012, *Solar Physics*, 281, 187
- Patsourakos, S., Vourlidas, A., & Stenborg, G. 2010, *Astrophys. J. Lett.*, 724, L188
- Pérez-Suárez, D., Higgins, P. A., Bloomfield, D. S., et al. 2011, Automated Solar Feature Detection for Space Weather Applications, 207–225
- Pesnell, W. D., Thompson, B. J., & Chamberlin, P. C. 2012, *solphys*, 275, 3
- Piantschitsch, I., Vršnak, B., Hanslmeier, A., et al. 2018, *The Astrophysical Journal*, 860, 24
- Pick, M. 2006, in *Solar and Heliospheric Origins of Space Weather Phenomena*, ed. J.-P. Rozelot, Vol. 699, 119
- Pick, M., Forbes, T. G., Mann, G., et al. 2006, Multi-Wavelength Observations of CMEs and Associated Phenomena, Vol. 21, 341
- Podladchikova, O. & Berghmans, D. 2005, *Solar Physics*, 228, 265
- Pomoell, J. & Poedts, S. 2018, *Journal of Space Weather and Space Climate*, 8, A35
- Priest, E. & Forbes, T. 2007, Magnetic Reconnection
- Pulkkinen, T. 2007, *Living Reviews in Solar Physics*, 4, 1
- Pulupa, M., Bale, S., Bonnell, J., et al. 2017, *Journal of Geophysical Research: Space Physics*, 122, 2836
- Pulupa, M., Bale, S. D., Badman, S. T., et al. 2020, *Astrophys. J. Suppl.*, 246, 49
- Pysz, M. A., Foygel, K., Panje, C. M., et al. 2011, *Investigative radiology*, 46, 187
- Qiu, S., Zhang, Z., Yousof, H., et al. 2022, *Advances in Space Research*, 70, 2047
- Ramstad, R., Holmström, M., Futaana, Y., et al. 2018, *Geophysical Research Letters*, 45, 7306
- Reames, D. V. 1999, *Space Science Reviews*, 90, 413
- Reames, D. V. 2000in , American Institute of Physics, 289–300
- Reames, D. V. 2013, *Space Science Reviews*, 175, 53

- Reames, D. V. 2021
- Reid, H. A. 2020, *Frontiers in Astronomy and Space Sciences*, 7, 56
- Reid, H. A. & Kontar, E. P. 2018a, *Astronomy & Astrophysics*, 614, A69
- Reid, H. A. & Kontar, E. P. 2018b, *The Astrophysical Journal*, 867, 158
- Reid, H. A. & Vilmer, N. 2017, *Astronomy & Astrophysics*, 597, A77
- Reid, H. A. S. & Ratcliffe, H. 2014, *Research in Astronomy and Astrophysics*, 14, 773
- Reiner, M. J., Goetz, K., Fainberg, J., et al. 2009, *Solar Physics*, 259, 255
- Richardson, I., von Rosenvinge, T., & Cane, H. 2016, *Solar Physics*, 291, 2117
- Ripley, B. D. 1996, *Pattern Recognition and Neural Networks* (Cambridge University Press)
- Rodriguez, J., Onsager, T., & Mazur, J. 2010, *Geophysical Research Letters*, 37
- Rouillard, A. P., Plotnikov, I., Pinto, R. F., et al. 2016, *The Astrophysical Journal*, 833, 45
- Rouillard, A. P., Sheeley, N. R., Tylka, A., et al. 2012, *The Astrophysical Journal*, 752, 44
- Saint-Hilaire, P., Vilmer, N., & Kerdraon, A. 2012, *The Astrophysical Journal*, 762, 60
- Saiz, E., Cerrato, Y., Cid, C., et al. 2013, *Journal of Space Weather and Space Climate*, 3, A26
- Samwel, S. & Miteva, R. 2023, *Advances in Space Research*, 72, 3440
- Savitzky, A. & Golay, M. J. 1964, *Analytical chemistry*, 36, 1627
- Schatten, K. H., Wilcox, J. M., & Ness, N. F. 1969, *Solar Physics*, 6, 442
- Schrijver, C. J. 2015, *Space Weather*, 13, 524
- Schrijver, C. J., Kauristie, K., Aylward, A. D., et al. 2015, *Advances in Space Research*, 55, 2745
- Schrijver, C. J. & Siscoe, G. L. 2010a, *Heliophysics: Evolving solar activity and the climates of space and Earth* (Cambridge University Press)
- Schrijver, C. J. & Siscoe, G. L. 2010b, *Heliophysics: Evolving solar activity and the climates of space and Earth* (Cambridge University Press)
- Schuster, M. & Paliwal, K. K. 1997, *IEEE transactions on Signal Processing*, 45, 2673
- Schwadron, N. A., Gorby, M., Török, T., et al. 2014, *Space Weather*, 12, 323
- Schwadron, N. A., Lee, M., Gorby, M., et al. 2015, *The Astrophysical Journal*, 810, 97
- Schwadron, N. A., Townsend, L., Kozarev, K., et al. 2010, *Space Weather*, 8
- Schwenn, R. 2006, *Living reviews in solar physics*, 3, 1
- Selvakumaran, R., Veenadhari, B., Akiyama, S., et al. 2016, *Journal of Geophysical Research: Space Physics*, 121, 8188
- Sheeley Jr, N., Walters, J., Wang, Y.-M., & Howard, R. 1999, *Journal of Geophysical Research: Space Physics*, 104, 24739
- Shibata, K. & Magara, T. 2011, *Living Reviews in Solar Physics*, 8, 1
- Singh, P., Manure, A., Singh, P., & Manure, A. 2020, *Learn TensorFlow 2.0: Implement Machine Learning and Deep Learning Models with Python*, 1
- Sokolov, I., Roussev, I., Gombosi, T., et al. 2004, *The Astrophysical Journal*, 616, L171
- Sokolov, I. V., Roussev, I. I., Skender, M., Gombosi, T. I., & Usmanov, A. V. 2009, *The Astrophysical Journal*, 696, 261

- Stansby, D., Yeates, A., & Badman, S. T. 2020, Journal of Open Source Software, 5, 2732
- Starck, J.-L. & Murtagh, F. 2002, Astronomical image and data analysis (Springer Netherlands)
- Stepanyuk, O., Kozarev, K., & Nedal, M. 2022, Journal of Space Weather and Space Climate, 12, 20
- Sundermeyer, M., Alkhouri, T., Wuebker, J., & Ney, H. 2014, in Proceedings of the 2014 conference on empirical methods in natural language processing (EMNLP) (Association for Computational Linguistics), 14–25
- Suzuki, S. & Dulk, G. 1985, Cambridge: Cambridge University Press, 289
- Švestka, Z. 1995, Advances in Space Research, 16, 27
- Szenicer, A., Fouhey, D. F., Munoz-Jaramillo, A., et al. 2019, Science Advances, 5, eaaw6548
- Temmer, M. 2016, Astronomische Nachrichten, 337, 1010
- Temmer, M. 2021, Living Reviews in Solar Physics, 18, 4
- Thernisien, A. 2011, The Astrophysical Journal Supplement Series, 194, 33
- Thernisien, A., Vourlidas, A., & Howard, R. 2009, Solar Physics, 256, 111
- Thompson, B. & Young, C. 2016, The Astrophysical Journal, 825, 27
- Thompson, B. c., Gurman, J., Neupert, W., et al. 1999, The Astrophysical Journal, 517, L151
- Thompson, B. J. & Myers, D. C. 2009, *Astrophys. J. Suppl.*, 183, 225
- Thompson, B. J., Plunkett, S. P., Gurman, J. B., et al. 1998, *grl*, 25, 2465
- Thompson, W. T. 2006, *A&A*, 449, 791
- Torsti, J., Valtonen, E., Lumme, M., et al. 1995, *Sol. Phys.*, 162, 505
- Trottet, G., Samwel, S., Klein, K.-L., Dudok de Wit, T., & Miteva, R. 2015, Solar Physics, 290, 819
- Truscott, P., Lei, F., Dyer, C., et al. 2000, in 2000 IEEE Radiation Effects Data Workshop. Workshop Record. Held in conjunction with IEEE Nuclear and Space Radiation Effects Conference (Cat. No. 00TH8527), IEEE, 147–152
- Tsurutani, B. T. 1985
- Tsurutani, B. T., Gonzalez, W. D., & Kamide, Y. 1997, Surveys in geophysics, 18, 363
- Vainio, R., Desorgher, L., Heynderickx, D., et al. 2009, Space science reviews, 147, 187
- Vainio, R. & Laitinen, T. 2008, Journal of Atmospheric and Solar-Terrestrial Physics, 70, 467
- van Diepen, G., Dijkema, T. J., & Offringa, A. 2018, Astrophysics Source Code Library, ascl
- van Haarlem, M. P., Wise, M. W., Gunst, A., et al. 2013, Astronomy & astrophysics, 556, A2
- Verbeeck, C., Delouille, V., Mampaey, B., & De Visscher, R. 2014, Astronomy and Astrophysics, 561, A29
- Verbeke, C., Mays, M. L., Kay, C., et al. 2022, Advances in Space Research
- Verkhoglyadova, O., Li, G., Zank, G., Hu, Q., & Mewaldt, R. 2009, The Astrophysical Journal, 693, 894
- Veronig, A., Muhr, N., Kienreich, I., Temmer, M., & Vršnak, B. 2010, The Astrophysical Journal Letters, 716, L57
- Vourlidas, A., Syntelis, P., & Tsinganos, K. 2012, Solar Physics, 280, 509
- Vourlidas, A., Wu, S. T., Wang, A. H., Subramanian, P., & Howard, R. A. 2003, *apj*, 598, 1392
- Vršnak, B. & Cliver, E. W. 2008, Solar Physics, 253, 215

- Vršnak, B., Žic, T., Vrbanec, D., et al. 2013, Solar physics, 285, 295
- Warmuth, A. 2015, Living Reviews in Solar Physics, 12, 1
- Webb, D. F. & Howard, T. A. 2012, Living Reviews in Solar Physics, 9, 1
- Whitman, K., Egeland, R., Richardson, I. G., et al. 2023, Advances in Space Research, 72, 5161, cOSPAR Space Weather Roadmap 2022: Scientific Research and Applications
- Wild, J. 1950a, Australian Journal of Chemistry, 3, 399
- Wild, J. 1950b, Australian Journal of Chemistry, 3, 541
- Wild, J. & McCready, L. 1950, Australian Journal of Chemistry, 3, 387
- Wild, J., Smerd, S., & Weiss, A. 1963, Annual Review of Astronomy and Astrophysics, 1, 291
- Wills-Davey, M., DeForest, C., & Stenflo, J. O. 2007, The Astrophysical Journal, 664, 556
- Wilson, J. W., Townsend, L. W., Chun, S. Y., et al. 1988, BRYNTRN: A baryon transport computer code, computation procedures and data base, Tech. rep.
- Wöllmer, M., Zhang, Z., Weninger, F., Schuller, B., & Rigoll, G. 2013, in 2013 IEEE International Conference on Acoustics, Speech and Signal Processing, IEEE, 6822–6826
- Wood, B., Howard, R., & Socker, D. 2010, The Astrophysical Journal, 715, 1524
- Wu, C.-C. & Lepping, R. P. 2016, Solar Physics, 291, 265
- Wu, C. S., Wang, C. B., Yoon, P. H., Zheng, H. N., & Wang, S. 2002, The Astrophysical Journal, 575, 1094
- Wuelser, J.-P., Lemen, J. R., Tarbell, T. D., et al. 2004, in Society of Photo-Optical Instrumentation Engineers (SPIE) Conference Series, Vol. 5171, Telescopes and Instrumentation for Solar Astrophysics, ed. S. Fineschi & M. A. Gummin, 111–122
- Xapsos, M. A., Stauffer, C. A., Jordan, T. M., Adams, J. H., & Dietrich, W. F. 2012, IEEE Transactions on Nuclear Science, 59, 1054
- Xie, H., Ofman, L., & Lawrence, G. 2004, Journal of Geophysical Research: Space Physics, 109
- Young, P. R., Tian, H., Peter, H., et al. 2018, Space Science Reviews, 214, 1
- Zank, G., Matthaeus, W., Bieber, J., & Moraal, H. 1998, Journal of Geophysical Research: Space Physics, 103, 2085
- Zhang, J., Cheng, X., & Ding, M.-d. 2012, Nature communications, 3, 747
- Zhang, J. & Dere, K. P. 2006, apj, 649, 1100
- Zhang, J., Richardson, I., Webb, D., et al. 2007, Journal of Geophysical Research: Space Physics, 112
- Zhang, P., Wang, C., Ye, L., & Wang, Y. 2019, Solar Physics, 294, 62
- Zhang, P., Wang, C. B., & Ye, L. 2018, Astronomy & Astrophysics, 618, A165
- Zhang, P., Zucca, P., Kozarev, K., et al. 2022a, The Astrophysical Journal, 932, 17
- Zhang, W., Zhao, X., Feng, X., et al. 2022b, Universe, 8, 30
- Zhu, H., Zhu, W., & He, M. 2022, Solar Physics, 297, 157